e-ISSN : 2776-2521

JOCPES

Journal of Computation Physics and Earth Science

Volume 5 No. 2
February, 2026

Email:
adm.jocpes@gmail.com
admin@physan.org

https://journal.physan.org/index.php/jocpes

Journal of Computation Physics and Earth Science
ISSN: 2776-2521 (online)
Volume 5, Number 2, February 2026, Page 129 - 136
https://journal.physan.org/index.php/jocpes/index

Design and Implementation of a Web-Based RFID-Enabled Library Visitor Attendance and Management System: A Case Study at STMKG

Ahmad Meijlan Yasir[1], Tonny Wahyu Aji[2],
[1,2]Undergraduate Program in Applied of Instrumentation Meteorology, Climatology Geophysics (STMKG)

Article Info

Article history:

Received December 31, 2025
Revised February 28, 2026
Accepted February 28, 2026

Keywords:

Library Management System
RFID
Information System
Digitalization
STMKG

A B S T R A C T

This study presents the design and implementation of a web-based, RFID-enabled library visitor attendance and management system as a single-site case study at STMKG. Academic libraries require structured visit data to support service evaluation and institutional reporting, yet manual logbooks often produce inconsistent records and limit timely analysis. To address this issue, the proposed system digitalizes attendance capture through three integrated workflows within one platform: RFID-based identification for cadets, controlled selection for employees, and a structured manual form for public visitors. The system also provides administrative capabilities for monitoring and reporting, including visit statistics dashboards, time-filtered logs with search, and spreadsheet export for routine reporting needs. The implementation adopts a cloud-backed architecture using a modern web application frontend and a managed backend with database persistence and authentication services. Baseline security controls were incorporated to protect administrative functions and reduce automated abuse at public-facing entry points, including access verification, bot protection, and database-level access boundaries. Functional verification through end-to-end scenario testing confirms that the core attendance workflows, reporting features, and security mechanisms operate as intended within the defined scope. The resulting artifact is deployable in STMKG and can be adapted for similar higher-education libraries seeking practical visitor attendance digitalization.

Corresponden Author:

Ahmad Meijlan Yasir,
Undergraduate Program in Applied of Instrumentation Meteorology, Climatology Geophysics (STMKG)
Tangerang, Indonesia
Email: yasirahmad220504@gmail.com

1. INTRODUCTION

Academic libraries routinely collect operational metrics to evaluate services and support institutional benchmarking. One of the most widely used indicators is visitor traffic, often measured as annual gate counts, which reflects the level of physical space utilization within library facilities. Large-scale benchmarking initiatives across higher education institutions use these metrics to compare operational performance and inform strategic planning for library services [1], [2]. Because visitor attendance data directly represent how frequently library spaces are used, these records become an essential evidence base for managerial decision making, including adjustments to service hours, staffing allocation, and infrastructure investment [3], [4]. Consequently, the availability of accurate and structured attendance data is a critical requirement for modern library management.

Despite the importance of this data, many institutions still rely on manual recording procedures or fragmented visitor management practices [1], [2]. Similar conditions were observed at the library of Sekolah Tinggi Meteorologi Klimatologi dan Geofisika (STMKG), where visitor attendance was historically recorded using physical logbooks and a conventional barcode-based system. Such approaches limit data accuracy, create inconsistencies in record formats, and complicate the generation of timely reports required for administrative evaluation [4], [5]. The modernization of operational systems within STMKG is part of a broader institutional effort to improve digital services and optimize user interaction across information platforms [6]. Within this context, the library environment presents a specific operational challenge because the attendance system must simultaneously accommodate three categories of visitors, namely cadets, internal staff, and public visitors. Without a systematic identification mechanism, the process of verifying visitor identity becomes a significant operational bottleneck that reduces service efficiency and reliability [1], [5].

Radio Frequency Identification (RFID) technology has been widely adopted in library environments to support fast and contactless identification of users, thereby reducing congestion at service entry points [7], [8]. However, standalone RFID deployments may introduce new concerns related to data integrity and security. Empirical studies have demonstrated that certain low-frequency RFID cards without encryption mechanisms are vulnerable to cloning attacks using widely available tools such as Proxmark3, highlighting the importance of complementary security mechanisms at the system level [9], [10]. In addition to hardware-related vulnerabilities, web-based attendance endpoints are also exposed to automated abuse by bots that repeatedly submit requests to exploit open interfaces. While many studies in RFID-based library automation focus on communication protocols between the card and the reader, comparatively less attention has been given to end-to-end security architectures that extend protection to the application layer and backend infrastructure.

These challenges indicate the need for an integrated system architecture that combines RFID-based identification with a structured web-based visitor management workflow while incorporating practical security controls. A unified system can enforce consistent data validation, store visit records in a centralized database, and provide administrative monitoring capabilities for reporting and analysis. At the same time, protective mechanisms such as bot-abuse mitigation and database-level authorization are necessary to preserve data integrity and system availability when attendance endpoints are publicly accessible.

Therefore, this study aims to design and implement a web-based RFID-enabled library visitor attendance and management system as a single-site case study at STMKG. The proposed system integrates RFID-based identification with a multi-category visitor workflow and centralized reporting features within a cloud-backed architecture. The contributions of this work are threefold. First, the study presents an end-to-end system design that supports RFID-based attendance capture alongside structured workflows for staff and public visitors. Second, it documents an implementation approach that combines a modern web application architecture with database-level authorization and bot-abuse mitigation mechanisms. Third, the study reports functional verification of key system capabilities, including attendance capture workflows, administrative reporting functions, and baseline security controls. The scope of the study is limited to the STMKG library environment, and user acceptance evaluation is outside the scope of this work

2. RESEARCH METHOD

This study follows a design-and-implementation approach, framed as a single-site case study at STMKG. The research output is a deployable software artifact that operationalizes library visitor attendance and management through a web interface and RFID-based identification for cadets, complemented by structured workflows for employees and public visitors. The method is organized into four stages: requirements elicitation, system design, implementation, and functional verification.

2.1. Requirements Elicitation

Requirements were derived from the operational workflow of STMKG library attendance, emphasizing a minimal but complete set of functions to record visits consistently and to support administrative reporting. The resulting functional and security requirements are summarized in Table 1, which is later used to maintain traceability to implemented modules (Section 3.1) and verification scenarios (Section 3.5).

Table 1. Summary of functional and security requirements

ID	Requirement	Operational intent
FR1	Support cadet attendance via RFID by resolving rfid_data to cadets and recording a visit in visitors	Reduce manual entry and standardize cadet identification
FR2	Support employee attendance via controlled selection from employees and record a visit in visitors	Ensure consistent employee records without free-text ambiguity
FR3	Support public visitor attendance via structured form input and record a visit in visitors	Enable standardized capture for external visitors
FR4	Provide RFID registration flow when an RFID is unregistered, with NPT format validation and RFID uniqueness	Preserve data integrity and prevent duplicate identifiers
FR5	Provide admin dashboard for visit statistics and a reporting module with filtering, search, and Excel export	Produce operational summaries and institutional reports efficiently
SR1	Enforce database access boundaries using row-level security: anon limited to lookup and visit insert, admin to management CRUD	Prevent unauthorized reads or edits while keeping attendance usable

ID	Requirement	Operational intent
SR2	Protect landing access with credential verification via landing-verify and bot protection via Turnstile	Reduce unauthorized usage and automated abuse on the attendance endpoint
SR3	Protect admin login with Turnstile validation and lockout after repeated failures	Reduce bot attempts and brute force against admin access

Table 1 reflects the need to accommodate three visitor categories within one platform, while ensuring that reporting and baseline security controls are available for operational deployment at STMKG.

2.2. System Design

The system was designed as a web application connected to a cloud backend, with RFID serving as an identifier input for cadet attendance. The frontend was implemented as a single-page application, while the backend relied on Supabase services, including PostgreSQL for persistence, authentication for administrator access, and Edge Functions for security-critical operations [11]. The core database schema was defined around five main tables: *admins*, *cadets*, *employees*, *rfid_data*, and *visitors*. The *rfid_data* table maps an RFID number to a cadet identifier (NPT), and the visitors table stores a unified visit log across all visitor types, enabling consistent reporting regardless of capture method.

Access control was enforced at the database layer using row-level security policies. In the deployed configuration, unauthenticated clients were restricted to read-only lookups for attendance resolution and were permitted only to insert visit records, while authenticated administrators were granted the CRUD privileges required for management and reporting functions. Security-sensitive flows were designed to minimize client exposure of privileged logic. Specifically, landing access verification was performed through an Edge Function that returns only a boolean validation result without creating a Supabase session on the client, and administrative login was protected with robot verification and lockout controls.

2.3. System Implementation

The artifact was implemented using a modern web stack to support maintainability and deployment simplicity. The frontend was built with React and TypeScript, while integration with backend services was handled through the Supabase JavaScript client and Edge Functions. Three visitor attendance workflows were implemented on the landing interface: (1) RFID-based cadet attendance using a lookup chain from rfid_data to cadets, followed by insertion into visitors; (2) employee attendance via dropdown selection sourced from employees; and (3) public visitor attendance via a structured form. If an RFID number is not registered, the system redirects to a registration page where the RFID number is prefilled and an NPT format constraint is enforced at the database layer to preserve data consistency.

Administrative functions were implemented under a protected route group, including login, dashboard statistics, master data management for cadets and employees, visit reporting with time filters and search, and spreadsheet export. The system includes bot protection through Cloudflare Turnstile on both landing verification and admin login, with server-side validation performed by the verify-turnstile Edge Function. Deployment was designed for a cloud-native setup where the web frontend can be hosted on Vercel and backend services operate within Supabase.

2.4. Functional Verification

Verification was limited to functional testing of critical end-to-end scenarios as a checklist, without user acceptance evaluation. The scenarios in Table II cover landing access verification, the three attendance paths, the unregistered RFID registration path, administrative reporting and export, and core security controls aligned with Table 1.

Table 2. Functional testing scenarios and outcomes

ID	Test scenario	Expected outcome
FT1	Landing verification with credentials and Turnstile	Access to attendance workflows is granted only after valid verification
FT2	RFID attendance with registered RFID and existing cadet	Visit record is inserted into visitors with type cadets, then redirected to welcome page
FT3	RFID attendance with unregistered RFID	User is redirected to /register with RFID number prefilled
FT4	Employee attendance submission	Visit record is inserted into visitors with type employee, then redirected to welcome page
FT5	Public visitor attendance submission	Visit record is inserted into visitors with type public, then redirected to welcome page
FT6	Admin login with username resolution, Turnstile, and lockout policy	Successful login requires Turnstile; repeated failures trigger lockout behavior
FT7	Dashboard and report retrieval	Admin can view statistics and query visit logs using filters and search

ID	Test scenario	Expected outcome
FT8	Export visit report to Excel	System generates an Excel file containing the visit log with required columns

Table 2 is referenced in Section 3.5 to report verification coverage and to demonstrate alignment with the requirements in Table 1.

3. RESULT AND DISCUSSION

3.1. Results of Requirements Analysis

The requirements analysis identified a minimal set of capabilities needed to operationalize visitor attendance at the STMKG library while producing structured outputs for administration. Functionally, the system must support three visitor categories within a single, consistent logging model: cadets recorded through RFID-based identification, employees recorded through controlled selection to avoid ambiguous free-text entries, and public visitors recorded through a structured manual form. To ensure operational continuity, an RFID enrollment path is also required when an RFID number is not yet registered, including identifier validation to preserve data consistency.

From the administrative perspective, the requirements emphasize monitoring and reporting rather than complex workflows. The system must provide a dashboard that summarizes visit trends, and a reporting module that supports time-based filtering, search, and export to spreadsheet format to enable routine institutional reporting. These features ensure that visit records are not only captured but also transformed into usable summaries without manual recapitulation.

Security requirements were defined as baseline controls appropriate for a publicly reachable attendance endpoint. The system must restrict administrative functions to authenticated users and include bot-abuse mitigation at public-facing verification and login steps. In addition, database-layer access boundaries are required to ensure that unauthenticated usage is limited to attendance-related lookups and visit record insertion, while administrative data management remains restricted. Table 3 summarizes the finalized functional and security requirements that guide the implementation discussed in subsequent sections.

Table 3. Finalized Functional and Security Requirements

ID	Requirement	Rationale
FR1	Record cadet attendance via RFID by resolving RFID to a cadet identifier and logging the visit	Automate identification and reduce manual entry errors
FR2	Record employee attendance via controlled selection and log the visit	Ensure consistent internal visitor records
FR3	Record public visitor attendance via structured manual form and log the visit	Provide standardized capture for external visitors
FR4	Provide RFID registration for unregistered RFID numbers with identifier validation and uniqueness checks	Maintain data integrity and prevent duplicate identifiers
FR5	Provide an admin dashboard for visit statistics and a reporting module with time filtering, search, and spreadsheet export	Enable routine monitoring and institutional reporting
SR1	Enforce database-layer access boundaries so unauthenticated clients are limited to necessary lookups and visit insertion	Prevent unauthorized access while keeping attendance usable
SR2	Require access verification at the attendance entry point and apply bot protection	Reduce unauthorized use and automated abuse
SR3	Protect admin login with bot protection and lockout after repeated failures	Reduce brute-force attempts against admin access

These requirements establish a complete but bounded scope for an operational attendance system, where data capture, reporting, and baseline security controls are treated as first-class design objectives.

3.2. System Architecture and Design

The implemented system adopts a web-and-cloud architecture where a browser-based single-page application performs visitor-facing attendance capture and administrative management, while Supabase provides the backend services for persistence, authentication, and server-side security logic. The architecture also integrates Cloudflare Turnstile for bot protection, validated server-side using an Edge Function.

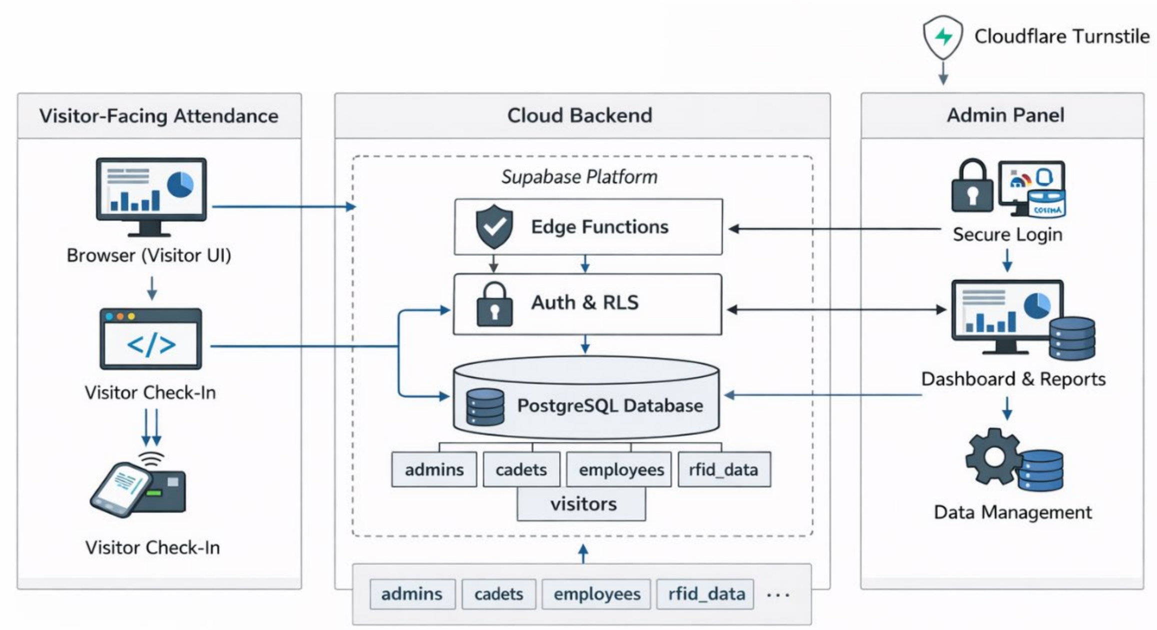

Fig. 1. High-level system architecture and component interactions

At the data layer, the design uses a unified visit log to support consistent reporting across all visitor types. The schema is organized around five core tables: admins, cadets, employees, rfid_data, and visitors, where rfid_data maps RFID numbers to cadet identifiers (NPT) and visitors stores the final visit record used for analytics and reporting. This design reduces fragmentation and allows the reporting module to operate over a single visit dataset regardless of the capture method.

3.3. Results of Requirements Analysis

The system was implemented as two main surfaces: a visitor-facing landing interface and an admin panel. The landing interface is the operational entry point and supports three attendance modes after a mandatory access verification step. The admin panel provides secured access to dashboards and data management modules, including master data maintenance for cadets and employees and visit reporting with export.

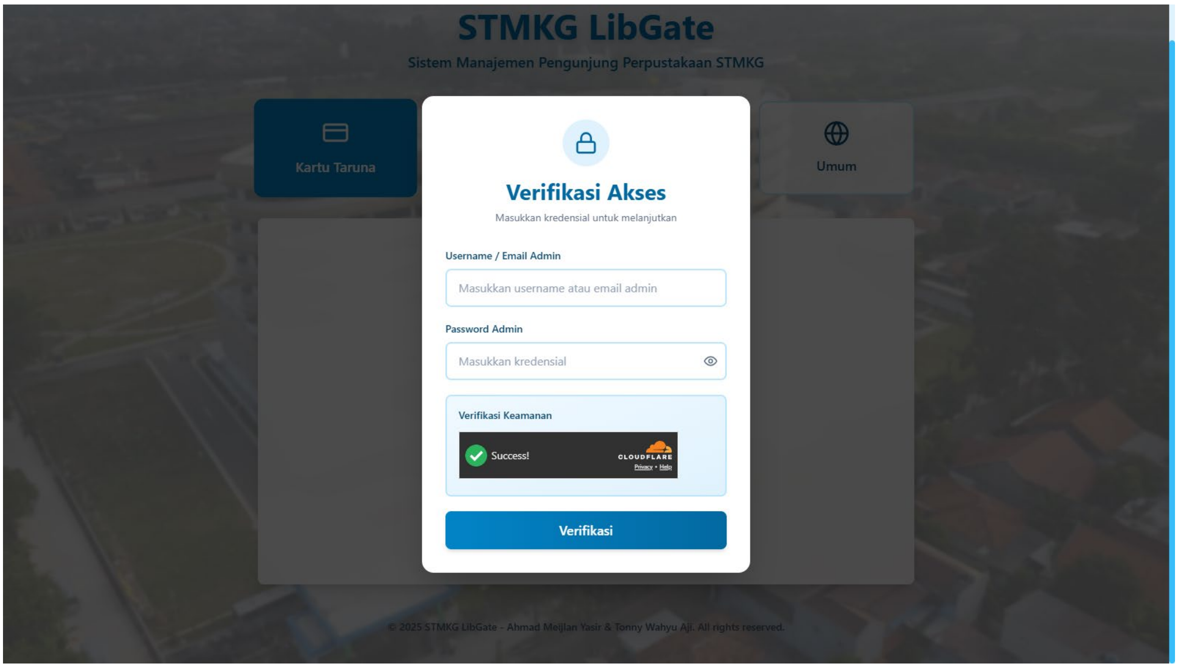

Fig. 2. Access verification form

Fig. 3. Main page for visitor attendance

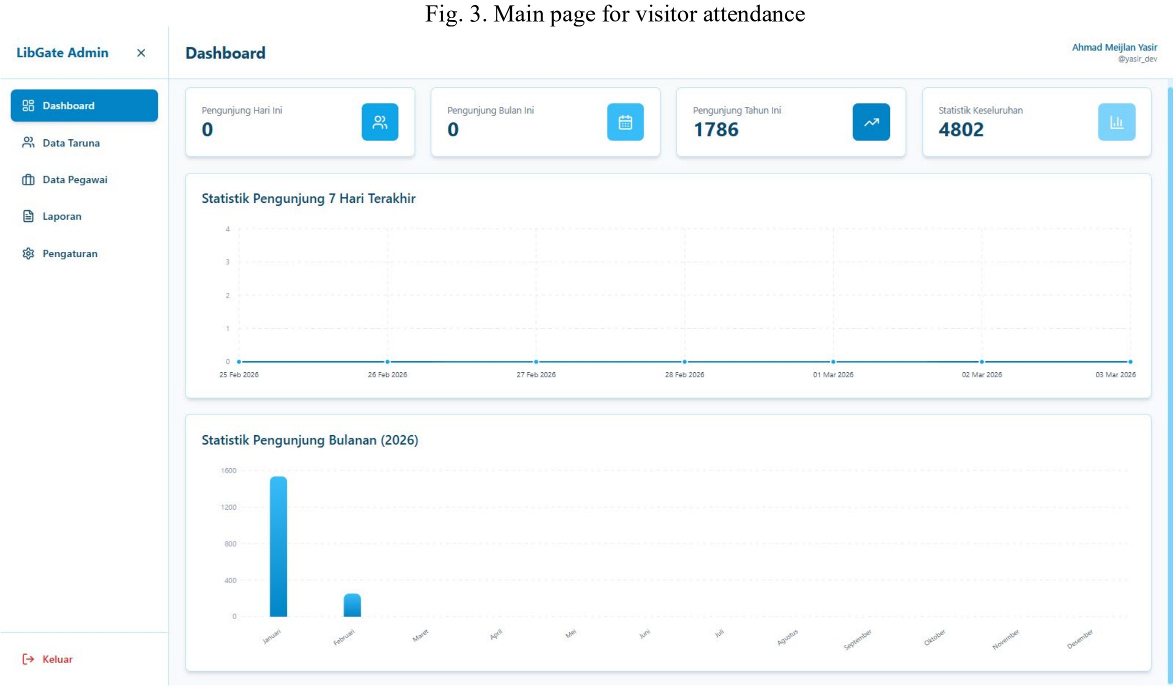

Fig. 3. Administrator panel

For reporting, the admin module includes time-window filtering, search, pagination, and Excel export with relevant columns such as timestamp, visitor name, visitor type, and cadet-derived fields when available. These features operationalize the reporting requirement without requiring manual recapitulation from paper logs.

3.4. RFID Integration

RFID integration is implemented as an identifier-driven workflow for cadet attendance. On RFID input, the system queries rfid_data to resolve the RFID number into an NPT, then queries cadets to obtain cadet details, and finally inserts the visit into visitors with type cadets. When an RFID number is not registered or the NPT cannot be resolved to an existing cadet record, the system redirects to /register with the RFID number prefilled to support controlled enrollment.

Data integrity for RFID enrollment is supported by database constraints, including NPT format validation and uniqueness constraints on both NPT and RFID number. This design reduces common failure modes of manual logging, such as inconsistent identifiers and duplicate entries, while preserving a manual path for non-cadet visitor types.

3.5. Functional Testing Results

Functional verification was conducted as scenario-based end-to-end checks aligned with Table I requirements. Each scenario validated both the user-visible behavior and the expected database state changes. The outcomes are summarized in Table 4.

Table 4. Functional Testing Outcomes

Scenario ID	Scenario (summary)	Result
FT1	Landing verification with credentials and Turnstile	Pass
FT2	RFID attendance with registered RFID and existing cadet	Pass
FT3	RFID attendance with unregistered RFID redirects to /register	Pass
FT4	Employee attendance submission via dropdown	Pass
FT5	Public visitor attendance submission via form	Pass
FT6	Admin login with Turnstile and lockout policy	Pass
FT7	Dashboard and report retrieval under authenticated admin	Pass
FT8	Export report to Excel	Pass

The results indicate that the minimal operational feature set in Table 1 is supported end-to-end, including the attendance capture paths, reporting workflow, and baseline protections required for deployment. No user acceptance evaluation is reported in this study, and the verification is restricted to functional correctness under the defined scenarios.

3.6. Security Mechanisms

Security controls are implemented at both the application and database layers. First, administrative identity is handled exclusively through Supabase Auth, while the system supports username-based login by resolving the username to an email via an Edge Function (resolve-admin-email) that uses service-role privileges. This avoids exposing the admins table to unauthenticated clients, consistent with the RLS configuration.

Second, the visitor-facing attendance endpoint is protected by a landing verification gate. The landing-verified Edge Function performs credential verification and returns only a boolean validation response, without creating a Supabase session on the client, and a per-browser trusted state is stored locally to reduce repeated prompts on the same device. Bot protection is applied to both landing verification and admin login using Cloudflare Turnstile, with server-side token validation performed by the verify-turnstile Edge Function. Finally, rate limiting and lockout behavior are enforced after repeated failures to reduce brute-force attempts against the verification and login flows.

At the database layer, row-level security policies enforce clear boundaries between unauthenticated attendance usage and authenticated administrative management. Unauthenticated clients are limited to lookup access for resolving attendance inputs and are permitted only to insert visit records, while authenticated administrators receive CRUD permissions consistent with management and reporting functions. This layered design supports the operational requirement of a publicly usable attendance interface while maintaining controlled access to administrative capabilities and sensitive data.

4. CONCLUSION

This paper presented the design and implementation of a web-based, RFID-enabled library visitor attendance and management system as a case study at STMKG. The system was developed to replace fragmented manual recording with a consistent digital workflow that supports three visitor categories within a unified visit log. Cadet attendance is captured through RFID-based identification, while employee visits are recorded through controlled selection and public visits through a structured manual form. Administrative functions were implemented to transform visit records into actionable outputs, including a statistics dashboard, report filtering and search, and spreadsheet export to support routine institutional reporting.

Beyond attendance capture, the implementation emphasizes deployable baseline security appropriate for a publicly reachable attendance endpoint. Administrative capabilities are restricted to authenticated users, bot-abuse mitigation is applied to the entry verification and login flows, and database-layer access boundaries are enforced to separate unauthenticated attendance usage from privileged management operations. Functional verification confirmed that critical end-to-end scenarios, including the three attendance paths, RFID registration for unregistered cards, reporting and export, and the essential security mechanisms, operate as intended within the defined scope.

The primary contribution of this work is a practical, end-to-end artifact that can be adopted in STMKG and adapted to similar higher-education libraries that require reliable attendance capture and structured reporting. The study is limited to a single institutional environment and does not include user acceptance evaluation, so broader generalization should be approached cautiously. Future work may incorporate usability and acceptance studies, multi-site replication, integration with institutional academic information systems, and longitudinal analysis of visit data to further support evidence-based library service improvements.

REFERENCE

[1] S. Mitha and M. Omarsaib, ‘Emerging Technologies and Higher Education Libraries: A Bibliometric Analysis of the Global Literature’, *Libr. Hi Tech*, vol. 43, no. 2–3, pp. 1248–1270, 2024, doi: 10.1108/lht-02-2024-0105.

[2] S. Nakaziba and P. Ngulube, ‘Harnessing Digital Power for Relevance: Status of Digital Transformation in Selected University Libraries in Uganda’, *Collect. Curation*, vol. 43, no. 2, pp. 33–44, 2024, doi: 10.1108/cc-11-2023-0034.

[3] K. Banleman, B. K. Dukper, and L. D. Banleman, ‘Evaluation of Academic Library Services and Programs in Ghana: Insight From the Sd Dombo University of Business and Integrated Development Studies’, *Int. J. Appl. Res. Soc. Sci.*, vol. 6, no. 1, pp. 89–105, 2024, doi: 10.51594/ijarss.v6i1.734.

[4] K. N. Igwe and A. S. Sulyman, ‘Smart Libraries: Changing the Paradigms of Library Services’, *Bus. Inf. Rev.*, vol. 39, no. 4, pp. 147–152, 2022, doi: 10.1177/02663821221110042.

[5] A. A. Adewojo and O. P. Monjolaoluwa, ‘Smart Library Environments: IoT and Automation for Next-Generation Services’, *Bus. Inf. Rev.*, 2025, doi: 10.1177/02663821251384884.

[6] T. W. Aji *et al.*, ‘Redesign of User Interface and Experience with Brand Identity Enhancement for the STMKG Website through WordPress Implementation’, *J. Comput. Phys. Earth Sci.*, vol. 5, no. 1, 2025, doi: 10.63581/JoCPES.v5i1.15.

[7] S. Saha and M. Roknuzzaman, ‘Library Practitioners’ Perceptions on the Applications of IoT in University Libraries of Bangladesh’, *Libr. Manag.*, vol. 45, no. 1/2, pp. 141–156, 2024, doi: 10.1108/lm-07-2023-0072.

[8] S. M. Wagner, M. Ramkumar, G. Kumar, and T. Schoenherr, ‘Supporting Disaster Relief Operations Through RFID: Enabling Visibility and Coordination’, *Int. J. Logist. Manag.*, vol. 35, no. 6, pp. 1681–1712, 2024, doi: 10.1108/ijlm-12-2022-0480.

[9] H. A. Abdulghani, N. A. Nijdam, and D. Konstantas, ‘Analysis on Security and Privacy Guidelines: RFID-Based IoT Applications’, *Ieee Access*, vol. 10, pp. 131528–131554, 2022, doi: 10.1109/access.2022.3227449.

[10] M. I. Khan, H. Tahir, M. I. Jobiullah, A. R. A. Khan, S. A. Begum, and I. Hafeez, ‘Enhancing IoT Security: A Lightweight Cloning Approach for RFID/NFC Access Control Systems’, *CDF*, vol. 52, no. 2, pp. 231–248, 2023, doi: 10.48047/qy0g4n52.

[11] A. M. Yasir *et al.*, ‘Comparative Performance Analysis of Firebase Realtime Database and Supabase Using Multi-Method Testing Approaches’, in *2025 5th International Conference on Electronic and Electrical Engineering and Intelligent System (ICE3IS)*, 2025, pp. 303–308. doi: 10.1109/ICE3IS66769.2025.11281116.

Journal of Computation Physics and Earth Science
ISSN: 2776-2521 (online)
Volume 5, Number 2, February 2026, Page 137 - 144
https://journal.physan.org/index.php/jocpes/index

Design and Implementation of an IoT-Based 3-Phase Electricity Usage Monitoring System: Case Study at Geophysics Station Class I Sleman, Yogyakarta

Arfany Dhimas Muftareza[1], Bagas Pamungkas Saputra[2], Dimas Aditya Wiranata[3], Fahar Rafif Arganto[4], Hilldegard Virgil Richard May[5], Kholid Amirudin[6], Muhammad Arya Bintang Pratama[7], Muhammad Ramdhani Setyo Nugroho[8], Arif Kurniawan[9]
[1,2,3,4,5,6,7,8]Undergraduate Program in Applied Instrumentation Meteorology, Climatology, and Geophysics (STMKG)
[9]Geophysics Station Class I Sleman (BMKG)

Article Info

Article history:

Received December 31, 2025
Revised March 2, 2026
Accepted March 2, 2026

Keywords:

Internet of Things (IoT)
ESP32
PZEM-004T
W5500
Website

A B S T R A C T

Efficient electrical energy management is increasingly important in supporting the sustainability of institutional operations and national budget efficiency policies. This study presents the design and implementation of an Internet of Things (IoT)-based 3-phase electricity usage monitoring system implemented at the Sleman Class I Geophysical Station, Yogyakarta. This system integrates a PZEM-004T energy sensor, an ESP32 microcontroller, a 16x2 Liquid Crystal Display, and a W5500 Ethernet module to acquire, process, and transmit real-time electrical parameters, including voltage, current, and kWh. A local network topology is implemented to ensure stable data transmission to a MySQL-based database server, which allows storing data according to a predefined table structure. A web-based user interface is developed to visualize real-time measurements, historical graphs, and electricity cost estimates. Several features are also developed. System evaluation is conducted by comparing the developed instrument with the official PLN kWh meter. Statistical analysis shows an average difference of 0.021 kWh with a standard deviation of 0.02132 kWh. The linear regression results show a slope of 1.000349, an intercept of −3.589572, and a coefficient of determination (R^2) of 0.9999988, indicating a near-perfect linear correlation. Error metrics including MAE (0.01934 kWh), RMSE (0.02696 kWh), and MAPE (0.0001885%) confirm the high accuracy and precision of the system. Therefore, the proposed system is reliable for real-time internal energy monitoring and supports data-driven electricity usage optimization.

Corresponden Author:

Arfany Dhimas Muftareza,
Undergraduate Program in Applied Instrumentation Meteorology, Climatology, and Geophysics (STMKG)
Tangerang, Indonesia
Email: arfanydhimuf@gmail.com

1. INTRODUCTION

Electrical energy usage in a building needs to be monitored and integrated to improve operational efficiency, optimize load management, and support data-based energy conservation strategies in smart building systems [1]. Internet of Things (IoT) is a technology paradigm that connects various physical devices through an internet network, enabling the process of collecting, exchanging, and analyzing data in real-time to support intelligent and automated systems has become very relevant [2]. The success of implementing IoT in electricity monitoring systems is demonstrated through the ability to acquire real-time energy consumption data, increase the accuracy of load analysis, and optimize energy management in smart building environments [3]. This approach also contributes to achieving long-term energy efficiency through adaptive control and dynamic response to changing electricity consumption patterns [4].

The application of microcontrollers in smart buildings acts as a control center in IoT systems to acquire sensor data, process information locally, and send data to monitoring platforms to increase the efficiency and automation of building energy management [5]. ESP32 implementations are very commonly used due to their built-in Wi-Fi capabilities that support wireless connections in Internet of Things (IoT) applications [6] and can transmit data via various communication protocols [7][8]. The PZEM-004T module is a digital-based electrical energy sensor that is capable of acquiring comprehensive electrical parameters including voltage, current, active power, energy, power factor, and frequency via serial communication, making it widely used in electrical monitoring systems [9][10][11]. The exchange of data between microcontrollers and sensors employs various communication protocols—such as UART, I2C, SPI, and Wi-Fi—selected based on system requirements including data rate, distance, power consumption, and hardware compatibility in Internet of Things (IoT) applications [12][13].

In an effort to improve the efficiency of national budget utilization, the Government of Indonesia has issued Presidential Instruction (Inpres) Number 1 of 2025 concerning Expenditure Efficiency in the Implementation of the State Budget (APBN) and Regional Budget (APBD) for the 2025 Fiscal Year. This Presidential Instruction mandates all ministries, government agencies, and local governments to conduct budget reviews and implement expenditure savings, with a targeted efficiency of IDR 306.69 trillion, consisting of IDR 256.1 trillion from ministries/agencies' expenditures and IDR 50.59 trillion from intergovernmental transfers to regions [14]. As part of the Meteorology, Climatology, and Geophysics Agency (BMKG), the Class I Sleman Geophysical Station Technical Implementation Unit (UPT) Yogyakarta is obligated to support this budget efficiency policy. One concrete action that can be taken is to optimize the use of electrical energy through an effective electricity usage monitoring system, because real-time energy monitoring allows the identification of inefficiencies and supports optimal energy management strategies and cost reductions [15].

In practice, electricity usage monitoring is done manually using conventional kWh meters located far from the office operational building, making it less efficient and seems to drain energy and time if done periodically and routinely, as well as hindering electricity load analysis and slowing down decision making related to energy savings. This research aims to develop a 3-phase electricity usage monitoring system that is able to record, process, and display electricity usage data in real-time. This system is expected to help the Class I Sleman Geophysical Station Technical Implementation Unit (UPT) in monitoring electricity usage more effectively, supporting the identification of wasteful electricity loads, and increasing budget efficiency in accordance with central government directives.

2. RESEARCH METHOD

2.1 Conceptual Framework and Methodology

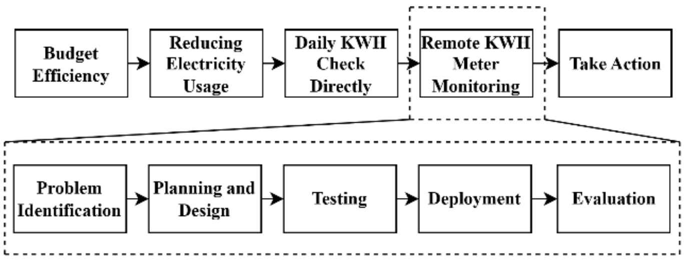

Figure 1. Conceptual Framework and Methodology

The Class I Geophysical Station in Sleman, Yogyakarta, is required to manage its resources more efficiently and measurably. One sector focused on efficiency is electricity usage. One initial step implemented was to record electricity usage (kWh) every morning by directly observing the readings on the PLN electricity meter. However, the location of the main panel, which is quite far from the operational building, presents a challenge. Therefore, an automated system is needed to record electricity usage periodically. With real-time electricity usage information available, all employees can make quick and informed decisions about energy conservation.

The process begins with the identification and analysis of problems related to the limitations in monitoring daily electricity usage in real-time due to the distance of the PLN main panel from the operational area. From this analysis, system requirements are formulated. The next stage is system planning and design, which includes hardware selection and software design. After the design stage, the system enters the prototype testing phase. The success of the prototype forms the basis for full system implementation or deployment within the UPT environment. During the evaluation stage, the results of electrical energy readings from the device are compared with reference data from the PLN kWh meter and will be analyzed further.

2.2 Design of Hardware

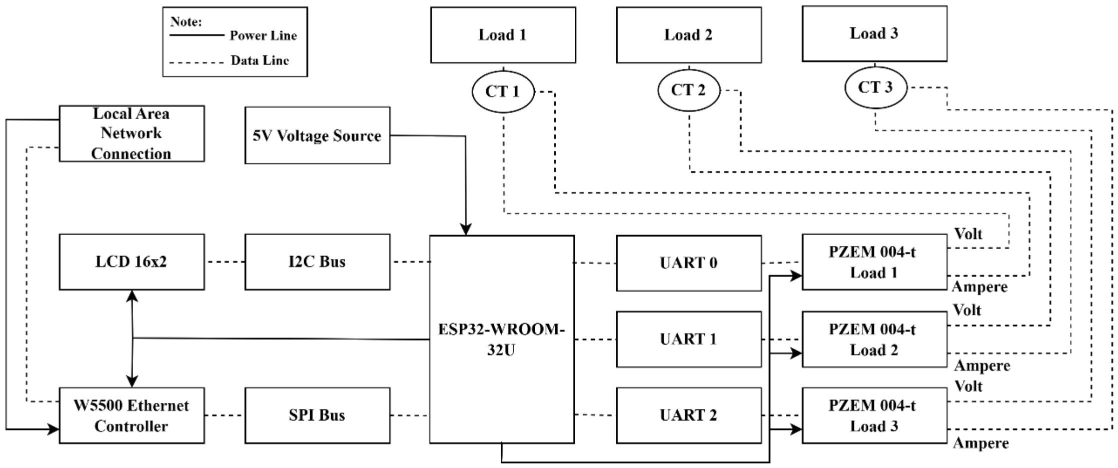

Figure 2. Design of Hardware

In this electricity usage monitoring system, the connection between devices is carried out by considering the data communication needs and the interface protocol used. The PZEM-004T sensor communicates with the ESP32 using the UART (Serial) protocol, while the W5500 Ethernet module is connected via the SPI interface. In addition, the 16x2 I2C LCD is connected to the ESP32 using the I2C protocol. The pin selection on the ESP32 is adjusted to avoid conflicts between devices and to maintain communication efficiency. All devices are connected to a stable power supply from the 5V adapter and 3.3V regulator available on the ESP32, to maintain the stability of the system. With this systematic wiring arrangement, the system is able to acquire and transmit electricity measurement data accurately and in real-time via a LAN network to a local server.

2.3 Data Communication Topology

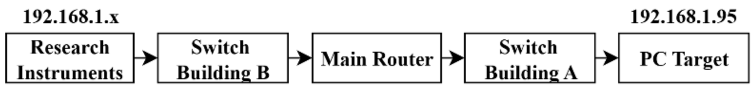

Figure 3. Data Communication Topology

The system developed in this research applies a local network topology as a data transmission medium between devices. The main device of the system is equipped with a W5500 Ethernet module, configured with a dynamic IP address on the local network with the format 192.168.1.x. This device is physically connected using a UTP cable to a network switch installed in the Graha Building. The switch has a direct connection to the central router of the office network, which functions as a data traffic controller and IP addressing in the LAN network. Another switch located in the Operational Room is also connected to the same router, thus allowing other devices, including the target PC which has a static IP of 192.168.1.95, to be able to receive data directly from the microcontroller through the same communication line.

2.4 Calculation of 3-Phase

The PZEM-004T sensor module installed on each load path (L1, L2, L3) only provides basic data in the form of voltage, current, and energy usage (kWh) per phase. To obtain a representation of the overall 3-phase system, aggregate calculations are performed using a microcontroller-based computing method.

The 3-phase voltage (V_{3ph}) is calculated using the Root Mean Square (RMS) method from the 3-phase voltages with the equation:

$$V_{3ph} = \sqrt{(V_1)^2 + (V_2)^2 + (V_3)^2} \tag{1}$$

Where V_1, V_2, and V_3 are the voltages on phases L1, L2, and L3 respectively.

The 3-phase current (I_{3ph}) is calculated adaptively based on the current availability conditions on each phase. The system applies conditional logic to calculate the average current only from active phases (value greater than zero), so that the calculation results remain representative even in the presence of unbalanced loads or inoperative phases. If all three phases are active, the 3-phase current is calculated as the arithmetic average of the three phases:

$$I_{3ph} = \frac{I_1 + I_2 + I_3}{3} \quad (2)$$

However, if only two phases are active, the 3-phase current is calculated from the average of both phases, and if only one phase is active, then the current value is directly used as I_{3ph}. If all phases are inactive, then I_{3ph} is set to zero.

The total 3-phase energy usage (kWh_{3ph}) is obtained by adding up the energy usage of the three phases and the initial energy value that was previously recorded:

$$kWh_{3ph} = kWh_1 + kWh_2 + kWh_3 \quad (3)$$

This calculation method allows the system to provide a comprehensive picture of 3-phase load conditions in real-time, while accommodating load imbalances that commonly occur in industrial and commercial electrical installations.

2.5 Design of Database

The database design for this research system is modular and structured to support the recording, monitoring, and analysis of electricity usage on an hourly, daily, and monthly basis, as well as displaying estimated electricity rates. This database uses the MySQL database management system and consists of several core tables, each with its own relationships and functions. Table 1 is a description of the main components in the database design.

Table 1. Design of Database

Tables	Information
data_kwh	Raw data storage center for electrical energy measurements on the PZEM-004t
data_jam_kwh	Record hourly electricity usage in kWh per hour.
data_harian_kwh	Records total daily electricity consumption calculated based on the accumulation of hourly consumption.
data_bulanan_kwh	An aggregation of daily data that stores the total number of kWh consumed each month.
baseline_kwh_harian	Stores initial kWh consumption data at the beginning of the day based on date.
tarif_terkini	Information on current electricity rates per kWh.
tarif_listrik_data	Record the electricity rates charged per day.
batas_kwh	Stores the daily consumption limit value determined as the electricity usage threshold.

2.6 User Interface

The user interface design for this web-based electricity usage monitoring information system was carried out using a modular and structured approach, using Visual Studio Code (VSCode) as the primary text editor. The programming languages used include HTML, CSS, JavaScript, and PHP, with integration with MySQL as the database management system (DBMS). This website is designed to present real-time and historical electricity measurement data, complete with visualizations and electricity rate calculations based on energy usage. The website consists of several main files, each with a specific role in data presentation and processing. This structure follows the principle of separation of concerns to separate the interface display, business logic, and database manipulation.

3. RESULTS AND DISCUSSION

Figure 4. Deployment Hardware and Software

The deployment phase aims to fully implement and integrate the system in a predetermined real-world environment. Deployment is carried out in stages, encompassing physical device installation, software system installation, and data communication network configuration. Installation is carried out with attention to occupational safety, electrical standards, and system reliability. All sensor and measurement system connections are protected using a waterproof and dustproof (IP65) panel enclosure to ensure long-term operational reliability. The average data transmission delay from the research instrument to the target PC data receiver is only 2 seconds (for example, data scheduled to be sent at 12:00 is received and recorded at 12:00:02). The successful integration of hardware and software systems enables comprehensive data acquisition and processing.

The system acquires electrical parameters through the PZEM-004T sensor, performs 3-phase calculations, and transmits the data to a target PC via a network communication protocol. All acquired data is processed based on predefined logic to make it more meaningful and used in highly useful features for users such as electricity usage alerts, data aggregation, and electricity bill estimation. The data is then systematically stored in a MySQL database according to a predefined table structure, ensuring data integrity and accessibility for long-term analysis. The visualization interface presents multiple layers of information. To increase flexibility and support further analysis, reporting, and administrative documentation, all data pages and tables are equipped with a data export feature that allows users to download records in CSV format for further processing or archiving purposes.

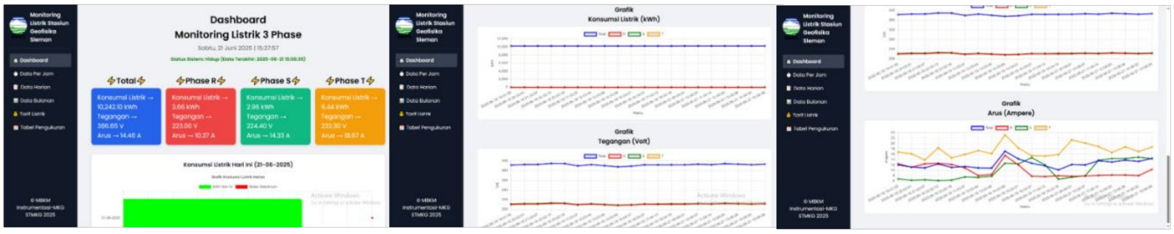

Figure 5. Dashboard Website

The developed web-based dashboard serves as a real-time interface that displays the latest voltage, current, and electricity usage (kWh) measurements for each phase (L1, L2, and L3), as well as aggregated results from the 3-phase calculations. The system continuously updates measurement data transmitted from embedded devices, allowing users to observe the latest electricity conditions. In addition to numerical indicators, the dashboard provides line graph visualizations for each parameter, depicting the temporal trends of 3-phase voltage, current, and electricity usage. This graphical representation serves as an analytical tool to support pattern recognition, load behavior evaluation, and anomaly detection in the electricity system. Furthermore, the platform includes a daily electricity consumption feature that displays the total kWh used on the current day. This feature is integrated with a configurable threshold mechanism, allowing administrators to define consumption limits. When daily usage exceeds a predetermined threshold, the system provides an alert indication, thus supporting proactive energy management and strengthening institutional electricity efficiency control strategies.

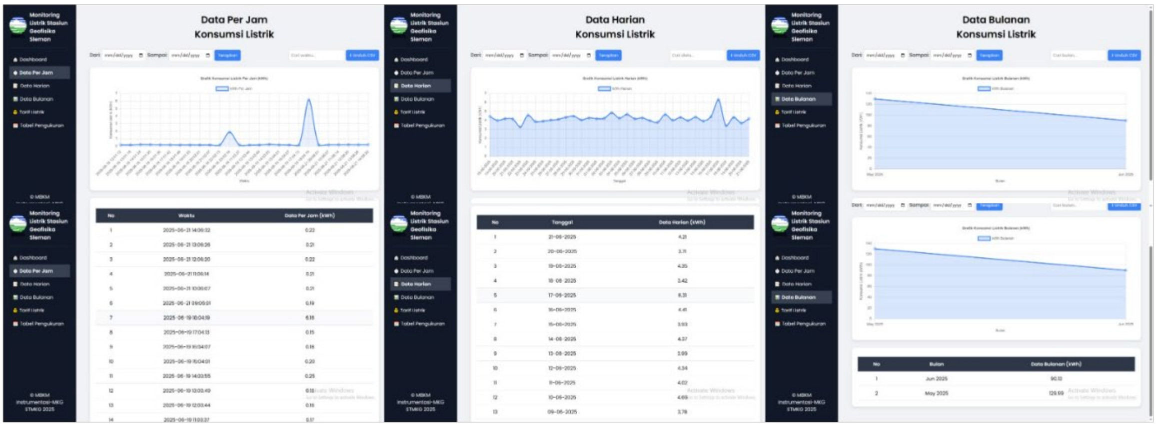

Figure 6. Electricity Usage Per Hour, Per Day, and Per Month

The user interface also presents structured electricity usage data in hourly, daily, and monthly formats as a hierarchical aggregation of recorded energy measurements. Hourly consumption data is obtained by calculating the difference between the cumulative kWh reading in the current hour and the kWh value recorded in the previous hour, thus representing the actual energy usage in a one-hour interval. Daily consumption data is generated by summing all hourly usage values recorded in the same calendar day, providing a comprehensive representation of total daily electricity demand. Furthermore, monthly consumption data is derived from the aggregation of total daily consumption within the same month, enabling broader trend analysis and long-term evaluation of energy usage patterns. This multi-level aggregation structure ensures data consistency across multiple time scales and facilitates detailed and strategic analysis of electricity consumption behavior.

Figure 7. Electricity Bill Estimate and Measurement Table

The designed research system also includes a feature to estimate the projected electricity bill in Indonesian Rupiah (IDR) that must be paid by the institution each month, which is an aggregation of the estimated daily electricity usage bill. This estimate is calculated based on the total 3-phase electricity usage (kWh_{3ph}), which is multiplied by the applicable electricity tariff according to the subscribed power category and the institution's building contract scheme. Tariff data determined by the government is stored in the system database and can be updated according to applicable regulatory policies, ensuring that the calculated cost estimates remain relevant and accurate when policy changes occur. In addition, the platform provides a comprehensive measurement table containing all recorded entries, including voltage, current, power, and energy parameters across all phases, thus enabling transparent data tracking and detailed review of each electrical parameter measurement.

Table 2. Data Evaluation

Timestamp	Instrumen Research	Data PLN	Gap
2025-06-18 13:51	10229,72	10229,71	0,01
2025-06-18 16:15	10230,25	10230,24	0,01
2025-06-21 08:07	10240,65	10240,67	0,02
2025-06-21 16:47	10242,45	10242,43	0,02
2025-06-24 09:01	10254,76	10254,68	0,08
2025-06-25 12:01	10260,68	10260,69	0,01
2025-06-29 12:14	10278,85	10278,84	0,01
2025-06-30 09:10	10282,34	10282,33	0,01
2025-07-02 14:22	10290,20	10290,18	0,02
2025-07-05 10:05	10302,49	10302,47	0,02
	Mean of Gap		0,021

System evaluation is conducted to test the reliability and accuracy of the data by comparing it to the primary reference source, namely the official PLN meter. The process involves manual recording by taking photographs of both devices simultaneously or within a very short time interval. The obtained data is then compared in tabular form to identify differences in values, which are then analyzed to quantitatively evaluate system performance. This difference represents the magnitude of the deviation between the instrument reading and the primary reference. After all the data has been compared, a simple statistical analysis is performed to obtain the average difference across all observations.

Based on the results of processing several comparative data, it was found that the difference in kWh readings between the monitoring device and the PLN meter was generally very small. The average error from all observation points was 0.021 kWh. This value indicates that the designed monitoring device has a very good level of accuracy, in accordance with the PZEM 004t sensor specifications for energy readings with a tolerance value of ±0.5%. With a deviation that is relatively low and acceptable in the context of non-commercial energy monitoring. This accuracy is quite representative for the needs of internal energy consumption monitoring and can be a valid basis for evaluating the efficiency of daily and monthly electricity use.

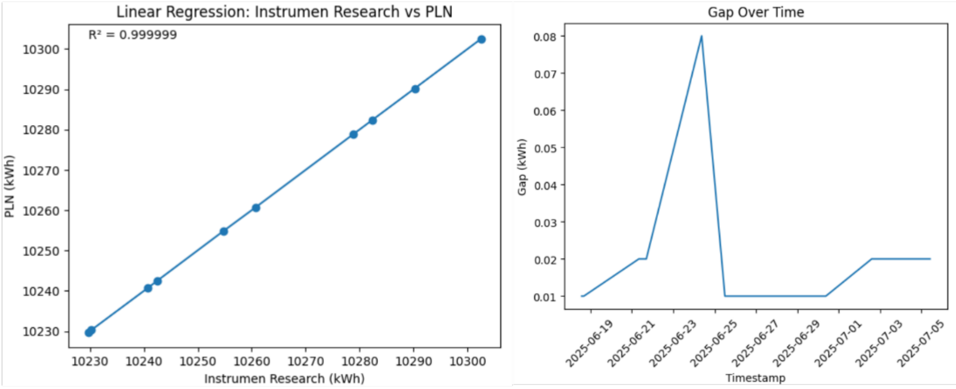

Figure 8. Measurement Data Analysis

Based on the results of statistical analysis of measurement data between research instruments and PLN reference meters, a Mean Gap value of 0.021 kWh with a standard deviation of 0.02132 kWh was obtained, which indicates that the average measurement difference is very small and the variation is relatively low. The maximum Gap value is 0.08 kWh and the minimum is 0.01 kWh, so that practically the measurement error is very low. The results of linear regression modeling show a Slope of 1.000349 and an Intercept of −3.589572, which indicates an almost ideal linear relationship between research instruments and PLN. The coefficient of determination (R^2) value of 0.9999988 confirms that almost all variations in instrument data can be explained by PLN reference data, which means the model's suitability level is very high. In addition, the MAE value of 0.01934 kWh, RMSE of 0.02696 kWh, and MAPE of 0.0001885% further strengthens that the system error rate is very small and is in the very low decimal order. Overall, these results indicate that the developed IoT-based monitoring system has a very high level of accuracy and precision and is suitable for use as a reliable electricity consumption monitoring system.

4. CONCLUSION

This research successfully designed and implemented an IoT-based 3-phase electricity usage monitoring system capable of acquiring, processing, and transmitting real-time electrical parameters with high accuracy and reliability. The development of this system was motivated by the operational need of the Class I Geophysical Station in Sleman, Yogyakarta, to manage electricity consumption more efficiently, as manual daily recording from a remotely located PLN main panel was time-consuming and inefficient. Through systematic stages consisting of problem identification, requirement analysis, hardware and software design, prototype testing, and full deployment, an automated monitoring solution was successfully realized to provide periodic and real-time electricity usage information for data-driven decision-making. The system reliably acquires voltage, current, and energy data from each phase using PZEM-004T sensors, processes the measurement data within the ESP32 microcontroller, and transmits the data via Ethernet (LAN) communication to a centralized database server. The implemented database logic supports multi-level aggregation (hourly, daily, and monthly), electricity usage thresholds, and automated tariff-based cost estimation.

Statistical validation against the official PLN reference meter demonstrates a mean gap of 0.021 kWh with a standard deviation of 0.02132 kWh, indicating very small measurement deviations and low variability. The maximum and minimum observed gaps were 0.08 kWh and 0.01 kWh, respectively, which remain within acceptable tolerance limits for non-commercial monitoring applications. Linear regression analysis produced a slope of 1.000349 and an intercept of −3.589572, reflecting an almost ideal linear relationship between the developed instrument and the reference meter. The coefficient of determination (R^2) of 0.9999988 confirms an extremely high level of agreement, while error metrics including MAE (0.01934 kWh), RMSE (0.02696 kWh), and MAPE (0.0001885%) further demonstrate the system's precision and stability. Overall, the proposed system is highly reliable for real-time internal electricity monitoring and effectively supports data-driven energy efficiency strategies aligned with institutional budget optimization policies.

REFERENCE

[1] M. Poyyamozhi, B. Murugesan, and N. Rajamanickam, "IoT—A promising solution to energy management in smart buildings: A systematic review, applications, barriers, and future scope," Buildings, vol. 14, no. 11, p. 3446, 2024, doi: 10.3390/buildings14113446.

[2] S. Kumar, P. Tiwari, and M. Zymbler, "Internet of Things is a revolutionary approach for future technology enhancement: A review," J. Big Data, vol. 6, no. 1, p. 111, 2019, doi: 10.1186/s40537-019-0268-2.

[3] I. Rojek, D. Mikołajewski, A. Mroziński, and M. Macko, "Internet of Things Applications for Energy Management in Buildings Using Artificial Intelligence—A Case Study," Energies, vol. 18, no. 7, p. 1706, 2025, doi: 10.3390/en18071706.

[4] D. K. Das, "Integrating IoT and AI for Sustainable Energy-Efficient Smart Building: Potential, Barriers and Strategic Pathways," Sustainability, vol. 17, no. 22, p. 10313, 2025, doi: 10.3390/su172210313.

[5] F. Dinmohammadi, A. M. Farook, and M. Shafiee, "Improving energy efficiency in buildings with an IoT-based smart monitoring system," Energies, vol. 18, no. 5, p. 1269, 2025, [Online]. Available: https://www.mdpi.com/1996-1073/18/5/1269

[6] A. Maier, A. Sharp, and Y. Vagapov, "Comparative analysis and practical implementation of the ESP32 microcontroller module for the Internet of Things," in 2017 Internet Technologies and Applications (ITA), IEEE, 2017, pp. 143–148. doi: 10.1109/ITECHA.2017.8101926.

[7] A. Gavrilov, M. Bergaliyev, and S. Tinyakov, "Using IoT protocols in real-time systems: Protocol analysis and evaluation of data transmission characteristics," Int. J. Commun. Syst., vol. 35, no. 12, p. e7368691, 2022, doi: 10.1155/2022/7368691.

[8] D. A. Noordin and N. Z. Nadzri, "Integration of IoT Platform Environment for Web Server and Global Connectivity Based on ESP32," in 2025 IEEE 6th International Conference on Smart Instrumentation, Measurement and Applications (ICSIMA), 2025. [Online]. Available: https://ieeexplore.ieee.org/abstract/document/11155577/

[9] A. Suryanto and S. Ammar, "Internet of Things (IoT)-Based Electrical Panel Monitoring System Utilizing Infrared Thermography Analysis," in IOP Conference Series: Earth and Environmental Science, 2024, p. 12026. [Online]. Available: https://iopscience.iop.org/article/10.1088/1755-1315/1381/1/012026

[10] U. Surahman, B. Trisno, and R. A. Budiman, "Empowering energy conservation: A prototype of household energy consumption monitoring based on Internet of Things," in IOP Conference Series: Earth and Environmental Science, 2024, p. 12056. [Online]. Available: https://iopscience.iop.org/article/10.1088/1755-1315/1404/1/012056

[11] M. Somantri, M. R. Fauzan, and I. Surya, "Optimization of IoT-based monitoring system for automatic power factor correction using PZEM-004T sensor," Indones. J. Electr. Eng. Comput. Sci., 2025, [Online]. Available: https://www.researchgate.net/profile/Irgi-Surya/publication/394447422_Optimization_of_IoT-based_monitoring_system_for_automatic_power_factor_correction_using_PZEM-004T_sensor.pdf

[12] M. Zibayiwa and T. Chigwagwa, "A review on the inter-processor communication: I2C, UART, and SPI interfacing techniques," Int. J. Innov. Res. Sci. Eng. Technol., vol. 10, no. 6, pp. 8003–8010, 2021, doi: 10.15680/IJIRSET.2021.1006103.

[13] D. Witczak and S. Szymoniak, "Review of monitoring and control systems based on Internet of Things," Appl. Sci., vol. 14, no. 19, p. 8943, 2024, [Online]. Available: https://www.mdpi.com/2076-3417/14/19/8943

[14] P. R. Indonesia, "Instruksi Presiden Republik Indonesia Nomor 1 Tahun 2025 tentang Efisiensi Belanja dalam Pelaksanaan Anggaran Pendapatan dan Belanja Negara dan Anggaran Pendapatan dan Belanja Daerah Tahun Anggaran 2025," 2025.

[15] J. Huang, S. Zhou, G. Li, and Q. Shen, "Real-time monitoring and optimization methods for user-side energy management based on edge computing," Sci. Rep., vol. 15, pp. 1–18, 2025.

Journal of Computation Physics and Earth Science
ISSN: 2776-2521 (online)
Volume 5, Number 2, February 2026, Page 145 - 151
https://journal.physan.org/index.php/jocpes/index

Design and Implementation of a React.js-Based Monitoring Dashboard for Tangerang Weather Radar and Server Room Air Conditioning Control

Muhammad Fadil Pradana Andi Alief[1], Nadila R Muhiddin[2], Bintoro Puspo Adi[3], Kadek Ari Sudama[4]
[1,2]Undergraduate Program in Applied Instrumentation Meteorology, Climatology, and Geophysics (STMKG)
[3,4]Indonesian Agency for Meteorology, Climatology, and Geophysics (BMKG)

Article Info

Article history:

Received December 30, 2025
Revised March 7, 2026
Accepted March 8, 2026

Keywords:

Weather Radar
Server Room Monitoring
React.js
Node.js
System Integration

ABSTRACT

The Tangerang Weather Radar Station plays a critical role in aviation safety, yet its maintenance workflow is currently fragmented. Technicians must monitor radar telemetry and control server room cooling systems using separate, non-integrated platforms. This study addresses this inefficiency by developing a centralized web dashboard based on the React.js and Node.js framework. The system integrates real-time BITE (Built-In Test Equipment) data from the radar and provides remote control for the air conditioning units via an existing IoT infrastructure. Testing results demonstrate that the dashboard accurately renders telemetry parameters (High Voltage Power Supply, Transmitter Power, and VSWR) and executes AC control commands with minimal latency within the local network environment. The responsive design ensures accessibility across desktop and mobile devices, providing a unified "Single Pane of Glass" solution for maintaining optimal radar operation and server environmental conditions.

Corresponden Author:

Muhammad Fadil Pradana Andi Alief,
Undergraduate Program in Applied Instrumentation Meteorology, Climatology, and Geophysics (STMKG)
Tangerang, Indonesia
Email: fadilpradana.student@stmkg.ac.id

1. INTRODUCTION

Indonesia's Agency for Meteorology, Climatology, and Geophysics (BMKG) plays a pivotal mandate in ensuring aviation safety in Indonesia by providing fast, precise, and accurate weather information [1]. To support this mission, the Directorate of Aviation Meteorology operates a network of advanced observation infrastructure, including weather radars. The Soekarno-Hatta Class I Meteorological Station relies heavily on the Tangerang Weather Radar to provide real-time weather data, which is crucial for early detection of significant weather phenomena [2]. Any disruption in radar operations can significantly impact vital decision-making processes regarding flight safety.

The continuity of radar operations (uptime) is strictly dependent on the critical supporting infrastructure in the server room, particularly the Air Conditioning (AC) system. Radar servers generate significant heat and operate within tight temperature tolerances. Failure of the cooling system can lead to overheating and subsequent server failure, making environmental monitoring and control a necessity to ensure device reliability [3] [4].

Currently, the operational workflow for technicians at the Tangerang Weather Radar is fragmented and inefficient. Radar operational data is monitored through a proprietary instrument system (EdgeBite) [5], while the control of vital infrastructure, such as the server room AC, is performed through a completely different platform: a Telegram Bot connected to an existing Internet of Things (IoT) device based on the NodeMCU microcontroller. This separation of instrument monitoring and infrastructure control into two distinct platforms creates operational inefficiencies and slows down response times in the event of temperature anomalies.

Furthermore, relying on fragmented systems introduces critical delays in mitigating thermal anomalies. Prolonged radar downtime due to server overheating directly results in observational "data gaps." In aviation meteorology, these data gaps can critically obscure the continuous detection of hazardous weather phenomena, such as severe wind shear or microbursts. Therefore, bridging the research gap between proprietary radar software and independent IoT tools into a unified platform is not merely an operational convenience, but a vital necessity to ensure zero-downtime meteorological surveillance.

To address this issue, this study proposes the design and implementation of a centralized, integrated web dashboard. Leveraging modern web technologies such as React.js and Node.js, this research aims to build a unified interface that retrieves real-time data from the radar database and integrates it with the existing AC control functionality. Unlike previous studies that focus on hardware construction, this research emphasizes system integration—bridging the gap between radar telemetry and the pre-installed IoT infrastructure to create a "single source of truth" for station technicians. Therefore, this study aims to design and implement an integrated web-based dashboard that unifies radar telemetry monitoring and server room AC control into a single operational interface.

Despite the existence of radar monitoring tools and IoT-based server room monitoring systems, there is still a lack of integrated platforms that unify radar telemetry monitoring with infrastructure control within a single operational dashboard. This research addresses this gap by integrating proprietary radar telemetry data with IoT-based environmental control systems into a unified web-based monitoring interface.

2. RELATED WORK

Research on the utilization of weather radar data and the development of server infrastructure monitoring systems has been extensively conducted in separate domains. In the field of meteorological observation, Wei and Hsu [2] conducted a study on the application of real-time radar reflectivity for early detection and weather forecasting. Their research, which focused on Volume Coverage Pattern (VCP) scanning strategies, demonstrated that rapid and accurate integration of radar data is crucial for risk mitigation decision-making. This finding underscores the necessity of real-time data visualization in operational environments. Furthermore, Hsu et al. [6] explored the concept of system integration by developing a unified surveillance platform that combined weather radar imagery with CCTV and water level sensors for urban flooding monitoring. This approach of integrating meteorological instruments with environmental monitoring devices serves as a foundational concept for the dashboard developed in this study.

Regarding infrastructure maintenance, several studies have focused on server room safety using Internet of Things (IoT) technologies. Putra et al. [3] designed a security and control system for server rooms using NodeMCU ESP32 and DHT22 sensors. Their system enabled web-based monitoring and provided alert notifications via SMS and Telegram gateways in the event of thermal anomalies. Similarly, Sadewa and Beta [7] developed a rack monitoring system using ESP8266 to maintain environmental conditions in accordance with ASHRAE standards, preventing server overheating. Their system also relied on a Telegram Bot for real-time technician alerts.

However, a limitation observed in these previous works, particularly [3] and [7], is the reliance on text-based notification platforms (SMS/Telegram) or fragmented monitoring tools. These methods often require technicians to switch between the radar observation system and the infrastructure control interface. This study addresses this gap by proposing a centralized web dashboard architecture. Unlike previous fragmented approaches, our system integrates real-time radar operational data with the existing AC control infrastructure into a single cohesive interface, offering comprehensive visualization and immediate control capabilities.

3. SYSTEM ARCHITECTURE

This study employs a modern full-stack web architecture designed to ensure high responsiveness and modularity. The system follows a decoupled client-server model, where the frontend interface is separated from the backend logic, communicating via RESTful APIs [8]. The overall system architecture and data flow are illustrated in Fig. 1.

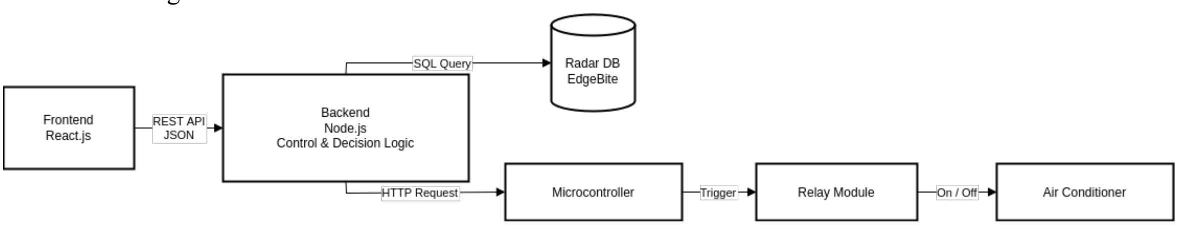

Fig. 1. System architecture diagram illustrating the data flow from the Radar Database (EdgeBite) and Existing IoT Hardware to the React.js Dashboard via Node.js Middleware

3.1. Backend Middleware (Node.js and Express)

The backend functions as an intermediary middleware layer that aggregates data from multiple sources and interfaces with the hardware control unit. Developed using Node.js with the Express framework, the server manages radar data acquisition, infrastructure monitoring, and control logic [9] [10]. Radar telemetry is retrieved from the existing EdgeBite database using the mysql2 library with connection pooling (limit: 10) by executing structured SQL queries to obtain the latest parameter values and a five-minute historical dataset for graphical visualization, without relying on direct API access to the radar system. For environmental monitoring, the backend queries a separate database (radmon), specifically the Air_Conditioner table, to collect real-time current load data (in amperes) from four AC units [11], which serves as a feedback mechanism to verify cooling system operation. Additionally, hardware control commands are implemented through a proxy-based mechanism, where AC toggle requests initiated from the frontend are processed by the Node.js server and forwarded as asynchronous HTTP requests using Axios to the microcontroller's static IP address, ensuring that the frontend does not directly expose hardware network endpoints [12].

To ensure the security of the critical AC infrastructure, the system implements Role-Based Access Control (RBAC) with a secure login mechanism. Users are categorized into general observers, who are restricted to viewing real-time radar telemetry, and administrators, who are granted exclusive privileges to download historical data and actuate the AC relay controls. This authentication layer strictly prevents unauthorized personnel from manipulating the server room's thermal environment. In the current deployment, the AC units retain their last operational state if the network connection is interrupted, ensuring that cooling continues even in the event of temporary communication failures.

3.2. Frontend Interface (React.js)

The user interface is developed using React.js and optimized with Vite to achieve rapid build performance and high responsiveness [13]. The dashboard is designed to provide a "Single Pane of Glass" experience by integrating real-time visualization, interactivity, and responsive layout design. Dynamic area charts rendered using Recharts display critical radar parameters, including HVPS voltage, current, and VSWR ratios, with automatic data refresh every five minutes to support performance trend analysis. Application state and lifecycle management are handled using React's useState and useEffect hooks, while a polling mechanism retrieves radar status at one-second intervals to ensure near real-time monitoring. Visual feedback is enhanced through Framer Motion animations [14], such as pulsing indicators, to represent data freshness and sensor states based on Active High and Active Low logic. Furthermore, the interface adopts a mobile-first responsive design implemented with Tailwind CSS, dynamically adapting from a multi-column grid layout [15] on desktop devices to a simplified vertical layout on mobile platforms, enabling technicians to monitor and control the system effectively within the local network environment.

4. RESULTS AND DISCUSSION

The proposed system was deployed and tested within the local intranet of the Tangerang Weather Radar Station to evaluate its operational feasibility. The experimental results are categorized into three key performance indicators: the usability of the interface design, the integrity of data synchronization between the dashboard and the database, and the latency of the control commands. The following sections detail how the integrated React.js and Node.js architecture successfully functions as a unified monitoring platform, replacing the previously fragmented workflow with a cohesive "Single Pane of Glass" solution.

4.1. Frontend Interface (React.js)

The proposed system has been successfully developed using the React.js framework, featuring a "Dark Mode" interface designed to minimize visual fatigue for operators monitoring the system continuously.

Fig. 2. Technician authentication login interface

Fig. 2 illustrates the authentication login interface designed to restrict system access to authorized technicians. The login mechanism serves as the first security layer of the monitoring platform, ensuring that only authenticated users can access the operational dashboard and control functions. Through this interface, technicians must provide valid credentials before entering the system. The authentication process is integrated with the backend middleware, which verifies user roles and permissions. This access control mechanism is particularly important because the dashboard provides not only monitoring capabilities but also remote control of the server room air conditioning system, which is considered critical infrastructure for maintaining stable radar operation.

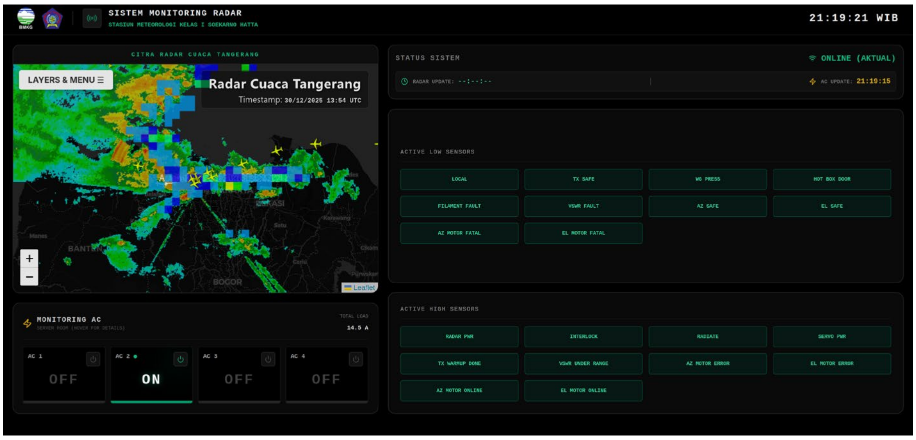

Fig. 3. Main dashboard interface integrating real-time weather radar imagery with server room air conditioning control

As illustrated in Fig. 3, the primary desktop interface integrates three core modules: real-time weather radar imagery, the Air Conditioning (AC) control panel, and BITE status monitoring. A key feature of this interface is the intelligent visualization of sensor statuses based on their specific logic characteristics. The system distinguishes between "Active High" and "Active Low" sensors to provide intuitive feedback. For Active High sensors, a logic value of '1' is rendered as a green indicator (Normal), whereas '0' triggers a red alert. Conversely, for Active Low sensors, a logic value of '0' represents a normal state displayed in green, while '1' indicates a fault condition displayed in red. This standardized color-coding mechanism allows technicians to assess the station's overall health and identify anomalies at a glance without needing to interpret raw binary data.

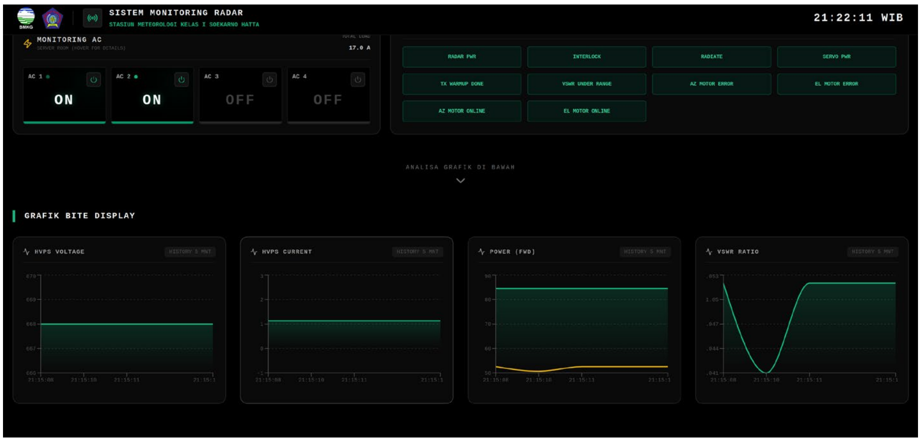

Fig. 4. Real-time BITE graphical monitoring showing HVPS voltage, current, transmission power, and VSWR ratio

To facilitate in-depth technical monitoring, Fig. 4 presents the graphical visualization of critical transmitter parameters. The dashboard renders real-time dynamic area charts for HVPS Voltage, HVPS Current, Forward Power (FWD), and VSWR Ratio. These graphs provide operators with historical trend visibility over a 5-minute window, enabling the early detection of signal fluctuations or power instability before they escalate into critical failures.

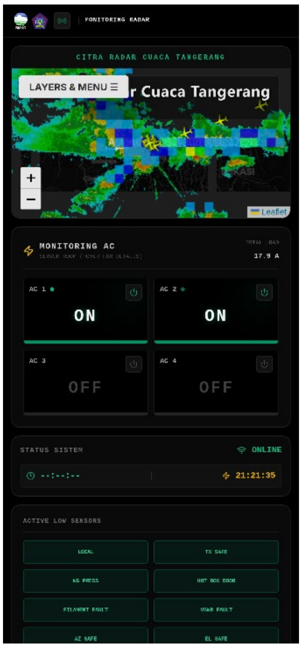

Fig. 5. Responsive mobile implementation featuring a vertical layout for radar surveillance and AC control accessibility

Furthermore, the system incorporates a responsive design approach using the Tailwind CSS utility framework. On mobile devices, as shown in Fig. 5, the application dynamically adapts the multi-column grid into a vertical stack layout. This adaptive capability ensures that essential control functions, particularly the AC power toggle, remain accessible and touch-optimized across various device viewports without compromising data readability.

4.2. Data Integration and Visualization

To validate the system's accuracy, a comparative analysis was conducted between the raw telemetry data transmitted by the backend API and the values rendered on the frontend dashboard. The backend middleware retrieves radar telemetry in JSON format, as exemplified by the raw data payload: {"hvps_v": 668, "hvps_i": 1.13, "forward_pwr": 84.5, "vswr": 1.052}.

Observation confirms that the dashboard successfully parses and renders these floating-point values with exact precision, showing no data discrepancy. The integration logic within the Node.js middleware effectively bridges the disparate database sources (EdgeBite and radmon), delivering synchronized updates to the client interface. Visual indicators for sensor status (e.g., "Active Low" logic) correctly correspond to the binary values received from the microcontroller API, validating the state management logic implemented in the React frontend.

4.3. System Responsiveness

The system's responsiveness relies on the architectural design and network deployment. Since the application, database server, and IoT control units operate within a dedicated Local Area Network (LAN) segment at the station, external network latency is effectively eliminated.

To quantitatively evaluate the responsiveness of the system, latency benchmarking was conducted using a repeated measurement method. Each API endpoint was tested 50 times within the local area network environment. The latency value was calculated as the time difference between the request initiation and the response reception at the client side. The results are summarized in Table 1.

Table 1. Latency benchmark results

System	Function	Mean Latency (ms)	Min (ms)	Max (ms)
Radar Retrieval (EdgeBite DB)	Retrieval of BITE operational parameters	43.58	22.68	208.49
Server Room Monitoring (radmon DB)	Monitoring of AC electrical current and server room temperature	81.20	59.36	365.61
AC Control Communication (ESP32 IoT)	Transmission of control commands from dashboard to AC relay controller	129.34	46.12	396.84

The radar telemetry retrieval subsystem, which accesses operational BITE parameters from the EdgeBite database, achieved the lowest average latency of 43.58 ms, indicating efficient data retrieval for radar operational monitoring. The server room monitoring subsystem, responsible for collecting electrical current data from the air conditioning units and temperature readings from the server environment, exhibited an average latency of 81.20 ms. Meanwhile, communication with the ESP32-based IoT controller used for AC relay actuation showed an average latency of 129.34 ms, reflecting the additional network and microcontroller processing overhead associated with hardware control operations.

Despite these differences, all measured subsystems operate well below the one-second threshold commonly associated with real-time monitoring systems. This demonstrates that the integrated dashboard provides sufficiently responsive performance for operational supervision of radar telemetry and environmental control within the radar station infrastructure.

To further evaluate the system's scalability and address potential high-frequency access scenarios, a stress test analysis was conducted simulating 100 concurrent user requests to the radar telemetry API endpoint. The test measured the system's data throughput and stability under simulated peak loads. The results demonstrated that the Node.js backend successfully processed all 100 concurrent requests with a 0% failure rate (no dropped connections or server crashes). The total execution time for handling this concurrent batch was 1,273.66 milliseconds, yielding an average data throughput of 78.51 requests per second. This quantitative performance analysis confirms that the REST API architecture, coupled with the database connection pooling mechanism, is highly robust. It ensures reliable data delivery and system stability even when accessed by multiple station personnel simultaneously during critical weather monitoring operations.

The use of the React.js Virtual DOM ensures efficient rendering updates, while the Node.js backend handles asynchronous HTTP requests non-blocking. Consequently, the software processing overhead is negligible. Commands initiated from the dashboard are dispatched immediately to the local network, ensuring that the limitation of the control speed is determined solely by the physical switching characteristics of the relay hardware rather than software transmission delays.

5. CONCLUSION AND FUTURE WORKS

This study has successfully achieved its primary objective of designing and implementing a centralized dashboard for the Tangerang Weather Radar Station, effectively resolving the issue of operational fragmentation between instrument surveillance and infrastructure control. By leveraging a robust modern web technology stack comprising React.js for the responsive frontend and Node.js for the backend middleware, the system provides a seamless integration of real-time BITE (Built-In Test Equipment) telemetry from the radar with the remote control mechanism of the server room's Air Conditioning (AC) units.

The empirical results demonstrate that the system maintains high data integrity, with the dashboard rendering critical telemetry parameters (HVPS, Power, and VSWR) that correspond precisely to the raw database values. The "Single Pane of Glass" architecture significantly reduces the cognitive load on technicians, eliminating the need to switch between disparate platforms. Furthermore, the deployment within a dedicated Local Area Network (LAN) ensures minimal latency, allowing for near-instantaneous actuation of the AC relay modules. The responsive design successfully adapts to mobile devices, providing technicians with flexible accessibility to maintain optimal radar operation aligned with international observation standards [16].

For future development, the system functionality can be significantly extended by implementing a customizable data export feature. This would allow operators to download historical monitoring logs based on user-defined time ranges, facilitating deeper retrospective analysis and operational reporting. Additionally, integrating an automated notification system triggered by specific temperature or voltage anomaly thresholds would further enhance the system's capability in supporting proactive maintenance strategies.

Despite the system's operational benefits, we acknowledge a current limitation regarding automated control logic and hardware fail-safes. Presently, the NodeMCU functions as a direct remote toggle operated manually by the administrator. It does not yet incorporate automated thermal threshold logic, such as hysteresis to prevent compressor short-cycling, nor an autonomous fail-safe to lock the AC relay in a 'Normally Closed' (ON) state during a network outage. Addressing this by embedding independent temperature threshold logic directly into the microcontroller's firmware is a primary focus for our future work. By maintaining stable environmental conditions for radar server infrastructure, the system indirectly contributes to minimizing radar downtime and preventing observational data gaps in meteorological monitoring.

REFERENCE

[1] Pemerintah Republik Indonesia, Undang-Undang Republik Indonesia Nomor 31 Tahun 2009 Tentang Meteorologi, Klimatologi, Dan Geofisika. 2009, pp. 1–60. [Online]. Available: https://peraturan.bpk.go.id/Details/38769/uu-no-31-tahun-2009

[2] C. C. Wei and C. C. Hsu, 'Real-time rainfall forecasts based on radar reflectivity during typhoons: Case study in southeastern taiwan', Sensors, vol. 21, no. 4, pp. 1–20, 2021, doi: 10.3390/s21041421.

[3] I. G. Y. Putra, I. G. M. N. Desnanjaya, and I. G. Adnyana, 'Jurnal Galaksi (Global Knowledge, Artificial Inteligence and Information System) Temperature Humidity Control System and Fire Detection for Room Server Based Internet Of Things', Galaksi Glob. Knowl. Artif. Intel. Inf. Syst., vol. 1, no. 2, pp. 81–91, 2024.

[4] Ashrae, '2021 Equipment thermal guidelines for data processing environments', ASHRAE TC 99 Ref. Card, no. 404, pp. 1–8, 2021.

[5] Enterprise Electronics Corporation, 'EDGE TM (Enterprise Doppler Graphics Environment)', 2000.

[6] S. Y. Hsu, T. B. Chen, W. C. Du, J. H. Wu, and S. C. Chen, 'Integrate Weather radar and monitoring devices for urban flooding surveillance', Sens. Switz., vol. 19, no. 4, pp. 1–15, 2019, doi: 10.3390/s19040825.

[7] E. E. Sadewa and S. Beta, 'Temperature, Humidity, and Power Outage Monitoring System of Pamapersada Nusantara's Server Racks', Jaict, vol. 7, no. 2, p. 90, 2022, doi: 10.32497/jaict.v7i2.3269.

[8] M. A. Novianto and S. Munir, 'Analisis dan Implementasi Restful API guna Pengembangan Sistem Informasi Akademik pada Perguruan Tinggi', J. Inform. Terpadu, vol. 8, no. 1, pp. 47–61, Mar. 2022, doi: 10.54914/jit.v8i1.409.

[9] D. Flanagan, JavaScript: The Definitive Guide, 7th edn. O'Reilly Media, 2020.

[10] E. Nurhayati and A. Agussalim, 'Rancang Bangun Back-end API pada Aplikasi Mobile AyamHub Menggunakan Framework Node JS Express', J. Sist. Dan Teknol. Inf. JustIN, vol. 11, no. 3, p. 524, July 2023, doi: 10.26418/justin.v11i3.66823.

[11] W. A. Suteja and A. Surya Antara, 'Analisis Sensor Arus Invasive ACS712 dan Sensor Arus Non Invasive SCT013 Berbasis Arduino', PROtek J. Ilm. Tek. Elektro, vol. 8, no. 1, pp. 13–21, May 2021, doi: 10.33387/protk.v8i1.2116.

[12] Espressif Systems, 'ESP32 Dev Kits Documentation', 2023.

[13] T. A. Rizzi, R. Aziz Abdillah, Y. Efani Yancandra, M. Wijaya, and A. Voutama, 'Implementasi React Vite Dalam Pengembangan Antarmuka Sistem Pemesanan Tiket Pesawat Dengan Metode Scrum', J. Process., vol. 20, no. 1, May 2025, doi: 10.33998/processor.2025.20.1.2231.

[14] J. A. Ramadhanti, L. Isyriyah, and R. Maulidi, 'Penerapan Motion UI untuk Meningkatkan Pengalaman Pengguna dan Penyampaian Informasi pada Website Kampus', SMATIKA J., vol. 15, no. 01, pp. 226–239, July 2025, doi: 10.32664/smatika.v15i01.2039.

[15] S. Azhariyah and Muhammad Mukhlis, 'Framework CSS: Tailwind CSS Untuk Front-End Website Store PT. XYZ', J. Inform., vol. 3, no. 1, pp. 30–36, Apr. 2024, doi: 10.57094/ji.v3i1.1601.

[16] World Meteorological Organization, Guide to Instruments and Methods of Observation (WMO-No. 8). Measurement of Precipitation, vol. III. 2021.

Journal of Computation Physics and Earth Science
ISSN: 2776-2521 (online)
Volume 5, Number 2, February 2026, Page 152 - 161
https://journal.physan.org/index.php/jocpes/index

Optimization of Electronic Control for a Monohull Leisure Boat Using Meteorological Data to Enhance Stability and Safety in Coastal Environments

Muhammad Ramdhani Setyo Nugroho[1], Thalia Salsabila[2], Yobel Eliezer Mahardika[3], Rizky Ramadhani[4], Anton Widodo[5]
[1, 3, 4]Undergraduate Program in Applied of Instrumentation Meteorology, Climatology and Geophysics (STMKG)
[2]Undergraduate Program in Applied Meteorology (STMKG)
[5]Department of Instrumentation Meteorology, Climatology and Geophysics (STMKG)

Article Info

Article history:

Received December 31, 2025
Revised February 28, 2026
Accepted February 28, 2026

Keywords:

Unmanned Surface Vehicles (USV)
Monohull Leisure Boat
Electronic Remote Control (ERC)
Static Stability Analysis
Marine Tourism

ABSTRACT

Indonesia's maritime geography offers significant potential for marine tourism but requires transportation systems capable of operating safely under variable coastal environmental conditions influenced by wind and wave variability. This study presents the design and evaluation of a compact monohull leisure boat integrated with an Electronic Remote Control (ERC) system to improve maneuverability and operational safety. The research applies an engineering design approach involving regression-based estimation of principal dimensions, digital hull modeling using Maxsurf, static stability evaluation through righting arm (GZ) analysis, and spatial optimization using a General Arrangement (GA) plan. Five alternative hull geometries were developed and analyzed to identify the most suitable configuration for marine tourism operations. The stability analysis indicates that all hull models exhibit positive righting arm values within the evaluated heel angle range, confirming adequate static stability under typical coastal conditions. Among the evaluated configurations, Model 4 demonstrates the most favorable stability characteristics. The integration of the ERC system further enhances vessel maneuverability and reliability during low-speed navigation and docking, supporting safer marine tourism transportation in coastal waters.

Corresponden Author:

Thalia Salsabila
Undergraduate Program in Applied Meteorology (STMKG)
Tangerang, Indonesia
Email: thaliasalsabila05@gmail.com

1. INTRODUCTION

Indonesia is one of the world's largest maritime nations, consisting of 17.508 islands distributed across the equatorial region. The country extends longitudinally from Sabang to Merauke and has a total area of approximately 8 million km², of which nearly two-thirds are marine waters. Indonesia's coastline stretches over 99,000 km, with a total marine area of approximately 3.257 million km² [1]. These geographical characteristics indicate that Indonesia possesses substantial potential in marine and coastal tourism, supported by the diversity of its marine environments and island landscapes. Consequently, the development of marine tourism has become an important national agenda to enhance regional economic growth and optimize the utilization of maritime resources.

According to Law No. 10 of 2009 concerning Tourism, marine tourism, also referred to as water-based tourism, includes tourism and water sport activities supported by facilities, infrastructure, and related services that are commercially managed in marine, coastal, river, lake, and reservoir areas [2]. Furthermore, the Directorate General of Tourism defines marine tourism as tourism activities directly associated with marine resources both above and below the sea surface, such as swimming, diving, snorkeling, and sailing. The development of marine tourism offers various benefits, including increased regional income, job creation, and support for environmental and cultural preservation [3].

At present, marine tourism transportation in Indonesia is predominantly served by conventional and traditional vessels operating between coastal areas and nearby islands. For example, traditional boats are commonly used to transport tourists to small island destinations such as Pulau Angso Duo in Pariaman [4]. While these vessels provide essential connectivity, their operation often presents limitations in terms of navigational safety, maneuverability, and operational reliability, particularly under varying sea and weather conditions. In addition to traditional vessels, cruise ships are also utilized for marine tourism; however, they require large international-standard port infrastructure and generally operate under fixed travel itineraries, which limit flexibility and reduce access to smaller island destinations [5].

Marine tourism activities in Indonesian waters are highly influenced by near-surface meteorological conditions, including wind variability, wave characteristics, and rapid weather changes commonly observed in coastal and inter-island regions. These environmental factors directly affect vessel motion, maneuverability, and operational safety, particularly for small-scale leisure boats. Consequently, the development of marine tourism transportation systems must consider not only technological and operational aspects, but also environmental conditions governed by meteorological and climatological variability. From this perspective, vessel design and control system integration play a critical role in supporting weather-sensitive marine operations within Indonesia's maritime environment [6][7].

These conditions indicate the need for technological innovation in marine tourism transportation, particularly in the context of vessel safety and operational control. The integration of modern ship design approaches and electronic control technologies offers potential solutions to improve navigational safety and maneuverability. In this regard, the application of an Electronic Remote Control (ERC) system enables electronically assisted vessel operation, allowing improved steering precision and reduced dependence on manual control. Such systems can contribute to minimizing human error and enhancing safety, especially during low-speed maneuvers and near-shore navigation [8].

Accordingly, this study presents the design and development of an electronic remote control–based monohull leisure boat intended to support safer marine tourism transportation in Indonesia. The study focuses on engineering-based vessel design, hydrodynamic considerations, system integration, and prototype evaluation to assess the feasibility and safety performance of the proposed ERC-based leisure boat.

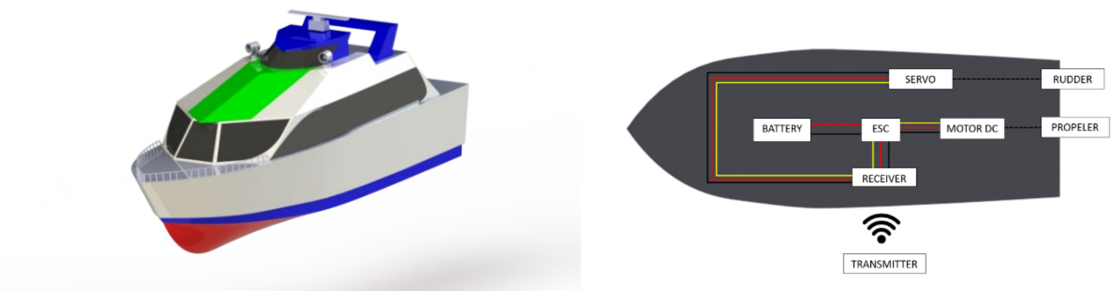

Fig. 1 Conceptual design and system overview of the electric remote control–based monohull leisure boat for marine tourism applications.

2. RESEARCH METHOD

This study employs an engineering design and prototype development methodology to develop a monohull leisure boat integrated with an Electronic Remote Control (ERC) system for marine tourism transportation. The research was conducted through a hull configuration selection, determination of the vessel's principal dimensions using a regression method based on reference data from comparable leisure boats, and hull analysis including hydrostatic and stability evaluation using Maxsurf Stability software. The subsequent stages involved control system integration, prototype fabrication, and overall performance evaluation of the proposed vessel system

The hull configuration selection process was conducted to determine the most appropriate vessel type for marine tourism operations. Several alternative hull configurations were considered during this stage, including monohull, catamaran, and trimaran designs. The selection was carried out through a literature review examining the hydrodynamic characteristics and operational performance of each hull type. Based on this assessment, the monohull configuration was selected due to its ability to effectively cut through waves, making it suitable for operation in waters with small to moderate wave conditions and enabling stable navigation on the water surface [9]. In addition, the single-hull configuration provides adequate cargo capacity and contributes to maintaining vessel balance and stability during inter-island tourism operations.

The principal dimensions of the vessel were determined using a regression-based approach derived from reference data of comparable leisure boats. A dataset consisting of several vessels with similar operational characteristics was compiled to establish proportional relationships among the main design parameters. Key parameters considered in the analysis include length overall (LoA), beam (B), depth (D), draft (T), and displacement. Linear regression analysis was applied to examine the relationship between vessel displacement and the principal dimensions, enabling the estimation of appropriate dimensional values for the proposed vessel. The resulting regression equations were then used to determine the preliminary principal dimensions of the monohull leisure boat design based on the average deadweight value as the primary design reference.

The hull design in this study was carried out using Maxsurf software, which was utilized to design and digitally model the geometric form of the vessel. The principal dimensions obtained from the previous stage, including length overall (LOA), beam (B), depth (D), and draft (T), were used as the primary parameters in the hull modeling process. These parameters served as the fundamental inputs for constructing the initial hull geometry within the software environment. The hull modeling process began with the development of the vessel's basic lines plan, consisting of buttock lines, waterlines, and stations, which define the three-dimensional geometric characteristics of the hull. Through this digital modeling approach, the hull form can be systematically developed and refined to represent the intended vessel configuration while maintaining consistency with the predefined principal dimensions.

The hull analysis in this study was conducted using Maxsurf Stability software to evaluate the vessel's stability characteristics based on the hull geometry model developed in the previous design stage using Maxsurf. The analysis process began by importing the hull geometry model along with the principal vessel parameters, including length overall (LOA), beam (B), depth (D), and draft (T), into the Maxsurf Stability environment. Load conditions were then defined to represent realistic operational scenarios, including vessel weight, load distribution, and the position of the vessel's center of gravity. In addition to internal loading conditions, environmental parameters derived from meteorological and oceanographic data were also considered to represent typical coastal operational environments, including wave height and wind speed commonly observed in Indonesian coastal waters. These environmental variables were used to simulate external disturbances that may influence vessel stability during operation.

The analysis was initiated with hydrostatic calculations to obtain key parameters such as displacement, waterplane area, and the center of buoyancy, which serve as fundamental indicators of the vessel's buoyancy characteristics. This stage was followed by a stability analysis to determine important stability parameters, including the metacentric height (GM), the static stability curve or righting arm curve (GZ curve), and the vessel's heel response under various loading conditions. The results of this analysis were used to evaluate the overall stability performance of the vessel and to ensure that the designed hull geometry satisfies the required stability criteria.

In addition to the stability analysis, the Savitsky method was applied as a supplementary approach to estimate resistance characteristics under planing conditions. This method provides an analytical estimation of hydrodynamic resistance and performance parameters for planing hulls, which are commonly used in high-speed leisure boat designs. In this study, the Savitsky method served as a supporting indicator to assess the hydrodynamic feasibility of the proposed vessel design rather than as a detailed performance optimization tool [10][11]. Through this numerical and analytical approach, the evaluation of vessel stability and hydrodynamic characteristics can be conducted systematically prior to physical fabrication or direct experimental testing.

The ERC system was implemented by utilizing electronic communication between the transmitter (Tx) and receiver (Rx) devices. These components were integrated to enable control of propulsion speed and steering direction during the navigation process. The integration process considered compatibility among electronic components, signal communication stability, and control system responsiveness to ensure proper operational performance during testing.

The fabrication process involved constructing the hull structure according to the designed geometry, followed by the installation of the propulsion system, steering mechanism, and electronic control components associated with the ERC system. Particular attention was given to the structural integrity of the hull and the placement of internal components to ensure proper weight distribution and balance. The resulting prototype was then used as a physical model for subsequent experimental testing.

Performance evaluation of the prototype was conducted through a series of functional and operational tests. These tests included buoyancy and balance tests to verify the floating condition and weight distribution of the vessel, maneuverability tests to evaluate steering response and directional control capability, and speed tests to observe the performance of the propulsion system under operational conditions.

3. RESULT AND DISCUSSION

The results of this study focus on several key stages of the vessel development process, including the determination of the principal dimensions of the vessel, the hull design and modeling process, the analysis of hull stability characteristics, and the integration of the Electronic Remote Control (ERC) system. These results illustrate how the proposed design methodology was translated into a functional vessel configuration suitable for marine tourism transportation. The discussion further examines the relationship between hull geometry, weight distribution, and stability performance, as well as the role of the ERC-based control system in supporting maneuverability and operational safety. These aspects are essential considerations in ensuring the feasibility, safety, and reliability of small-scale leisure boats operating in coastal tourism environments.

3.1 Determination of Principal Dimensions

A monohull configuration was selected due to its structural simplicity, predictable hydrodynamic behavior, and suitability for leisure boat operations in low to moderate wave environments. The principal dimensions of the vessel were determined using a linear regression approach based on reference data obtained from comparable leisure boats, providing an initial framework for hull geometry development. In this stage, a dataset of existing leisure boats with similar operational characteristics was compiled to serve as reference data for the regression analysis. The dataset includes several principal parameters commonly used in preliminary ship design, such as vessel length, beam, draft, and displacement. These reference vessel data are summarized in Table 1.

Table 1. Principal Dimensions of Reference Vessels Used for Regression Analysis

No.	Vessel Name	DWT	Length (LoA)	Beam (B)	Depth (D)	Draft (T)
1	Javanese Boat		21	5	2.1	0.6
2	Sport Yacht 170 FT	495	52.4	9.5	3	2.44
3	2009 Palmer Johnson	223	37.9	7.44	2.15	1.98
4	Sport Yacht 120 FT	223	37.9	7.6	2.15	2.1

The collected data were subsequently analyzed using a linear regression method to identify the relationships between displacement and the principal dimensions of the vessels. This approach enables the estimation of appropriate dimensional proportions for the proposed leisure boat design based on empirical trends observed in existing vessels. The resulting regression relationships derived from the reference dataset are illustrated in Fig. 2.

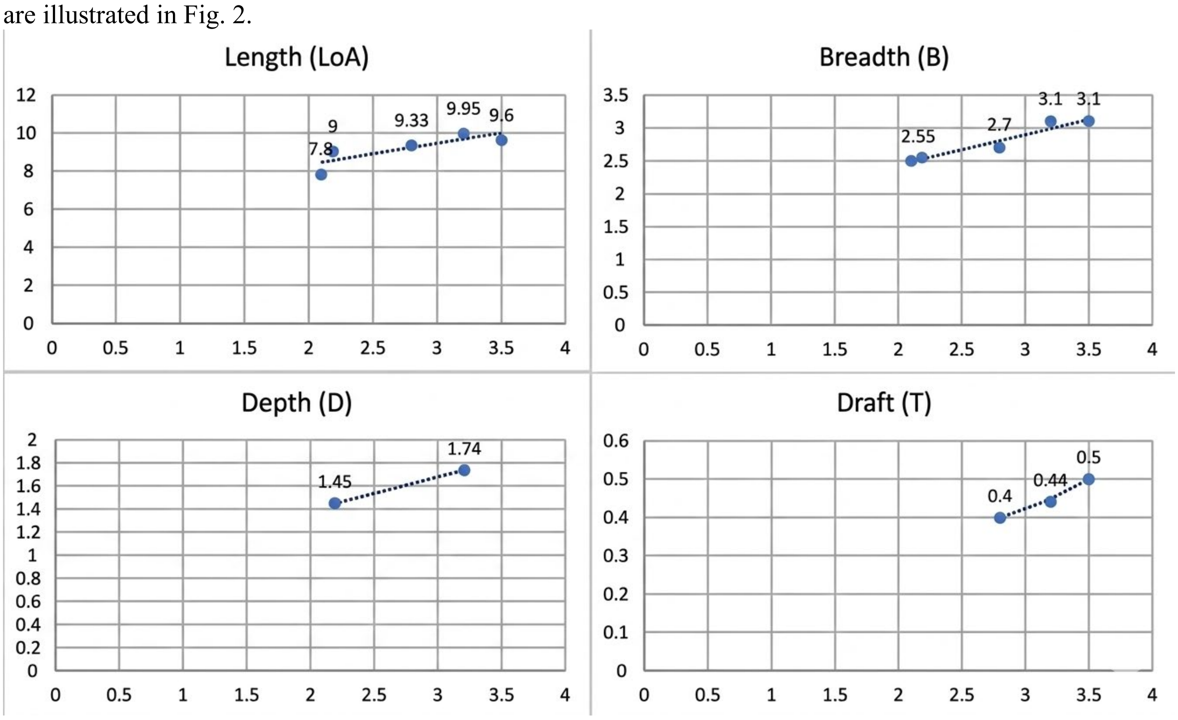

Fig. 2 Linear regression relationships between vessel displacement and principal dimensions (LoA, Beam, Depth, and Draft) derived from reference vessel data.

Based on the regression equations obtained from the analysis, the principal dimensions of the proposed vessel were determined using the average deadweight value as the primary design reference. The resulting regression equations were applied to estimate the appropriate dimensions of the vessel to be developed in this study. The calculated principal dimensions derived from this process are summarized in Table 2 and subsequently serve as the fundamental basis for the hull modeling process and the stability analysis conducted in the following stages of the study.

Table 2. Principal design parameters of the proposed vessel obtained from regression analysis.

Principal Vessel Parameters	Value (cm)
Length (LoA)	60
Beam (B)	22
Depth (D)	14
Draft (T)	5,5

3.2 Hull Geometry Design and Modeling

The hull geometry of the proposed leisure boat was developed using Maxsurf software, which is widely used in naval architecture for digital hull modeling and hydrostatic evaluation. The use of Maxsurf in this study enables the visualization and development of the vessel's three-dimensional hull form based on the principal dimensions determined in the previous stage. Through this software, the hull geometry can be systematically modeled and adjusted to achieve an appropriate balance between hydrodynamic performance, stability characteristics, and structural feasibility [12].

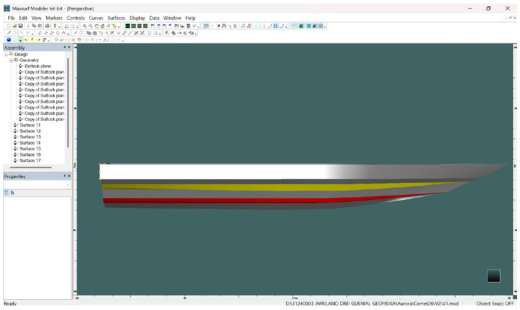

Model 1

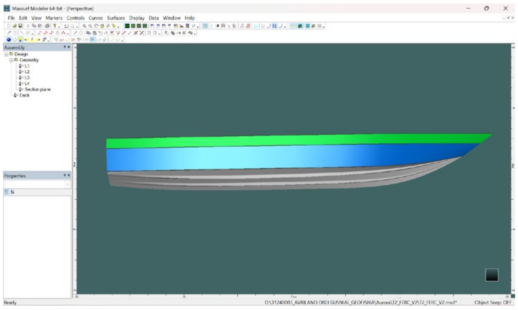

Model 2

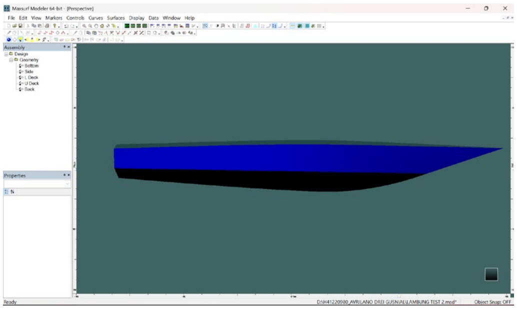

Model 3

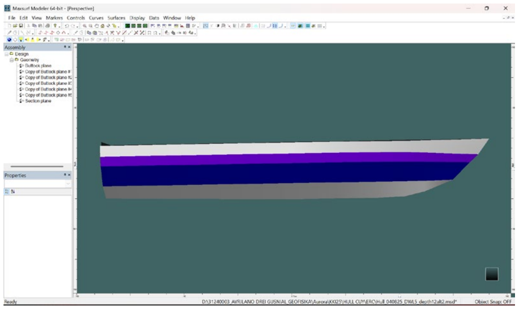

Model 4

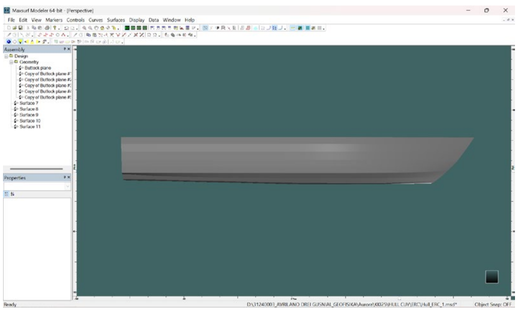

Model 5

Fig. 3 Variations of hull geometry models developed using Maxsurf

The hull modeling process was initiated by defining the main geometric parameters obtained from the regression-based principal dimension estimation, including the length overall (LOA), beam (B), depth (D), and draft (T). These parameters served as the fundamental constraints for constructing the digital hull surface. The modeling procedure involved the development of the lines plan consisting of stations, waterlines, and buttock lines, which together form the three-dimensional geometry of the hull. This digital modeling process allows detailed control of the hull curvature and overall shape, which are important for determining the vessel's hydrodynamic behavior and stability performance.

Five different hull models were developed during the design stage to evaluate alternative hull characteristics and to identify the most suitable hull configuration for the proposed vessel. Each hull variation was generated by modifying several geometric parameters of the hull form while maintaining the same principal dimensions. The variations primarily focused on differences in hull curvature and sectional shapes, which may influence hydrodynamic resistance, buoyancy distribution, and overall vessel stability.

The five hull configurations were subsequently analyzed and compared to identify the most appropriate hull form for the proposed leisure boat design. The comparison considered aspects such as geometric feasibility, hydrostatic characteristics, and suitability for small-scale marine tourism operations in coastal waters. The modeled hull geometries developed using Maxsurf are presented in Fig. 3, which illustrates the five design variations evaluated in this study.

3.3 Hull Stability Analysis

The static stability performance of the proposed monohull leisure boat was evaluated through numerical analysis to assess its ability to maintain equilibrium under external disturbances. The assessment was conducted by analyzing the righting arm (GZ) values at various heel angles derived from the finalized hull geometry [13]. GZ values were calculated for five hull model configurations to examine their stability characteristics under transverse inclinations. The resulting numerical values are summarized in Table 1, while the corresponding GZ curves are illustrated in Fig. 4, which depict the relationship between heel angle and righting moment and provide a clear visualization of the static stability behavior of each hull configuration.

Table 3. Static Stability (GZ) Values at Various Heel Angles

Degree	Model 1	Model 2	Model 3	Model 4	Model 5
0	0	0	0	0	0
10	0.91	0.95	1.5	1.55	1.07
20	1.53	1.64	2.27	2.39	1.75
30	1.86	2.17	2.74	2.91	2.26
40	2.16	2.65	3.09	3.28	2.76
50	2.51	2.95	3.43	3.55	3.19
60	2.60	3.01	3.49	3.45	3.31
70	2.38	2.81	3.17	2.93	3.10
80	1.87	2.41	2.51	2.15	2.58
90	1.19	1.84	1.67	1.21	1.85
100	0.40	1.15	0.72	0.19	1.01
110	-0.41	0.40	-0.27	-0.84	0.11
120	-1.21	-0.37	-1.23	-1.81	-0.79
130	-1.93	-1.10	-2.11	-2.66	-1.64
140	-2.58	-1.75	-2.86	-3.29	-2.37
150	-3.02	-2.24	-3.39	-3.73	-2.89
160	-3.09	-2.42	-3.51	-3.79	-3.03
170	-2.19	-1.82	-2.62	-2.82	-2.27
180	0	0	0	0	0

The numerical results presented in Table 3 indicate that all evaluated hull models exhibit positive righting arm (GZ) values over the assessed heel angle range, confirming initial static stability of the proposed monohull configuration. For all models, GZ values increase progressively with heel angle from 0° up to approximately 50°–60°, where the maximum righting arm is observed [14]. The range of positive stability for all evaluated models extends approximately up to heel angles close to 100°, where the righting arm approaches zero. Beyond this point, negative GZ values indicate the loss of restoring capability and the onset of capsizing tendency. This behavior reflects the vessel's increasing restoring moment as transverse inclination develops, which is a desirable characteristic for small leisure craft operating in coastal waters. Beyond the angle corresponding to maximum GZ, a gradual reduction in righting arm magnitude is observed, indicating the onset of decreasing restoring capability at higher heel angles. Among the evaluated configurations, Models 3 and 4 consistently demonstrate higher peak GZ values compared to the other models, suggesting superior transverse stability performance. These numerical trends provide a quantitative basis for assessing hull stability prior to visual interpretation through stability curves and support the suitability of the selected hull geometry for safe marine tourism operations under typical coastal environmental conditions.

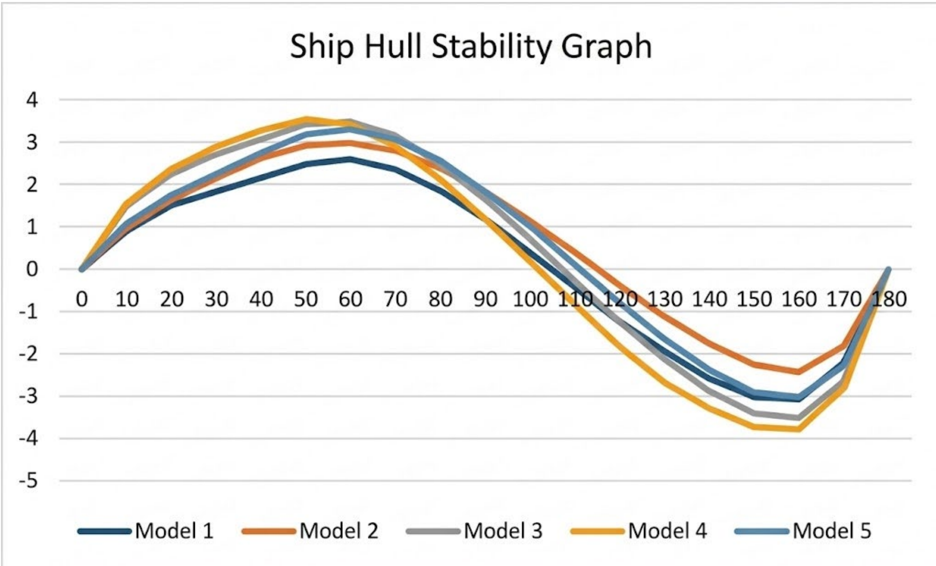

Fig. 4 Static stability curves of the monohull leisure boat

As shown in Fig. 4, all evaluated hull models exhibit a positive righting arm over a wide range of heel angles, indicating that the vessel is capable of returning to its upright position after experiencing heeling forces caused by wave action or maneuvering. The stability curves generally increase to a maximum righting moment at moderate heel angles before gradually decreasing toward larger angles. This trend reflects a stable equilibrium condition and sufficient initial stability, which are essential requirements for leisure boats operating in marine tourism environments [15].

Based on the stability curves obtained from the Maxsurf Stability analysis, Model 4 demonstrates the most favorable stability performance among the evaluated configurations. This is indicated by the highest maximum GZ value, reaching approximately 3.5-3.7 at a heel angle of around 50°–60°. A higher GZ value represents a stronger restoring moment, meaning that the vessel has a greater ability to return to its upright position when subjected to external heeling forces. In addition, the stability curve of Model 4 shows a relatively smooth and consistent variation, indicating a stable and predictable restoring response during increasing heel conditions.

From a meteorological perspective, the selection of Model 4 becomes particularly relevant because marine environmental conditions are strongly influenced by atmospheric factors such as wind speed, wave height, and air pressure variations. Strong winds, typically measured using anemometers in meteorological observations, can generate lateral forces acting on the hull and superstructure, resulting in vessel heel. Furthermore, sea waves generated through wind–sea interactions can induce rolling motions that disturb vessel equilibrium. Under such conditions, vessels require sufficient restoring capability to counteract these disturbances and maintain operational stability.

The stability curve analysis also shows that Model 4 maintains relatively large positive GZ values up to heel angles approaching 100°, indicating that the vessel still possesses the ability to generate restoring moments even under significant inclination. This characteristic is particularly important when the vessel operates under unstable weather conditions, such as strong winds or elevated wave heights that are frequently associated with atmospheric dynamics in coastal environments. The higher maximum stability value of Model 4 suggests that this configuration provides the best resistance to environmental disturbances, thereby reducing the likelihood of stability loss or capsizing compared to the other evaluated hull models.

Based on these considerations, Model 4 was selected as the final hull configuration for the proposed monohull leisure boat design. Its superior restoring capability and wider stability margin indicate that the hull geometry is better suited to withstand environmental disturbances influenced by meteorological variability, ensuring safer and more reliable operation for marine tourism activities in coastal waters.

3.4 Electronic Remote Control System Integration

An Electronic Remote Control (ERC) system was integrated as the primary vessel control mechanism to enhance maneuverability and navigational safety. The ERC architecture consists of a remote transmitter, electronic speed controller, steering servo mechanism, and onboard electronic components that enable responsive control of vessel speed and steering. The application of ERC technology aims to reduce dependence on continuous manual control and mitigate potential human error, particularly during low-speed maneuvers, docking operations, and navigation in confined or near-shore environments. The architecture of the ERC system used in this study is illustrated in Fig. 5.

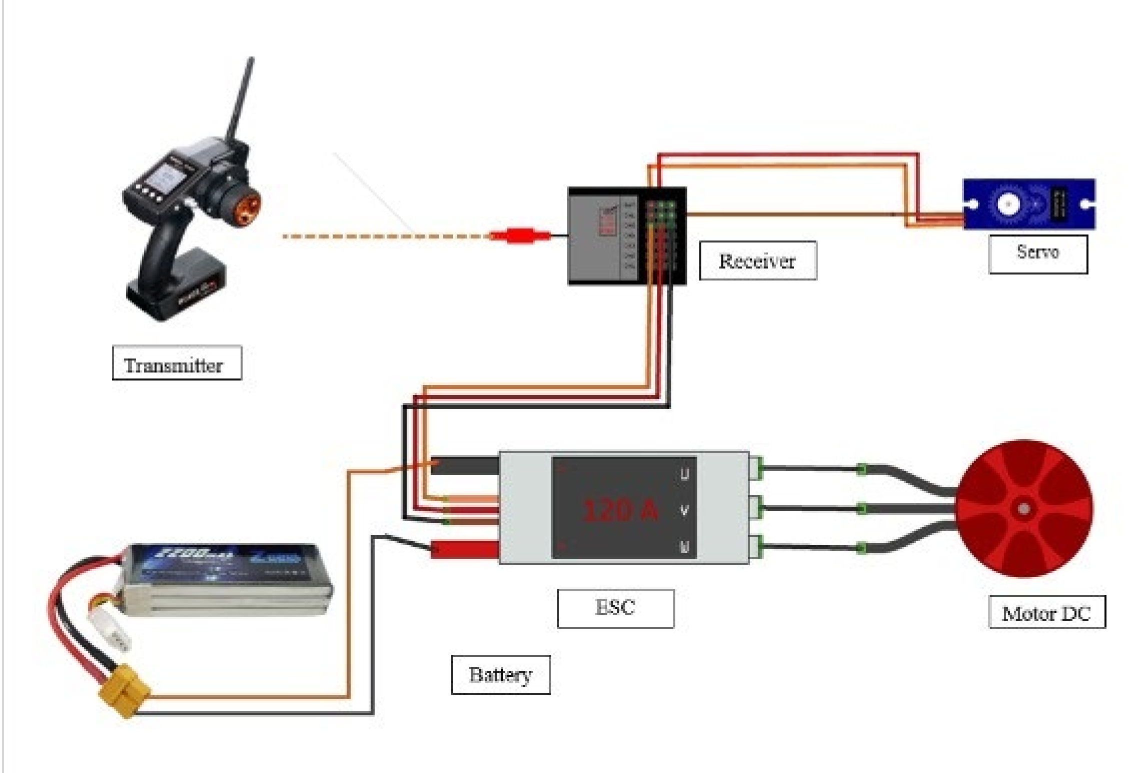

Fig. 5 Architecture of the Electronic Remote Control (ERC) system used for vessel propulsion and steering control.

Table 4. Electronic Component Specifications.

Name	Specification
Battery	2200 mAh
	4 cell
	6 s
Electronic Speed Controller	120 a
Motor Brushless	2200 Kv
	3000 W
Servo	20 Kg
Transmitter	2.4 GHz
Receiver	2.4 GHz

The ERC system operates using a 2.4 GHz radio communication protocol employing Frequency Hopping Spread Spectrum (FHSS), which enhances signal stability and reduces the risk of interference commonly encountered in coastal operational environments. The receiver processes control signals from the transmitter and distributes them to the electronic speed controller (ESC) and steering servo mechanism, enabling real-time adjustment of propulsion and rudder angle. To improve operational safety, the system incorporates a fail-safe mechanism that automatically returns the throttle to a neutral state and stabilizes the steering system in the event of signal interruption or communication loss, ensuring operational safety under unexpected circumstances.

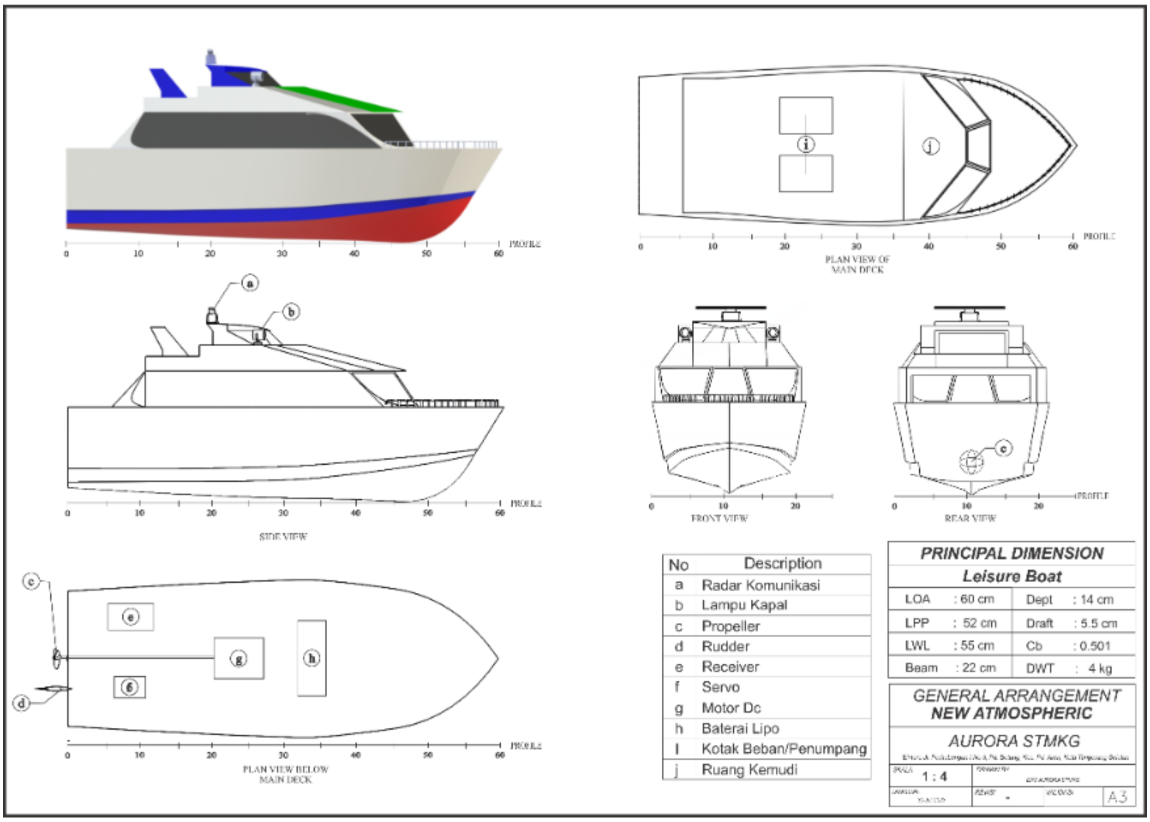

Fig. 6 General arrangement plan of the electronic remote control–based monohull leisure boat

General Arrangement Plan of the *Atmospheric* AURORA STMKG leisure boat was developed to optimize spatial efficiency, operational functionality, and safety within a compact monohull configuration. The layout defines the allocation of key functional spaces, including the accommodation area, equipment compartment, and electronic control system placement, arranged to support balanced load distribution and ease of operation. The accommodation space is positioned to maintain passenger comfort while ensuring sufficient clearance for movement, whereas the electronic and control components are strategically located to enable efficient remote operation and system accessibility. This spatial configuration reflects a design approach that integrates operational requirements, safety considerations, and practical constraints typical of small-scale marine tourism vessels, as illustrated in Fig. 2. This spatial configuration supports safe vessel operation under variable environmental conditions commonly encountered in coastal marine tourism areas, where wind-induced motion and wave response must be adequately accommodated.

During the fabrication process, the hull geometry was constructed in accordance with the design model to maintain dimensional accuracy and geometric symmetry. Structural assembly and surface finishing were performed to ensure sufficient strength and a smooth hull surface, which are essential for minimizing hydrodynamic resistance and maintaining predictable vessel behavior. Particular attention was given to the distribution of onboard components to achieve a balanced center of gravity. This consideration is crucial, as improper weight distribution can negatively affect vessel stability, maneuverability, and safety during operation. The fabrication results indicate that the designed hull configuration can be practically realized and is suitable for further performance evaluation.

4. CONCLUSION

This study demonstrates the feasibility of integrating hull design optimization, spatial layout planning, and Electronic Remote Control (ERC) technology into a compact monohull leisure vessel as an adaptive platform for marine tourism transportation. The proposed design framework emphasizes operational safety and functional efficiency under environmental conditions influenced by meteorological variability commonly observed in Indonesian coastal and inter-island waters. The General Arrangement Plan confirms a rational distribution of functional spaces and control components, while numerical stability analysis based on righting arm characteristics indicates that the hull configuration provides sufficient static stability within the evaluated heel angle range. The incorporation of an ERC-based control system enhances maneuverability and operational reliability during low-speed navigation and docking, which are critical under variable wind and wave conditions. Beyond its immediate application, the developed vessel concept offers a scalable foundation for safety-oriented and environmentally adaptive marine transportation, supporting the long-term development of sustainable marine tourism in Indonesia.

REFERENCE

[1] M. E. Prof. Dr. H. Rahardjo Adisasmita, Pembangunan Ekonomi Maritim. Yogyakarta: Graha Ilmu, 2013.

[2] Undang-Undang Republik Indonesia Nomor 10 Tahun 2009 tentang Kepariwistaan (PDF)

[3] Direktorat Jenderal Pariwisata. 1998. Pedoman Pengembangan Ekowisata. Jakarta: Ditjen Pariwisata.

[4] R. Ardiwidjaja, “Daya Tarik Kapal Tradisional Sebagai Kapal Wisata,” KALPATARU Maj. Arkeol., vol. 25, no. 1, pp. 65–74, 2016.

[5] U. Persson-Fischier, K. Wigger, J. Olsen, and Á. M. Sveinsdóttir, “Managing cruise volume at Nordic cruise destinations,” Scandinavian Journal of Hospitality and Tourism, vol. 25, no. 3, pp. 1–18, May 2025, doi: https://doi.org/10.1080/15022250.2025.2499269.

[6] A. Fathurohman, G. Napitupulu, G. Fujiawati, and M. Napitupulu, “IMPACT OF SIGNIFICANT WAVE HEIGHT, WIND SPEED, AND PRECIPITATION VARIABILITY ON SHIPPING SAFETY IN INDONESIAN ARCHIPELAGIC SEA LANES,” BULLETIN OF THE MARINE GEOLOGY, vol. 40, no. 1, Aug. 2025, doi: https://doi.org/10.32693/bomg.40.1.2025.895.

[7] S. Hermawan, E. Mihardja, D. A. Pambudi, and J. Jason, “Hydrodynamic Model Optimization for Marine Tourism Development Suitability in Vicinity of Poso Regency Coastal Area, Central Sulawesi, Indonesia,” Sustainability, vol. 15, no. 4, p. 3150, Feb. 2023, doi: https://doi.org/10.3390/su15043150.

[8] Y. Zhou et al., “Human errors analysis for remotely controlled ships during collision avoidance,” Frontiers in Marine Science, vol. 11, Nov. 2024, doi: https://doi.org/10.3389/fmars.2024.1473367.

[9] H. R. Syafnil, R. E. Putera, I. A. Azre, J. A. Publik, and U. Andalas, “Keywords : Marine Tourism Ship , Supervision,” vol. 2, 2020.

[10] D. Endro W, "HIGH SPEED SHIP TOTAL RESISTANCE CALCULATION (AN EMPIRICAL STUDY)," Kapal: Jurnal Ilmu Pengetahuan dan Teknologi Kelautan, vol. 11, no. 1, pp. 13 - 20, Feb. 2014. https://doi.org/10.14710/kpl.v11i1.6338

[11] D. Q. Khai, N. M. Chien, and N. T. T. Quynh, “A COMPARISON STUDY ON THE RESISTANCE CALCULATION OF PLANNING BOAT,” International journal of engineering applied science and technology, vol. 5, no. 12, Apr. 2021, doi: https://doi.org/10.33564/ijeast.2021.v05i12.003.

[12] U. Godwin and K. Wugha, “Design Analysis of Ship Hull Preliminary Hydrostatic Properties(Case Study: Offshore Patrol Boat),” Quest Journals Journal of Architecture and Civil Engineering, vol. 7, no. 8, pp. 2321–8193, 2022.

[13] B. Santoso, R. Romadhoni, P. Nasution, H. Hardiyanto, and Z. Ariany, “Assessment of Safe Loading Conditions for the SPCB Deck Crane Using Hydrostatic and GZ Curve Analysis,” International Journal of Marine Engineering Innovation and Research, vol. 10, no. 2, pp. 458–470, Jul. 2025, doi: https://doi.org/10.12962/j25481479.v10i2.6422.

[14] B. G. Tentua, S. J. Litiloly, and R. B. Luhulima, “Comparative Analysis of Monohull and Catamaran Passenger Vessels: Performance in Shallow Waters,” Engineering and Technology Journal, vol. 10, no. 04, Apr. 2025, doi: https://doi.org/10.47191/etj/v10i04.05.

[15] U. Budiarto, E. S. Hadi, and N. M. D. Sunarto, "STUDI PERANCANGAN KAPAL WISATA TRIMARAN HYBRID UNTUK PERAIRAN KEPULAUAN KARIMUNJAWA," Kapal: Jurnal Ilmu Pengetahuan dan Teknologi Kelautan, vol. 11, no. 2, pp. 69 - 76, May. 2014. https://doi.org/10.14710/kpl.v11i2.7238

Journal of Computation Physics and Earth Science
ISSN: 2776-2521 (online)
Volume 5, Number 2, February 2026, Page 162 - 172
https://journal.physan.org/index.php/jocpes/index

Meteorological Analysis of Strong Wind-Producing Clouds: A Case Study of Klaten, 18 November 2024

Febby Debora Abigael[1], Ahmad Hanif Al'aziz[2], Arya Zaki Ramadhan[3], Achmad Zakir[4], Aditya Mulya[5]
[1,2,3,4,5]Undergraduate Program in Meteorology (STMKG)

Article Info

Article history:

Received December 31, 2025
Revised March 5, 2026
Accepted March 5, 2026

Keywords:

Strong winds
Atmospheric dynamics
Cloud characteristics
Cumulonimbus cloud
Klaten

ABSTRACT

Klaten Regency, Central Java, has frequently experienced extreme convective weather in the form of strong surface winds that have caused damage to residential areas and public facilities. This study analyzed a strong wind event that occurred on 18 November 2024 between 15:30 and 16:30 Local Time, which had significant impacts across several sub-districts in Klaten. The objective of this research was to evaluate the atmospheric dynamics and cloud characteristics responsible for the event. A descriptive–analytical approach was applied using secondary data, including the Dipole Mode Index, the Madden–Julian Oscillation Diagram, streamline map, and atmospheric stability indices to assess atmospheric dynamics. In addition, dual-polarization weather radar products were used to examine convective cloud structure, vertical development, wind convergence and divergence patterns, and indications of vortex formation. The results showed that the event was dominated by a rapidly developing Cumulonimbus cloud system, with maximum reflectivity values reaching approximately 69 dBZ and cloud-top heights of about 10 km. Low-level wind convergence and horizontal wind shear played a critical role in triggering deep convection. Atmospheric stability indices indicated sufficiently unstable conditions, although instability was not extreme. Doppler radar analysis revealed strong updraft–downdraft interactions, intense convergence–divergence patterns, and vortex formation during the mature stage of the storm.

Corresponden Author:

Febby Debora Abigael,
Undergraduate Program in Meteorology (STMKG)
Tangerang, Indonesia
Email: febbydeboraabigael@gmail.com

1. INTRODUCTION

Klaten Regency is a region in Central Java that is highly susceptible to severe convective weather, particularly strong winds [1]. This study is centered on a major event that occurred on 18 November 2024, from 15:30 to 16:30 Local Time (LT) (08:30 – 09:30 UTC), which caused extensive damage to residential buildings and public facilities across several sub-districts, including Gantiwarno, Kalikotes, Karanganom, and Klaten Utara [2]. The intensity and rapid development of this event necessitate a comprehensive evaluation of the atmospheric dynamics involved to better understand the storm's lifecycle and enhance local early warning systems. Severe convective weather is primarily driven by the rapid growth of Cumulonimbus clouds, where vertical air motion is a defining factor [3]. The interaction between extreme updrafts and powerful downdrafts is the fundamental mechanism behind damaging surface winds, such as downbursts [4]. Monitoring the vertical extension of reflectivity cores provides insight into the evolution of these updrafts, while Doppler radar technology is essential for identifying wind shear and vortex signatures that precede such destructive events. Specifically in Indonesia, low-level air mass convergence has been identified as a primary trigger for deep convection in tropical environments [5]. This research provides a novel contribution by integrating radar analysis to reconstruct the kinematic structure of a specific localized storm in Klaten. Consequently, the objective of this research is to evaluate the atmospheric dynamics and radar signatures associated with the severe wind event in Klaten by examining the spatial and vertical growth patterns of convective cells, investigating the kinematic structures related to convergence and divergence zones, and assessing the potential for vortex formation and atmospheric instability during the storm's peak intensity. Unlike typical convective storms in Java, which are generally characterized by disorganized multi-cell systems or short-lived orographic rain, this event is uniquely distinguished by its rapid transition into a highly organized structure capable of producing extreme downbursts and localized vortex signatures. Such features are rarely observed in standard tropical convection over the region, making this case a critical benchmark for understanding small-scale yet high-impact wind phenomena in Central Java.

2. RESEARCH METHOD

This study uses descriptive–analytical and qualitative methods to describe and analyze phenomena in detail and to understand their patterns, relationships, and meanings [6]. The focus of the research is the Klaten Regency area, as shown in Figure 1, with data consisting of IOD, MJO, streamlines, atmospheric stability indices, and radar images related to strong winds, which are discussed in the following subpoints. To facilitate this study, observational data is derived from the Semarang Weather Radar located in Tambakaji, Ngaliyan (7.002° S, 110.350° E), which operates with a surveillance radius of 250 kilometers.

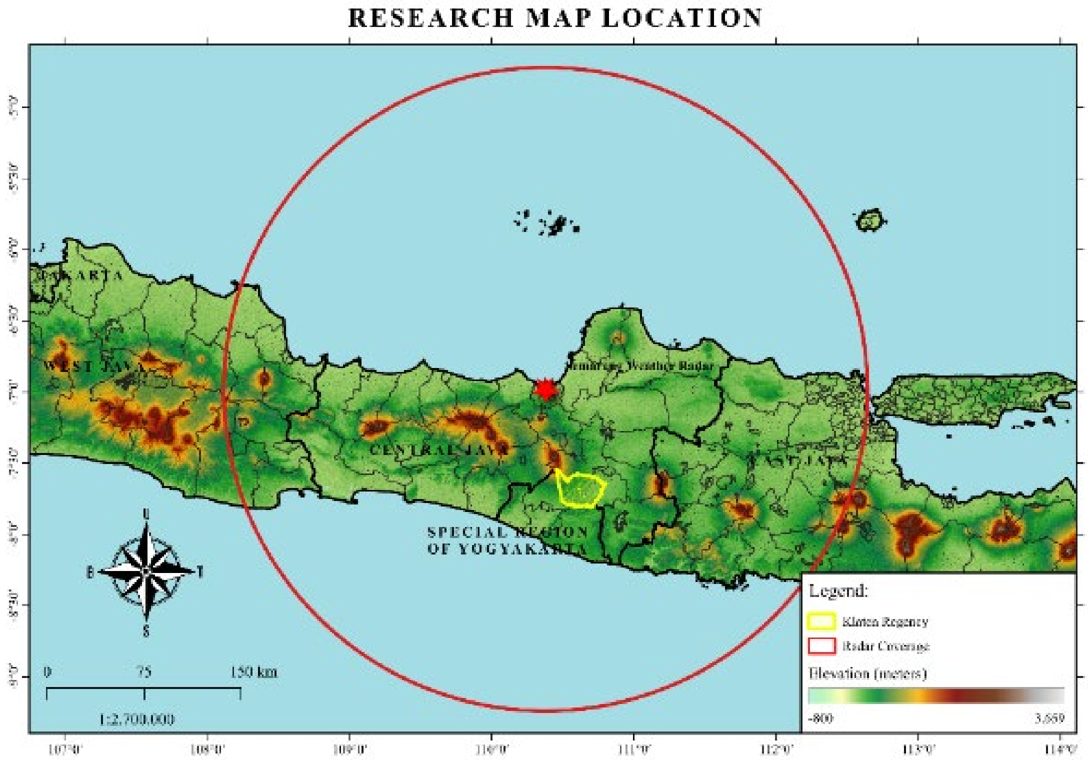

Fig. 1. Research Map Location

2.1. Data Collection Methods

This study uses secondary data for the analysis of IOD, MJO, streamlines, atmospheric stability, and cloud identification using radar imagery. The IOD data were accessed from NASA Jet Propulsion Laboratory (JPL) through https://sealevel.jpl.nasa.gov/overlay-iod/ in the form of the Dipole Mode Index (DMI), which represents the difference in sea surface temperature (SST) anomalies between the western and eastern Indian Ocean. This index was first introduced by Saji et al. (1999) [7] and is widely used in studies on regional climate variability in Indonesia.

Meanwhile, MJO data were obtained from the Australian Bureau of Meteorology (BoM) through the website https://www.bom.gov.au/climate/mjo/, including the RMM1 and RMM2 indices, amplitude, and daily MJO phases. The RMM index is used because it effectively represents the global position and strength of MJO convection, as developed by Wheeler and Hendon based on the Madden–Julian concept.

Streamline and atmospheric stability data were derived from the ERA5 Reanalysis Single Levels dataset provided by the Copernicus Climate Data Store (CDS) of the European Centre for Medium-Range Weather Forecasts (ECMWF) at a spatial resolution of 0.25° × 0.25°. ERA5 represents a fifth-generation global atmospheric reanalysis that combines observational records with numerical weather prediction models to ensure a physically consistent depiction of atmospheric conditions [8]. Streamline patterns were examined using the zonal (u) and meridional (v) wind components [9], on 18 November 2024 from 08:00 to 10:00 UTC, whereas atmospheric stability was assessed using CAPE, CIN, KI, and TTI during 06:00–12:00 UTC on the same day.

The radar data used in this research were obtained from the Agency for Meteorology, Climatology, and Geophysics (BMKG) at the Ahmad Yani Meteorological Station, Semarang. The dataset was provided in .vol format and subsequently processed using Rainbow5 Software. The system utilized is a dual-polarization radar with a scanning interval of 10 minutes.

2.2. Data Processing Methods

IOD and MJO data processing only involves selecting the analysis time period, because the DMI values and MJO diagrams are obtained directly from the data source without recalculation. The u and v data for the streamline map, along with CAPE, CIN, KI, and TTI for atmospheric stability analysis, were obtained by selecting the study period and area and downloaded in NetCDF format, and furthermore, these data were processed using GrADS to produce streamline maps and atmospheric stability index graphs. Radar data were processed using Rainbow5 software via several specialized applications, with preprocessing performed using the 3D-RAVE application, which included Z-based attenuation correction, bright band correction, and clutter filtering to ensure data quality. Following this, the RainDART-TS application was used to generate various radar products, specifically Column Maximum (CMAX), Storm Structure Analysis (SSA), Vertical Cut (VCUT), Constant Altitude Plan Position Indicator (CAPPI/MCAPPI) Velocity, Tornado Vortex Detection (TVD), and the Severe Weather Indicator (SWI) [10], [11], where CMAX and SSA are used to identify the structure of Cumulonimbus cloud cells based on their reflectivity profiles [12], [13], while CAPPI Velocity is utilized to determine wind movement derived from particle displacement [14], [15], and finally, TVD and SWI are used to detect potential vortices, as well as wind divergence and convergence.

2.3. Data Analysis Method

IOD analysis focuses on the interpretation of DMI and its impact on Indonesia's climate. A positive IOD (DMI > +0.4) is characterized by a warmer western Indian Ocean and a cooler eastern Indian Ocean, resulting in reduced rainfall and increased drought potential. A neutral IOD (−0.4 ≤ DMI ≤ +0.4) has a weak influence, with weather more affected by other factors such as the monsoon and MJO. A negative IOD (DMI < −0.4) is marked by a warmer eastern Indian Ocean, increasing water vapor and leading to generally higher rainfall. Each IOD phase is associated with tendencies for wet or dry seasons in Indonesia, following the framework of Saji et al. (1999) [7] and supported by subsequent studies, such as Adiwira et al. (2018) [16]. MJO analysis was carried out descriptively and focused on the phases that affect Indonesia, particularly the Maritime Continent, namely phases 4–5, where convection increases, cloud development occurs, and there is a high potential for rainfall. Conversely, when the MJO is in phases 2–3 (Indian Ocean) and 6–7 (Western Pacific), Indonesia tends to experience subsidence and low rainfall [17].

Streamline is a curve where at every point it is tangent to the instantaneous flow velocity vector and is used to depict atmospheric circulation patterns [18]. In this study, streamline analysis is applied to identify the dominant direction of lower-level winds, detect zones of convergence and divergence, and examine the influence of synoptic-scale circulation on regional wind patterns. High wind speeds are indicated by closely spaced streamlines due to strong pressure gradients, while convergent streamline patterns indicate potential upward motion and atmospheric instability.

Atmospheric stability analysis is conducted by reviewing CAPE, CIN, KI, and TTI according to their categories in Table 1. CAPE indicates the energy available for convection, CIN measures vertical air resistance [19], [20], KI represents thunderstorm potential, whereas TTI reflects conditions conducive to severe weather [21]. The higher the values of CAPE, KI, and TTI, the more unstable the atmosphere. Conversely, high CIN indicates a more stable atmosphere [19], [20], [21].

Table 1. Classification of Atmospheric Stability Index Values [22]

Level	CAPE (J/kg)	CIN (J/kg)	KI (°C)	TTI (°C)
Weak	<1000	<50	<29	<42
Moderate	1000–2500	51–199	29–37	42–46
Strong	>2500	>200	>37	>46

Radar imagery analysis begins by evaluating the spatial and temporal evolution of convective cells through the CMAX and Storm Structure Analysis SSA products [12], [13]. These tools are used to monitor the initiation of cloud growth and track the intensification of reflectivity cores as the storm system develops. To further examine the vertical characteristics of the storm, the Vertical Cut VCUT product is applied to generate cross-sectional profiles [23]. This method allows for the determination of convective depth and the vertical extension of high-reflectivity cores, which are essential for identifying the mature stage of a convective system and assessing its potential to produce significant weather. The second phase of the analysis focuses on the kinematic properties and severe weather signatures using Doppler velocity and specialized detection algorithms. Radial velocity products, including CAPPI and MPPI, are analyzed at various altitudes to identify airflow patterns, specifically targeting areas of wind convergence and divergence that trigger vertical updrafts and downdrafts [24], [25]. Furthermore, the Tornado Vortex Detection (TVD) and Severe Weather Indicator (SWI) are utilized to locate vortex signatures and extreme wind shear within the storm cell. By correlating the interaction between vertical air movements and these automated detection signals, the analysis establishes the physical mechanisms responsible for severe weather phenomena occurring at the surface.

3. RESULTS AND DISCUSSION

The results and discussion in this case study include the analysis of IOD, MJO, streamlines, atmospheric stability, and radar image interpretation, which are described as follows:

3.1. Indian Ocean Dipole

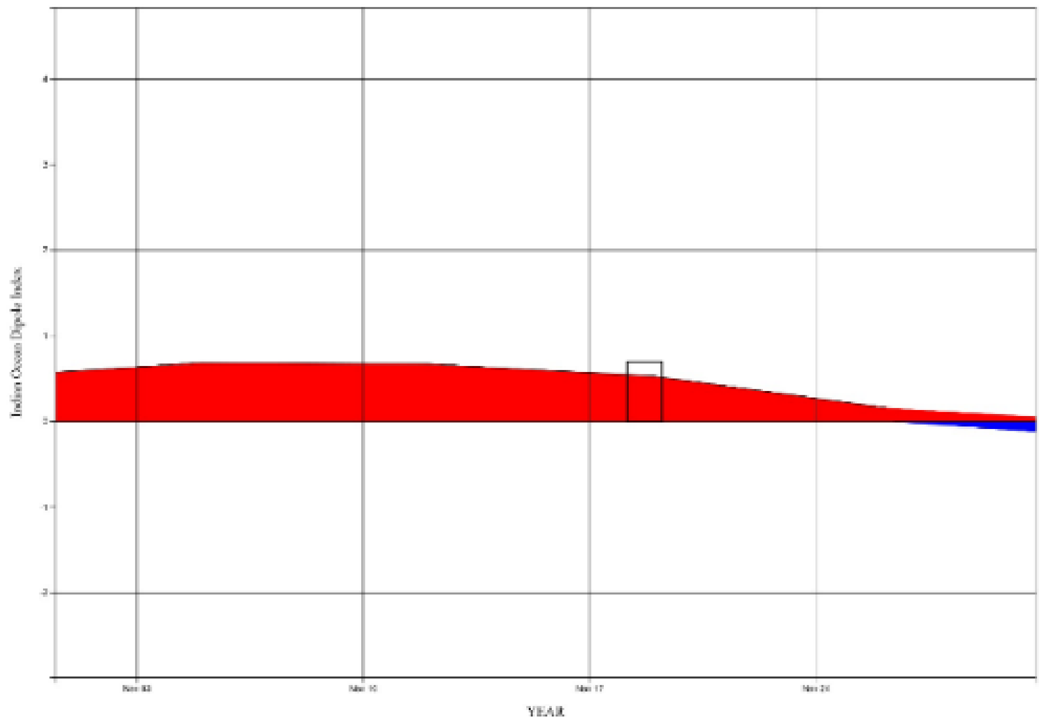

Fig. 2. DMI Chart

Based on Figure 2, during November 2024, the IOD remained in a positive phase during the first half of the month, with DMI values around +0.5 to +0.7, before gradually weakening towards neutral conditions. On 18 November 2024, the DMI was still positive at about +0.5, indicating a positive IOD event that was fading but still active. Positive IOD conditions are associated with cooler sea surface temperatures in the eastern Indian Ocean near Sumatra–Java and warmer conditions in the western basin, resulting in a strong zonal SST gradient [7]. Even during the weakening phase, residual SST and pressure gradients can persist and continue to influence atmospheric circulation. These conditions support abnormal east to southeast winds at the sea surface level in the eastern Indian Ocean, affecting the western regions of Sumatra and Java [16]. As a result, the weakening positive IOD on 18 November 2024, still contributed to the increase in surface wind conditions over Java.

3.2. Madden-Julian Oscillation

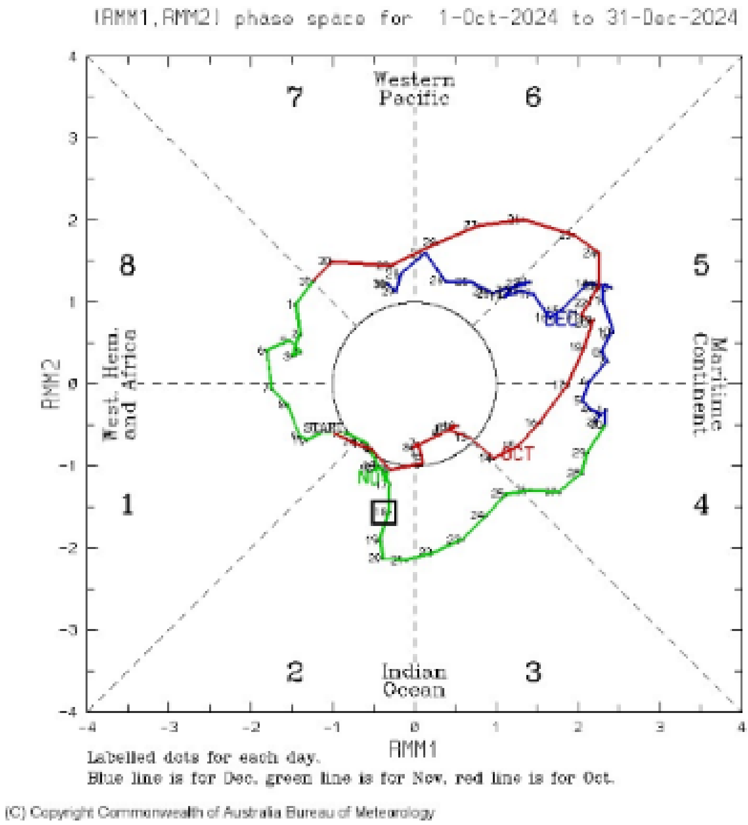

Fig. 3. MJO Diagram

As shown in Figure 3, the RMM phase-space diagram for October–December 2024 shows that on 18 November 2024 the Madden–Julian Oscillation (MJO) was active, as it lay outside the unit circle, and was positioned in Phase 2, approaching Phase 3. According to Madden and Julian (1972), an active MJO represents a large-scale coupled circulation–convection system capable of significantly modulating tropical atmospheric dynamics, indicating a dynamically important influence over Indonesia at that time [26]. Although MJO did not directly cause the storm, but it could enhance the background moisture and wind field, creating a preconditioned environment in which local mesoscale convergence could rapidly intensify [27]. Pattipeilohy and Asri (2019) showed that MJO Phases 2–3 are often linked to strengthened zonal wind anomalies due to enhanced convection over the eastern Indian Ocean [17]. Consequently, Java, located downstream of this convective region, is particularly sensitive to MJO-induced westerly wind intensification.

3.3. Streamline

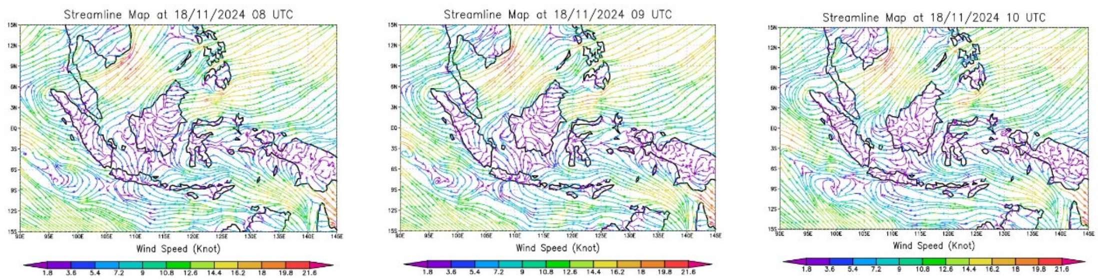

Fig. 4. Streamline Map on 18 November 2024

According to Figure 4, the low-level streamline evolution on 18 November 2024 between 08:00 and 10:00 UTC indicates that the strong wind event over Klaten and surrounding areas of Central Java was driven by regional-scale dynamics. At 08:00 UTC, a strengthening westerly to northwesterly monsoonal flow crossed Java, initiating low-level convergence over southern and central Java. By 09:00 UTC, the convergence intensified and became more organized, accompanied by increased wind curvature and horizontal shear, with wind speeds reaching 10–14 knots. These conditions favored convective development and the generation of strong downdrafts and gust fronts, leading to damaging surface winds over Klaten. At 10:00 UTC, the convergence zone persisted but shifted slightly eastward, indicating a transition toward a weakening phase of the event.

3.4. Atmospheric Stability Index

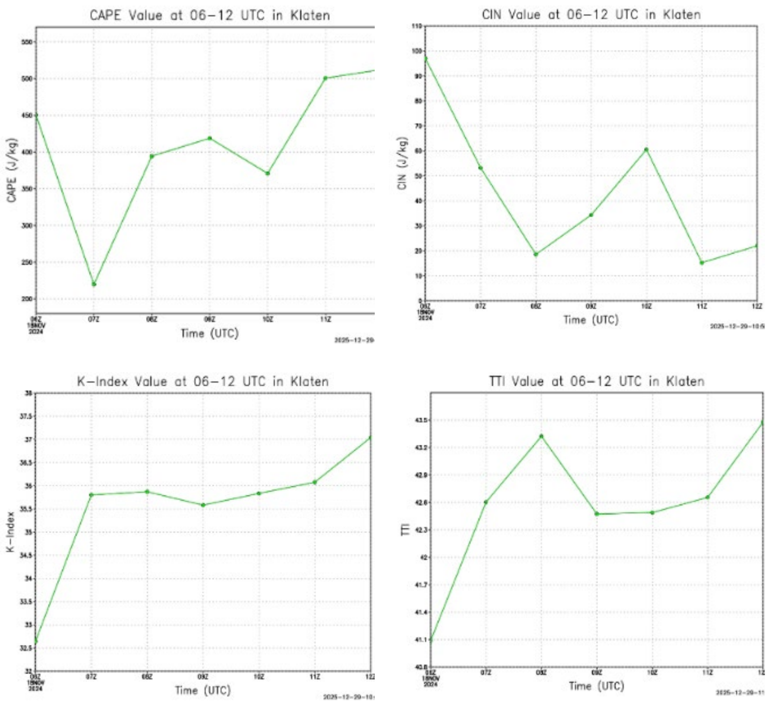

Fig. 5. Atmospheric Stability Index Chart

From Figure 5, it can be seen that the CAPE values are generally in the weak category [22], [28]. Nevertheless, there is a fairly significant increase at 08:00 UTC, and it continues to rise until 09:00 UTC with values around 390–420 J/kg, indicating an increase in convective activity, although the values are still relatively low. Meanwhile, CIN is in the moderate to weak range [22], with the weak category observed at 08:00–09:00 UTC and at 11:00 UTC. A significant decrease at 08:00 UTC, around 20 J/kg, indicates a relatively low inhibition to convection, allowing air to rise more easily into the upper layers of the atmosphere [19], [20]. Furthermore, KI is in the moderate category with values around 32.6–37°C [22], [28]. These values rise significantly towards 07:00–08:00 UTC and then experience slight fluctuations, indicating sufficient atmospheric instability to support the formation of local convection. Similarly, the TTI was in the weak to moderate range [22], [28], with moderate values recorded from 07:00 to 12:00 UTC. The most significant increase occurred at 08:00 UTC with a value of around 43.3°C, indicating that atmospheric instability reached a relatively high point during this period before slightly decreasing or remaining stable in the moderate range until 12:00 UTC. Like the KI, the TTI reflects sufficient atmospheric instability to support convective activity.

3.5. Weather Radar Imagery

Radar products used to analyze hail events include SSA overlay on CMAX, VCUT, MCAPPI (at an altitude of 3 km), TVD, and SWI.

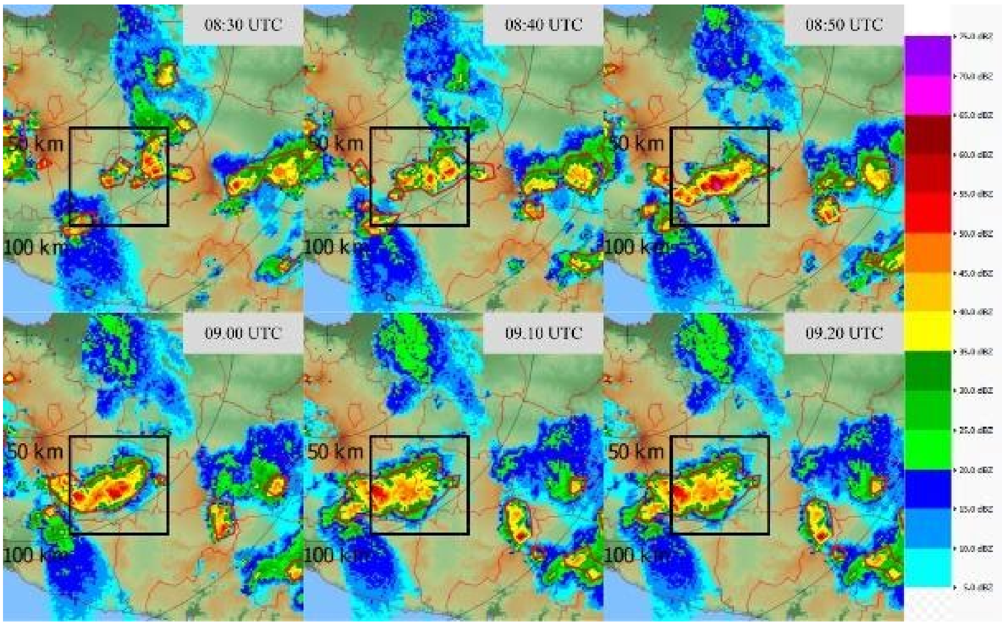

Fig. 6. SSA Overlay on CMAX Product

Table 2. Timeseries of Maximum Reflectivity

Maximum Reflectivity (dBZ)					
08:30	08:40	08:50	09:00	09:10	09:20
56.5	55.5	69	59	60.5	55.5

The CMAX product shows the growth of Cumulonimbus clouds starting to be seen at 08:30 UTC from the northeast of Klaten Regency. As delineated in Table 2, the storm's intensity experienced a rapid temporal evolution, highlighted by a surge in reflectivity from 55.5 dBZ at 08:40 UTC to its peak of 69 dBZ at 08:50 UTC while moving to the west. This significant growth in a fairly short time shows the presence of massive convective activity occurring at the location, indicating the potential for very strong cloud convergence and divergence. This intensification is further detailed by the Storm Structure Analysis (SSA), where red polygons delineate the active storm cells and the yellow polygons represent the cores of the Cumulonimbus cells. Initially, a single Cumulonimbus cell core was detected at 08:30 UTC, which subsequently developed into two distinct cores with very high reflectivity reaching peak intensity at 08:50 UTC. Reflectivity values remained high with a secondary maximum of 60.5 dBZ recorded at 09:10 UTC. Following this, the Cumulonimbus cells began to dissipate, characterized by the expansion of the cloud area and the fragmentation of the cores, as indicated by a notable decrease in reflectivity recorded between 09:00 and 09:20 UTC.

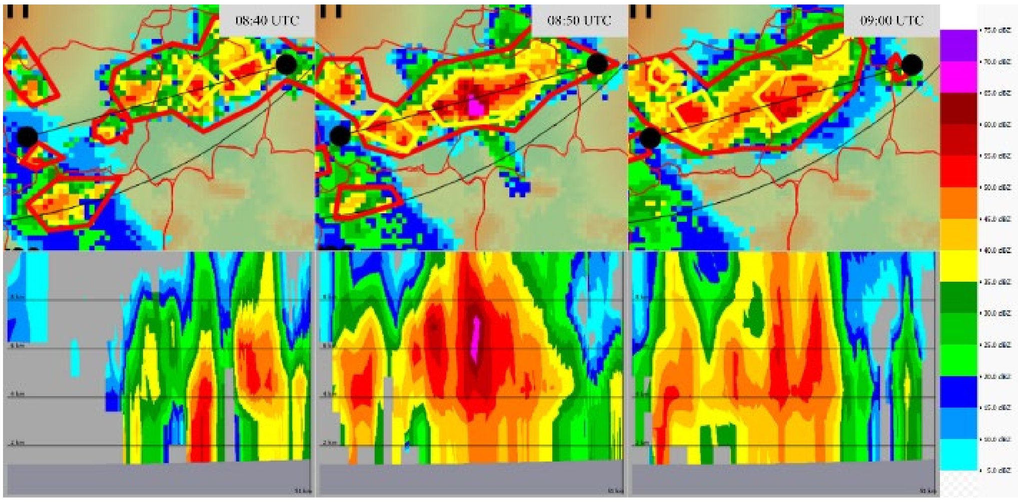

Fig. 7. SSA Overlay on CMAX Product and VCUT Product

The CMAX and VCUT products in Figure 7 illustrate the rapid development of Cumulonimbus clouds between 08:40 and 09:00 UTC. At 08:40 UTC, the clouds already showed significant vertical growth. By 08:50 UTC, the system reached its peak intensity, with reflectivity reaching a maximum of 69 dBZ (indicated by the magenta core). The vertical cross-section at that time confirmed that the convective core towered up to about 10 km, indicating very strong convective activity. At 09:00 UTC, the cloud system remained intense and continued to develop, reflecting ongoing strong convergence and divergence within the atmosphere.

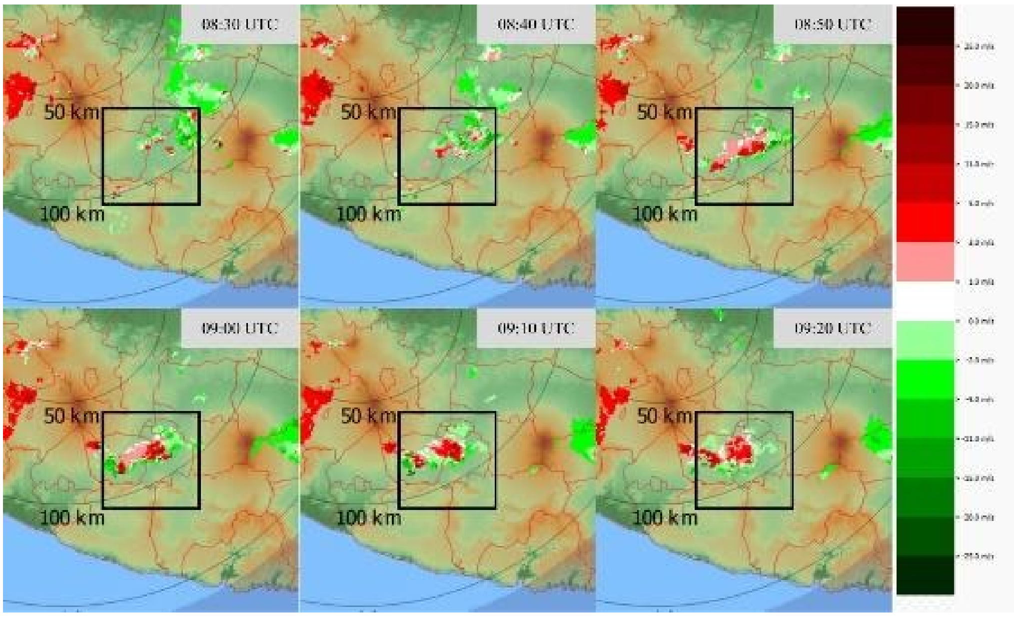

Fig. 8. MCAPPI Product

Weather conditions over Klaten Regency appeared to change drastically, as seen in Figure 8. Around 08:40 UTC, radar data showed a relatively uniform airflow moving toward the region. However, this situation did not last long. At an altitude of 3 kilometers above ground level, two air masses moving in opposite directions began to emerge. From one direction, the wind blew toward the radar (green), while from the other, the wind moved away from the radar (red). By 09:00 UTC, these two wind forces met directly over Klaten and its surroundings, creating a strong convergence zone. This collision of air masses forced the air at the meeting point to rise rapidly (updraft), triggering the formation of dense and towering Cumulonimbus clouds. It is within this storm cloud that the processes causing strong surface winds occurred. Cold air laden with raindrops inside the cloud became very heavy and eventually plunged downward at high speed.

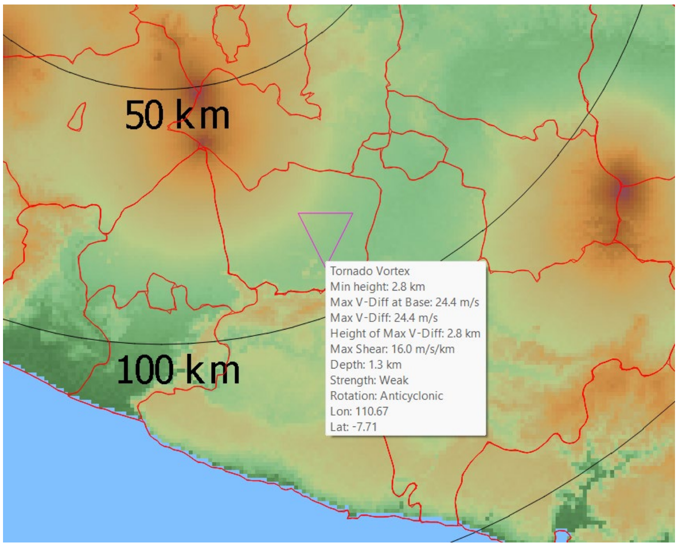

Fig. 9. TVD Product

Based on Figure 9, tornado vortex was detected at 09:10 UTC directly over the Klaten Regency area. This signifies the presence of opposing wind movements or shear, consistent with the interpretation of the previous wind velocity product.

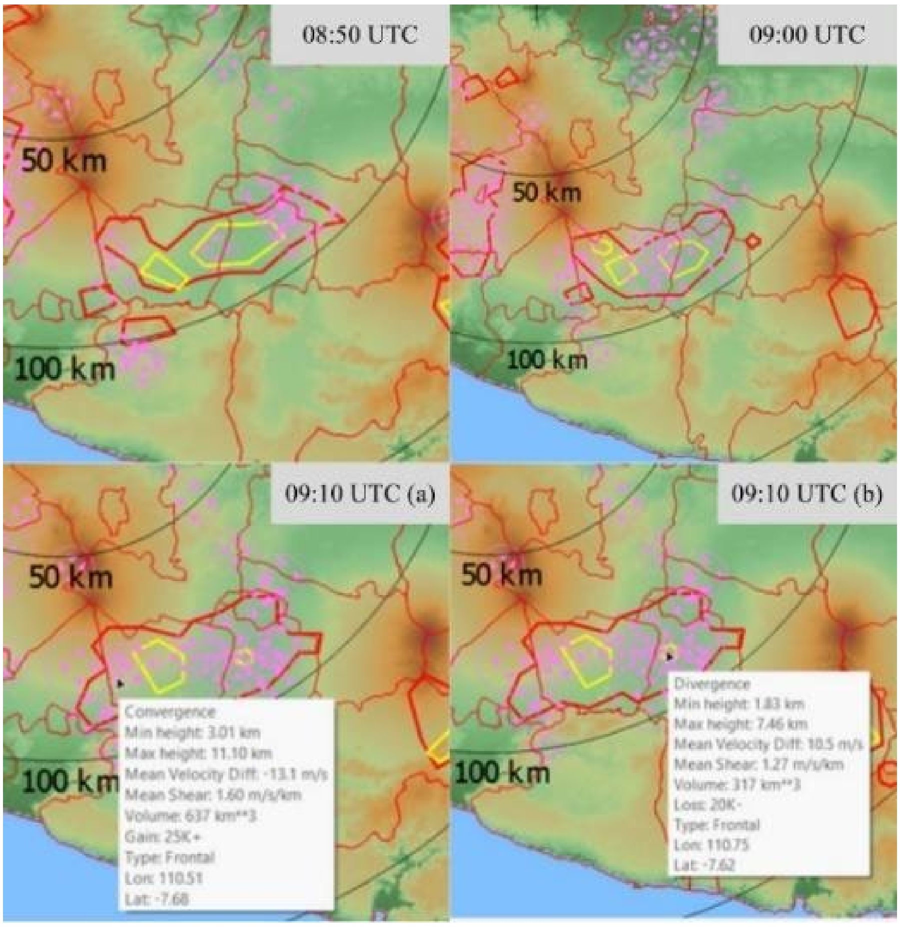

Fig. 10. SWI Product

According to Figure 10, it is observed that numerous convergence and divergence activities occurred within the same storm cell. Its rapid development is also visible, with the potential to cause significant weather at that time. The peak intensity of convective activity occurred at 09:10 UTC, when the radar simultaneously detected extreme convergence and divergence. The wind dynamics analysis was conducted by calculating horizontal divergence ($\nabla \cdot V$) through the spatial derivatives of the horizontal wind components u and v as in Equation (1):

$$Div = \frac{\partial u}{\partial x} + \frac{\partial v}{\partial y} \tag{1}$$

Radar products such as the SWI is estimated based on the radial velocity difference ($\Delta V = V_{r,out} - V_{r,in}$) within a storm cell, where $\Delta V < 0$ represents convergence triggering updrafts, while $\Delta V > 0$ indicates divergence reflecting surface-bound downdrafts. Furthermore, the vortex intensity in TVD products was calculated based on the radial wind shear ($S = \Delta V_r / L$) to confirm the presence of a vortex [29]. The quantitative data indicates very strong convergence, extending vertically from an altitude of 3 km to the cloud top at 11.10 km, signaling a very powerful updraft. At the same time, strong divergence was detected, representing a downdraft from within the storm. The interaction between this extreme vertical updraft and the strong downdraft provides definitive evidence of a mature and intense storm cell, which served as the direct mechanism causing the damaging strong winds on the ground in Klaten.

4. CONCLUSION

The strong wind event in Klaten Regency on 18 November 2024, was triggered by a local mesoscale convective process, characterized by vertical growth of Cumulonimbus clouds, high reflectivity, significant convergence in the lower layers, and vortex formation, with downbursts as the main mechanism of the strong winds. The positive IOD phase (DMI ≈ +0.5) and active MJO (phase 2–3) over the eastern Indian Ocean enhanced the regional westerly flow and moisture transport toward Java. These large-scale drivers may not directly trigger the storm, but they helped the precondition of the atmosphere by supporting low-level convergence and a moderately unstable environment. Lower-layer streamlines indicated significant convergence and horizontal shear supporting the formation of local convection. Atmospheric stability indices

(CAPE, CIN, KI, TTI) showed the atmosphere was sufficiently unstable, facilitating cloud growth, albeit not extreme. Radar imagery shows the direct mechanism of strong winds occurring at the surface in Klaten, where CMAX recorded a maximum reflectivity of 69 dBZ at 08:50 UTC, SSA showed the core of the Cumulonimbus cell and active storm cells, VCUT indicated the convective core rising up to 10 km, MCAPPI indicated the meeting of two opposing air masses forming a strong convergence zone around 09:00 UTC, TVD detected a tornado vortex at 09:10 UTC, and SWI showed the presence of convergence and divergence resulting in damaging strong winds.

REFERENCE

[1] I. N. Saputro, F. A. Wakid, and S. S. Dewi, "Pembuatan Sistem Peringatan Dini Angin Puting Beliung di Desa Demakijo, Kecamatan Karangnongko, Kabupaten Klaten," BEMAS: Jurnal Bermasyarakat, vol. 4, no. 2, pp. 351–356, Mar. 2024, doi: 10.37373/bemas.v4i2.845.

[2] BNPB, "Data Informasi Bencana Indonesia (DIBI)," https://dibi.bnpb.go.id/. [Accessed: Dec. 26, 2025].

[3] B. HK. Tjasyono, Meteorologi Indonesia I: Karakteristik dan Sirkulasi Atmosfer, 4th ed., vol. 1. Badan Meteorologi, Klimatologi, dan Geofisika, 2012.

[4] R. R. Rogers and M. K. Yau, A Short Course in Cloud Physics, 3rd ed. Elsevier, 1989.

[5] D. Kurniawan, F. O. Hidayat, B. H. Aritonang, R. A. Aliyafi, and S. Amri, "A 30-Year Climatological Analysis of Atmospheric Dynamics Anomalies during CENS in Western Indonesia," Journal of Maritime Policy Science, vol. 2, no. 3, pp. 146–157, 2025, doi: 10.31629/jmps.v2i3.7974.

[6] D. Septian, W. S. Zahran, and R. A. Utami, "Analisis Kinerja Anggota Satpol PP Kota Bekasi Dalam Penertiban Pedagang Kaki Lima di Kota Bekasi," Jurnal Ilmu Administrasi Publik, vol. 3, no. 3, pp. 363–370, 2023.

[7] N. H. Saji, B. N. Goswami, P. N. Vinayachandran, and T. Yamagata, "A Dipole Mode in the Tropical Indian Ocean," Nature, vol. 401, pp. 360–363, 1999.

[8] H. Hersbach, B. Bell, P. Berrisford, S. Hirahara, A. Horányi, J. Muñoz-Sabater, J. Nicolas, C. Peubey, R. Radu, D. Schepers, A. Simmons, C. Soci, S. Abdalla, X. Abellan, G. Balsamo, P. Bechtold, G. Biavati, J. Bidlot, M. Bonavita, G. D. Chiara, P. Dahlgren, D. Dee, M. Diamantakis, R. Dragani, J. Flemming, R. Forbes, M. Fuentes, A. Geer, L. Haimberger, S. Healy, R. J. Hogan, E. Hólm, M. Janisková, S. Keeley, P. Laloyaux, P. Lopez, C. Lupu, G. Radnoti, P. D. Rosnay, I. Rozum, F. Vamborg, S. Villaume, and J. Thépaut, "The ERA5 Global Reanalysis," Quarterly Journal of the Royal Meteorological Society, vol. 146, no. 730, pp. 1999–2049, Jul. 2020, doi: 10.1002/qj.3803.

[9] A. Lumbangaol and A. Munandar, "Atmosphere Dynamic Analysis of Hail and Whirl Wind in Cianjur Regency, West Java (Case Study November 07, 2016)," in the 1st International Conference on Science, Mathematics, Environment, and Education (ICoSMEE), ICoSMEE PROCEEDING, 2018, pp. 127–135.

[10] N. H. Muzaki, E. Diniyati, R. R. Pratama, and A. Mulya, "Analisis Kondisi Atmosfer Saat Kejadian Hujan Lebat dan Angin Kencang di Probolinggo Berdasarkan Citra Satelit Dan Citra Radar," JIIF (Jurnal Ilmu dan Inovasi Fisika), vol. 5, no. 2, pp. 142–156, 2021.

[11] A. N. Efendi and S. Kuncorojati, "Analisis Hujan dan Angin Kencang di Melawi Mengunakan Data Radar dan Satelit Cuaca (Studi Kasus Tanggal 29 Desember 2018)," Jurnal Widya Climago, vol. 2, no. 1, 2020.

[12] R. Rafi, D. Kuncoro, B. Arzhida, N. J. Indriyani, and Warjono, "Identifikasi Penyebab Awan Konvektif Pada Fenomena Hujan Ekstrem Disertai Es Berbasis Citra Radar Dual Polar," Jurnal Penelitian Saintek, vol. 3, no. 2, pp. 58–73, 2025, doi: 10.21831/jps.v30i2.89950.

[13] W. Sulistiyono, N. H. S. Salsabil, and S. A. Ramadhan, "Aplikasi Produk Radar C-Band dalam Identifikasi Awan Penghasil Hujan Es (Studi Kasus: Bogor, 24 Januari 2022)," GEOGRAPHIA, vol. 5, no. 2, pp. 137–143, 2024, doi: 10.53682/gjppg.v5i2.8577.

[14] E. I. V. Manurung, S. Humaidi, and Y. Darmawan, "Analysis of Strong Wind Characteristics Using Doppler Weather Radar over Kualanamu Airport Indonesia," JOURNAL OF APPLIED GEOSPATIAL INFORMATION, vol. 8, no. 1, pp. 6–11, 2024.

[15] M. Montopoli, C. Annella, L. Baldini, E. Adirosi, V. Capozzi, and G. Vulpiani, "Rain Motion Vectors Analysis from the Radar Network in Italy," IEEE J. Sel. Top. Appl. Earth Obs. Remote Sens., vol. 17, pp. 11655–11669, 2024, doi: 10.1109/JSTARS.2024.3410031.

[16] H. Adiwira, N. P. Purba, S. A. Harahap, and M. L. Syamsuddin, "Variabilitas Suhu Laut Pada Kejadian IOD (Indian Ocean Dipole) di Perairan Barat Sumatera Menggunakan Data Argo Float," Depik, vol. 7, no. 1, pp. 28–41, Apr. 2018, doi: 10.13170/depik.7.1.8089.

[17] W. J. Pattipeilohy, F. M. B, and D. P. Asri, "Analisis Pengaruh Madden Julian Oscillation (Mjo) Terhadap Anomali Curah Hujan di Wilayah Ngurah Rai," Jurnal Meteorologi Klimatologi dan Geofisika, vol. 6, no. 2, 2019.

[18] J. R. Holton and G. J. Hakim, An Introduction to Dynamic Meteorology, 5th ed. Academic Press, 2013.

[19] M. Sawal, D. A. Siregar, and Y. H. M. Hutabarat, "Analisis Dinamika Atmosfer Kejadian Angin Puting Beliung Tanjung Balai Karimun (Studi Kasus: 14 Mei 2024)," Megasains, vol. 15, no. 2, pp. 38–48, 2024, doi: 10.46824/megasains.v15i2.237.

[20] W. Sulistiyono, R. Surya Ramadhan, and Y. D. Haryanto, "Kajian Kondisi Atmosfer Saat Kejadian Hujan Lebat di Kota Surakarta Menggunakan Analisis Skala Meteorologi (Studi Kasus: 3 Februari 2021)," OPTIKA, vol. 7, no. 1, pp. 32–45, 2023.

[21] N. Kusumawardani and A. A. Azani, "Kajian Indeks Stabilitas Atmosfer Terhadap Kejadian Hujan Lebat Di Kota

Bitung:(Studi Kasus Tahun 2020-2021),” Jurnal Widya Climago, vol. 4, no. 1, 2022.
[22] A. G. Fernanda, A. Ihwan, and R. Adriat, “Analisis Indeks Stabilitas Udara pada Saat Kejadian Angin Puting Beliung di Kota Pontianak,” PRISMA FISIKA, vol. 12, no. 01, pp. 6–19, 2024.
[23] D. L. A. Purba, I. J. A. Saragih, and D. S. Sosaidi, “Utilization of weather-radar data to observe the Sea Breeze Front (SBF) over the North Coast of Banten-Jakarta (case study in 2018),” in IOP Conference Series: Earth and Environmental Science, IOP Publishing Ltd, Nov. 2021, pp. 1–14. doi: 10.1088/1755-1315/893/1/012055.
[24] T. M. Smith and K. L. Elmore, “The Use of Radial Velocity Derivative to Diagnose Rotation and Divergence,” in 11th Conference on Aviation, Range, and Aerospace Meteorology (ARAM) and 22nd Conference on Severe Local Storms (SLS), American Meteorological Society (AMS), 2004.
[25] M. A. Miller, S. E. Yuter, N. P. Hoban, L. M. Tomkins, and B. A. Colle, “Detecting wave features in Doppler radial velocity radar observations,” Atmos. Meas. Tech., vol. 15, no. 6, pp. 1689–1702, Mar. 2022, doi: 10.5194/amt-15-1689-2022.
[26] R. A. Madden and P. R. Julian, “Description of Global-Scale Circulation Cells in the Tropics with a 40-50 Day Period,” J. Atmos. Sci., vol. 29, pp. 1109–1123, 1972.
[27] Y. M. Yang and B. Wang, “Improving MJO simulation by enhancing the interaction between boundary layer convergence and lower tropospheric heating,” Clim. Dyn., vol. 52, no. 7–8, pp. 4671–4693, Apr. 2019, doi: 10.1007/s00382-018-4407-9.
[28] Selex ES GmbH, “Rainbow® 5 File Format: Phenomena Detection Products,” Neuss, Germany, 2016.

Journal of Computation Physics and Earth Science
ISSN: 2776-2521 (online)
Volume 5, Number 2, February 2026, Page 173 - 179
https://journal.physan.org/index.php/jocpes/index

Revealing the Subsurface Geometry of the 2023 Sumedang Earthquake Sequence Using Double-Difference Relocation and Cross-Section Analysis

Rayhan Irfan Hielmy[1]
[1]Undergraduate Program in Geophysics (STMKG)

Article Info

Article history:

Received December 27, 2025
Revised March 1, 2026
Accepted March 2, 2026

Keywords:

Sumedang Earthquake
Hypocenter Relocation
Double-Difference
Cross-Section Analysis
Baribis Fault

A B S T R A C T

The Sumedang Regency experienced a significant tectonic earthquake sequence beginning on December 31, 2023, which raised concerns regarding active fault structures in the region. Identifying the precise causative fault geometry was essential for seismic hazard mitigation but remained challenging due to the complex local geology and potential location errors in preliminary data. This study investigated the source mechanism and subsurface geometry of the aftershocks recorded between December 31, 2023, and January 8, 2024. The Double-Difference (HypoDD) method was applied to relocate earthquake hypocenters by minimizing travel-time residuals, utilizing a 1-D velocity model with a variable Vp/Vs ratio. Subsequently, vertical cross-section analysis was conducted to interpret the dip patterns and fault orientation perpendicular to the seismicity trend. The results revealed a significant transformation in the spatial distribution pattern; while initial data exhibited a linear north-south trend, the relocated hypocenters formed a distinct curved cluster extending from the south toward the west. The seismic activity was concentrated at shallow depths ranging from 3 km to 17 km. Cross-section interpretations suggested two potential fault geometries: a near-vertical alignment indicating a strike-slip mechanism potentially associated with the Subang Segment of the Baribis Fault, or an inclined, slab-like structure indicative of a thrust fault system. These findings provided critical constraints for future moment tensor inversion studies.

Corresponden Author:

Rayhan Irfan Hielmy,
Undergraduate Program in Geophysics (STMKG)
Tangerang, Indonesia
Email: rayhanirfanhielmy@stmkg.ac.id

1. INTRODUCTION

Indonesia is an archipelagic country with highly complex and dynamic geological conditions because it is located at the convergence of three major tectonic plates: the Indo-Australian Plate, the Eurasian Plate, and the Pacific Plate. The interaction of these three plates places Indonesia within the Pacific Ring of Fire, making the region highly vulnerable to various natural hazards, particularly earthquakes. This high level of tectonic activity results in an earthquake occurrence frequency in Indonesia that is significantly higher than in most other countries worldwide. Based on seismic statistical data, Indonesia is ranked among the top ten countries globally with the highest frequency of earthquakes [1]. Specifically in West Java, the complexity of active onshore fault structures often triggers damaging shallow earthquakes, even when their magnitudes are relatively moderate [2].

An earthquake is defined as a sudden release of energy in the form of seismic waves that propagate throughout the Earth's surface due to disturbances or fractures within the Earth's crust. This natural phenomenon is one of the most feared disasters because it is extremely difficult to predict and can cause destructive impacts, ranging from infrastructure damage and economic losses to loss of life [3]. The initial point within the Earth where energy release begins is referred to as the hypocenter or earthquake focus, while the visual representation of the spatial distribution of such events is known as a seismic map [4]. Accuracy in determining earthquake parameters, particularly hypocenter locations, is crucial for understanding the geometry of the causative fault and for mitigating potential future disaster risks.

To improve the accuracy of earthquake source locations, relocation methods that can minimize errors caused by heterogeneous velocity models are required, one of which is the Double-Difference or HypoDD method. The HypoDD method is an earthquake relocation technique developed to obtain more precise hypocenter positions by minimizing travel-time residuals between pairs of earthquakes [5]. The basic principle of this method involves measuring the differential travel times of seismic waves from two closely spaced earthquake events recorded at the same station, under the assumption that the raypaths traveled are identical [6]. In its implementation, HypoDD performs iterative calculations to update locations and partial derivatives in order to minimize the differences between observed and calculated travel times [7].

The case study in this research focuses on a tectonic earthquake sequence that struck Sumedang Regency, West Java. The mainshock, with a magnitude of M 4.1, occurred on Sunday, 31 December 2023 at 14:35 WIB, followed by a series of aftershocks. The Meteorology, Climatology, and Geophysics Agency (BMKG) reported that the epicenter of the mainshock was located at coordinates 6.85° S and 107.93° E, situated on land approximately 1 km northeast of Sumedang Regency at a depth of 7 km. As of 8 January 2024, a total of 11 aftershocks had been recorded, increasing the urgency for a more detailed analysis of the characteristics of this earthquake source. Therefore, this study aims to compare changes in hypocenter positions before and after relocation and to identify the fault structures triggering the earthquakes in the region through cross-section analysis.

2. RESEARCH METHOD

The primary data used in this study include seismic waveform data, recording station coordinates, and initial earthquake catalog parameters for events that occurred in Sumedang Regency, West Java. The analyzed data span earthquakes recorded from 31 December 2023 to 8 January 2024, obtained from the seismic network of the Meteorology, Climatology, and Geophysics Agency (BMKG). The initial stage of data processing began with the identification and determination of arrival times (picking) of P-wave and S-wave phases from digital seismogram recordings. This picking process was carried out using Linux-based seismic analysis software, namely SAC (Seismic Analysis Code).

The subsequent stage involved hypocenter relocation using the Double-Difference (HypoDD) algorithm, which integrates the picked travel-time data with a seismic velocity model. In this modeling, a P- to S-wave velocity ratio (Vp/Vs) of 1.75 was applied, along with a 1-D velocity model that varies with depth. This specific velocity structure and Vp/Vs ratio were adopted based on the standard regional velocity model utilized by the BMKG, which has been proven reliable for resolving shallow crustal seismicity in the West Java region, including the Sumedang basin [2]. The P-wave velocity was assumed to start at 2.3 km/s at the surface (0.0 km), increase significantly to 5.8 km/s at a depth of 2.0 km, then to 6.3 km/s at 12.0 km depth, 6.9 km/s at 22.0 km depth, and finally reach 8.0 km/s at a depth of 32.0 km. The application of an accurate velocity model in the HypoDD algorithm aims to minimize travel-time residuals between pairs of earthquake events, thereby producing more precise hypocenter locations [8].

After obtaining the relocated hypocenter coordinates, spatial visualization was performed to compare the distribution of earthquakes before and after relocation. The analysis was further extended by constructing cross-sections perpendicular to the trend of earthquake distribution to identify dip patterns and the geometry of subsurface structures. The results of these cross-sections consist of projected hypocenter depth points that assist in interpreting the relationship between seismicity and tectonic activity or the presence of active faults in the study area [9]. All epicenter distribution mapping and cross-section visualizations were generated using GMT (Generic Mapping Tools), which is widely recognized for its reliability in geophysical data processing [10], [11]. The complete sequence of data processing steps in this study is presented in the flowchart shown in Figure 1.

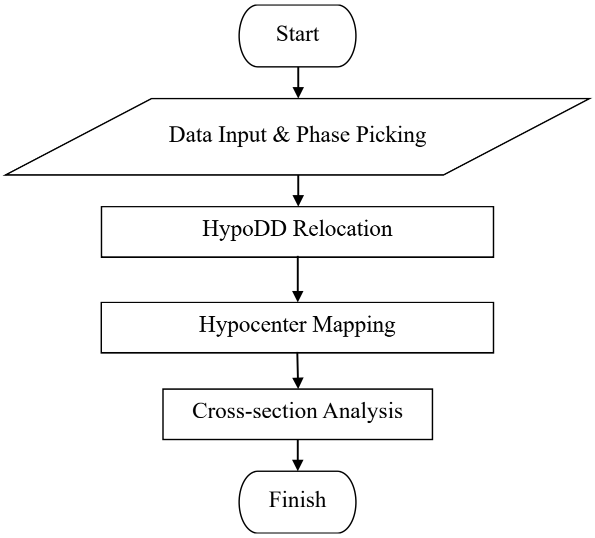

Fig. 1. Research Flowchart

3. RESULTS AND DISCUSSION

3.1. Seismicity and Initial Earthquake Distribution

The pattern of seismicity distribution in West Java during the observation period from 31 December 2023 to 8 January 2024 shows a significant concentration of activity in Sumedang Regency. As illustrated in Figure 2, earthquake epicenters are predominantly concentrated on land and are characterized by shallow depths, generally less than or equal to 20 km. The recorded earthquake magnitudes vary considerably, ranging from small events (M ~3.0) to relatively significant earthquakes approaching M 5.0, indicating energy release associated with local fault activity. Spatially, this earthquake cluster is located very close to the trace of the Baribis Fault, Subang Segment, which has long been identified as one of the main active structures in northern West Java [12]. The proximity of the epicenters to this fault trace suggests an initial hypothesis that the tectonic activity in Sumedang is closely related to the dynamics of the Baribis Fault, which is known to exhibit a relatively active geodetic slip rate [13].

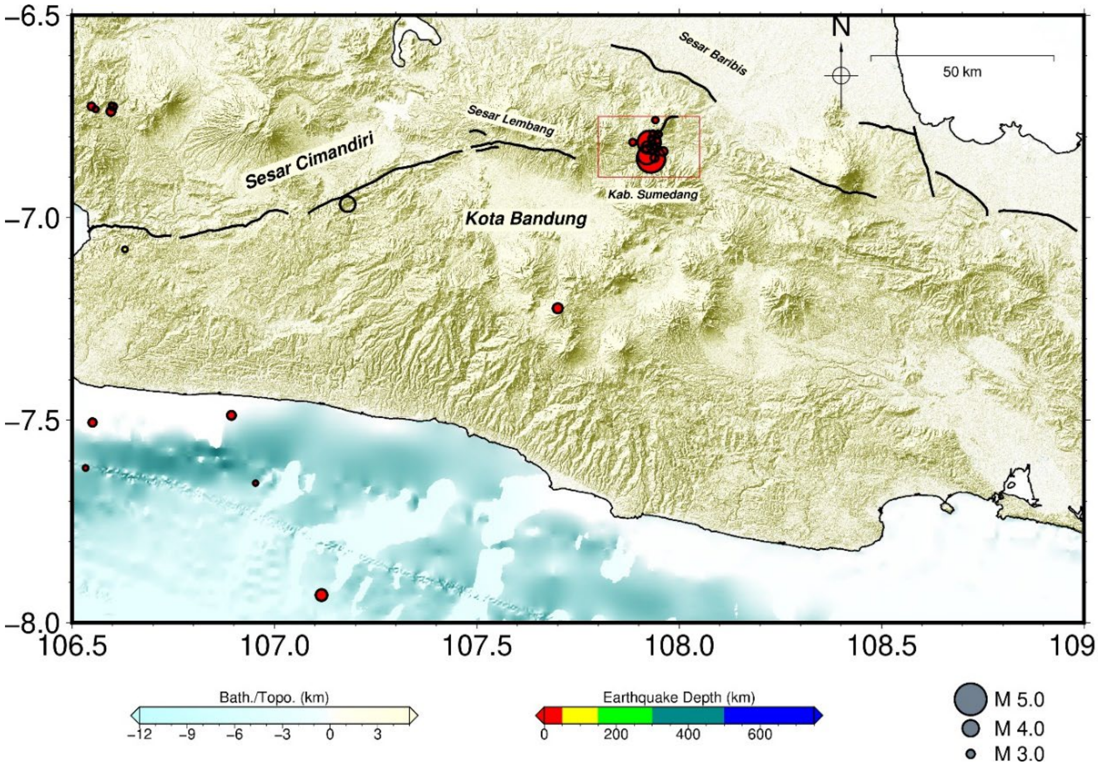

Fig. 2. Earthquake Distribution Map in West Java during 31 December 2023 – 8 January 2024

3.2. Hypocenter Relocation Analysis

To validate the association between earthquake distribution and geological structures, a comparison of hypocenter distributions before and after relocation was conducted. In Figure 3, the initial data (prior to relocation) show an aftershock distribution pattern that tends to be linear with a north–south orientation, which at first glance appears perpendicular to the general trend of regional structures in West Java. However, after relocation using the Double-Difference method, the spatial distribution pattern in Figure 4 changes significantly, with epicenters forming a more curved cluster extending from the south toward the west. Such post-relocation changes in orientation are common, as improvements in travel-time residuals can reveal the complexity of fault geometry that was previously obscured by location errors [14]. Although this curved pattern may indicate a complex fault geometry, the possibility of bias resulting from the sensitivity of P- and S-wave picking within the local station network cannot be ruled out [15].

The stability of the HypoDD algorithm, despite the limited number of events, is demonstrated by the stable convergence of the inversion and a consistent reduction in travel-time residuals. The overall Root Mean Square (RMS) error decreased significantly following the relocation process compared to the initial catalog. This successful convergence confirms the computational reliability of the relocated hypocenter coordinates, proving that the method effectively minimized errors caused by the unmodeled velocity structure.

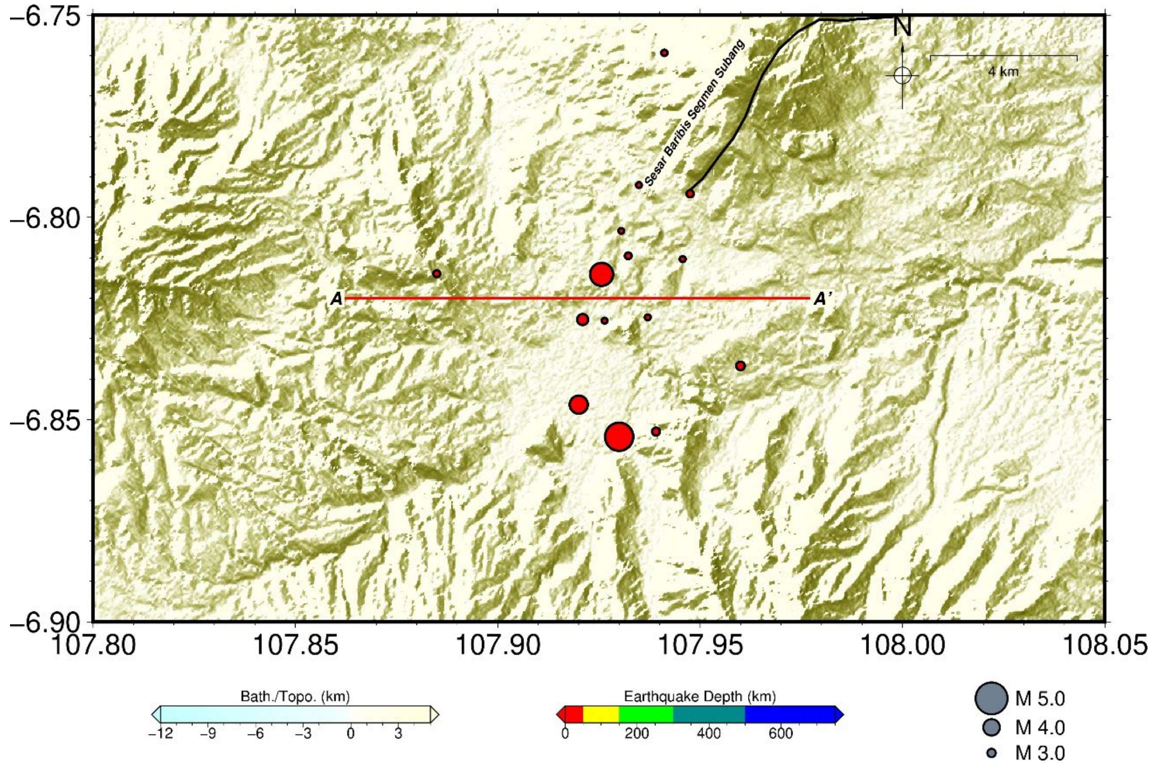

Fig. 3. Distribution map of aftershocks in Sumedang before relocation

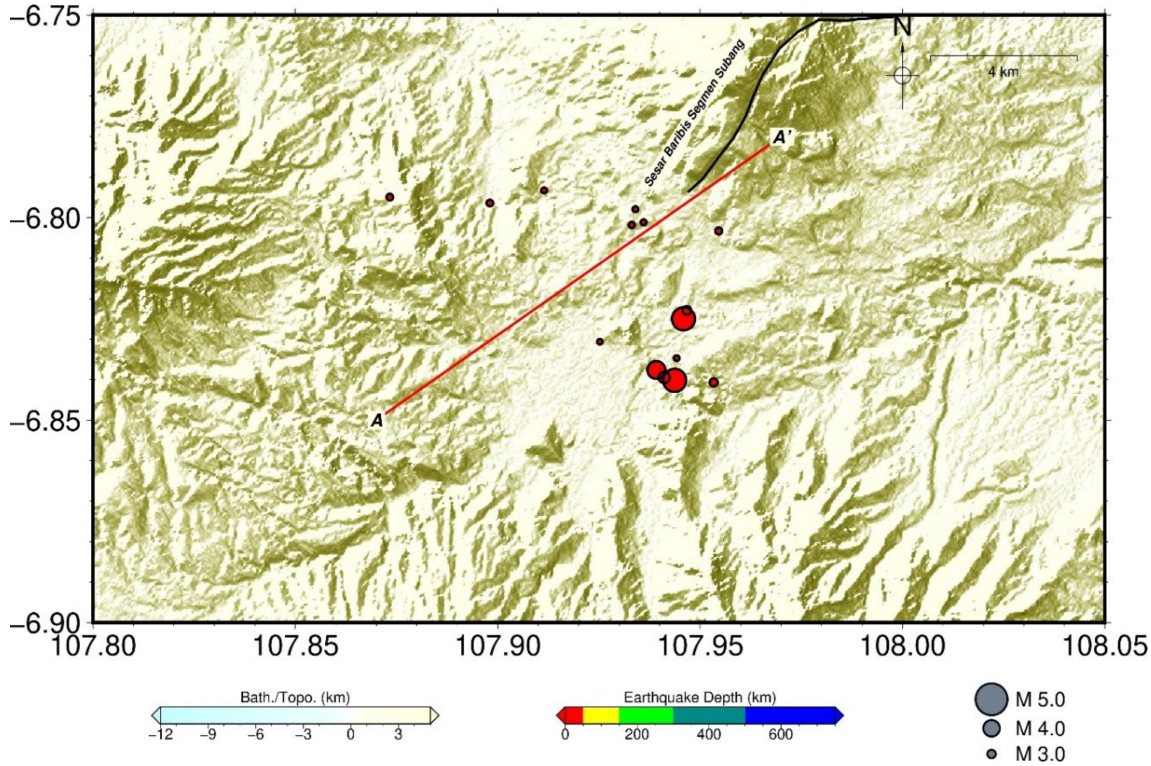

Fig. 4. Distribution map of aftershocks in Sumedang after relocation

3.3. Structural Interpretation Through Cross-Section Analysis

A more detailed analysis was carried out by constructing vertical cross-sections to better understand the subsurface geometry of the earthquake source zone. Based on Figure 5, the vertical section of the initial data shows hypocenter distributions spread over a depth range of approximately 3 km to 17 km, displaying a generally vertical but still diffuse pattern. In contrast, the relocated results shown in Figure 6 exhibit a more focused depth distribution that forms patterns interpretable under two possible source mechanism scenarios. The first possibility is that the nearly vertical alignment observed in the cross-section indicates a strike-slip faulting mechanism, which is consistent with the general characteristics of the Baribis Fault in several of its segments [16].

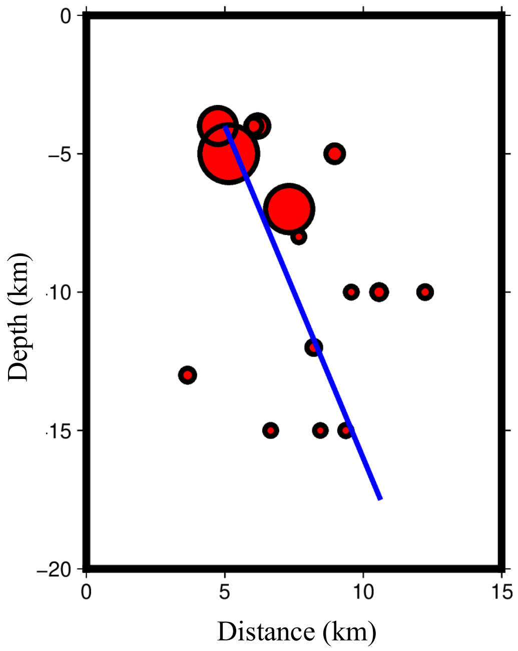

Fig. 5. Vertical cross-section of hypocenter distribution before relocation

On the other hand, the pattern in Figure 6 also shows a tendency toward an inclined geometry resembling a slab or curved fault plane. This feature opens a second possibility, namely the presence of a thrust or normal fault mechanism, which is often associated with shallow crustal deformation in the back-arc region of Java. This complexity suggests that the Baribis Fault, Subang Segment, may exhibit a mixed or oblique geometry at certain depths.

Therefore, although the relocated cross-section analysis provides a clearer depiction of subsurface geometry, definitive identification of the fault kinematics generally requires further analysis, such as moment tensor inversion, to accurately determine the strike, dip, and rake parameters [17]. To resolve the structural ambiguity in this study, we integrated our relocated cross-section with the official focal mechanism solution published by BMKG for the M 4.1 mainshock. The BMKG moment tensor indicates a predominantly strike-slip mechanism. By overlaying this kinematic constraint with the near-vertical alignment observed in Figure 6, it can be conclusively interpreted that the causative structure of the 2023 Sumedang sequence is a strike-slip fault associated with the Baribis Fault system (Subang Segment).

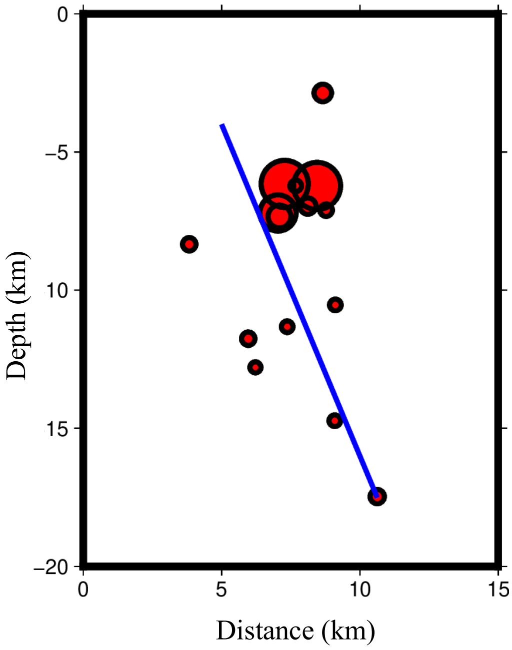

Fig. 6. Vertical cross-section of hypocenter distribution after relocation

4. CONCLUSION

The application of the Double-Difference relocation method to the Sumedang aftershock sequence successfully revealed a significant change in the hypocenter distribution pattern, from an initial north–south trend to a curved orientation toward the southwest. The identified earthquake activity is concentrated at shallow depths ranging from 3 to 17 km. Based on the cross-section analysis and corroborated by the BMKG focal mechanism solution for the mainshock, the causative fault is definitively interpreted as a near-vertical strike-slip structure. This resolves the spatial ambiguity and firmly associates the Sumedang earthquake sequence with the active strike-slip dynamics of the Baribis Fault system.

REFERENCE

[1] R. Meilani, Rosida Tiurma Manurung, Maria Yuni Megarini, Tessalonika Sembiring, and Karthy Priyathy Mastovani, “Penanganan psikologis pasca gempa bumi Sumedang,” BEGAWE J. Pengabdi. Masy., vol. 2, no. 1, pp. 59–62, 2024.

[2] P. Supendi, A. D. Nugraha, N. T. Puspito, S. Widiyantoro, and D. Daryono, “Identification of active faults in West Java, Indonesia, based on earthquake hypocenter determination, relocation, and focal mechanism analysis,” Geosci. Lett., vol. 31, pp. 4–10, 2018, doi: 10.1186/s40562-018-0130-y.

[3] D. Purwanto, D. D. Permadi, U. S. Saputri, U. Aditiawarman, D. O. D. Handayani, and D. A. Dewi, “Kajian tentang bencana dan dampak gempa bumi di cianjur bersama mahasiswa teknik sipil nusaputra,” J. Pengabdi. Kpd. Masy. Abdi Nusa, vol. 3, no. 1, pp. 36–39, 2023.

[4] M. Aritonang, A. F. T. Parera, and N. Nasution, “Relokasi Hiposenter Gempabumi Di Segmen (Toru, Angkola, Barumun) Dengan Menggunakan Metode Double Difference (Hypo-DD),” Pendidik. Fis. dan Sains, vol. 4, no. 2,

pp. 24–29, 2021.
[5] F. Waldhauser and W. L. Ellsworth, “A Double-difference Earthquake location algorithm: Method and application to the Northern Hayward Fault, California,” Bull. Seismol. Soc. Am., vol. 90, no. 6, pp. 1353–1368, 2000, doi: 10.1785/0120000006.
[6] S. Wulandari, A. F. T. Parera, and L. H. Lubis, “Relokasi Gempabumi di Sesar Renun A, B, Dan C dengan Menggunakan Metode Double Difference (Hypo-DD),” GRAVITASI J. …, vol. 4, no. 2, pp. 30–35, 2021, [Online]. Available: https://ejurnalunsam.id/index.php/JPFS/article/view/4560
[7] W. T. Baskoro, I. G. A. Kasmawan, I. K. Putra, N. N. Ratini, and Sismanto, “Metode Double-Difference Untuk Merelokasi Hiposenter Gempabumi Susulan Seririt Singaraja,” Kappa J., vol. 8, no. 1, pp. 28–33, 2024, doi: 10.29408/kpj.v8i1.24434.
[8] F. Waldhauser, hypoDD: A computer program to compute double-difference earthquake locations. 2001.
[9] M. P. Lestari, Budiarta, Darsono, and Y. H. Perdana, “Penggunaan Software GMT 6 Dan Python Untuk Menampilkan Peta Seismisitas Dan Menghitung Besar Sudut Subduksi Di Pulau Jawa,” J. Stasiun Geofis. Sleman, vol. 1, no. 2, p. 19, 2023.
[10] A. Arimuko, B. M. T. F. Nanda, and Rasmid, “Identifikasi Struktur Bawah Permukaan Berdasarkan Pemodelan Kecepatan 1D Hasil Relokasi Hiposentrum Gempa di Pulau Lombok, Gunung Sinabung, dan Jailolo,” J. Geofis., vol. 18, no. 02, pp. 40–48, 2021.
[11] P. Wessel et al., “The Generic Mapping Tools Version 6,” Geochemistry, Geophys. Geosystems, vol. 20, no. 11, pp. 5556–5564, 2019, doi: 10.1029/2019GC008515.
[12] B. E. B. Nurhandoko et al., “Subsurface Characterization and Revealing Geometry of the Baribis Fault in the Eastern Part of West Java Using Long-Offset Resistivity Tomography,” J. Earthq. Tsunami, vol. 19, no. 2, pp. 1–25, 2025, doi: 10.1142/S1793431124500313.
[13] A. Koulali et al., “Crustal strain partitioning and the associated earthquake hazard in the eastern Sunda-Banda Arc,” Geophys. Res. Lett., vol. 43, no. 5, pp. 1943–1949, 2016, doi: 10.1002/2016GL067941.
[14] V. I. C. Sinaga, M. A. F. Aolindar, M. A. N. Pramudita, P. Supendi, K. H. Kirana, and M. U. Hasanah, “Relocation of Earthquake Hypocenter Using Double-Difference Method in Western Part of Sumatera,” J. Phys. Conf. Ser., vol. 2582, no. 1, pp. 1–8, 2023, doi: 10.1088/1742-6596/2582/1/012004.
[15] A. D. Nugraha et al., “Hypocenter Relocation of Earthquake Swarm in West Halmahera, North Molucca Region, Indonesia by using Double-Difference Method and 3D Seismic Velocity Structure,” in IOP Conference Series: Earth and Environmental Science, 2017. doi: 10.1088/1755-1315/62/1/012053.
[16] D. H. Natawidjaja, B. Sapiie, G. I. Marliyani, and M. R. Daryono, “Baribis-Kendeng Thrust-Fold Zone of Java, Indonesia: New Evidences of Active Back-Arc Tectonics and Their Implications to Seismic Hazards,” Proc. Jt. Conv. MALANG 2017, no. Jcm, 2017.
[17] L. Ye et al., “The 22 December 2018 tsunami from flank collapse of Anak Krakatau volcano during eruption,” Sci. Adv., vol. 6, no. 3, pp. 1–9, 2020, doi: 10.1126/sciadv.aaz1377.

Journal of Computation Physics and Earth Science
ISSN: 2776-2521 (online)
Volume 5, Number 2, February 2026, Page 180 - 188
https://journal.physan.org/index.php/jocpes/index

Estimation of Jayapura 2023 Aftershock Decay Time Using Python-Based Secant Algorithm

Rayhan Irfan Hielmy[1], Sandy Tri Gustono[2]
[1,2]Undergraduate Program in Geophysics (STMKG)

Article Info

Article history:

Received December 26, 2025
Revised February 28, 2026
Accepted February 28, 2026

Keywords:

Aftershock Decay
Secant Method
Mogi II Model
Computational Seismology
Jayapura Earthquake

A B S T R A C T

Accurately determining the termination time of aftershocks is crucial for disaster mitigation and establishing safe periods for community recovery. This study aimed to estimate the decay time of the January 2023 Jayapura aftershock sequence (M 5.4) using a numerical computational approach. The Mogi II decay model was selected due to its high compatibility with local seismicity. To resolve its complex non-linear exponential equations without analytical derivatives, the Secant Method was implemented using Python. The algorithm was initialized with starting guess values of x_0=0 and x_1=1, and an error tolerance of 0.0001. To validate algorithmic robustness and efficiency, a sensitivity test was conducted, and the method was benchmarked against the Bisection method. Results demonstrated that the Secant algorithm achieved superior computational efficiency, converging in exactly 10 iterations (~0.000115 seconds) compared to Bisection's 18 iterations, while remaining highly stable under arbitrary extreme initial guesses. The numerical solution predicted the decay termination at day 12.765, subsequently rounded to 13 days following the mainshock. This finding showed exact agreement with manual observational data, successfully extrapolating the decay trajectory beyond the 10-day BMKG recording window. The study concluded that the Python-based Secant algorithm is effective, rapid, robust, and precise in solving the Mogi II equation, demonstrating significant potential as an automated analytical tool to enhance disaster mitigation decision-making.

Corresponden Author:

Rayhan Irfan Hielmy,
Undergraduate Program in Geophysics (STMKG)
Tangerang, Indonesia
Email: rayhanirfanhielmy@stmkg.ac.id

1. INTRODUCTION

Indonesia is a country with a highly complex tectonic setting, situated at the convergence of major global tectonic plates and traversed by the Circum-Pacific Belt (Ring of Fire). These geological conditions place Indonesia in a region with a high level of vulnerability to natural hazards, particularly earthquakes and volcanism. Such sudden-onset disasters have the potential to cause significant loss of life, especially in archipelagic regions that face logistical accessibility challenges during emergency response [1]. Based on hypocenter depth, earthquakes are classified into deep, intermediate, and shallow events, with shallow earthquakes often being the most destructive due to the proximity of the energy source to the Earth's surface. Recent studies on active fault activity, as revealed by various damaging earthquakes in Java, indicate that understanding fault patterns and aftershock activity is crucial for the mitigation of shallow earthquake hazards [2].

In the seismic activity cycle, the phenomena of mainshocks and aftershocks constitute an inseparable sequence of events [3]. After the release of the main energy, the Earth's crust surrounding the rupture zone undergoes an adjustment process toward a new equilibrium, which triggers a series of aftershocks. Theoretically, the magnitude and frequency of these aftershocks are smaller than those of the mainshock and decay over time in accordance with the theories of Stress Change, Energy Transfer, and Readjustment [4].

Estimating the time at which the aftershock phase ends is vital information for stakeholders in determining a safe period for communities to resume normal activities. Various empirical statistical methods, such as the Omori Law, Mogi I, Mogi II, and Utsu models, have been widely applied to model these decay characteristics [5].

Recent comparative studies also show that the selection of an appropriate decay method is highly dependent on the characteristics of local seismicity data in order to produce accurate predictions of the termination time [6]. The foundational modified Omori-Utsu formula and its generalized computational forms remain the global standard for capturing the temporal clustering and relaxation mechanisms of aftershock sequences [7], [8], [9]. Recent applications of these statistical models have proven highly effective in evaluating aftershock decay rates in complex fault zones globally, such as the 2023 Türkiye earthquake doublet [10], as well as in highly active subduction zones across Indonesia, including recent seismic sequences in West Sumatra [11] and Bengkulu [12].

One significant case study is the Jayapura earthquake sequence that occurred in early 2023. The mainshock, with a magnitude of M 5.4, occurred on January 2, 2023, at a depth of 10 km (coordinates 140.74°E and 2.53°S), approximately 19 km northeast of Jayapura City, with an intensity reaching IV MMI. Up to January 11, 2023, a total of 135 aftershocks with magnitudes ranging from 1.7 to 4.9 were recorded in the region. The distribution of this seismic activity is shown in Figure 1, which visualizes the spatial distribution of aftershock epicenters in and around the Jayapura area. Previous research concluded that the Mogi II method provided termination time predictions that were closest to BMKG observational data compared to other methods for this case [13].

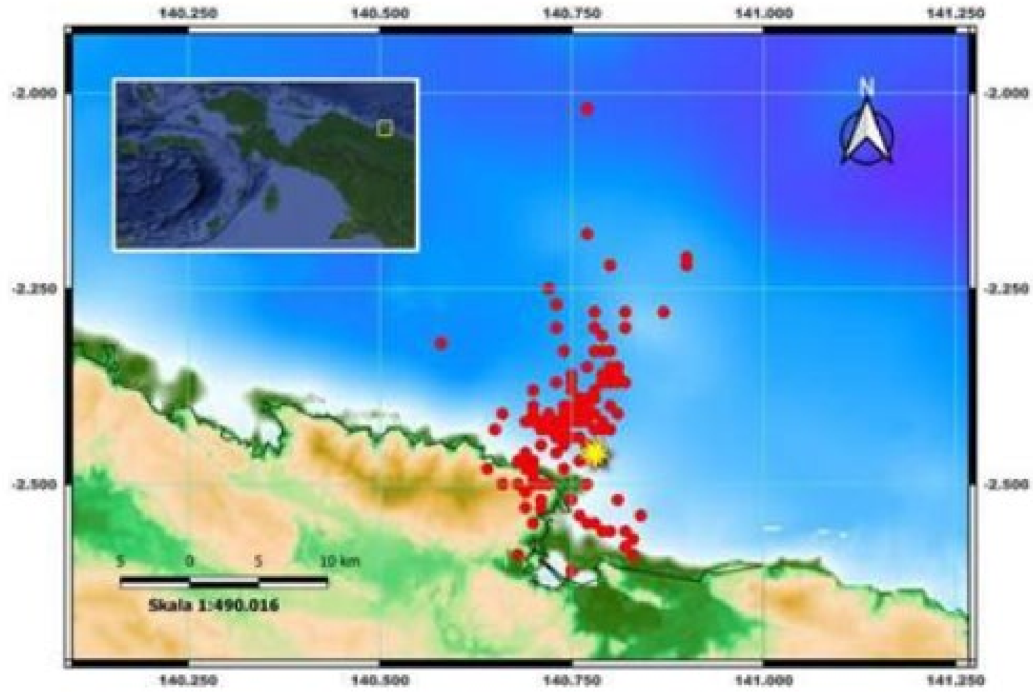

Fig. 1 Map of aftershock distribution of the Jayapura earthquake, January 2–11, 2023 [13]

The solution of mathematical models for disaster prediction, such as in the Mogi II method, often involves complex exponential or logarithmic functions. In various fields of science and engineering, problems involving non-linear mathematical models are often difficult to solve analytically (exactly) due to the complexity of the equations. When analytical methods cannot be applied efficiently, numerical methods become the primary approach to obtain approximate numerical solutions [14]. The efficiency of a numerical method is largely determined by the number of iterations required to achieve convergence with minimal error [15]. The development of computational-based earthquake decay software has increasingly facilitated the automated and precise analysis of these parameters, replacing manual calculations that are prone to error [16].

In the context of solving systems of non-linear equations to determine earthquake termination time, reliable and efficient numerical algorithms are required. Non-linear equations are defined as equations that seek the value of a variable that satisfies a zero-function condition, for which direct algebraic formulas often do not exist [17]. The Secant method emerges as an effective numerical solution because it does not require the calculation of function derivatives, in contrast to the Newton–Raphson method, which requires analytical derivatives. This method works by iteratively updating approximation points based on the gradient of a line passing through two initial points until the desired error tolerance is achieved [18].

This study implements the Secant method using the Python programming language to determine the termination of aftershock activity. As an object-oriented programming language that is popular among scientists, Python offers concise syntax, high code readability, and extensive support for numerical libraries [19]. These features enable the development of aftershock termination algorithms to be faster, easily modifiable, and compatible with various operating system platforms. Therefore, this research aims to examine the mechanism and effectiveness of the Python-based Secant numerical method in predicting the end of aftershock sequences, as well as to compare the validity of the results with previous studies.

2. RESEARCH METHOD

This research was conducted using a numerical computational approach with hardware in the form of a laptop and software using the Python programming language as the main processing tool. Python was chosen because it has flexible data structures and reliable numerical libraries for efficiently solving iterative computational problems [20]. The data used in this simulation are secondary data adopted from previous studies, sourced from the earthquake catalog of the Meteorology, Climatology, and Geophysics Agency (BMKG). The dataset includes parameters of aftershock occurrence frequency from the Jayapura Earthquake event that occurred on January 2, 2023. The spatial scope of the data is limited to coordinates 2.00°S to 2.65°S and 140.50°E to 141.00°E. The temporal range of the data covers a 10-day critical phase, from January 2, 2023 to January 11, 2023.

The data processing stage was carried out by implementing the mathematical model of earthquake decay using the Mogi II method into a program algorithm [21]. Based on regression parameters that had been validated in previous studies, the decay equation of seismic activity (frequency) with respect to time is defined as follows:

$$n(t) = 40.9415e^{-0.2908t} \tag{1}$$

where n(t) represents the frequency of aftershocks and t is the time (days) after the mainshock. In the context of a root-finding algorithm, the variable t is substituted with x to conform to standard numerical programming notation. The objective of this simulation is to determine the time (t or x) when aftershock activity is considered to have completely decayed, which is assumed to occur when the event frequency approaches one ($n \approx 1$). Therefore, to prevent divergence and enable root-finding, the equation is modified into a zero function ($f(x) = 0$) by shifting the constant 1 to the left-hand side:

$$f(x) = 40.9415e^{-0.2908x} - 1 \tag{2}$$

The iterative algorithm applied to solve the non-linear function above is the Secant Method. This method requires the initialization of two initial guess values to allow the iteration to proceed; in this study, the values were set as $x_0 = 0$ and $x_1 = 1$. To ensure the accuracy of the predicted decay time, the error tolerance was set to 0.0001. The program was designed to automatically execute repeated calculations, updating the approximation values based on the secant line gradient, until the relative difference between successive values falls below the specified tolerance threshold. The systematic workflow of this research methodology, from variable initialization to obtaining the final decay time result, is visualized in detail in Figure 2.

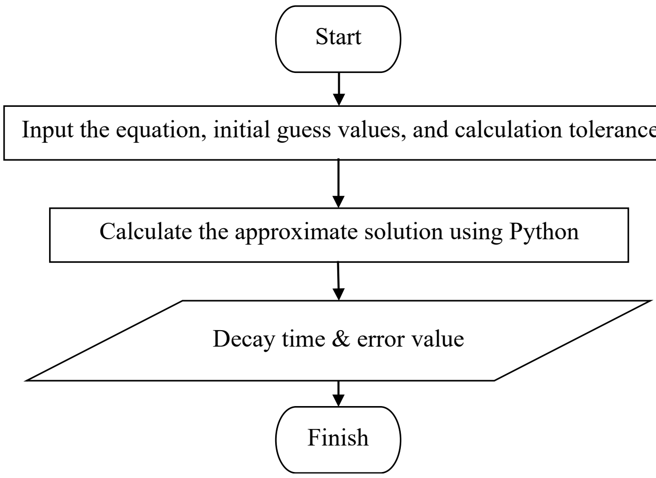

Fig. 2 Flowchart of the research methodology

3. RESULTS AND DISCUSSION

3.1. Python Script and Algorithmic Justification

The programming script developed for this research utilizes a modular structure within a Google Collaboratory environment. The script imports the math and numpy modules to handle mathematical operations, as well as the sympy module to evaluate symbolic expressions dynamically. To address computational efficiency and robustness, two numerical approaches were formulated: the Secant method and the Bisection method. The core of this program lies in the integration of algorithmic fail-safes. As shown in Figure 3, a condition is set in the Secant method to prevent division by zero.

```python
import math
import time
import numpy as np
import matplotlib.pyplot as plt
from sympy import symbols, lambdify, sympify

def secant_method(f, x0, x1, epsilon, max_iter=100):
    iteration = 0
    error = epsilon + 1
    print("-" * 75)
    print("SECANT METHOD")
    print("-" * 75)
    print(f"{'Iter':<5} | {'x0':<12} | {'x1':<12} | {'x_next':<12} | {'Error':<12}")
    start_time = time.perf_counter()
    while error > epsilon and iteration < max_iter:
        iteration += 1
        fx0 = f(x0)
        fx1 = f(x1)
        if fx1 - fx0 == 0:
            print("Fail-safe triggered: Division by zero detected.")
            return None, iteration, None
        x_next = x1 - fx1 * ((x1 - x0) / (fx1 - fx0))
        error = abs(x_next - x1)
        print(f"{iteration:<5} | {x0:<12.6f} | {x1:<12.6f} | {x_next:<12.6f} | {error:<12.6f}")
        x0 = x1
        x1 = x_next
    end_time = time.perf_counter()
    exec_time = end_time - start_time
    if iteration == max_iter:
        print("Fail-safe triggered: Maximum iterations reached without convergence.")
    return x_next, iteration, exec_time
```

Fig. 3 Python script defining the Secant method with fail-safe features

```python
def bisection_method(f, a, b, epsilon, max_iter=100):
    iteration = 0
    error = epsilon + 1
    print("\n" + "-" * 75)
    print("BISECTION METHOD")
    print("-" * 75)
    print(f"{'Iter':<5} | {'a':<12} | {'b':<12} | {'c (mid)':<12} | {'Error':<12}")
    start_time = time.perf_counter()
    if f(a) * f(b) >= 0:
        print("Fail-safe triggered: Assumption f(a) * f(b) < 0 is not met.")
        return None, iteration, None
    c = a
    while error > epsilon and iteration < max_iter:
        iteration += 1
        c_old = c
        c = (a + b) / 2
        error = abs(c - c_old) if iteration > 1 else abs(b - a)
        print(f"{iteration:<5} | {a:<12.6f} | {b:<12.6f} | {c:<12.6f} | {error:<12.6f}")
        if f(c) == 0:
            break
        elif f(a) * f(c) < 0:
            b = c
        else:
            a = c
    end_time = time.perf_counter()
    exec_time = end_time - start_time
    return c, iteration, exec_time
```

Fig. 4 Python script defining the Bisection method for comparative analysis

For comparative purposes, the Bisection method is defined in Figure 4. It includes an initial check to ensure the starting brackets have opposite signs. Both functions are strictly bounded by a maximum iteration limit to prevent infinite computational loops if the algorithm fails to converge. Furthermore, execution timing is embedded within both algorithms to accurately benchmark computational speed.

```python
def plot_results(root_val):
    t_all = np.linspace(0, 15, 100)
    plt.figure(figsize=(10, 6))
    t_obs = t_all[t_all <= 10]
    n_obs = 40.9415 * np.exp(-0.2908 * t_obs)
    plt.plot(t_obs, n_obs, 'b-', linewidth=2, label='BMKG Observation Phase (0-10 Days)')
    t_extrap = t_all[t_all > 10]
    n_extrap = 40.9415 * np.exp(-0.2908 * t_extrap)
    plt.plot(t_extrap, n_extrap, 'r--', linewidth=2, label='Extrapolation Phase (Prediction)')
    if root_val:
        plt.plot(root_val, 1, 'go', markersize=8, label=f'Termination Point (x ≈ {root_val:.3f})')
        plt.axvline(x=root_val, color='g', linestyle=':', alpha=0.7)
        plt.axhline(y=1, color='g', linestyle=':', alpha=0.7)
    plt.axvline(x=10, color='gray', linestyle='-.', alpha=0.5)
    plt.text(10.2, 20, 'Observation Limit', rotation=90, color='gray')
    plt.title('Estimation of Jayapura Aftershock Decay (Mogi II Model)', fontsize=14)
    plt.xlabel('Time after Mainshock (Days)', fontsize=12)
    plt.ylabel('Aftershock Frequency (Events/Day)', fontsize=12)
    plt.legend()
    plt.grid(True, linestyle='--', alpha=0.6)
    plt.tight_layout()
    plt.show()
```

Fig. 5 Python script for data visualization and extrapolation

```
print("NUMERICAL METHOD PROGRAM: AFTERSHOCK DECAY ESTIMATION")
equation_str = "40.9415*exp(-0.2908*x) - 1"
epsilon = 0.0001
x = symbols('x')
f_sym = sympify(equation_str)
f = lambdify(x, f_sym, modules=['math'])
print(f"Equation: {equation_str}")
print(f"Error Tolerance (Epsilon): {epsilon}")
x0_sec, x1_sec = 0.0, 1.0
root_sec, iter_sec, time_sec = secant_method(f, x0_sec, x1_sec, epsilon)
a_bis, b_bis = 0.0, 15.0
root_bis, iter_bis, time_bis = bisection_method(f, a_bis, b_bis, epsilon)
print("\n" + "=" * 75)
print("METHOD COMPARISON SUMMARY")
print("=" * 75)
print(f"{'Parameter':<20} | {'Secant Method':<22} | {'Bisection Method':<22}")
print("-" * 75)
print(f"{'Initial Guess':<20} | x0={x0_sec}, x1={x1_sec:<14} | a={a_bis}, b={b_bis:<15}")
print(f"{'Equation Root (x)':<20} | {root_sec:<22.6f} | {root_bis:<22.6f}")
print(f"{'Number of Iterations':<20} | {iter_sec:<22} | {iter_bis:<22}")
print(f"{'Execution Time (s)':<20} | {time_sec:<22.8f} | {time_bis:<22.8f}")
print("=" * 75)
plot_results(root_sec)
```

Fig. 6 The main execution cell compiling the numerical methods and visualizing the output

Figure 5 and Figure 6 display the plotting functionality and the main execution program, respectively. The Secant method was primarily chosen over gradient-based methods like Newton-Raphson because it approximates the derivative using secant lines, eliminating the need for complex analytical differentiation of the Mogi II exponential model, while generally offering faster convergence than the Bisection method.

3.2. Calculation Results and Computational Efficiency

The execution of the program for the Jayapura earthquake case study utilized Equation (2) as the primary input. To validate the algorithm's stability, the Secant method was initialized with x0 = 0 and x1 = 1, while the Bisection method required a wider bracketing interval of a = 0 and b = 15. The error tolerance was strictly set to 0.0001. Furthermore, to address the sensitivity of the initial parameters, the Secant method was subjected to robustness testing using arbitrary extreme guesses (e.g., x0 = 5 and x1 = 10). The algorithm demonstrated high stability, consistently converging to the exact same termination point of 12.765 days without necessitating manual tuning.

```
NUMERICAL METHOD PROGRAM: AFTERSHOCK DECAY ESTIMATION
Equation: 40.9415*exp(-0.2908*x) - 1
Error Tolerance (Epsilon): 0.0001
======================================================================
SECANT METHOD
----------------------------------------------------------------------
Iter    | x0            | x1            | x_next        | Error
1       | 0.000000      | 1.000000      | 3.866192      | 2.866192
2       | 1.000000      | 3.866192      | 5.903110      | 2.036917
3       | 3.866192      | 5.903110      | 8.080786      | 2.177677
4       | 5.903110      | 8.080786      | 9.913880      | 1.833093
5       | 8.080786      | 9.913880      | 11.381084     | 1.467205
6       | 9.913880      | 11.381084     | 12.294737     | 0.913653
7       | 11.381084     | 12.294737     | 12.678671     | 0.383934
8       | 12.294737     | 12.678671     | 12.759515     | 0.080844
9       | 12.678671     | 12.759515     | 12.765210     | 0.005695
10      | 12.759515     | 12.765210     | 12.765283     | 0.000072

======================================================================
BISECTION METHOD
----------------------------------------------------------------------
Iter    | a             | b             | c (mid)       | Error
1       | 0.000000      | 15.000000     | 7.500000      | 15.000000
2       | 7.500000      | 15.000000     | 11.250000     | 3.750000
3       | 11.250000     | 15.000000     | 13.125000     | 1.875000
4       | 11.250000     | 13.125000     | 12.187500     | 0.937500
5       | 12.187500     | 13.125000     | 12.656250     | 0.468750
6       | 12.656250     | 13.125000     | 12.890625     | 0.234375
7       | 12.656250     | 12.890625     | 12.773438     | 0.117188
8       | 12.656250     | 12.773438     | 12.714844     | 0.058594
9       | 12.714844     | 12.773438     | 12.744141     | 0.029297
10      | 12.744141     | 12.773438     | 12.758789     | 0.014648
11      | 12.758789     | 12.773438     | 12.766113     | 0.007324
12      | 12.758789     | 12.766113     | 12.762451     | 0.003662
13      | 12.762451     | 12.766113     | 12.764282     | 0.001831
14      | 12.764282     | 12.766113     | 12.765198     | 0.000916
15      | 12.765198     | 12.766113     | 12.765656     | 0.000458
16      | 12.765198     | 12.765656     | 12.765427     | 0.000229
17      | 12.765198     | 12.765427     | 12.765312     | 0.000114
18      | 12.765198     | 12.765312     | 12.765255     | 0.000057

======================================================================
METHOD COMPARISON SUMMARY
======================================================================
Parameter            | Secant Method             | Bisection Method
----------------------------------------------------------------------
Initial Guess        | x0=0.0, x1=1.0              | a=0.0, b=15.0
Equation Root (x)    | 12.765283                 | 12.765255
Number of Iterations | 10                        | 18
Execution Time (s)   | 0.00011588                | 0.00012212
======================================================================
```

Fig. 7 Output results comparing the iteration steps, absolute error, and execution time between the Secant and Bisection methods.

As presented in Figure 7, the computational benchmark demonstrates the superior efficiency of the Secant method for this specific seismic dataset. The Secant algorithm achieved stable convergence in exactly 10 iterations with an execution time of approximately 0.000115 seconds. In contrast, the Bisection method required 18 iterations and 0.000122 seconds to reach the same tolerance. Both algorithms successfully isolated the root at approximately 12.765. For practical interpretation in disaster mitigation, this value is rounded up to 13 days following the mainshock.

Validation of this calculation result was conducted by comparing it with data from previous studies, as presented in Table 1. It is evident that the predicted end time of aftershock activity obtained using the Secant numerical method, namely 13 days, shows exact agreement with the results of earlier references. This indicates that the Secant algorithm implemented using Python is capable of working with high accuracy in solving the non-linear equation of the Mogi II model. Therefore, this method is proven to be valid and effective as an alternative computational tool for predicting the decay time of aftershock activity.

Table 1. Comparison of Aftershock Termination Time Using the Secant Method and Previous Studies

Aftershock Termination (days)	Method Used
13	Secant
13	Previous Study

3.3. Model Validation and Visual Extrapolation

To properly validate the Mogi II model within the local geological setting, the numerical output must be contextualized against actual seismic observations. The primary BMKG dataset utilized in this study captures the aftershock frequency trend over a 10-day window (January 2 to January 11, 2023).

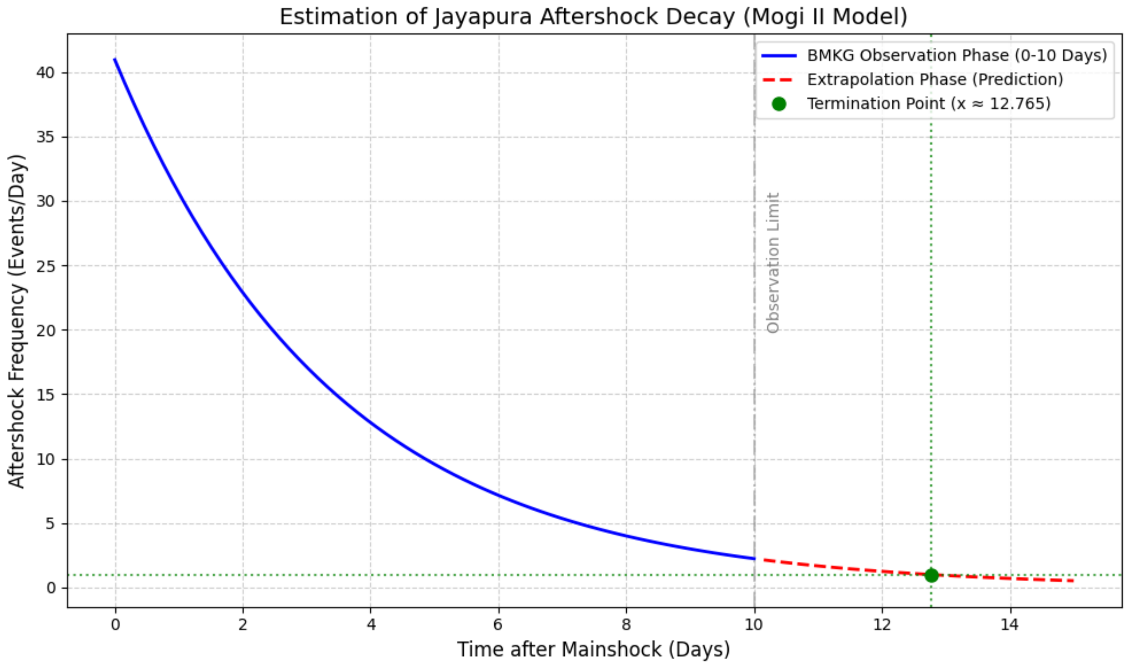

Fig. 8 Visual plot of the Jayapura aftershock decay sequence. The solid blue line represents the 10-day BMKG observation window, while the dashed red line indicates the Mogi II extrapolation trajectory leading to the predicted termination point at day 13.

Figure 8 illustrates the decay curve, highlighting the boundary between recorded data and mathematical prediction. Because the computational termination point occurs at 12.765 days, the period beyond day 10 represents an extrapolated prediction rather than a direct observation. The algorithm extends the decay trajectory of the established Mogi II model (dashed red line) until the aftershock frequency falls to the threshold of 1 event per day. The exact alignment of this extrapolated 13-day termination with the results of prior manual studies confirms the robustness of the algorithm in projecting the end of the critical phase.

4. CONCLUSION

This study concludes that the implementation of the Secant numerical method using the Python programming language is proven to be highly effective in predicting the termination time of aftershock activity. Based on the computational results, an approximate solution value of $x \approx 12.765$ was obtained, which was rounded to 13 days. This result shows exact and consistent agreement with the calculations reported in previous studies, thereby validating the accuracy of the developed algorithm.

Furthermore, computational benchmarking revealed that the Secant method outperformed the Bisection approach in terms of execution speed (~0.000115s vs ~0.000122s) and iteration efficiency (10 vs 18 iterations). The algorithm also proved exceptionally robust during sensitivity testing with extreme initial guesses and successfully extrapolated the termination phase mathematically beyond the 10-day observational limit. The application of the Secant method offers the advantage of efficiently solving the non-linear equation of the Mogi II model without requiring complex analytical differentiation. Furthermore, the support of computational libraries in Python facilitates easy modification of parameters for different earthquake cases. Therefore, this numerical approach is highly recommended as a precise, stable, and computationally efficient analytical tool in seismological studies and disaster mitigation.

REFERENCE

[1] D. R. Apalem and R. Serang, "PELATIHAN MITIGASI BENCANA GEMPABUMI BAGI SISWA-SISWI SD NEGERI 2 TIAKUR, KABUPATEN MALUKU BARAT DAYA," J. Pengabdi. Masy., vol. 3, no. 1, pp. 19–23, 2024.

[2] P. Supendi et al., "A conjugate fault revealed by the destructive Mw 5.6 (November 21 , 2022) Cianjur earthquake , West Java , Indonesia," J. Asian Earth Sci. J., vol. 257, p. 105830, 2023.

[3] Y. Prananda, T. Zera, and D. Sunarya, "Parameter Seismotektonik Wilayah Jawa Barat dan Banten Berdasarkan A-Value dan B-Value Periode 1971-2021," Bul. Meteorol. Klimatologi, dan Geofis., vol. 2, no. 3, pp. 24–34, 2022.

[4] N. R. Permana and Rendinis, “Prediksi Waktu Berakhirnya Gempa Bumi Susulan Dengan Empat Metode Untuk Kejadian Di Lebak, Banten, Pada 07-17 Juli 2018,” J. Mater. Sci. Geophys. Instrum. Theor. Phys., vol. 2, no. 2, pp. 68–72, 2019.

[5] V. N. Islamiati, S. Supardiono, Y. H. Perdana, and A. R. Setyahagi, “Analisis Peluruhan Gempa Bumi Susulan Di Ambon Tahun 2019 Dengan Pendekatan Statistik Menggunakan Software Peluruhan V2.0,” J. Inov. Fis. Indones., vol. 9, no. 2, pp. 163–172, 2020, doi: 10.26740/ifi.v9n2.p163-172.

[6] N. N. Faiza, A. Mukti Wibowo, and R. Fatimah, “ANALISIS METODE WAKTU PELURUHAN GEMPA BUMI SUSULAN BERDASARKAN METODE OMORI, MOGI DAN UTSU (STUDI KASUS GEMPA BUMI PASAMAN BARAT 25 FEBRUARI 2022),” JIIF (Jurnal Ilmu dan Inov. Fis., vol. 08, no. 02, pp. 65–72, 2024, [Online]. Available: https://doi.org/10.24198/jiif.v8i2

[7] T. Utsu, Y. Ogata, and R. S. Matsu’ura, “The Centenary a Decay of the Omori Formula Activity for Law of Aftershock Tokuji Utsu ,* Yosihiko Ogata , and Ritsuko S . Matsu ’ ura,” J. Phys. Earth, vol. 43, pp. 1–33, 1995.

[8] R. Shcherbakov, D. L. Turcotte, and J. B. Rundle, “A generalized Omori ’ s law for earthquake aftershock decay,” Geophys. Res. Lett., vol. 31, pp. 1–5, 2004, doi: 10.1029/2004GL019808.

[9] T. Omi, Y. Ogata, Y. Hirata, and K. Aihara, “Forecasting large aftershocks within one day after the mainshock,” Sci. Rep., vol. 3, pp. 1–7, 2013, doi: 10.1038/srep02218.

[10] S. M. Ali and K. Abdelrahman, “Analysis of the Fractal Dimension, b-value, Slip Ratio, and Decay Rate of Aftershock Seismicity Following the 6 February 2023 (Mw 7.8 and 7.5) Türkiye Earthquakes,” Fractal Fract., vol. 8, no. 5, p. 252, 2024.

[11] D. Fitria, S. Syafriani, H. Hamdi, and L. Dwiridal, “Earthquake Decay Analysis to Determine the Aftershock end Time in West Sumatra in 2021-2023 Using The Omori-Utsu Method,” URANUS J. Ilm. Tek. Elektro, Sains dan Inform., vol. 3, no. 2, pp. 55–64, 2025.

[12] F. Tobamba, I. U. Meidji, and H. Jayadi, “Seismicity Analysis of Earthquakes in Bengkulu Using Gutenberg-Richter and Omori Laws,” FARADAY J. Fundam. Physics, Res. Appl. Sci., vol. 2, no. 1, pp. 7–15, 2026.

[13] H. Syarifuddin and P. Arianto, “Analisis Perkiraan Waktu Berakhirnya Gempabumi Susulan Pada Gempabumi M 5.4 Jayapura 2 Januari 2023,” Bul. Meteorologi, Klimatologi dan Geofis., vol. 4, no. 5, pp. 46–53, 2023, [Online]. Available: https://repogempa.bmkg.go.id/eventca

[14] L. S. Utami, “Perbandingan Analisis Numerik Menggunakan Metode Secant dan Metode Iterasi Satu Titik Untuk Menentukan Koefisien Gesek Udara Pada Kubus Dan Silindris,” Paedagoria | FKIP UMMat, vol. 5, no. 2, p. 43, 2018, doi: 10.31764/paedagoria.v5i2.89.

[15] Yahya and A. M. Nur, “Pengaruh Aplikasi C# dalam Proses Perhitungan Numerik Terhadap Solusi Persamaan Non Linier,” J. Inform. dan Teknol., vol. 1, no. 2, pp. 79–87, 2018.

[16] M. Saefurohmah, D. B. Susanti, and M. Effendi, “Analisis Perbandingan Waktu Peluruhan Gempa Bumi Menggunakan Metode Omori dan Mogi 1 dengan Software Peluruhan V2.0,” J. Stasiun Geofis. Sleman, vol. 2, no. 1, pp. 7–13, 2024.

[17] Q. S. Akmala, N. Ekaswati, Syaharuddin, M. Ibrahim, and V. Mandailina, “Metode Biseksi Menggunakan Gui Matlab: Sebuah Simulasi Dan Solusi Persamaan Non-Linier,” in FORDETAK: Seminar Nasional Pendidikan: Inovasi Pendidikan di Era Society 5.0, 2022, pp. 659–664. [Online]. Available: https://e-proceedings.iain-palangkaraya.ac.id/index.php/PSNIP/article/view/810

[18] P. Batarius, “Perbandingan Metode Newton-Raphson Modifikasi Dan Metode Secant Modifikasi Dalam Penentuan Akar Persamaan,” in Seminar Nasional Riset dan Teknologi Terapan, 2018, pp. 53–63.

[19] A. Triono, A. S. Budi, and R. Abdillah, “Implementasi Peretasan Sandi Vigenere Chiper Menggunakan Bahasa Pemrograman Python,” J. JOCOTIS - J. Sci. Inform. Robot., vol. 1, no. 1, pp. 1–9, 2023, [Online]. Available: https://jurnal.ittc.web.id/index.php/jumri

[20] E. Sunandar and I. Indrianto, “Perbandingan Metode Newton-Raphson & Metode Secant Untuk Mencari Akar Persamaan Dalam Sistem Persamaan Non-Linier,” Petir Jurnal Pengkaj. dan Penerapan Tek. Inform., vol. 13, no. 1, pp. 72–79, 2020, doi: 10.33322/petir.v13i1.893.

[21] K. Mogi, Study of elastic shocks caused by the fracture of heterogeneous materials and its relations to earthquake phenomena, vol. 40. 1962.

Journal of Computation Physics and Earth Science
ISSN: 2776-2521 (online)
Volume 5, Number 2, February 2026, Page 189 - 201
https://journal.physan.org/index.php/jocpes/index

Fault Mapping of the Central Aceh Segment of the Sumatran Fault as an Extension of the Great Sumatran Fault (GSF) Using Gravity Analysis

Qisthi Mursyida[1], Muhamad Syirojudin[2]
[1]Undergraduate Program in Geophysics (STMKG)
[2]Indonesian Agency for Meteorology, Climatology, and Geophysics (BMKG)

Article Info

Article history:

Received December 27, 2025
Revised March 6, 2026
Accepted March 6, 2026

Keywords:

Gravity
First Horizontal Derivative (FHD)
Second Vertical Derivative (SVD)
Central Aceh Segment

A B S T R A C T

Aceh is known as one of the most tectonically active regions in Indonesia with a relatively high level of seismicity. One of the active zones is the Central Aceh Segment, which forms part of the Sumatra Fault as an extension of the Great Sumatran Fault. This study aims to identify the distribution and characteristics of fault zones and types in the Central Aceh Segment using gravity data from GGMplus. The analysis was carried out by applying the First Horizontal Derivative (FHD) and Second Vertical Derivative (SVD) methods. The results indicate significant lateral density contrasts that delineate the presence of a major fault and several secondary fault structures within the study area. Interpretation of SVD values along several profiles suggests that many of the inferred structures exhibit reverse fault characteristics, with some indications of normal faults. These features are interpreted as secondary deformation structures that may develop within a strike-slip fault under localized transpressional or transtensional stress regimes. Subsurface geological modelling along profiles AA′–BB′, BB′–CC′, and EE′–FF′ shows variations in rock density that highlight zones of high-density distribution.

Corresponden Author:

Qisthi Mursyida,
Undergraduate Program in Geophysics (STMKG)
Tangerang, Indonesia
Email: mursyidaq@gmail.com

1. INTRODUCTION

The Sumatran (Great Sumatran Fault) is an important geological structure that contributes significantly to the high level of seismic activity in Indonesia [1]. Due to its location at the convergence of three major tectonic plates, the Indo-Australian, Eurasian, and Pacific plates. Indonesia is highly vulnerable to earthquakes. The Great Sumatran Fault extends approximately 1900 km from Lampung in the south to the Andaman region in the north and is divided into twenty fault segments, each with distinct characteristics [2].

The Aceh Fault represents the northernmost segment of the GSF and has a total length of approximately 250 km [3]. It plays an important role in right lateral strike-slip motion resulting from the oblique convergence between the Indo-Australian Plate and the Eurasian Plate with a convergence rate of about 70 mm/year along the Sunda subduction zone [4]. According to the Indonesian National Earthquake Hazard Map, the Aceh Fault is divided into three segments: the North Aceh Segment, the Central Aceh Segment, and the South Aceh Segment. As the central portion of the Aceh Fault System, the Central Aceh Segment serves as a structural link between the North and South Aceh segments. Deformation within this segment may therefore influence other segments along the fault zone. Historical records indicate moderate seismic activity along the Aceh Fault, particularly within the Central Aceh Segment, over the past 170 years; however, no major earthquakes have been recorded [5]. This condition suggests the potential accumulation of significant tectonic stress in the region.

This study employs gravity analysis to identify the Central Aceh Segment. Based on Newton's law of gravitation, [6] stated that the gravitational force between two objects is directly proportional to their masses and inversely proportional to the square of the distance between them. This principle forms the basis of gravity analysis in geophysics, particularly for fault identification. The gravity method was selected because it can reveal subsurface structural features through variations in gravity anomalies caused by differences in rock density [7]. Residual and regional gravity anomaly patterns in the study area were analyzed using secondary gravity data from GGMPlus and TOPEX. Furthermore, First Horizontal Derivative (FHD) and Second Vertical Derivative (SVD) analyses were applied to enhance the delineation of fault locations and geometries [8].

2. RESEARCH METHOD

The fault trace crossing the Central Aceh Segment within the study area is shown on the topographic map in Figure 1. The topographic map illustrates significant elevation variations, with lowland areas and coastal waters located to the west and north of the Aceh region. This study area is defined by longitude coordinates ranging from 95.9° to 96.3° and latitude coordinates from 4.7° to 5.0°, which were subsequently analyzed to obtain Free Air Anomaly (FAA) data, as shown in Figure 2. Gravity data from GGMPlus were used in this study with a spatial resolution of 7.2 arc-seconds (220 m).

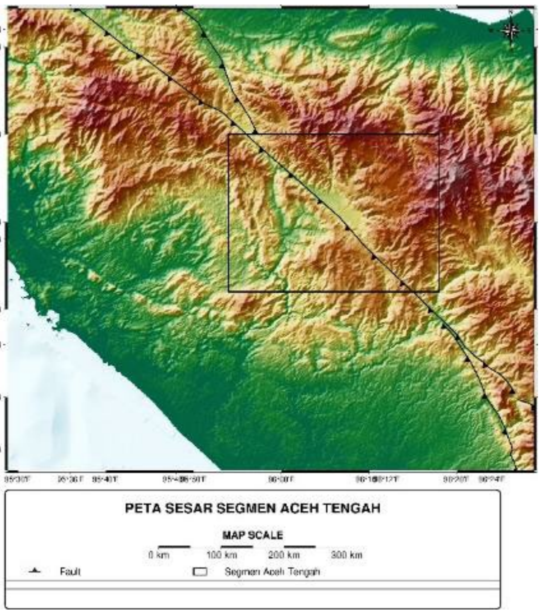

Fig. 1. Map of the Study Area

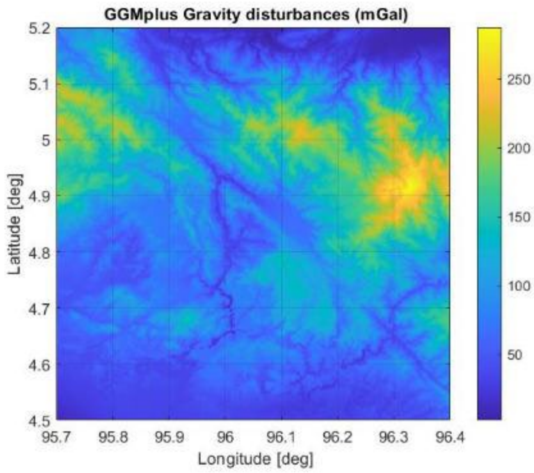

Fig. 2. Free Air Anomaly (FAA) Map of the Study Area

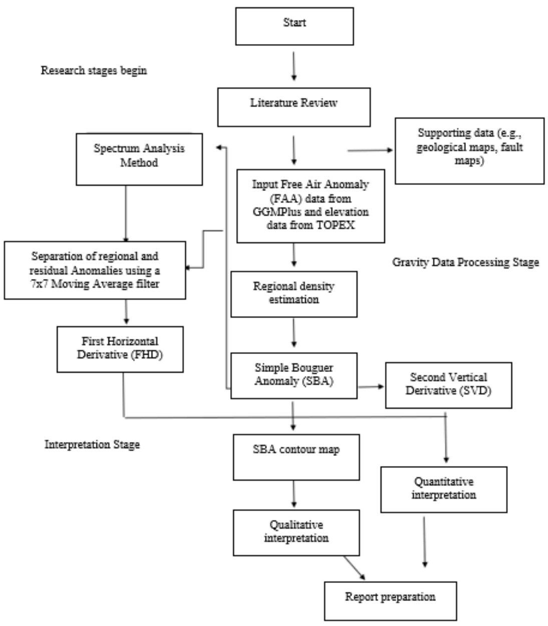

Fig. 3. Flowchart of Gravity Data Processing

Figure 3 illustrates the stages of gravity data processing applied in this study. The first stage involves determining the estimated regional density value for the boundary of the study area. The Parasnis method was employed to perform this calculation, as it is commonly used to estimate the average rock density. According to [9], the determination of rock density requires elevation data (h), Free Air Anomaly (FAA), field corrections, and Bouguer corrections.

Subsequently, Microsoft Excel was used to process the FAA data in order to obtain the average density value, Bouguer correction, and Simple Bouguer Anomaly (SBA). The FAA values were derived from data that had undergone automatic corrections, including tidal, drift, and latitude corrections. The FAA values can be calculated using equation (1):

$$FAA = 0.04192 \times \rho_a \times h + L_g \tag{1}$$

Where:

FAA	: Free air anomaly (mGal)
ρ_a	: Average air density (gr/cm^3)
h	: Elevation (m)
L_g	: Latitude gravity correction (mGal)

The next step is to determine the Simple Bouguer Anomaly (SBA) by subtracting the Bouguer correction from FAA values. This procedure is performed based on Equation (2) to calculate the mass effect between the observation point and the Earth's surface [10]. Equation (3) can then be used to obtain the SBA values.

$$BC = 0.04192 \times \rho_a \times h \tag{2}$$

$$SBA = FAA - BC \tag{3}$$

Where:

BC	: Bouguer correction (mGal)
ρ_a	: Average air density (gr/cm^3)
h	: Elevation (m)
SBA	: Simple bouguer anomaly (SBA)
FAA	: Free air anomaly (mGal)

Surfer software was used to process the SBA values in this study. Because the topographic variation in the Central Aceh Segment is relatively stable, the SBA values are considered sufficient for analysis, although some areas may exhibit elevation differences related to geological structures. The next step involved determining the regional anomaly using a second order polynomial method with a low pass filter, which aims to remove high frequency components and retain only low frequency data. This process highlights the regional anomaly, which reflects large scale density patterns in greater detail. Subsequently, the corresponding SBA values were subtracted from the regional anomaly to obtain the residual anomaly. These two anomalies provide a clearer representation of subsurface patterns based on depth and density distribution [11].

Furthermore, the SBA data were processed using a 7x7 moving average filter to generate residual anomalies that facilitate the interpretation of subsurface structures in the study area. The moving average filter separates regional and residual anomalies by emphasizing low frequency signals in the Bouguer Anomaly, which are then used to derive the regional anomaly. The residual anomaly is subsequently obtained by subtracting the regional anomaly from the total Bouguer anomaly, as expressed in equation (4):

$$\Delta g_{Residual} = \Delta g_{Bouguer} - \Delta g_{Regional} \tag{4}$$

Where:

$\Delta g_{Residual}$	: Residual anomaly (mGal)
$\Delta g_{Bouguer}$	: Bouguer anomaly (mGal)
$\Delta g_{Regional}$	: Regional anomaly (mGal)

To identify fault structures, the previously determined regional anomaly was further analyzed using First Horizontal Derivative (FHD) and Second Vertical Derivative (SVD) techniques. SVD analysis is applied to interpret the sources of gravity anomalies and to determine fault mechanism [12]. Meanwhile, FHD analysis enables the identification of horizontal density contrast boundaries. Zones exhibiting the highest FHD values are interpreted as potential fault locations. The inferred fault locations correspond to zones where the maximum values of the FHD coincide with the zero contour of the SVD response.

In this study, the Henderson and Zietz matrix filter (Table 1) was selected for SVD analysis. SVD is a derivative of FHD and is used to identify fault mechanism as well as to validate the presence of fault structures. Fault locations are identified when the FHD values reach a maximum while the corresponding SVD values approach zero.

Table 1. Henderson and Zietz (1949) matrix used as a 7x7 SVD filter

Henderson and Zietz (1949)

0	0	-0.0838	0	0
0	+1.0000	-2.6667	+1.0000	0
-0.0838	-2.6667	17.0000	-2.667	-0.0838
0	+1.0000	-2.6667	+1.0000	0
0	0	-0.0838	0	0

The criteria presented in equation (5) can then be applied to determine the faulting mechanism based on the SVD values [9].

$$\left[\frac{\partial^2 \Delta g}{\partial z^2}\right]_{min} < \left|\frac{\partial^2 \Delta g}{\partial z^2}\right|_{max} \quad normal\,fault \tag{5}$$

$$\left[\frac{\partial^2 \Delta g}{\partial z^2}\right]_{min} > \left|\frac{\partial^2 \Delta g}{\partial z^2}\right|_{max} \quad reverse\,fault \tag{6}$$

$$\left[\frac{\partial^2 \Delta g}{\partial z^2}\right]_{min} \approx \left|\frac{\partial^2 \Delta g}{\partial z^2}\right|_{max} \quad strike-slip\,fault \tag{7}$$

3. RESULTS AND DISCUSSION

3.1. Average Density

The average rock density value obtained is required for mapping the Central Aceh Segment fault. In this study, the average rock density was calculated using the Parasnis method. The average rock density in the Central Aceh Segment is 2.5343 g/cm$^{3.}$

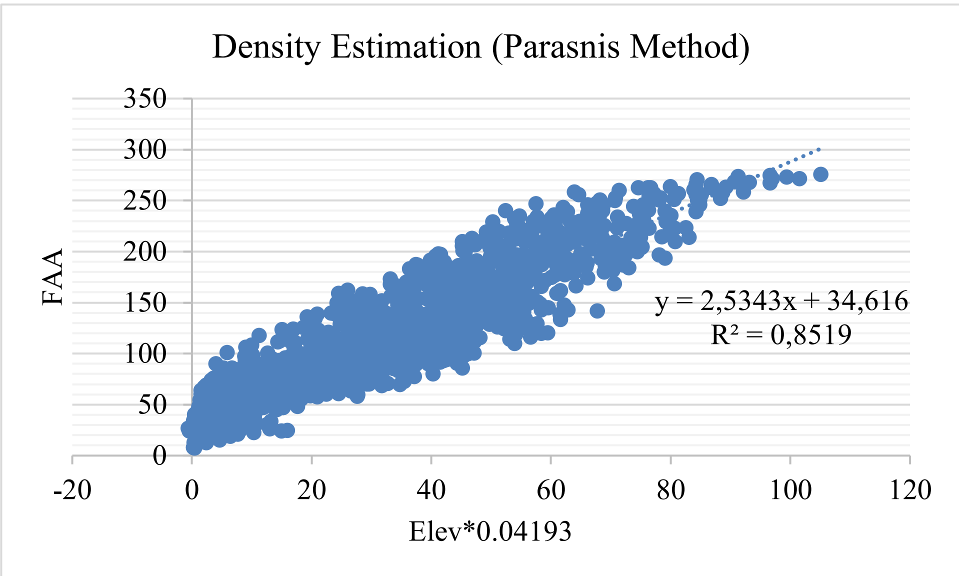

Fig. 4. Determination of average rock density using the Parasnis method

The Central Aceh Segment has an average density of 2.5343 g/cm3. As stated by [13], rocks can be classified into sedimentary, igneous, and metamorphic types based on their density ranges and average density values for each rock type. Figure 4 shows that several rock types may dominate the Central Aceh region with a density of approximately 2.5343 g/cm3. Based on standard rock density tables, this density range may indicate the presence of sedimentary rocks such as limestone (1.93-2.90 Mg/m3), igneous rocks such as granite (2.55-2.75 Mg/m3), and andesite (2.40-2.80 Mg/m3).

Jenis batuan	Rentang densitas(Mg/m^3)	Rata-rata(Mg/m^3)
Sedimentary rocks		
Alluvium	1.96 – 2.00	1.98
Clay	1.63 – 2.60	2.21
Gravel	1.70 – 2.40	2.00
Loess	1.40 – 1.93	1.64
Silt	1.80 – 2.20	1.93
Soil	1.20 – 2.40	1.92
Sand	1.70 – 2.30	2.00
Sandstone	1.61 – 2.76	2.35
Shale	1.77 – 3.20	2.40
Limestone	1.93 – 2.90	2.55
Dolomite	2.28 – 2.90	2.70
Chalk	1.53 – 2.60	2.01
Halite	2.10 – 2.60	2.22
Glacier ice	0.88 – 0.92	0.90
Igneous rocks		
Rhyolite	2.35 – 2.70	2.52
Granite	2.50 – 2.81	2.64
Andesite	2.40 – 2.80	2.61
Syenite	2.60 – 2.95	2.77
Basalt	2.70 – 3.30	2.99
Gabbro	2.70 – 3.50	3.03
Metamorphic rocks		
Schist	2.39 – 2.90	2.64
Gneiss	2.59 – 3.00	2.80
Phylite	2.68 – 2.80	2.74
Slate	2.70 – 2.90	2.79
Granulite	2.52 – 2.73	2.65
Amphibolite	2.90 – 3.04	2.96
Eclogite	3.20 – 3.54	3.37

Fig. 5. Determination of average rock density [13]

3.2. Simple Bouguer Anomaly (SBA)

The Simple Bouguer Anomaly (SBA) values were calculated using an average density of 2.5343 g/cm3. The SBA values on the map range from -35 mGal to 105 mGal, as shown in Figure 6. The minimum SBA value of -35 mGal occurs in the dark blue area located in the upper right part of the map, while the maximum SBA value of 105 mGal is observed in the bright red area around the upper left portion of the map.

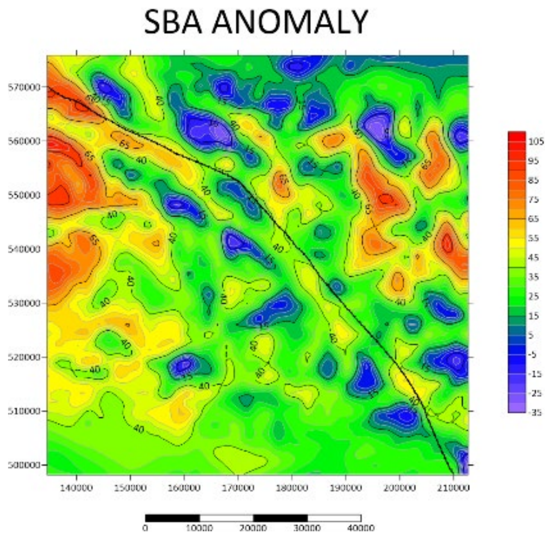

Fig. 6. Simple Bouguer Anomaly (SBA) map of the suspected fault zone in the study area

3.3. Spectral Analysis

Spectral analysis was performed to separate regional and residual gravity anomalies within the study area. The analysis was conducted using the radially averaged power spectrum method to determine the cut-off frequency separating regional and residual anomaly components. The identified cut-off frequency was subsequently used to define the moving window size for the moving average filter applied in the regional-residual separation. Prior to conducting spectral analysis, the SBA data were examined by constructing several profiles across the study area. Two horizontal profiles and three vertical profiles were constructed to provide a more comprehensive representation of gravity anomalies within the Central Aceh Segment. This approach enables the identification of gravity anomaly patterns based on depth and lateral variations in subsurface mass distribution. The three vertical profiles illustrate variations in gravity anomaly characteristics along the north-south direction, while the two horizontal profiles depict lateral distributions along the east-west direction, as shown in Figure 7.

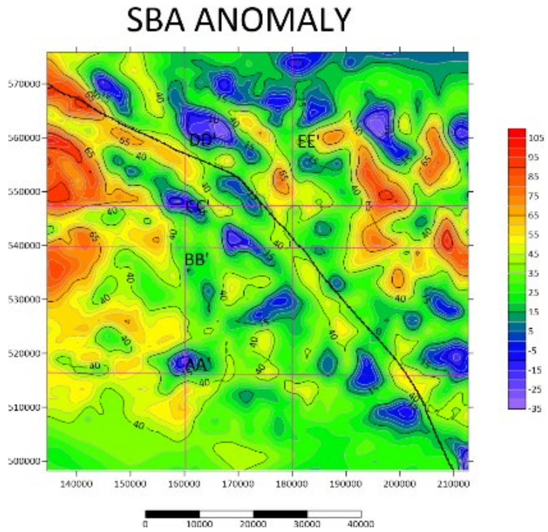

Fig. 7. SBA map with five profiles

The spectral method is applied to separate regional and residual anomalies from gravity data. Residual anomalies represent local sources, such as shallow intrusions or sedimentary basins, whereas regional anomalies reflect large scale density variations, including those associated with the deeper crust.

Table 2. Depth of regional and residual zones, cut-off frequency, and predicted window width derived from spectral analysis

	Regional Zone	Residual Zone	Cut-Off Frequency (k)	Predicted Window Width (n)
Profile AA’	146.08 m	13.499 m	0.0036956	7.728091
Profile BB’	177.95 m	72.995 m	0.0036956	7.728091
Profile CC’	175.25 m	19.994 m	0.0036956	7.728091
Profile DD’	154.16 m	55.081 m	0.0038465	7.424914
Profile EE’	144.2 m	23.959 m	0.0038465	7.424914

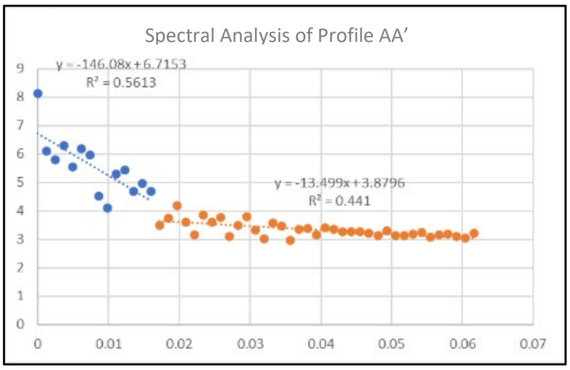

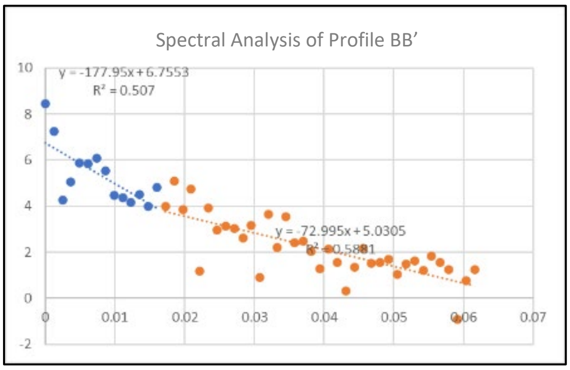

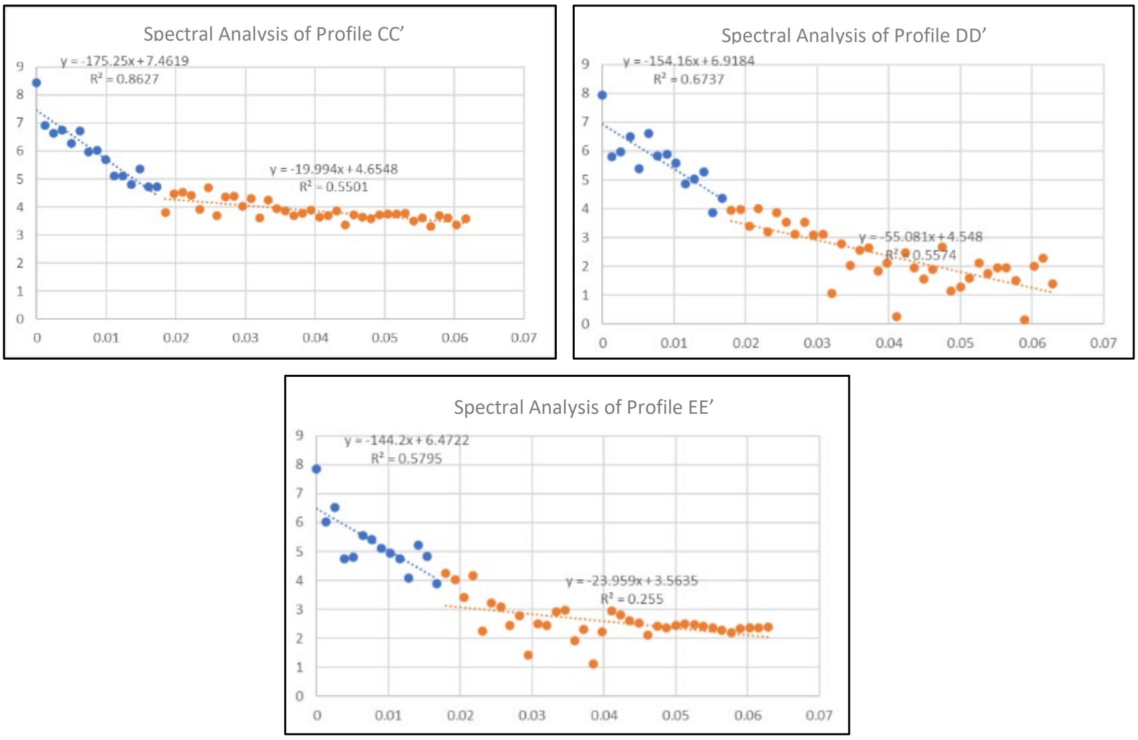

Fig. 8. Spectral analysis graphs of the five profiles

3.4. Separation of Regional and Residual Anomalies

After defining the regional and residual zones based on the results of spectral analysis, the separation of regional and residual anomaly values was carried out to identify the presence of fault structures. Regional anomaly values can be used to map geological structures associated with relatively low seismic activity. Therefore, the regional anomaly was utilized for mapping the Central Aceh Segmen Fault after obtaining the SBA value.

The regional anomaly was calculated using the moving average method, which smooths data values over a specified area (a 7x7 grid was applied in this study). Once the regional anomaly was obtained, the residual anomaly was calculated by subtracting the regional anomaly from the total gravity data. The residual anomaly aids in identifying shallow geological structures, such as active faults within the Central Aceh Segment. This method reduce noise in gravity data, thereby enhancing the visibility of regional geological structures at specific depths.

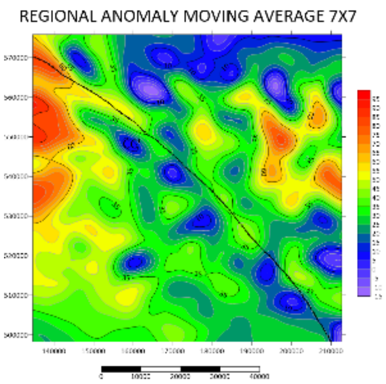

Fig. 9. Regional anomaly map

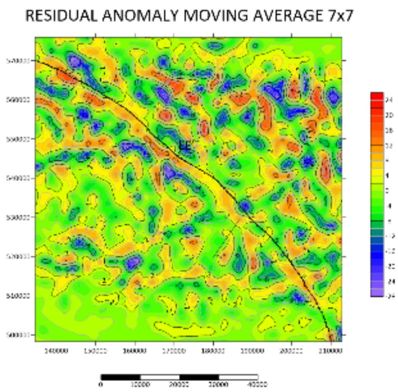

Fig. 10. Residual anomaly map

3.5. First Horizontal Derivative (FHD) and Second Vertical Derivative (SVD) Analysis

Figure 11 presents the 7x7 moving average anomaly map, which is characterized by the dominance of green to blue colors with value ranging from 0 to 95 mGal, indicating variations in rock density within the shallow subsurface layers. The black fault lines shown on both maps represent the main faults mapped by [14]. These faults reflect major tectonically active geological structures that play a significant role in the crustal deformation pattern of the region.

In this study, nine profiles were selected to analyze variations in gravity gradient patterns along the Central Aceh Segment. The FHD values, which are predominantly shown in green and yellow colors, are higher in areas closer to the fault traces identified by [14], indicating higher density materials. In contrast, lower FHD values are observed in areas farther from the fault lines, particularly in the southern part of the study area, suggesting the presence of lower density rocks.This result indicates a significant density contrast between the northern and southern regions of the Central Aceh Segment.

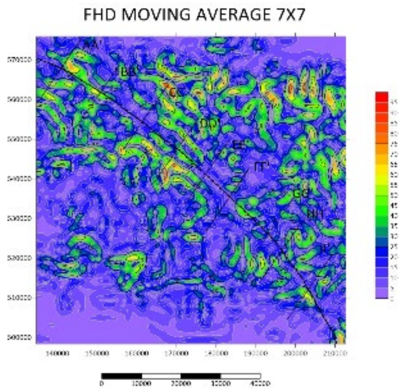

Fig. 11. FHD value map

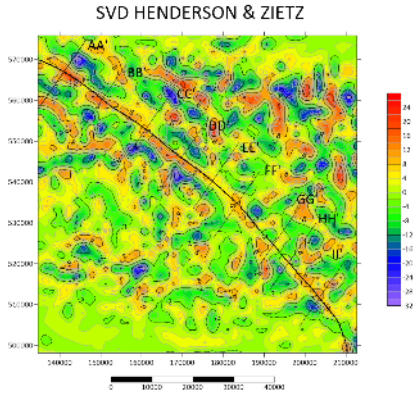

Fig. 12. SVD value map

Meanwhile, the SVD values shown in Figure 12 were used tp strengthen the gravity interpretation by emphasizing vertical gravity variations. Positive values on the map (red zones) indicate high density rocks, such as magmatic intrusions or hard igneous rocks (e.g., granite or basalt), whereas negative values (blue zones) represent low density rocks, such as unconsolidated sediments or weathered rocks. The black fault lines displayed on both maps represent the main faults mapped by the National Center for Earthquake Studies [14]. These faults reflect major tectonically active geological structures that play a significant role in crustal deformation patterns in the region. In this study, nine profiles were selected to analyze variations in gravity gradient patterns along the Central Aceh Segment.

3.6. Fault Type Determination

The results of the FHD and SVD profile analyses were used to determine the faulting mechanism. Based on the interpretation of the FHD and SVD maps, several areas exhibiting significant anomaly values were identified in the vicinity of the fault zone. Overall, the anomalies are more dominant in the western part of the study area, as indicated by the vertical lines shown in each profile plot.

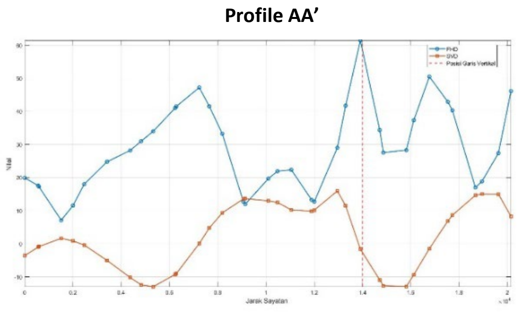

Fig. 13. Profile AA' plot

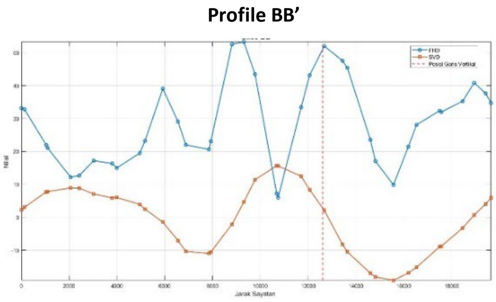

Fig. 14. Profile BB' plot

Profile CC’

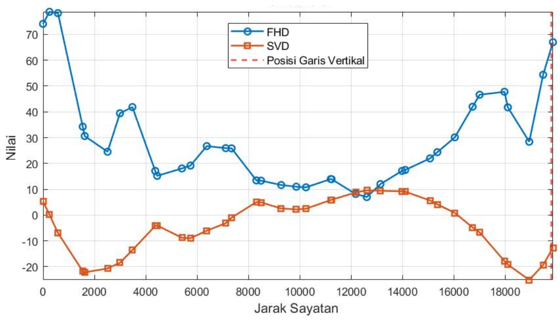

Fig. 15. Profile CC’ plot

Profile DD’

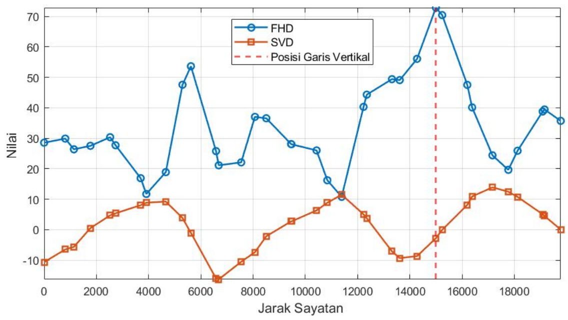

Fig. 16. Profile DD’ plot

Profile EE’

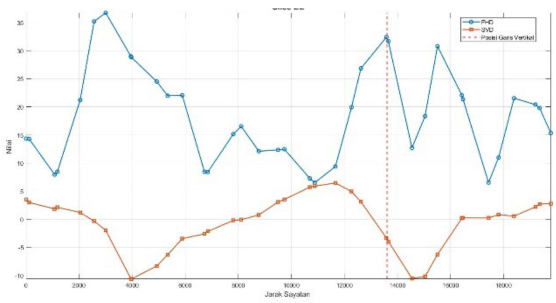

Fig. 17. Profile EE’ plot

Profile FF’

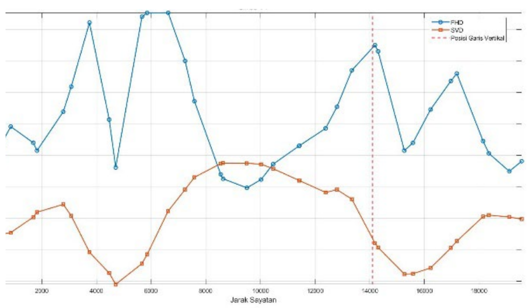

Fig. 18. Profile FF’ plot

Profile GG’

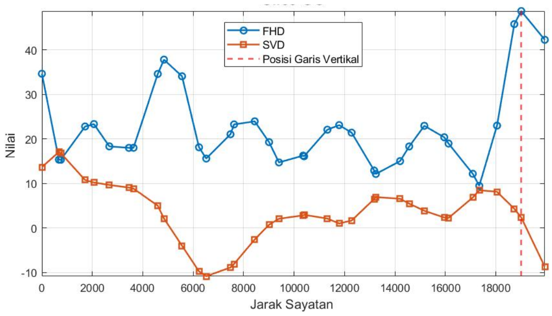

Fig. 19. Profile GG’ plot

Profile HH’

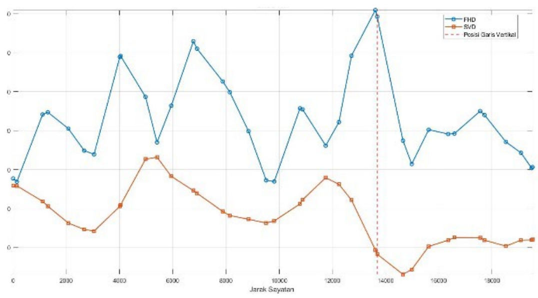

Fig. 20. Profile HH’ plot

Profile II’

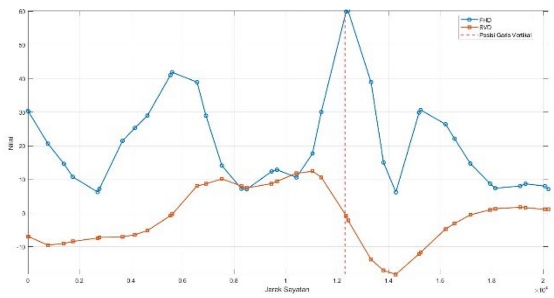

Fig. 21. Profile II’ plot

The vertical lines from each profile were subsequently reinterpreted on the FHD and SVD maps. The red lines shown in Figures 22 and 23 represent the interpreted trace of the inferred fault, identified based on the results of the FHD and SVD analyses. These lines indicate locations where significant changes in gravity anomaly values occur, which commonly reflect major geological contacts such as faults. The inferred fault is interpreted to separate subsurface masses with contrasting densities, likely representing boundaries between geological formations that have been displaced by tectonic activity. The continuity of the red lines across all profiles reflects the regional extent of the fault structure, indicating that his fault extends laterally and constitutes a dominant structural element within the geological framework of the Central Aceh Segment.

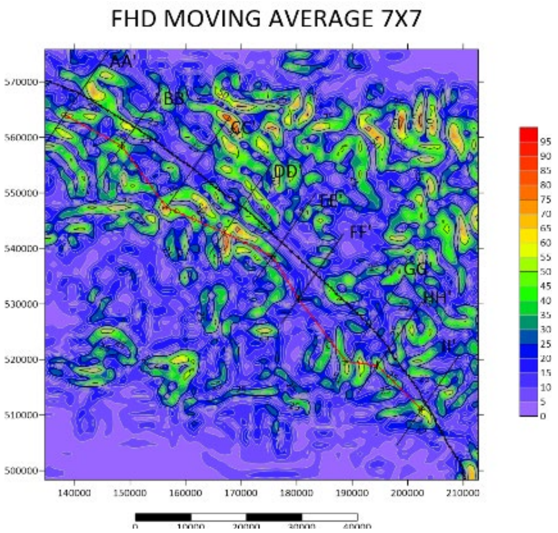

Fig. 22. FHD map with red lines indicating the inferred fault traces

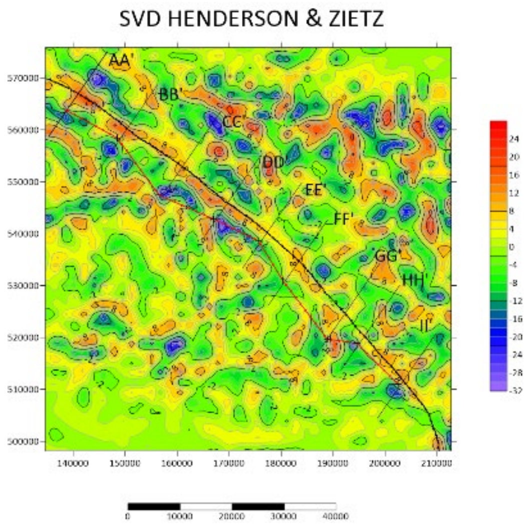

Fig. 23. SVD map with red lines indicating the inferred fault traces

The SVD analysis of nine profiles (AA', BB', CC', DD', EE', FF', GG', HH', and II') reveals significant patterns of lateral density variation. These variations are critical for interpreting the fault type analyzed in this study. Vertical lines identified in each profile indicate locations where the density gradient reaches minimum and maximum values. These vertical lines represent lateral density contrast boundaries, which suggest the presence of subsurface fault structures.

Table 3. Coordinates of density contrast boundaries and SVD value analysis

Profile	SVD Values		Fault Type
	Max	Min	
AA'	15.9535331194	-13.0035986565	Normal Fault
BB'	15.6510554835	-19.1467587229	Reverse Fault
CC'	9.58175155155	-25.1163248523	Reverse Fault
DD'	13.9040073916	-16.3071743018	Reverse Fault
EE'	6.46795543255	-10.624170777	Reverse Fault
FF'	8.78673984857	-10.475106417	Reverse Fault
GG'	17.0612422091	-10.8636700368	Normal Fault
HH'	13.1624224529	-16.8928254433	Normal Fault
II'	12.4525926134	-18.2321410379	Reverse Fault

Based on the SVD values and fault types interpreted in Table 3, most of the inferred fault traces in the Central Aceh Segment exhibit characteristics of reverse (thrust) faults. However, it should be noted that the Sumatran Fault is generally classified as a strike-slip fault by the [14]. Nevertheless, further analysis within [14] studies indicates that, in the deeper part of the accretionary prism, deformation zones in the form of arc-parallel reverse faults (backthrust) have developed, as observed in the Andaman Sea. Such backthrust structures are commonly associated with oblique convergence and transpressional tectonic regimes, where compressional components are locally accommodated within an overall strike-slip fault system. This mechanism allows reverse faulting to coexist with strike-slip deformation and may explain the dominance of thrust fault characteristics inferred from the SVD analysis in the Aceh Segment. In addition, strike-slip fault zones commonly develop secondary structures such as reverse or normal faults depending on the prevailing stress regime. Under transpressional conditions, strike-slip deformation may generate positive flower structures characterized by reverse faulting, whereas transtensional regimes may produce negative flower structures associated with normal faulting [15]. Therefore, this explains the dominance of reverse fault observed in this study.

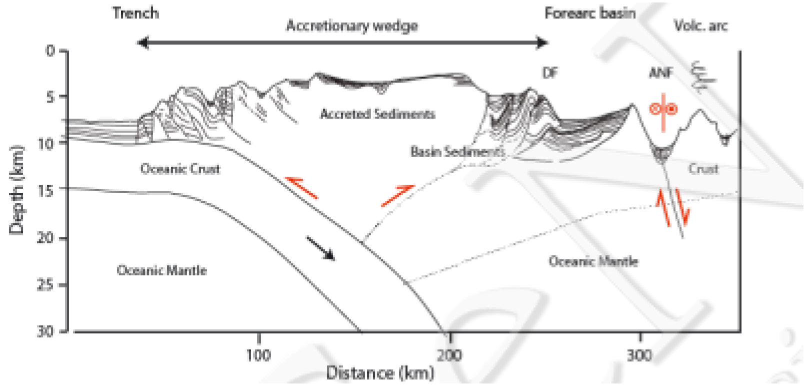

Fig. 24. Cross section of the Andaman subduction system showing the accretionary prism, forearc basin, and volcanic arc

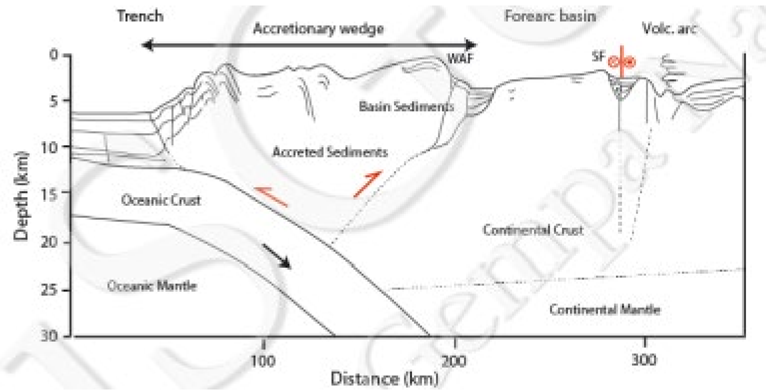

Fig. 25. Cross section of the Northern Sumatra subduction system showing the accretionary prism, forearc basin, and volcanic arc

In Aceh and its surrounding regions, a similar phenomenon can be observed, where arc-parallel reverse fault form boundaries between the accretionary prism and the forearc basin. Seismic and bathymetric data in this region support the presence of reverse faults as part of the tectonic deformation dynamics resulting from plate convergence. This zone serves as an important structural link between the Andaman Sea to the north and deformation zones in southern Sumatra.

3.7. Geological Modelling from Residual Anomalies

Red profile lines were again delineated as inferred fault traces in Figure 26, which require further analysis to better understand the subsurface conditions. The inferred fault trace exhibits a significant lateral density contrast, reflecting differences in the physical properties of rocks on either side of the fault as well as within its central zone. The three profiles (AA', BB', and CC') show consistent gravity anomaly patterns, indicating the presence of a fault in the central part of the study area (marked by a black line within the blue anomaly zone) in Figure 26.

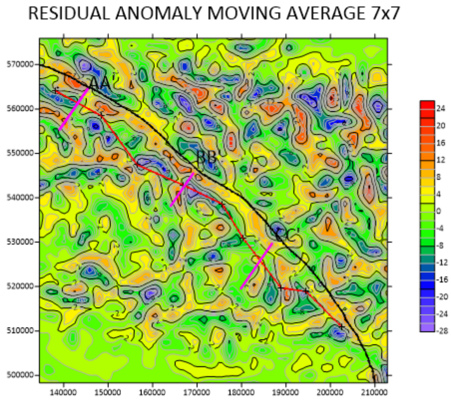

Fig. 26. Residual anomaly map of the Central Aceh Segment study area with red lines indicating the inferred fault traces

The main objective of this interpretation is to understand subsurface geological modelling, including density distribution, structural orientation, and their potential relationship with active faults, such as other segments of the Sumatran Fault as an extension of the Great Sumatran Fault (GSF). By utilizing residual anomaly data, local geological rock conditions can be effectively delineated.

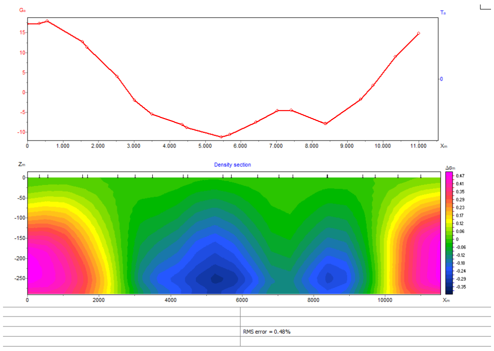

Fig. 27. Geological model along profile AA’

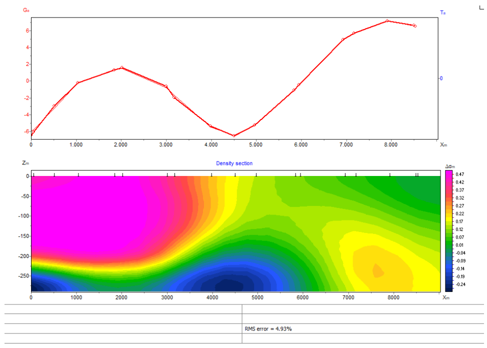

Fig. 28. Geological model along profile BB’

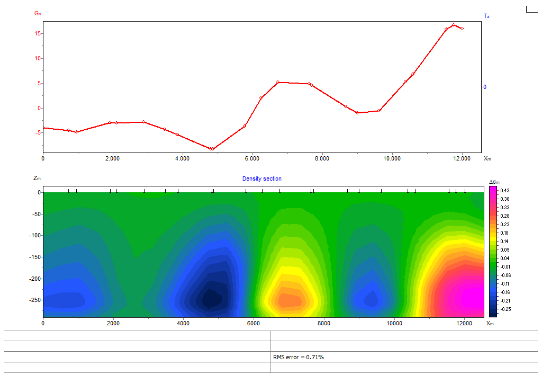

Fig. 29. Geological model along profile CC’

Along profile AA’ in Figure 27, a significant change in gravity values is observed, with a zone of higher density material on one side and lower density material on the other. This contrast indicates a lithological difference that is most likely caused by faulting. Profile BB in Figure 28 further supports this interpretation, showing a sharp gravity gradient that reflect subsurface material displacement characteristic of geological faulting. A similar pattern is also evident along profile CC’ in Figure 29, where asymmetric gravity anomaly patterns indicate displacement of subsurface layers. The consistency of anomaly patterns across these three profiles supports the interpretation that a fault is present in the central part of the study area, which likely a normal fault or a reverse fault.

4. CONCLUSION

The inferred fault traces indicate significant tectonic deformation patterns within the Central Aceh Segment, which are predominantly characterized as reverse faults based on the SVD analysis. This deformation patterns are consistent with tectonic processes observed in the Andaman Sea, where arc-parallel reverse faults develop within the accretionary prism dynamics. These finding support the hypothesis that tectonic deformation in northern Sumatra, including the Aceh region, is tectonically connected to the Andaman subduction, reflecting the continuity of deformation zones from the Andaman Sea to Sumatra.

REFERENCE

[1] Y. Muhammad, A. Faisal, A. Yenny, Z. Muzakir, M. Abubakar, and I. Nazli, "Continuity of Great Sumatran fault in the marine area revealed by 3D inversion of gravity data," J. Teknol., vol. 83, no. 1, pp. 145–155, 2021, doi: 10.11113/jurnalteknologi.v83.14824.

[2] B. Munir, "Penggunaan Data Gempa dan Data Geologi Untuk Menganalisa Pola-Pola Sesar di Daratan Pulau Sumatra," p. 136, 2015.

[3] L. Y. Roodhiyah et al., "Interpretation of a 3D Magnetotellurics Model of the Aceh and Seulimeum Segments of the Sumatran Fault Zone," Appl. Sci., 2024.

[4] G. I. Marliyani et al., "Exploring Aceh Fault Zone for Slip Rates and Paleoseismic Trenching Potential along Sumatran Fault," Indones. J. Geogr., vol. 56, no. 1, pp. 138–148, 2024, doi: 10.22146/IJG.93456.

[5] A. K. Hady and G. I. Marliyani, Dr., "Updated Segmentation Model and Cumulative Offset Measurement of the Aceh Segment of the Sumatran Fault System in West Sumatra, Indonesia," J. Appl. Geol., vol. 5, no. 2, p. 84, 2021, doi: 10.22146/jag.56134.

[6] R. I. Hackney and W. E. Featherstone, "Geodetic versus geophysical perspectives of the 'gravity anomaly,'" Geophys. J. Int., vol. 154, no. 1, pp. 35–43, 2003, doi: 10.1046/j.1365-246X.2003.01941.x.

[7] M. Yanis, F. Abdullah, N. Zaini, and N. Ismail, "The northernmost part of the Great Sumatran Fault map and images derived from gravity anomaly," Acta Geophys., vol. 69, no. 3, pp. 795–807, 2021, doi: 10.1007/s11600-021-00567-9.

[8] N. A. Sunarto, Identifikasi Struktur Geologi Bawah Permukaan Berdasarkan Metode Second Vertical Derivative (SVD) Data Gravitasi di Kabupaten Bantul. 2021.

[9] Taufiquddin, "Identifikasi Struktur Bawah Permukaan daerah Potensi Panas Bumi Dengan Metode Gravity (Studi Kasus Di Daerah Sumber Air Panas Desa Lombang Kecamatan Batang-Batang Kabupaten Sumenep)," UIN Maulana Malik Ibrahim, pp. 1–100, 2014.

[10] K. Nozaki, "The generalized Bouguer anomaly," Earth, Planets Sp., vol. 58, no. 3, pp. 287–303, 2006, doi: 10.1186/BF03351925.

[11] I. Setiadi, C. Purwanto, D. Kusnida, and Y. Firdaus, "Interpretasi Geologi Bawah Permukaan Berdasarkan Analisis Data Gayaberat Menggunakan Filter Optimum Upward Continuation Dan Pemodelan 3D Inversi : (Studi Kasus: Cekungan Akimeugah Selatan, Laut Arafura)," J. Geol. Kelaut., vol. 17, no. 1, 2019, doi: 10.32693/jgk.17.1.2019.579.

[12] P. Sumintadireja, D. Dahrin, and H. Grandis, "A note on the use of the second vertical derivative (SVD) of gravity data with reference to Indonesian cases," J. Eng. Technol. Sci., vol. 50, no. 1, pp. 127–139, 2018, doi: 10.5614/j.eng.technol.sci.2018.50.1.9.

[13] W. M. Telford, L. P. Geldart, R. E. Sheriff, and A. Keys, D, "Applied Geophysics, Second Edition," Cambridge Univ. Press, 1990.

[14] P. S. G. Nasional, PETA SUMBER DAN BAHAYA GEMPA INDONESIA TAHUN 2017. 2017.

[15] K. Sieh and D. Natawidjaja, "Neotectonics of the Sumatran fault, Indonesia' Now," J. Geophys. Res., vol. 105, 2000.

Subsurface Structural Identification and Seismicity Correlation in West Java Using EMAG2 Geomagnetic Data

Rayhan Irfan Hielmy[1]
[1]Undergraduate Program in Geophysics (STMKG)

Article Info

Article history:

Received December 26, 2025
Revised February 28, 2026
Accepted February 28, 2026

Keywords:

Geomagnetic Anomaly
EMAG2
Derivative Analysis
Fault System
Tasikmalaya Earthquake

A B S T R A C T

West Java represents one of Indonesia's most seismically active regions, characterized by complex interactions between the Indo-Australian subduction zone and active onshore fault systems. This study investigated subsurface geological configurations and their relationship to earthquake occurrences using Earth Magnetic Anomaly Grid (EMAG2) data with a 2-arc-minute resolution. The research methodology utilized Reduction to the Pole (RTP) to eliminate dipolar effects caused by the equatorial location, followed by spectral analysis to separate regional and residual anomalies. To precisely map structural lineaments, First Horizontal Derivative (FHD) and Second Vertical Derivative (SVD) techniques were applied to the residual data. The processed maps revealed distinct anomaly contrasts, with high magnetic intensities (up to 300 nT) associated with volcanic intrusions and low anomalies (approximately −100 nT) indicating sedimentary basins or hydrothermally altered zones. A critical analysis of the December 15, 2017, Tasikmalaya earthquake (Mw 6.5) identified a strong correlation between the epicenter and a significant low magnetic anomaly zone of −150 nT. This specific signature was interpreted as a fracture zone characterized by rock demagnetization resulting from tectonic stress accumulation. These findings confirm that integrating EMAG2 data with derivative filtering is a robust approach for delineating active tectonic structures, thereby contributing essential data for regional seismic hazard mitigation.

Corresponden Author:

Rayhan Irfan Hielmy,
Undergraduate Program in Geophysics (STMKG)
Tangerang, Indonesia
Email: rayhanirfanhielmy@stmkg.ac.id

1. INTRODUCTION

Indonesia is an archipelagic country with highly complex geographical conditions and tectonic settings because it is located in the Pacific Ring of Fire. This region represents a convergence zone of three major tectonic plates of the world, namely the Indo-Australian Plate moving northward, the relatively stable Eurasian Plate, and the Pacific Plate moving westward. The convergent interaction among these plates generates an active subduction zone extending from Sumatra, Java, to Nusa Tenggara, which serves as the main source of seismic activity in the Indonesian region [1]. The three tectonic plates in the Indonesian region are among the most active in the world, resulting in a higher frequency of earthquakes in Indonesia compared to other countries. This fact places Indonesia at the top rank among the ten countries with the highest frequency of earthquakes worldwide [2].

One of the regions with a very high level of seismic vulnerability is the western part of Java Island. This area is prone to earthquakes due to the presence of the subduction zone south of Java as well as the existence of active onshore faults that contribute to the complexity of the geological structure. Seismic activity in this region is highly intensive because of continuous energy accumulation along plate convergence zones and fault systems [3]. Within this geological framework, various folds and faults are formed, acting as pathways for the release of seismic energy. In West Java, six major regional faults have been identified, namely the Cimandiri, Cipeles, Baribis, Lembang, Palabuhanratu, and Citanduy faults [4].

An earthquake is defined as a sudden release of energy in the form of vibrational waves that propagate throughout the Earth's surface due to disturbances or fractures within the Earth's crust. Such seismic events are very difficult to predict accurately in terms of their specific time and location, and therefore often result in destructive disasters, including the potential generation of tsunamis that can cause severe damage and loss of life when they occur in coastal areas. The identification of earthquake hazard potential is therefore crucial, considering the continuous growth of infrastructure and population density in earthquake-prone regions [5]. Consequently, earthquakes are among the most feared natural phenomena due to their impacts, which can result in loss of life, significant material damage, and destruction of vital infrastructure [6].

The movement of tectonic plates and subsurface rock deformation have been shown to exert a significant influence on the Earth's magnetic field [7]. When tectonic plates shift or experience stress, the distribution of ferromagnetic minerals in the Earth's crust may undergo changes in orientation or magnetic properties due to piezomagnetic effects or thermal processes. For example, magnetite minerals may lose their magnetization when exposed to temperatures exceeding the Curie temperature and regain their magnetic properties when the temperature decreases again, thereby recording traces of past tectonic processes. This phenomenon leads to variations in magnetization patterns within igneous rocks as well as geologically altered rocks. Variations in rock susceptibility values beneath the surface are subsequently measured as magnetic anomalies that differ from the Earth's main magnetic field [8].

This study aims to analyze the sources of magnetic field anomalies in order to identify subsurface geological structures in the study area. The spatial distribution map of magnetic field anomalies in West Java is shown in Figure 1, which indicates variations in high and low magnetic intensity values associated with regional geological structures. Closely spaced anomaly contours on the map often indicate lithological boundaries or fault zones that separate rocks with different magnetic susceptibilities [9]. By analyzing these anomaly patterns, it is expected that potential geological structures relevant to future geohazard mitigation can be mapped.

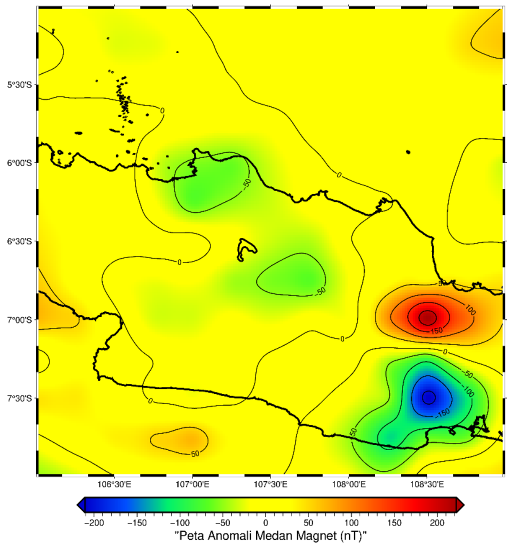

Fig. 1. Map of Magnetic Field Anomalies in West Java

2. RESEARCH METHOD

The primary data used in this study were obtained from the Earth Magnetic Anomaly Grid (EMAG2) with a spatial resolution of 2 arc-minutes. The study area is focused on West Java, bounded by geographic coordinates of 5° S – 8° S and 106° E – 109° E, based on data from 2017. The use of EMAG2 data is highly effective for regional-scale analysis because this compilation integrates satellite, marine, and aeromagnetic measurements capable of representing global lithospheric magnetic anomalies [10]. The initial stage of the study began with the collection and extraction of the grid data, which were then processed to produce a Total Magnetic Field Anomaly map as the basis for preliminary interpretation prior to further geophysical corrections.

After the raw data were obtained, a crucial processing step was the application of Reduction to the Pole (RTP) correction. This mathematical process aims to transform the inclination angle of the data as if the measurements were conducted at the Earth's magnetic pole (inclination of 90 degrees), thereby eliminating dipole effects caused by the low-latitude (equatorial) location of the study area. At polar inclination, the anomaly response takes the form of a monopole, in which the anomaly peak is positioned directly above the causative body, thus minimizing errors in target location determination [11]. This transformation is particularly important because magnetic anomalies in equatorial regions such as Indonesia often exhibit complex patterns due to interactions with the predominantly horizontal main geomagnetic field vector. After the calculations were completed, the RTP magnetic anomaly map was used as the fundamental dataset for anomaly separation processes. To mitigate instability and edge-effect artifacts common at low/equatorial latitudes, a spatial grid padding technique was applied (xrft.pad) prior to the RTP transformation. The grid was padded by one-third of its size in both easting and northing directions. The transformation was computed using the harmonica Python library, which effectively stabilizes the anomaly response without requiring a separate Pseudo-gravity transform. The grid was subsequently unpadded for further spatial analysis.

The next stage involved the separation of regional and residual anomalies to distinguish responses from deep sources (regional) and shallow sources (residual). In this study, the regional-residual separation was performed purely through spatial mathematical modeling. After reprojecting the RTP data into a Cartesian coordinate system, a third-order polynomial trend surface was fitted to the grid using the verde Python library (verde.Trend(degree=3)). This third-order polynomial approach acts as an effective low-pass filter, which suppresses high-frequency local information while enhancing and clarifying regional patterns [12]. The regional component was then mathematically subtracted from the original RTP data to obtain the residual anomaly. Theoretically, this separation leverages the principle that deeper sources are characterized by longer wavelengths compared to shallow sources [13]. Because this method relies on direct spatial polynomial fitting rather than spectral frequency cut-offs, Radially Averaged Power Spectrum (RAPS) depth estimations were not utilized in this workflow.

After the residual anomaly was successfully separated from its regional component, the analysis was continued using anomaly image enhancement techniques through derivative methods. The first transformation applied was the First Horizontal Derivative (FHD), which functions to detect edges or lateral boundaries of the anomalous source bodies. The FHD method is highly sensitive to horizontal changes in magnetic susceptibility, and therefore peaks in the FHD curve are often associated with the locations of geological contact boundaries or fault zones [14]. Subsequently, the Second Vertical Derivative (SVD) method was applied to delineate more detailed structures and to separate overlapping anomalies. SVD has the capability to enhance high-frequency anomalies related to shallow geological features, allowing structural boundaries in the study area to be mapped more distinctly.

Computationally, both FHD and SVD were processed using the harmonica library after the residual grid was converted to Cartesian coordinates. It is important to note that no prior smoothing was applied to the residual grid before derivation, as the robust third-order polynomial separation naturally provided a stable, low-noise baseline. The FHD was derived directly from the first-order easting (x) and northing (y) derivatives, formulated as:

$$FHD = \sqrt{\left(\frac{\partial M}{\partial x}\right)^2 + \left(\frac{\partial M}{\partial y}\right)^2} \tag{1}$$

Following Laplace's equation, the SVD was calculated mathematically as the negative sum of the second-order horizontal derivatives:

$$SVD = -\left(\left(\frac{\partial M}{\partial x}\right)^2 + \left(\frac{\partial M}{\partial y}\right)^2\right) \tag{2}$$

The entire sequence of data processing stages in this study, from EMAG2 data acquisition to derivative analysis, is systematically summarized in a flowchart. This diagram illustrates the logical sequence of data processing steps to ensure the validity of the final interpretation results. The technical procedures, along with the inputs and outputs of each process, are presented in detail in figure 2. This workflow was designed to ensure that the interpretation of subsurface structures is based on data that have been properly corrected and methodologically verified.

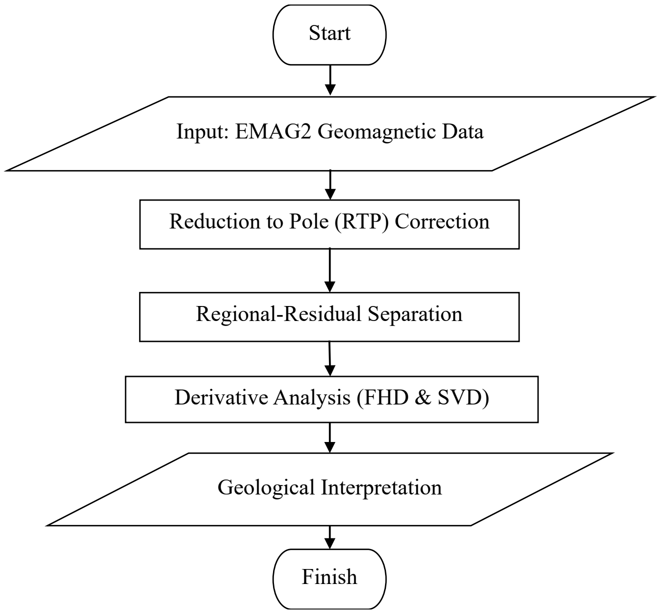

Fig. 2. Flowchart of the research methodology

3. RESULTS AND DISCUSSION

3.1. Magnetic Anomaly Data Processing

The initial stage of data interpretation began with the analysis of the Reduction to the Pole (RTP) magnetic anomaly map. This process is crucial for magnetic data in equatorial regions such as Indonesia to eliminate the asymmetry of anomaly shapes caused by the low inclination of the Earth's magnetic field. Figure 3 shows the distribution of corrected magnetic anomaly intensities, with color gradations from dark blue to red representing variations in subsurface rock susceptibility values. Red and yellow areas indicate high (positive) anomaly intensities reaching up to 300 nT, which are generally associated with intrusive igneous rocks or volcanic rocks rich in ferromagnetic minerals. In contrast, dark blue colors represent low (negative) anomalies of approximately −100 nT, which can be interpreted as thick sedimentary rocks or demagnetized zones caused by hydrothermal alteration [11]. With the RTP correction, the anomaly centers are now positioned directly above their causative bodies, thereby minimizing distortion due to dipolar effects and enabling more accurate source location interpretation.

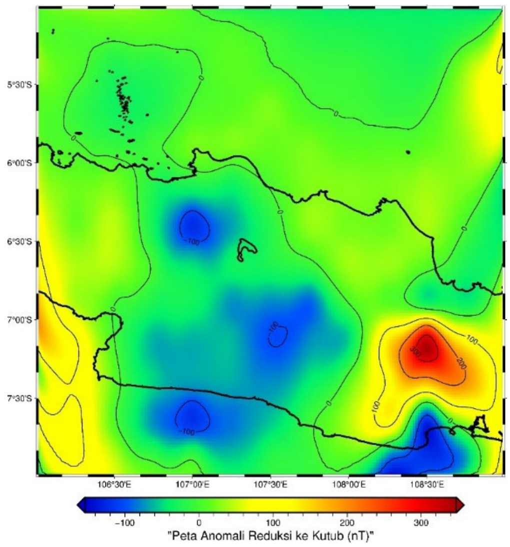

Fig. 3. Reduction to the Pole (RTP) Magnetic Anomaly Map

After obtaining the RTP data, spectral separation was performed to generate the Regional Magnetic Anomaly Map. This map represents magnetic responses originating from very deep and extensive sources, such as basement rocks or large-scale crustal structures. Figure 4 displays the regional anomaly pattern produced using a third-order polynomial method, which was selected because it effectively models long-wavelength regional geological trends without removing important features. The polynomial function models the regional trend of the total magnetic field data, which is then subtracted from the original data to obtain the local component [15]. The contour patterns on the regional map appear smoother and dominated by long-wavelength variations, reflecting regional geological structures located at significant depths beneath West Java.

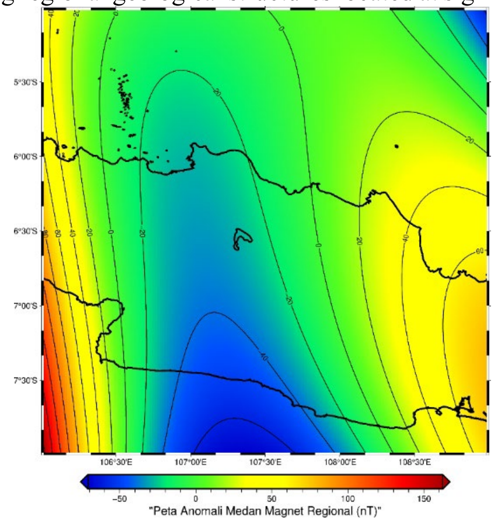

Fig. 4. Regional Magnetic Anomaly Map

The next step was the extraction of the Residual Magnetic Anomaly Map, obtained by subtracting the regional anomaly from the RTP data. Figure 5 presents the residual anomaly map, which visualizes local magnetic field variations related to shallow exploration targets, such as shallow intrusions or near-surface fault zones. In this map, the focus of interpretation becomes sharper, allowing local geological structures to be identified more clearly than in the total magnetic data. Concentrations of high anomalies reaching up to 300 nT are observed in relatively narrow and localized areas, indicating strong contrasts in rock susceptibility within the shallow crust. These residual anomalies provide the most relevant information regarding subsurface geological configurations directly associated with potential earthquake sources or other active tectonic features [16].

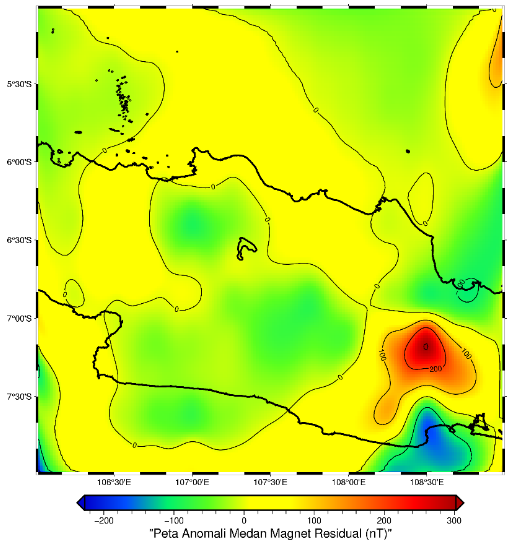

Fig. 5. Residual Magnetic Anomaly Map

3.2. Derivative Analysis and Structural Boundaries

To further delineate the geological structural boundaries indicated on the residual anomaly map, a First Horizontal Derivative (FHD) analysis was performed. Figure 6 shows the FHD filtering results, which function to detect edges or lateral boundaries of the anomalous source bodies (edge detection). This method is highly sensitive to horizontal changes in magnetic intensity values, where peak (maximum) values in the FHD curve generally coincide with lithological contact boundaries or fault zones [14]. In the map, two dominant regions with anomaly gradient values of approximately 0.01 nT/m are identified. The lineament patterns formed by these FHD peak values can be interpreted as fault pathways or intrusion boundaries separating rock blocks with different magnetic properties.

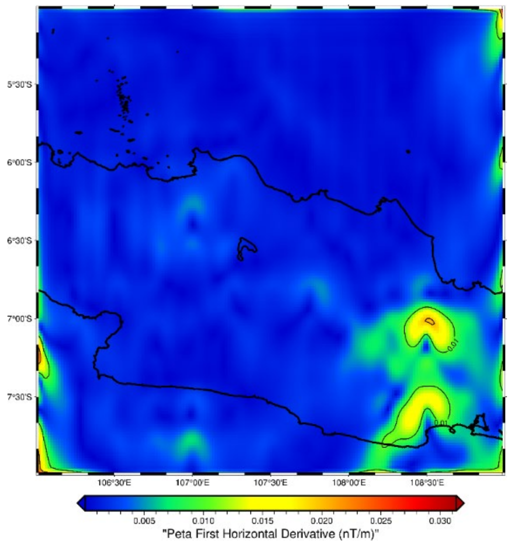

Fig. 6. First Horizontal Derivative (FHD) Map

The analysis was continued using the Second Vertical Derivative (SVD) method to separate overlapping local anomalies and enhance the effects of shallow sources. Figure 7 presents the SVD map, where anomalies appear more isolated and focused on more specific areas. Zero (0) derivative values on the SVD map are often used to delineate the exact boundaries of subsurface anomaly sources. In southeastern West Java, a relatively strong anomaly response is observed with values ranging from -4×10^{-6} nT/m² to 4×10^{-6} nT/m². These high-frequency anomaly patterns confirm the presence of complex shallow geological structures, which are most likely related to active fault systems in the region [17].

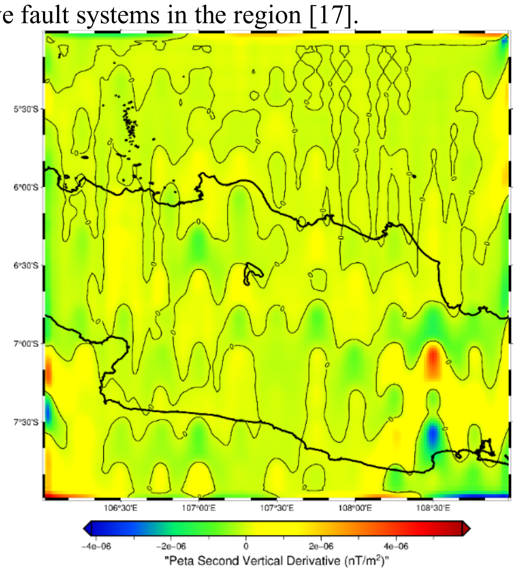

Fig. 7. Second Vertical Derivative (SVD) Map

While the FHD and SVD zero-contours highlight regions of high structural contrast, it is essential to acknowledge the inherent limitations of the 2-arc-minute (~4 km) spatial resolution of EMAG2v3. However, these magnetic lineaments are interpreted as the deep-seated basement architecture that controls the formation of active faults at the surface. A qualitative comparison shows that the major NW-SE and W-E magnetic lineaments identified in this study align with the orientation of regional fault systems mapped in the National Source and Fault Map (PusGen), such as the Cimandiri and Baribis zones. These magnetic anomalies likely delineate the boundaries of crustal blocks or 'zones of weakness' that act as the structural framework for the active fault segments reported by PusGen. Thus, while the resolution prevents a 1:1 mapping of individual fault segments, the results successfully capture the regional tectonic grain that governs the seismicity of West Java.

3.3. Correlation between Magnetic Anomalies and Seismicity

The final interpretation was conducted by correlating magnetic anomaly patterns with historical earthquake data to identify earthquake-generating structures. Figure 8 presents the map of a significant earthquake that occurred on 15 December 2017 with a magnitude of Mw 6.5. This earthquake was centered at coordinates −7.4921° S and 108.1743° E with a depth of 90 km, which is administratively located in Tasikmalaya Regency, West Java. While the ~90 km depth indicates an intermediate-depth intraslab mechanism, its spatial alignment with a prominent onshore -150 nT magnetic anomaly suggests a physical coupling. Intermediate-depth intraslab earthquakes often project their tectonic stress upward, exploiting and reactivating long-lived zones of crustal weakness, such as ancient fractures or the boundaries of deep sedimentary basins in the overlying lithosphere. Consequently, the low magnetic signature is computationally interpreted as a pre-existing structural boundary characterized by rock demagnetization—potentially facilitated by hydrothermal fluid alteration or stress accumulation along these projected crustal pathways [3]. Therefore, the magnetic anomaly maps the crustal vulnerability zone that responds to the deeper tectonic regime, rather than representing the direct seismogenic source of the 90 km event.

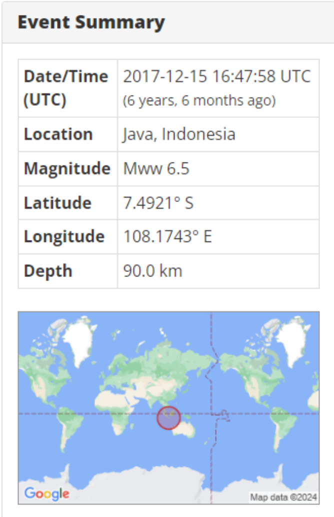

Fig. 8. Earthquake Map of 15 December 2017

4. CONCLUSION

This study successfully identified subsurface structures and tectonic settings in the West Java region through the analysis of EMAG2 geomagnetic data. The application of the Reduction to the Pole (RTP) correction method and the separation of regional–residual anomalies proved to be effective in isolating magnetic responses originating from the shallow Earth's crust. Further analysis using derivative methods, namely the First Horizontal Derivative (FHD) and the Second Vertical Derivative (SVD), was able to enhance lithological boundaries and delineate lineament zones associated with geological fault structures [14]. The resulting anomaly patterns provide a clear depiction of the complexity of geological structures that cannot be observed solely from total magnetic anomaly data.

The integrated interpretation indicates a strong spatial correlation between residual magnetic anomalies and seismic activity, particularly for the Tasikmalaya earthquake event on 15 December 2017. At the earthquake epicenter location (latitude −7.5° and longitude 108.5°), a low magnetic anomaly value of approximately −150 nT was identified, supported by contrasting patterns on the SVD map, which indicate the presence of a fracture zone or rock demagnetization due to tectonic energy release. This finding confirms that active fault zones are often characterized by a decrease in magnetic intensity resulting from rock alteration along fault planes [3]. Nevertheless, the anomalies detected around latitude −7° and longitude 108.5° have not yet shown a direct relationship with the available earthquake data; therefore, further complementary geological or geophysical investigations are required to determine the sources of these anomalies.

REFERENCE

[1] R. Hall and W. Spakman, "Mantle structure and tectonic history of SE Asia," Tectonophysics, vol. 658, pp. 14–45, 2015, doi: 10.1016/j.tecto.2015.07.003.

[2] R. Meilani, Rosida Tiurma Manurung, Maria Yuni Megarini, Tessalonika Sembiring, and Karthy Priyathy Mastovani, "Penanganan psikologis pasca gempa bumi Sumedang," BEGAWE J. Pengabdi. Masy., vol. 2, no. 1, pp. 59–62, 2024.

[3] P. Supendi, A. D. Nugraha, N. T. Puspito, S. Widiyantoro, and D. Daryono, "Identification of active faults in West Java, Indonesia, based on earthquake hypocenter determination, relocation, and focal mechanism analysis," Geosci. Lett., vol. 31, pp. 4–10, 2018, doi: 10.1186/s40562-018-0130-y.

[4] R. A. Munandar and R. Sulsaladin, “Karakteristik Tektonik Dan Periode Ulang Gempabumi Pada Sesar Cimandiri Jawa Barat,” Bul. Meteorol. Klimatologi, dan Geofis., vol. 3, no. 3, pp. 42–51, 2022.

[5] M. Irsyam et al., “Development of the 2017 national seismic hazard maps of Indonesia,” Earthq. Spectra, vol. 36, no. 1_suppl, pp. 112–136, 2020, doi: 10.1177/8755293020951206.

[6] D. Purwanto, D. D. Permadi, U. S. Saputri, U. Aditiawarman, D. O. D. Handayani, and D. A. Dewi, “Kajian tentang bencana dan dampak gempa bumi di cianjur bersama mahasiswa teknik sipil nusaputra,” J. Pengabdi. Kpd. Masy. Abdi Nusa, vol. 3, no. 1, pp. 36–39, 2023.

[7] R. A. Sari, “Penentuan Persamaan Empiris untuk Memprediksi Magnitudo Gempabumi Menggunakan Parameter Prekursor Gempabumi Dari Anomali Magnetik Lombok Nusa Tenggara Barat,” 2019.

[8] T. Zubaidah, M. Korte, M. Mandea, and M. Hamoudi, “New insights into regional tectonics of the Sunda–Banda Arcs region from integrated magnetic and gravity modelling,” J. Asian Earth Sci., vol. 80, pp. 172–184, 2014.

[9] N. A. Santoso, R. Rizki, R. A. Hakim, and W. Ashuri, “Identification Distribution of Hot Spring in Cisarua Using Magnetic Method,” in IOP Conference Series: Earth and Environmental Science, 2020. doi: 10.1088/1755-1315/537/1/012006.

[10] S. Maus et al., “EMAG2: A 2-arc min resolution Earth Magnetic Anomaly Grid compiled from satellite, airborne, and marine magnetic measurements,” Geochemistry, Geophys. Geosystems, vol. 10, no. 8, pp. 1–12, 2009, doi: 10.1029/2009GC002471.

[11] M. Ö. Arisoy and Ü. Dikmen, “Potensoft: MATLAB-based software for potential field data processing, modeling and mapping,” Comput. Geosci., vol. 37, no. 7, pp. 935–942, 2011, doi: 10.1016/j.cageo.2011.02.008.

[12] M. B. Puspita, C. A. Perwita, Sukir Maryanto, and I. Suyanto, “Analisis Metode Magnetik pada Daerah Manifestasi Panas Bumi Karangrejo, Kabupaten Pacitan,” INSOLOGI J. Sains dan Teknol., vol. 2, no. 5, pp. 907–916, 2023, doi: 10.55123/insologi.v2i5.2662.

[13] B. H. Jacobsen, “A case for upward continuation as a standard separation filter for potential-field maps,” Geophysics, vol. 52, no. 8, pp. 1138–1148, 1987.

[14] B. Verduzco, J. D. Fairhead, C. M. Green, and C. MacKenzie, “New insights into magnetic derivatives for structural mapping,” Lead. Edge (Tulsa, OK), vol. 23, no. 2, pp. 116–119, 2004, doi: 10.1190/1.1651454.

[15] P. Keating and P. Sailhac, “Use of the analytic signal to identify magnetic anomalies due to kimberlite pipes,” Geophysics, vol. 69, no. 1, pp. 180–190, 2004, doi: 10.1190/1.1649386.

[16] R. J. Blakely, Potential Theory in Gravity and Magnetic Applications. 1995.

[17] T. Jeon, H. Rim, and Y.-S. Park, “A Comparative Analysis of Edge Detection Methods in Magnetic Data,” J. Korean earth Sci. Soc., vol. 36, no. 5, pp. 437–446, 2015, doi: 10.5467/jkess.2015.36.5.437.

Journal of Computation Physics and Earth Science
ISSN: 2776-2521 (online)
Volume 5, Number 2, February 2026, Page 210 - 216
https://journal.physan.org/index.php/jocpes/index

Estimating Aftershock Termination Time Using Statistical Decay Models: A Case Study of the March 22, 2024 Bawean Earthquake

Martha Lisauli Rajagukguk[1], Rayhan Irfan Hielmy[2]
[1,2]Department of Geophysics (STMKG)

Article Info

Article history:

Received December 31, 2025
Revised February 28, 2026
Accepted February 28, 2026

Keywords:

Bawean Earthquake
Aftershocks
Omori
Mogi I
Mogi II
Utsu

A B S T R A C T

An earthquake struck Bawean Island on March 22, 2024 with a magnitude of 6.5 followed by a series of aftershocks. In this study, the decay of aftershocks in the Bawean region was analyzed from March 22 to March 31, 2024 using the Omori Method, Mogi I Method, Mogi II Method, and Utsu Method. The purpose of this research is to determine the duration of aftershock decay in Bawean and to identify the most suitable statistical method for predicting aftershock decay time in the region. The analyzed data were obtained from the BMKG earthquake repository. By applying the four methods, results were obtained in the form of aftershock decay duration and correlation coefficients for each method. The analysis shows that the most appropriate statistical methods for calculating aftershock decay time in Bawean are the Mogi I Method and the Utsu Method both producing a correlation coefficient of approximately -0.806 and an aftershock decay duration of 24 days consistent with the BMKG earthquake catalog data.

Corresponden Author:

Martha Lisauli Rajagukguk,
Department of Geophysics (STMKG)
Tangerang, Indonesia
Email: marthalisauli2004@gmail.com

1. INTRODUCTION

Indonesia is a country with a high potential for geological hazards, such as volcanic eruptions and earthquakes. This condition is primarily caused by its location along active tectonic belts, characterized by the presence of numerous active faults and subduction zones [1]. Indonesia is geographically located at the intersection of three major tectonic plates, the Indo-Australian, Eurasian, and Pacific plates. In the Bali-Nusa Tenggara region, the tectonic setting becomes increasingly complex due to the subduction of the Australian Plate beneath the Nusa Tenggara Islands, forming an opposing arcuate structure [2].

The Bali–Nusa Tenggara region is also well known for its high seismic activity, particularly in the northern part. The elevated level of seismicity in this area is strongly influenced by the presence of the Flores Backarc Thrust, an active fault zone that frequently generates large earthquakes, such as the Lombok earthquake on August 5, 2018 [3]. Following a mainshock, seismic activity is typically accompanied by a sequence of aftershocks over a certain period of time [4].

The aftershock phenomenon can be explained by the Elastic Rebound Theory which describes earthquakes as a process of stress release toward a new equilibrium state along a fault following a mainshock [5]. During this adjustment process, the frequency of aftershocks gradually decreases and eventually ceases once the fault reaches a stable condition. This decreasing trend in aftershock frequency is referred to as aftershock decay [6].

To estimate the termination time of aftershock sequences, statistical approaches such as the Omori, Mogi I, Mogi II, and Utsu methods are commonly applied. Each method exhibits different levels of suitability depending on the study area which can be evaluated using the correlation coefficient (r) with values approaching 1 or -1 indicating a strong fit. Previous studies have reported varying results. For example, a study on aftershock decay following the Sunda Strait earthquake on May 23, 2021 concluded that the Mogi I method provided the best fit to BMKG data [7]. Meanwhile, the Mogi I and Utsu methods were found to be suitable for application in the Lombok region [8].

On March 22, 2024, a significant earthquake with a magnitude of 6.5 occurred near Bawean Island resulting in damage to approximately 4,300 buildings. The mainshock was followed by 878 aftershocks recorded between March 22 and June 12, 2024 based on analyses conducted by the Malang Geophysical Station [9]. This seismic activity is associated with the offshore Muria Fault which had previously been considered inactive [10][11]. This offshore fault differs from the active Muria Fault located on the Muria Peninsula which has been documented in the 2017 Indonesian Active Fault Map published by the National Center for Earthquake Studies [12] .

This study aims to validate the results of previous research related to the March 22, 2024 Bawean earthquake. The estimated termination time of the aftershock sequence is expected to serve as a reference for disaster mitigation efforts in the Bawean region and its surroundings. In addition, this study is expected to provide further insight into the characteristics and patterns of seismic activity in the area.

2. RESEARCH METHOD

2.1 Data

The earthquake data used in this study were obtained from the BMKG earthquake repository website (https://repogempa.bmkg.go.id/eventcatalog). The observation period spans from March 22 to March 31, 2024, covering the Bawean region and its surroundings within the coordinate boundaries of 111.4°–113.7° E longitude and 5.2°– 6.8° S latitude. The spatial distribution of the study area is illustrated in Fig. 1.

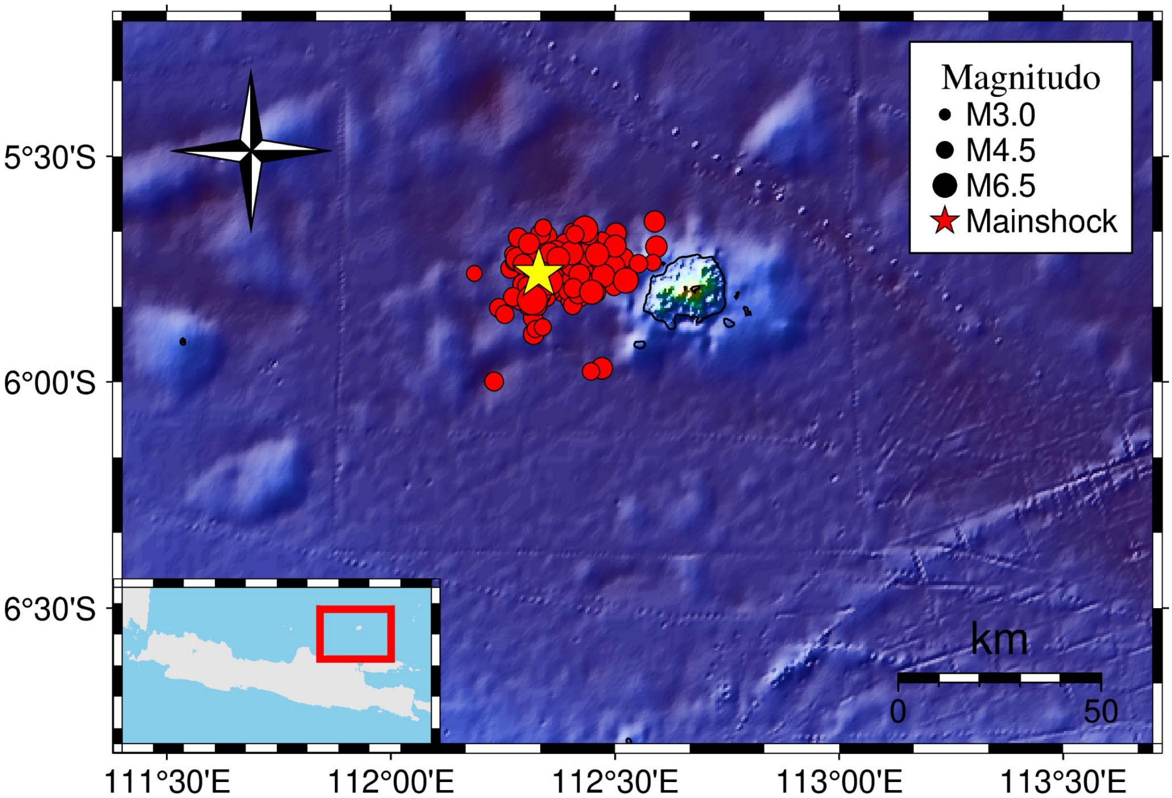

Fig. 1 Map of the study area boundaries in Bawean and its surroundings, showing the mainshock and aftershocks used as research data.

The acquired earthquake data were subsequently processed using Microsoft Excel to generate a daily earthquake frequency distribution graph for the study period. This graph was then analyzed using the Omori, Mogi I, Mogi II, and Utsu methods.

2.2 Omori Method

The Omori method describes the temporal decay of aftershock frequency as a function of time following the mainshock [13]. The mathematical expression of the Omori law is given by:

$$n(t) = k(c + t)^{-1} \quad (1)$$

Where:
$n(t)$: the aftershock frequency,
t : the time elapsed since the mainshock,
k and c :constants dependent on geological conditions.

2.3 Mogi I Method

The Mogi I method is applied to analyze aftershock sequences with durations longer than 100 days [13]. The formulation of this method is expressed as:

$$n(t) = a \cdot b^t \quad (2)$$

Where:
$n(t)$: the aftershock frequency,
t : the time elapsed since the mainshock,
a and b : constants influenced by the surrounding geological conditions

2.4 Mogi II Method

The Mogi II method is used for aftershock sequences with durations shorter than 100 days [13]. The mathematical expression is given by:

$$n(t) = a \cdot e^{-bt} \quad (3)$$

Where:
$n(t)$: the aftershock frequency,
t : the time elapsed since the mainshock,
a and b : constants influenced by the surrounding geological conditions

2.5 Utsu Method

The Utsu method is a development of the Omori method and is more suitable for describing aftershock frequency per unit time [13]. The equation for the Utsu method is written as:

$$n(t) = k(t + c)^{-p} \quad (4)$$

Where:
$n(t)$: the aftershock frequency,
t : the time elapsed since the mainshock,
k and p :constants dependent on geological conditions

2.6 Correlation Analysis

Since several methods are used to estimate the termination of aftershock activity, a comparative analysis is required to determine the most suitable method. The best-performing method is selected by comparing the correlation coefficient (r) between the observed data and the calculated results. The correlation coefficient is computed using the following equation:

$$r = \frac{n\sum x_i y_i - (\sum x_i)(\sum y_i)}{\sqrt{(n\sum x_i^2 - (\sum x_i)^2)(n\sum y_i^2 - (\sum y_i)^2)}} \quad (5)$$

Where:
r : the aftershock frequency,
x : the time elapsed since the mainshock,
y : constants dependent on geological conditions
n : the total number of data points.

3. RESULT AND DISCUSSION

The frequency distribution of aftershocks following the M6.5 Bawean earthquake on March 22, 2024, is shown in Figure 2. Based on the BMKG earthquake catalog, a total of 94 aftershocks were recorded between March 22 and March 31, 2024.

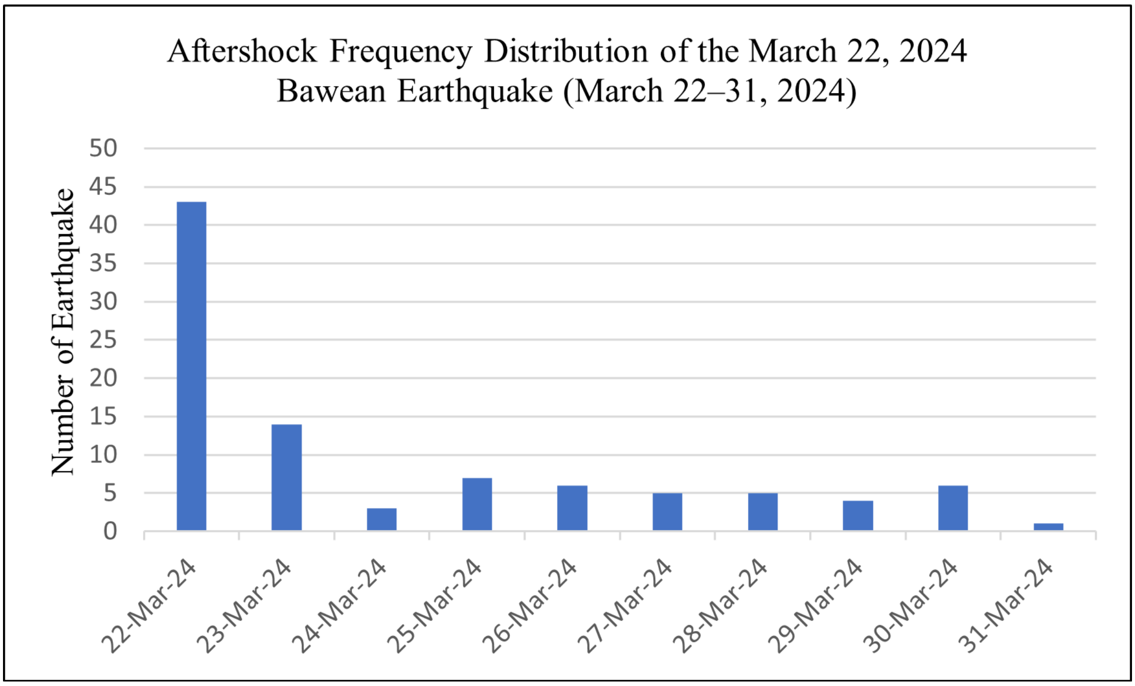

Fig. 2 Aftershock frequency distribution from March 22 to March 31, 2024.

The highest aftershock frequency occurred on the first day, March 22, 2024 with a total of 43 aftershocks. On the second day, the aftershock frequency decreased significantly to 14 events. Subsequently, the frequency fluctuated from the third to the tenth day following the mainshock.

Using statistical approaches based on the four aftershock decay methods discussed previously, the aftershock frequency distributions, correlation coefficients, and aftershock decay durations were obtained. Aftershock decay is considered to occur over time when the correlation coefficient has a negative value, as the relationship between aftershock frequency and time is inversely proportional. A correlation coefficient value closer to -1 indicates a stronger inverse relationship [16].

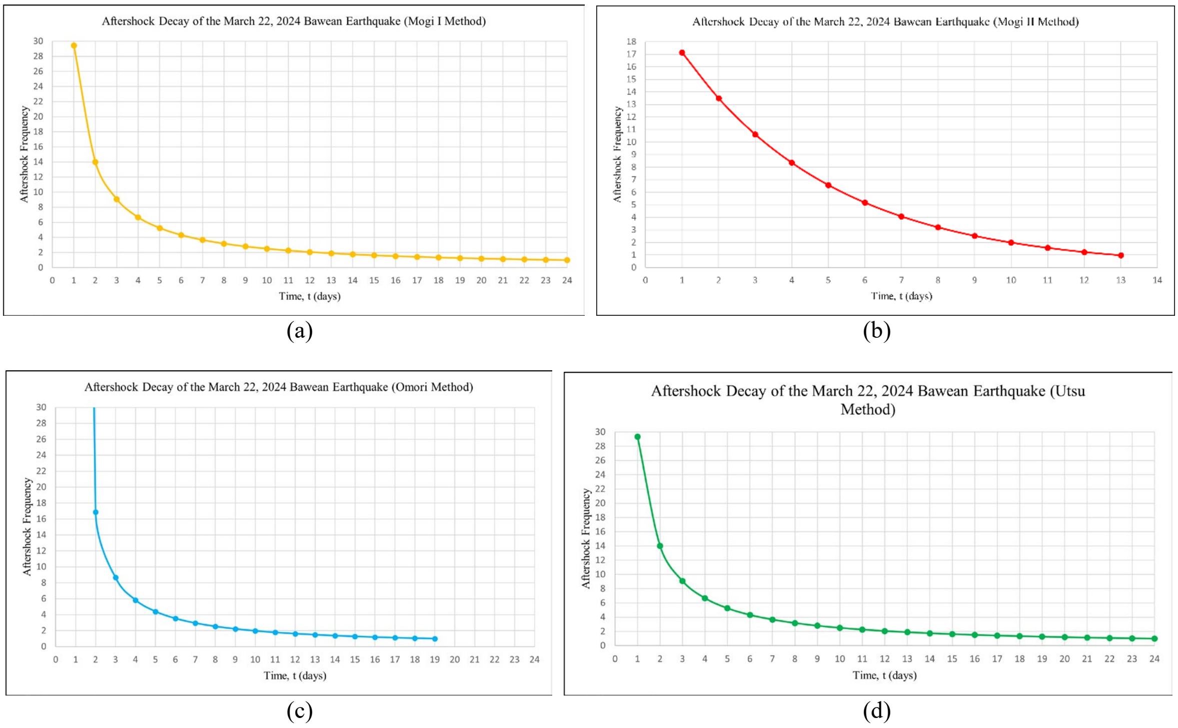

Fig. 3 Aftershock decay curves of the March 22, 2024 Bawean earthquake using (a) Mogi I, (b) Mogi II, (c) Omori, and (d) Utsu methods.

The estimation of aftershock decay duration was conducted using the Omori, Mogi I, Mogi II, and Utsu methods, as illustrated in Figure 3. The decay curves indicate that the aftershock frequency decreases with time. The final analysis results, including the correlation coefficients, decay durations, and estimated termination dates of aftershock activity, are presented in Table 1.

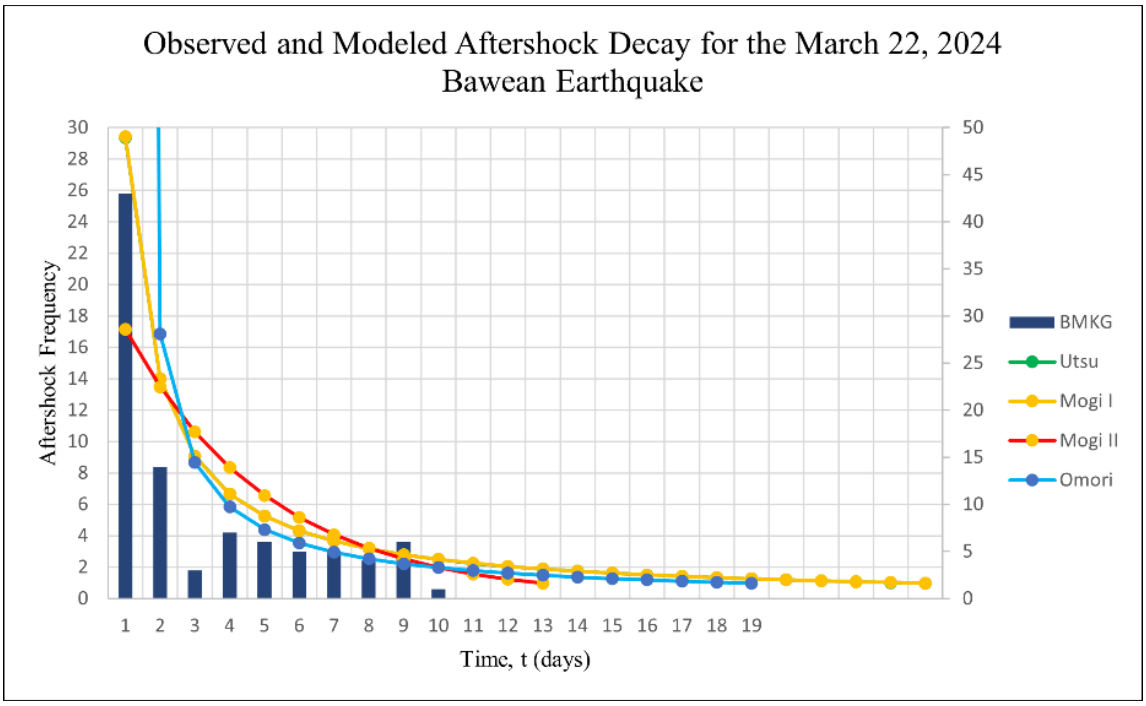

Fig. 4 Observed daily aftershock frequency and fitted statistical decay models (Omori, Mogi I, Mogi II, and Utsu) for the March 22, 2024 Bawean earthquake. The histogram represents the observed BMKG aftershock catalog while the curves indicate the theoretical decay functions of each model.

Each method yields different results in terms of decay patterns, correlation coefficients, and aftershock durations. The Omori method produces a correlation coefficient of 0.628, with the aftershock sequence estimated to end on the 19th day, corresponding to April 9, 2024. The Mogi I method yields a correlation coefficient of −0.806, estimating the aftershock termination on the 24th day, April 14, 2024. The Mogi II method produces a correlation coefficient of −0.745, with the aftershock sequence ending on the 13th day, April 3, 2024. Similarly, the Utsu method results in a correlation coefficient of −0.806, with an estimated aftershock termination on the 24th day, April 14, 2024.

Figure 4 shows the comparison between the observed daily aftershock frequency and the theoretical decay curves derived from the Omori, Mogi I, Mogi II, and Utsu models. The histogram represents the observed aftershock occurrences obtained from the BMKG earthquake catalog while the curves illustrate the expected temporal decay behavior predicted by each statistical model. As shown in the figure, the aftershock frequency decreases with time following the mainshock, indicating a typical decay pattern of aftershock activity.

The correlation coefficients and aftershock decay functions $n(t)$ derived from the four methods show noticeable differences. The Mogi I, Mogi II, and Utsu methods yield negative correlation coefficients indicating an inverse relationship between the independent variable (time) and the dependent variable (aftershock frequency). A negative correlation implies that as time increases, the aftershock frequency $n(t)$ decreases [11][17][18].

Table 1. Estimated termination time of aftershock activity following the March 22, 2024 Bawean earthquake

Method	Correlation Coefficient	Day	Estimated Termination Date
Omori	0,627622094	19	April 09,2024
Mogi I	-0,806582947	24	April 14,2024
Mogi II	-0,744988914	12	April 03,2024
Utsu	-0,806362935	24	April 14,2024

Based on the BMKG earthquake catalog, no seismic activity was recorded on April 14, 2024. This observation is consistent with the results obtained using the Mogi I and Utsu methods. Both methods also produce strong correlation coefficients, indicating good agreement with the observed data. Therefore, it can be concluded that the most appropriate statistical methods for estimating aftershock decay in the Bawean region are the Mogi I and Utsu methods. These two methods yield nearly identical correlation coefficients (-0.806) and aftershock decay durations with the aftershock sequence estimated to last for 24 days and terminate on April 14, 2024. As shown in the BMKG earthquake catalog (Figure 5), no aftershock activity was recorded on the 24th day following the mainshock.

EQ Repository | Requested Data

No	Event ID	Date time	Latitude	Longitude	Magnitude	Mag Type	Depth (km)	Phase Count	Azimuth Gap	Location	Agency
1	bmg2024hqks	2024-04-18T14:20:46.000721Z	-5.777413368225098	112.35114288330078	3.3164708819801976	M	5	35	218.12582397460938	Java Sea	BMKG
2	bmg2024hode	2024-04-17T08:15:06.022261Z	-5.751312255859375	112.3438949584961	4.972398040082093	M	10	134	35.356359481811523	Java Sea	BMKG
3	bmg2024hgkk	2024-04-13T02:49:14.511042Z	-5.733510971069336	112.39298248291016	3.426603945104656	M	10	24	229.34959411621094	Java Sea	BMKG
4	bmg2024hfwc	2024-04-12T19:35:37.588224Z	-5.670433521270752	112.3717269897461	3.258673138559679	M	10	36	240.0229797363281	Java Sea	BMKG
5	bmg2024hfmm	2024-04-12T14:43:41.242323Z	-5.740666389465332	112.55815887451172	4.032386473010134	M	10	90	76.98638916015625	Java Sea	BMKG
6	bmg2024hehv	2024-04-11T23:14:35.979355Z	-5.715095520019531	112.51365661621094	4.370323574430225	M	10	85	99.1903018951416	Java Sea	BMKG

Fig. 5 BMKG earthquake catalog showing no recorded aftershocks on April 14, 2024.

4. CONCLUSION

In this study, the estimation of the termination time of aftershock activity following the March 22, 2024 Bawean earthquake indicates that the Mogi I method provides the highest correlation coefficient with a value of -0.806582947. Based on this method, the aftershock sequence is estimated to have ended on the 24th day corresponding to April 14, 2024. Similar results are obtained using the Utsu method which yields a correlation coefficient of -0.806362935 and predicts the same aftershock termination date, namely the 24th day (April 14, 2024).

These findings are consistent with the BMKG earthquake catalog which shows no recorded seismic activity in the study area on April 14, 2024. Therefore, the Mogi I and Utsu methods can be considered reliable for accurately estimating the termination time of aftershock sequences associated with the March 22, 2024 Bawean earthquake.

REFERENCE

[1] N. N. Faiza, A. Mukti Wibowo, and R. Fatimah, "ANALISIS METODE WAKTU PELURUHAN GEMPA BUMI SUSULAN BERDASARKAN METODE OMORI, MOGI DAN UTSU (STUDI KASUS GEMPA BUMI PASAMAN BARAT 25 FEBRUARI 2022)," vol. 08, no. 02, pp. 65–72, 2024, [Online]. Available: https://doi.org/10.24198/jiif.v8i2

[2] D. A. Pramadhana, "ANALYSIS OF AFTERSHOCK METHODS IN KARANGASEM BASED ON THE KARANGASEM EARTHQUAKE Mw 5 , 2 2022," *Bul. Meteorol. Klimatologi Dan Geofis.*, vol. 4, no. 6, pp. 44–52, 2023, [Online]. Available: https://balai2bmkg.id/index.php/buletin_mkg/article/view/67

[3] X. Yang, S. C. Singh, and A. Tripathi, "Did the Flores backarc thrust rupture offshore during the 2018 Lombok earthquake sequence in Indonesia?," *Geophys. J. Int.*, vol. 221, no. 2, pp. 758–768, 2020, doi: 10.1093/gji/ggaa018.

[4] P. Maulida, R. Putra, and A. Kurniawan, "Studi Pergeseran Koseismik Gempa Pasaman M6.1 2022 Menggunakan Data Pengamatan GPS harian," *Geoid*, vol. 18, no. 1, p. 176, 2022, doi: 10.12962/j24423998.v18i1.14410.

[5] K. Salsabil A., R. A. Ginting, Q. A., and M. Kamal A., "Analisis Peluruhan Gempa Bumi Menggunakan Metode Omori,Mogi-Utsu I Dan Mogi-Utsu Ii (Studi Kasus Gempa Bumi Banten 23 Januari 2018)," vol. VIII, pp. SNF2019-PA-7–14, 2019, doi: 10.21009/03.snf2019.02.pa.02.

[6] H. Syarifuddin and P. Ariyanto, "Analisis Perkiraan Waktu Berakhirnya Gempabumi Susulan Pada Gempabumi M 5.4 Jayapura 2 Januari 2023," *Bul. Meteorol. Klimatlogi dan Geofis.*, vol. 4, no. 5, pp. 46–53, 2023, [Online]. Available: https://repogempa.bmkg.go.id/eventca

[7] Y. Januarti and P. Ariyanto, "Analisis Peluruhan Gempabumi Susulan di Selat Sunda Pada Tanggal 23 Mei 2021," *Semin. Nas. FIsika 2021*, pp. 97–102, 2021, [Online]. Available: https://fisika.fmipa.unesa.ac.id/proceedings/index.php/snf/article/view/179/158

[8] A. Vellicia, K. Suarbawa, and R. Darsono, "Penentuan Asumsi Waktu Berakhirnya Gempa Susulan Studi Kasus Gempabumi Lombok 5 Agustus 2018," *Kappa J.*, vol. 3, no. 2, pp. 99–104, 2019, doi: 10.29408/kpj.v3i2.1609.

[9] R. Yulinda, L. Nisa, I. Ilham, and J. Purba, "The Relocation Of Bawean Earthquake Aftershock Using Double Difference Method," *J. Rekayasa Geofis. Indones.*, vol. 7, no. 01, pp. 013–025, 2025, doi: 10.56099/jrgi.v7i01.147.

[10] D. A. Pramadhana, B. H. P. P. Putra, and M. Syirojudin, "STUDI PEMETAAN SESAR REMBANG-MADURA-KANGEAN-SAKALA TURUNAN," vol. 10, no. 1, pp. 51–62, 2024.

[11] M. Asrurifak, I. M., B. B., T. W., and Hendriyawan, “Development of Spectral Hazard Map for Indonesia with a Return Period of 2500 Years using Probabilistic Method,” vol. 12, no. 1, pp. 52–62, 2010.

[12] A. A. Justiono, E. Rahmadi, and R. Fadly, “Analisis Pergeseran Horisontal Akibat Gempa Bawean 22 Maret 2024 Menggunakan Pengamatan GPS Kontinu,” vol. 7, no. 2024, pp. 181–185, 2025.

[13] T. Utsu, Y. Ogata, and R. S. Matsu’ura, “The Centenary a Decay of the Omori Formula Activity for Law of Aftershock Tokuji Utsu ,* Yosihiko Ogata , and Ritsuko S . Matsu ’ ura,” *J. Phys. Earth*, vol. 43, no. 1, pp. 1–33, 1995, doi: 10.4294/jpe1952.43.1.

[14] J. Hardebeck, A. Llenos, A. Michael, M. Page, M. Schneider, and N. Elst, “Aftershock Forecasting,” *Annu. Rev. Earth Planet. Sci.*, vol. 52, 2023, doi: 10.1146/annurev-earth-040522-102129.

[15] H. Kubo and K. Shiomi, “Short-Term Forecasting of Aftershock Ground-Motion Hazards Within a Few Hours After a Large Earthquake in Japan,” *Seismol. Res. Lett.*, vol. 97, no. 1, pp. 283–294, 2025, doi: 10.1785/0220250113.

[16] E. Asanti, D. B. Susanti, L. Silfia, and P. Boli, “Analisis Waktu Berakhirnya Gempa Bumi Susulan Menggunakan Metode Mogi II dan Utsu (Studi Kasus Gempa Bumi Bantul 30 Juni 2023),” *J. Stasiun Geofis. Sleman*, vol. 2, no. 1, pp. 27–32, 2024.

[17] V. M. Zakhra, Y. Styawan, E. I. Fattah, and F. Alhada, “Analisis Gempa Cianjur 2022 dengan Pendekatan Spasial Temporal a-Value dan b-Value,” *J. Geofis. Eksplor.*, vol. 09, pp. 217–230, 2023.

[18] I. I. Pertiwi, “Analisis Statistik Distribusi Kejadian Gempabumi Di Luwu Timur, Morowali, Dan Morowali Utara, Sulawesi,” vol. 20, no. 01, 2022.

Journal of Computation Physics and Earth Science
ISSN: 2776-2521 (online)
Volume 5, Number 2, February 2026, Page 217 - 226
https://journal.physan.org/index.php/jocpes/index

Subsurface Structure of Palu-Koro Fault Zone Using TOPEX Satellite Gravity Data and Regional-Residual Anomaly Separation

Rayhan Irfan Hielmy[1]
[1]Undergraduate Program in Geophysics (STMKG)

Article Info

Article history:

Received December 26, 2025
Revised February 28, 2026
Accepted February 28, 2026

Keywords:

Gravity Anomaly,
Palu-Koro Fault,
TOPEX Satellite,
Parasnis Method,
Regional-Residual Separation

A B S T R A C T

The Palu-Koro Fault in Central Sulawesi represents a highly active tectonic feature with significant seismic hazard potential, yet detailed subsurface mapping remains challenging due to the difficult terrain in the region. This study analyzed the subsurface structure of the fault zone by utilizing TOPEX satellite gravity data to overcome accessibility issues. The primary objective was to delineate the fault geometry and characterize subsurface lithological boundaries through density contrasts. The data processing stage initially determined the average surface rock density using the Parasnis method, which yielded a precise value of 2.45 grams per cubic centimeter. This density was subsequently applied to generate the Simple Bouguer Anomaly map. To distinguish between deep-seated regional trends and shallow local structures, the study employed two filtering approaches: the second-order polynomial method and the Moving Average method. The results demonstrated that both filtering techniques yielded consistent residual anomaly patterns. The main trace of the Palu-Koro Fault was clearly identified as a continuous low-anomaly zone, interpreted as a fracture system filled with low-density sedimentary deposits. Conversely, significant high-amplitude positive anomalies were detected adjacent to the fault trace, suggesting the existence of shallow high-density bodies such as igneous intrusions or uplifted basement blocks. This research concluded that the integration of satellite gravity data with regional-residual anomaly separation successfully mapped the structural complexity of the area, providing critical baseline data for updating seismic hazard models and enhancing disaster mitigation strategies in Sulawesi.

Corresponden Author:

Rayhan Irfan Hielmy,
Undergraduate Program in Geophysics (STMKG)
Tangerang, Indonesia
Email: rayhanirfanhielmy@stmkg.ac.id

1. INTRODUCTION

Indonesia is located at the convergence of three major tectonic plates of the world, namely the Eurasian Plate, the Indo-Australian Plate, and the Pacific Plate, which makes it one of the regions with the most complex geological settings and highest disaster susceptibility globally [1]. The dynamic interactions among these plates generate very high seismic and volcanic activity, causing frequent earthquakes and volcanic eruptions that have significant socio-economic impacts on society [2]. One of the most prominent tectonic features that plays a major role in seismic activity in eastern Indonesia is the Palu–Koro Fault on Sulawesi Island [3]. This fault is known to be highly active and has triggered numerous destructive earthquakes, with historical records indicating 19 significant seismic events between 1910 and 2013, most of which were associated with the Palu Valley and the movement of the Palu–Koro Fault [4]. The complexity of the geological structure in this region necessitates continuous monitoring and the application of appropriate geophysical methods to mitigate future disaster risks. Studies on crustal deformation and the identification of subsurface structures in this zone are therefore crucial, given the high seismic hazard potential and the tectonic complexity evidenced by a series of large earthquakes in the past [5].

In the field of geophysical exploration, the gravity method is one of the most fundamental and effective techniques for mapping subsurface structures, both for energy resource exploration and disaster mitigation purposes. Since the early twentieth century, this method has been widely applied in oil and gas exploration and has continued to advance rapidly in terms of instrumentation, data acquisition, processing, and interpretation [6]. The basic principle of this method relies on variations in the density of subsurface rock materials, which cause anomalies in the Earth's gravitational field. Significant lateral density contrasts are often strong indicators of geological structures such as faults, igneous intrusions, or sedimentary basins, which can be identified through gravity anomaly maps [7]. This method has thus become a reliable tool for detecting and characterizing rock formations and geological structures that are not directly observable at the surface.

The application of the gravity method for active fault analysis involves separating regional and residual anomalies to better highlight targets at specific depths. Analyses of Bouguer anomalies and Free Air Anomalies (FAA) are routinely used to provide detailed images of subsurface structures, where discontinuities in anomaly values are often associated with the presence of fault planes [8]. The effectiveness of this method has been demonstrated in various case studies in Indonesia, such as research on the Lembang Fault in Bandung, which revealed Bouguer anomalies ranging from −2 mGal to 52 mGal and identified normal fault characteristics through Second Vertical Gradient (SVG) analysis [9]. In addition, studies in Nabire Regency, Papua, successfully utilized secondary data to identify potential faults, with the analysis results showing linear patterns indicative of two main fault zones [10]. The use of satellite-based gravity data has become increasingly popular because it can cover wide and inaccessible regional areas, offering greater time and cost efficiency compared to conventional terrestrial measurements [11].

Based on the success of previous studies, this research aims to apply gravity analysis in Central Sulawesi to map the characteristics of the Palu–Koro Fault in a more comprehensive manner. Considering the challenging terrain along several segments of the fault, this study will utilize satellite gravity data from TOPEX to analyze anomalies around the fault zone. The use of satellite data allows for the identification of regional structural patterns that may be missed by local surveys, while also enabling the separation of anomalies originating from the main fault and other secondary anomaly sources. By integrating Bouguer anomaly analysis and regional-residual anomaly separation methods, it is expected that the boundaries, orientation, and continuity of the Palu–Koro Fault can be mapped more accurately. The results of this study are expected to provide an important contribution to the updating of seismic hazard maps in the Sulawesi region.

2. RESEARCH METHOD

This research was conducted in the active tectonic region surrounding the Palu–Koro Fault, Central Sulawesi, which is geographically bounded by coordinates 119.7417° E to 120.0083° E and 0.9249° S to 1.4581° S. The primary data used in this study were obtained from the TOPEX satellite, which provides essential geophysical parameters including positional data (longitude and latitude), surface elevation, and Free-Air Anomaly (FAA) values. The TOPEX satellite gravity data utilized in this study has a spatial resolution of 1 arc-minute (approximately 1.8 km grid spacing). To generate the continuous maps, the data was interpolated using the Kriging gridding method. While satellite gravity data has grid resolution limits for pinpointing very narrow, near-surface fault ruptures, it is highly effective and reliable for delineating the broader, deep-seated regional fault zone dynamics and major lithological boundaries. The use of satellite data in preliminary studies is considered highly efficient for identifying regional geological structures over wide areas that are difficult to access through terrestrial surveys [12]. All stages of the research, from data acquisition and processing to final interpretation, are systematically summarized in a flowchart presented in Figure 1.

The data processing stage began with the determination of the average surface rock density using the Parasnis graphical method, which aims to minimize the correlation between topography and Bouguer anomalies. In this method, the average density value (ρ) is obtained from the slope of a linear regression resulting from a plot of FAA values versus elevation, as represented by Equations (1) to (4). Accurate density determination is crucial because errors in density estimation can lead to the appearance of spurious anomalies correlated with topography [13]. The density value derived from the Parasnis method was subsequently used as input to calculate the Simple Bouguer Anomaly (SBA) at each measurement point in order to reduce the effect of rock mass above the reference datum.

$$y = a + xb \tag{1}$$

$$FAA = a + 0.04194hb \tag{2}$$

$$SBA = FAA - 0.04192h\rho \tag{3}$$

$$Residual = SBA - Regional \tag{4}$$

After obtaining the Simple Bouguer Anomaly (SBA) map, the analysis was continued using anomaly separation techniques to distinguish the responses of shallow and deep geological structures with the aid of Surfer software. In this study, the separation of regional and residual anomalies was carried out by comparing two mathematical filtering methods, namely the second-order polynomial method and the Moving Average method with a 21×21 window size. This separation is based on the principle that regional anomalies with long wavelengths represent deep sources, whereas residual anomalies with short wavelengths represent shallow sources [14], [15]. The residual anomaly was then calculated mathematically by subtracting the regional anomaly values from the total SBA values at each grid point.

The final result of the filtering process produced two variants of residual anomaly maps (polynomial-based and moving-average-based) that were ready for interpretation. The interpretation focused on the residual anomaly maps by applying slicing techniques to areas exhibiting high anomaly gradients around the Palu–Koro Fault zone. These profile slices were analyzed to identify the continuity of fault structures and subsurface lithological boundaries based on the measured density contrasts. The interpretation results were subsequently validated against local geological conditions to explain the deformation mechanisms occurring in the study area [16].

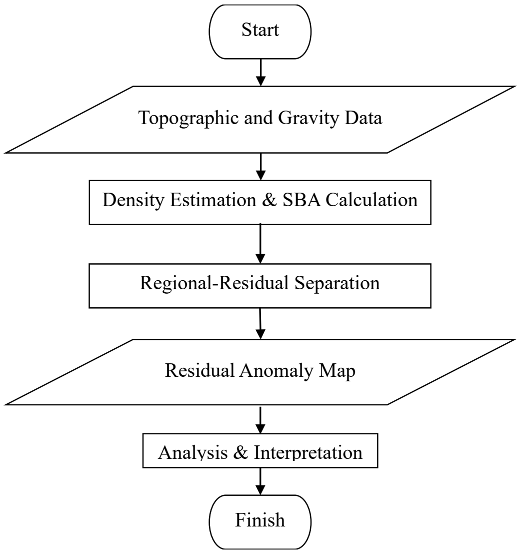

Fig. 1. Flowchart

3. RESULTS AND DISCUSSION

3.1. Topography and Geological Setting of the Study Area

The surface physical conditions of the study area are visualized through a topographic map presented in Figure 2. This map shows significant elevation variations around the Palu–Koro Fault zone, where the main fault trace is marked by a bold black line cutting across the study area. The presence of the fault is indicated by linear morphological features (lineaments) expressed as contrasting valleys and mountain ranges, which are characteristic of active left-lateral (sinistral) strike-slip fault zones in Sulawesi [17]. In addition, the map is complemented by a red box inset that clarifies the data acquisition boundaries within a regional context. This topographic observation represents a crucial initial step for correlating surface features with subsurface anomaly responses discussed in subsequent sections.

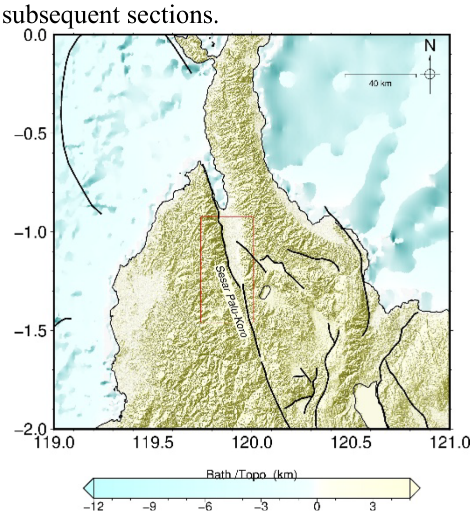

Fig. 2. Topographic map of the Palu–Koro Fault

3.2. Rock Density Estimation (Parasnis Method)

The determination of the average surface rock density was conducted using the Parasnis method to ensure accurate gravity data reduction. Based on the regression graph shown in Figure 3, a strong linear relationship is observed between elevation values (X-axis) and Free Air Anomaly values (Y-axis). The slope of the linear regression derived from this plot yields an average density value of 2.45 g/cm³ (converted from 2.4498 for standard unit simplification). This density value represents upper crustal rocks in the study area and falls within the typical range for sedimentary to altered igneous rocks [13]. The use of this precise density value is essential to minimize spurious correlations between topography and the resulting Bouguer anomalies. The linear regression yielded a high correlation coefficient of $R^2 = 0.8734$. This high statistical confidence demonstrates that the estimated density of 2.45 g/cm³ is exceptionally robust for topographic reduction in this specific area. Consequently, minor density variations (e.g., ±0.05 g/cm³) are statistically constrained and will not significantly alter the overarching structural patterns of the resulting Bouguer and residual anomalies.

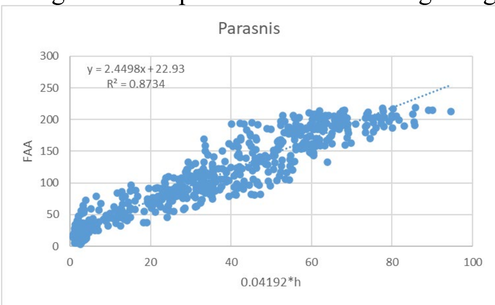

Fig. 3. Density estimation using the Parasnis method

3.3. Simple Bouguer Anomaly (SBA) Map

The distribution of gravity anomalies corrected for topographic effects is presented in the Simple Bouguer Anomaly (SBA) map shown in Figure 4. This map displays highly variable contour patterns, including zones with very low gravity anomaly values, approaching zero, that coincide with the interpreted Palu–Koro Fault trace. Such low anomaly values along the fault zone are commonly associated with fracture zones or graben structures filled with low-density sediments [16]. Conversely, on the western side of the fault trace, a pronounced high anomaly response is observed, reaching values of up to 2300 mGal. The sharp contrast between low anomalies along the fault zone and high anomalies in surrounding areas indicates the presence of strong structural discontinuities or distinct subsurface lithological boundaries.

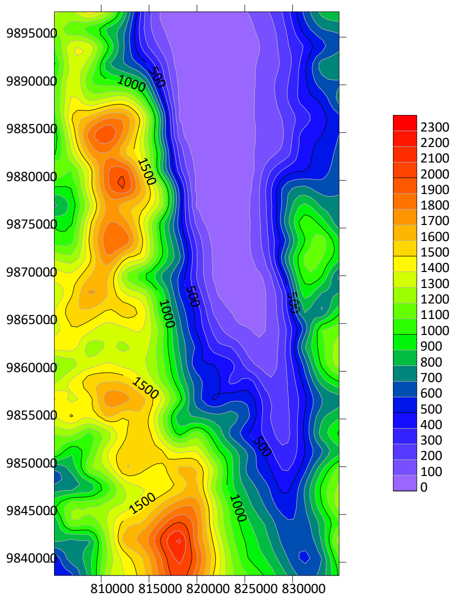

Fig. 4. Simple Bouguer Anomaly (SBA) map of the Palu–Koro Fault

3.4. Regional Anomaly Analysis

The separation of regional anomalies from the SBA data was performed using two comparative approaches: the second-order polynomial method and the 21×21 Moving Average method, as shown in Figure 5 and Figure 6, respectively. The second-order polynomial method was selected due to its capability to model regional geological trends characterized by long-wavelength curvature, which often represent basement rocks or deep-seated structures [7]. Meanwhile, the Moving Average method with a 21×21 window smooths anomaly values by averaging surrounding data points, effectively reducing high-frequency noise and producing a smoother regional trend. The application of both methods aims to ensure that the resulting residual anomalies genuinely represent shallow geological targets rather than mathematical artifacts. Both regional anomaly maps exhibit consistent regional gravity trends, with gradual increases and decreases from east to west across the study area.

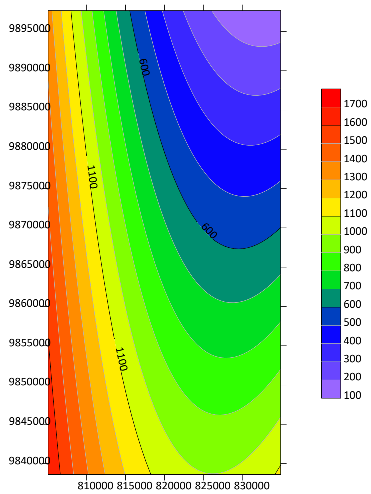

Fig. 5. Regional anomaly map derived from second-order polynomial filtering of the Palu–Koro Fault

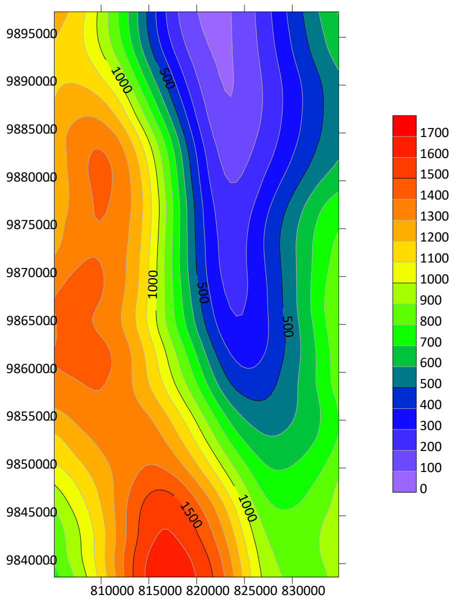

Fig. 6. Regional anomaly map derived from 21×21 Moving Average filtering of the Palu–Koro Fault

3.5. Residual Anomaly Interpretation Along the Palu–Koro Fault

A detailed analysis of residual anomalies was conducted to delineate the geometry of the Palu–Koro Fault using results from the second-order polynomial filter (Figure 7 and Figure 8) and the Moving Average filter (Figure 9 and Figure 10). In both filtering results, the fault trace is consistently marked by a low-anomaly pattern, visualized by white dashed lines on the maps. This interpretation is supported by cross-sectional slicing analysis along three different profiles, which reveals significant gravity value decreases at distances between 10 km and 20 km along each profile. These gravity deficits indicate the presence of weak zones or fractured rocks along the fault plane, characterized by lower densities compared to the surrounding wall rocks. The consistent "valley-shaped" anomaly pattern observed across all three slices provides strong geophysical evidence for the continuity of the Palu–Koro Fault beneath the surface.

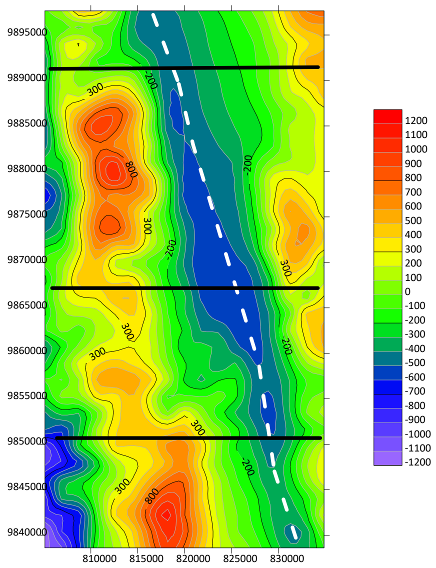

Fig. 7. Residual anomaly map from second-order polynomial regional-residual separation of the Palu–Koro Fault with three slices

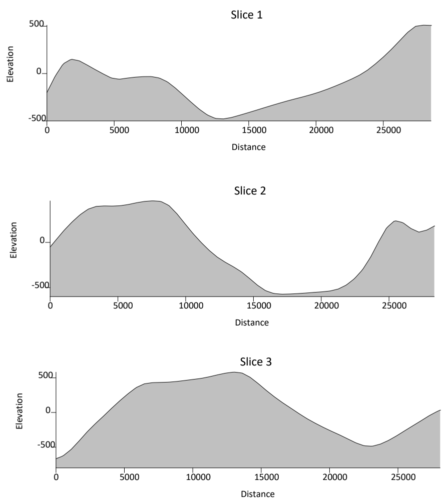

Fig. 8. Two-dimensional slice visualization of the residual anomaly map from second-order polynomial regional-residual separation with three slices

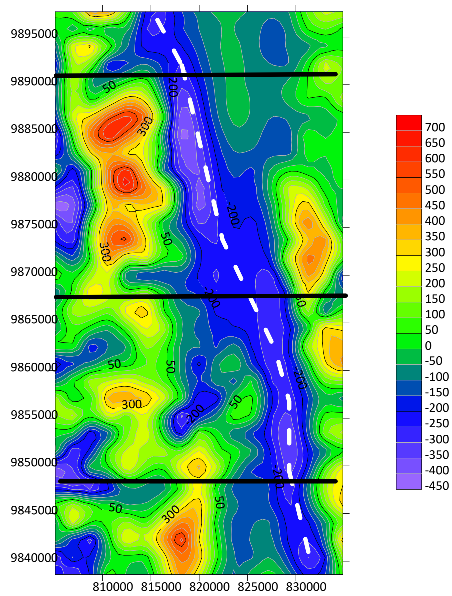

Fig. 9. Residual anomaly map from 21×21 Moving Average regional-residual separation of the Palu–Koro Fault with three slices

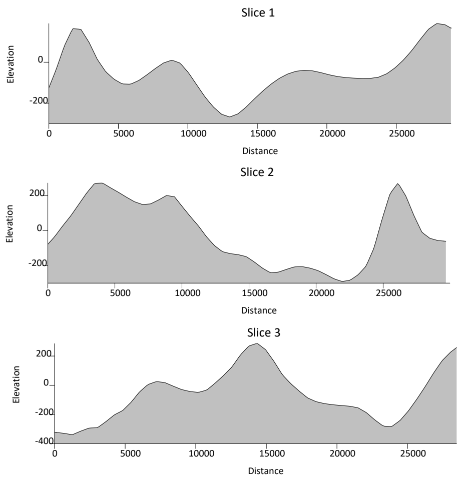

Fig. 10. Two-dimensional slice visualization of the residual anomaly map from 21×21 Moving Average regional-residual separation with three slices

3.6. Identification of Local High Anomalies Near the Fault Zone

In addition to the low anomalies associated with the fault zone, high positive residual anomalies were also identified around the Palu–Koro Fault, as shown in Figure 11 through Figure 14. Analysis using four slice profiles on both polynomial and Moving Average residual maps reveals sharp anomaly peaks with amplitudes reaching 800–1000 mGal at distances of approximately 0.5 km to 2 km. These narrow yet high-amplitude anomalies indicate the presence of shallow, high-density geological bodies, such as igneous intrusions or uplifted basement blocks. The irregular anomaly pattern observed in the fourth slice suggests that the geometry of the causative body may be non-uniform or affected by complex structural deformation. The coexistence of high-density anomalies adjacent to low-density fault-related anomalies further emphasizes the structural complexity of the Palu–Koro Fault zone.

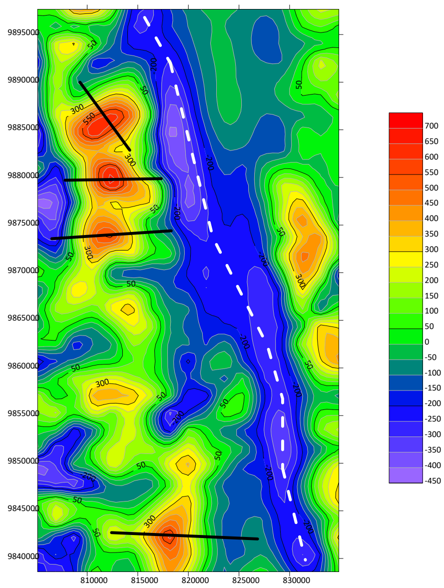

Fig. 11. Residual anomaly map from second-order polynomial regional-residual separation of the Palu–Koro Fault with four slices

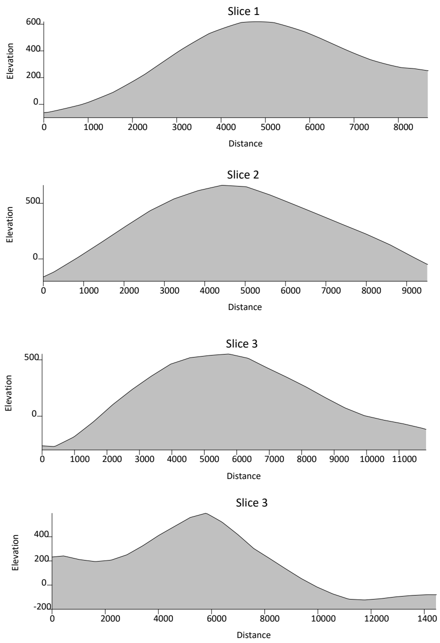

Fig. 12. Two-dimensional slice visualization of the residual anomaly map from second-order polynomial regional residual separation with four slices

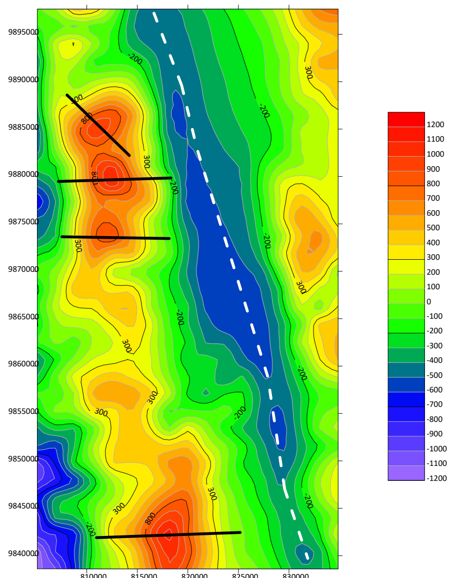

Fig. 13. Residual anomaly map from 21×21 Moving Average regional-residual separation of the Palu–Koro Fault with four slices

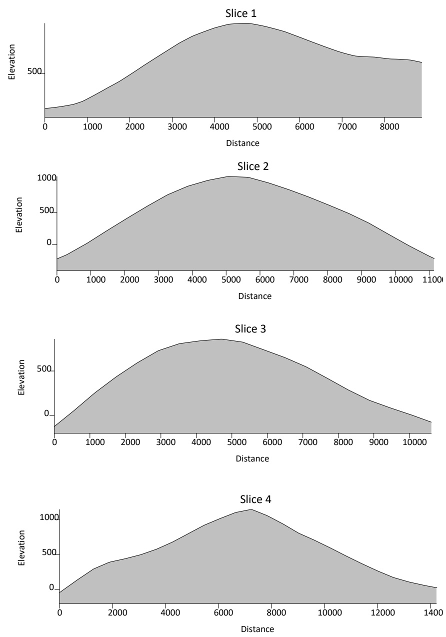

Fig. 14. Two-dimensional slice visualization of the residual anomaly map from 21×21 Moving Average regional-residual separation with four slices

3.7. Validation with Previous Geological Studies

The continuous low-anomaly zone delineated from the residual maps strongly correlates with the established geological trace of the Palu-Koro Fault. By comparing our interpreted fault trace (dashed lines in the residual maps) with the surface rupture and seismicity distribution mapped by Natawidjaja et al. [3], a high degree of spatial agreement is observed. The pronounced gravity deficit precisely coincides with the highly deformed, multi-segment fault geometry associated with the 2018 Mw7.5 Palu earthquake. Furthermore, the structural lineaments derived from the gravity data align with the high slip-rate fault segments previously identified by Bellier et al. [17]. This corroborates that the low-density anomaly accurately represents the heavily fractured zone and sedimentary fill within the active fault structure, validating the effectiveness of the chosen separation methods without the strict necessity of secondary derivative filtering.

4. CONCLUSION

This study successfully mapped the subsurface structural characteristics of the Palu–Koro Fault zone using TOPEX satellite gravity data. The gravity data reduction process was based on an average surface rock density of 2.45 g/cm³, obtained through the Parasnis method. The application of this density value resulted in a Simple Bouguer Anomaly (SBA) map that accurately reflects geological variations within the study area. The resulting anomaly contour patterns indicate significant density contrasts between the fault deformation zone and the surrounding regional rocks.

Further analysis through regional and residual anomaly separation demonstrates a high degree of consistency between the second-order polynomial and Moving Average methods. The main trace of the Palu–Koro Fault is clearly identified as a low-anomaly zone, representing a fractured zone or low-density sedimentary rocks. In contrast, cross-sectional slicing analysis also reveals the presence of very high local anomalies adjacent to the fault trace. These positive anomalies are interpreted as responses from intrusive rock bodies or uplifted basement blocks associated with the complexity of tectonic activity in the region.

Overall, the gravity method is proven to be an effective geophysical approach for delineating geological structures in seismically active regions such as Central Sulawesi. The combination of applied anomaly separation techniques successfully separates shallow and deep anomaly responses, thereby enhancing geological interpretation. The mapping of subsurface density variations provides an important contribution to understanding fault geometry and earthquake-generating structures. These findings are expected to serve as a fundamental reference for disaster mitigation efforts and for the development of more detailed geophysical surveys in the future.

REFERENCE

[1] I. M. Watkinson and R. Hall, "Fault systems of the eastern Indonesian triple junction: Evaluation of Quaternary activity and implications for seismic hazards," Geol. Soc. Spec. Publ., vol. 441, no. 1, pp. 71–120, 2017, doi: 10.1144/SP441.8.

[2] I. Irawan, Y. Subiakto, and B. Kustiawan, "Manajemen Mitigasi Bencana Pada Pendidikan Anak Usia Dini untuk Mengurangi Risiko Bencana Gempa Bumi," PENDIPA J. Sci. Educ., vol. 6, no. 2, pp. 609–615, 2022, doi: 10.33369/pendipa.6.2.609-615.

[3] D. H. Natawidjaja et al., "The 2018 Mw7.5 Palu 'supershear' earthquake ruptures geological fault's multisegment separated by large bends: Results from integrating field measurements, LiDAR, swath bathymetry and seismic-reflection data," Geophys. J. Int., vol. 224, no. 2, pp. 985–1002, 2021, doi: 10.1093/gji/ggaa498.

[4] Supartoyo, C. Sulaiman, and D. Junaedi, "Kelas tektonik sesar Palu Koro, Sulawesi Tengah," J. Lingkung. dan Bencana Geol., vol. 5, no. 2, pp. 111–128, 2014.

[5] A. Cipta, R. Robiana, J. D. Griffin, N. Horspool, S. Hidayati, and P. Cummins, "A probabilistic seismic hazard assessment for Sulawesi, Indonesia," Geol. Soc. Spec. Publ., vol. 441, no. 1, pp. 133–152, 2017, doi: 10.1144/SP441.6.

[6] A. F. Lestari, N. T. Widayati, R. Rusman, S. Supriyadi, and K. Khumaedi, "Analisis Gaya Berat di Trangkil Gunungpati Semarang," J. Sains dan Edukasi Sains, vol. 3, no. 2, pp. 53–57, 2020, doi: 10.24246/juses.v3i2p53-57.

[7] R. J. Blakely, Potential Theory in Gravity and Magnetic Applications. 1995.

[8] A. K. Maimuna, A. F. Miftakhunnisa, and Y. A. Segoro, "Pemodelan Inversi 3 Dimensi untuk Identifikasi Dugaan Keberadaan Sesar menggunakan Data Anomali Gaya Berat di Laut Flores (Studi Kasus Gempa Flores 14 Desember 2021)," Prog. J. Geofis., vol. 1, no. 1, pp. 55–62, 2022, [Online]. Available: https://jurnal.stmkg.ac.id/index.php/pjg/article/view/260

[9] M. W. Firdaus, A. Setyawan, and M. Yusuf, "Identifikasi Letak dan Jenis Sesar Berdasarkan Metode Gayaberat Second Vertical Gradient Studi Kasus Sesar Lembang, Kota Bandung, Jawa Barat," Youngster Phys. J., vol. 5, no. 1, pp. 21–26, 2016.

[10] H. Syarifuddin and M. Yusuf, "Identifikasi Sebaran dan Jenis Sesar Lokal di Sekitar Sesar Waipoga Dengan Analisis Anomali Gravitasi," J. Teor. dan Apl. Fis., vol. 12, no. 02, pp. 97–108, 2024, doi: 10.23960/jtaf.v12i02.409.

[11] D. T. Sandwell, R. D. Müller, W. H. F. Smith, E. Garcia, and R. Francis, "New global marine gravity model from CryoSat-2 and Jason-1 reveals buried tectonic structure," Science (80)., vol. 346, no. 6205, pp. 65–67, 2014, doi: 10.1126/science.1258213.

[12] W. J. Hinze, R. R. B. von Frese, and A. H. Saad, Gravity and Magnetic Exploration. 2013.

[13] W. M. Telford, L. P. Geldart, R. E. Sheriff, and D. A. Keys, Applied-Geophysics. 1976.

[14] Muhardi, Nasharuddin, and Y. Prastika, "Identification of the Subsurface Structure Using Gravity method in Kasihan village, Pacitan Regency," in The 4th International Conference on Science and Technology (ICST, 2023, pp. 1–7).

[15] P. Kearey, M. Brooks, and I. Hill, An introduction to geophysical exploration. 1991.

[16] J. M. Reynolds, Second Edition and Environmental to Applied An Introduction Geophysics, no. 606. 2010.

[17] O. Bellier, L. Siame, T. Beaudouin, M. Villeneuve, and R. Braucher, "High slip rate for a low seismicity along the Palu-Koro active fault in Central Sulawesi (Indonesia)," Terra Nov., vol. 13, no. 6, pp. 463–470, 2001, doi: 10.1046/j.1365-3121.2001.00382.x.

Journal of Computation Physics and Earth Science
ISSN: 2776-2521 (online)
Volume 5, Number 2, February 2026, Page 227 - 231
https://journal.physan.org/index.php/jocpes/index

Deterministic Seismic Hazard Analysis (DSHA) and Peak Ground Acceleration Mapping in West Java (2018–2024)

Rayhan Irfan Hielmy[1]
[1]Undergraduate Program in Geophysics (STMKG)

Article Info

Article history:

Received December 25, 2025
Revised February 28, 2026
Accepted February 28, 2026

Keywords:

DSHA
PGA
West Java
BMKG Catalog
Megathrust

A B S T R A C T

West Java is a region with one of the most complex tectonic settings in Indonesia, influenced by the Sunda Megathrust subduction zone and an active inland fault system. This study aimed to estimate the Peak Ground Acceleration (PGA) values in the West Java region using a Deterministic Seismic Hazard Analysis (DSHA) approach with the Maximum of Maxima criteria. The data used is sourced from the BMKG earthquake catalog for the 2018–2024 period, which includes the most recent epicenter, hypocenter depth, and magnitude parameters. PGA calculations were performed using the Milne attenuation model for each grid point in the target area, followed by spatial interpolation using PyGMT software. The analysis results reveal a significant bimodal seismic hazard characteristic. An absolute maximum PGA value of 0.46 g was identified, triggered by a local shallow crustal earthquake with a magnitude of M 5.8 at a shallow depth within the inland region. Meanwhile, the southern coastal zone is dominated by the influence of a large Megathrust earthquake (M 8.7), although its shaking impact attenuates as it moves inland toward northern population centers. These findings confirm that while subduction sources possess greater energy potential, local active inland faults pose a more direct and destructive shaking threat to densely populated inland areas. The hazard map generated in this study is expected to serve as a crucial technical reference for resilient infrastructure planning and the updating of earthquake mitigation strategies in West Java Province.

Correspondent Author:

Rayhan Irfan Hielmy,
Undergraduate Program in Geophysics (STMKG)
Tangerang, Indonesia
Email: rayhanirfanhielmy@stmkg.ac.id

1. INTRODUCTION

West Java is one of the regions with the most complex seismic activity in Indonesia. This condition is triggered by active tectonic interactions between the Indo-Australian Plate, which subducts beneath the Eurasian Plate, forming the Sunda Megathrust zone in the south [1]. In addition to the threat from the subduction zone, the West Java mainland is also cut by various active fault systems, including the Cimandiri Fault, Lembang Fault, and Baribis Fault, which have the potential to trigger shallow crustal earthquakes with significant damage [2], [3], [4], [5]. As a result, this region has the potential for continuous seismic energy release, both from interplate and intraplate sources, which can produce significant ground acceleration [6].

Technically, the high frequency of seismic activity in West Java necessitates a measurable and up-to-date mapping of ground-shaking hazard potential. Earthquake catalog data covering the period 2018–2024 provide crucial information on the distribution of epicenters and hypocentral depths, which serve as the primary basis for evaluating the characteristics of seismic sources. The distribution of seismic activity in this region during that period can be observed in Figure 1, which shows a concentration of earthquake events along the subduction zone and active onshore faults. The accuracy of source location determination, as presented in the seismicity map, is critical for modeling wave propagation from bedrock to the surface through appropriate attenuation models [7].

This study applies the Deterministic Seismic Hazard Analysis (DSHA) method to estimate Peak Ground Acceleration (PGA) values across the entire West Java region. Unlike probabilistic approaches, DSHA focuses on deterministic scenarios derived from the most threatening seismic sources based on maximum magnitude and the shortest distance to the study site [8], [9]. While Probabilistic Seismic Hazard Analysis (PSHA) is widely utilized for national building codes, DSHA remains highly relevant for evaluating extreme, worst-case ground shaking scenarios for specific local critical infrastructure. In this baseline deterministic screening, the empirical Milne formulation was deliberately selected because it provides a conservative, generalized upper-bound hazard estimate across a mixed tectonic regime, without requiring the complex parameterizations of modern subduction or crustal-specific Ground Motion Prediction Equations (GMPEs). By utilizing the latest BMKG earthquake catalog and selecting relevant Ground Motion Prediction Equations (GMPEs), this research aims to produce a representative PGA hazard map to support infrastructure planning with adequate resistance to seismic dynamic loads. West Java's complex tectonic setting, characterized by the convergence of the Sunda Megathrust and various active inland faults, necessitates a detailed evaluation of seismic potential [10]. The deterministic approach remains a critical tool for infrastructure resilience by simulating the most extreme ground motion scenarios for specific sites [11].

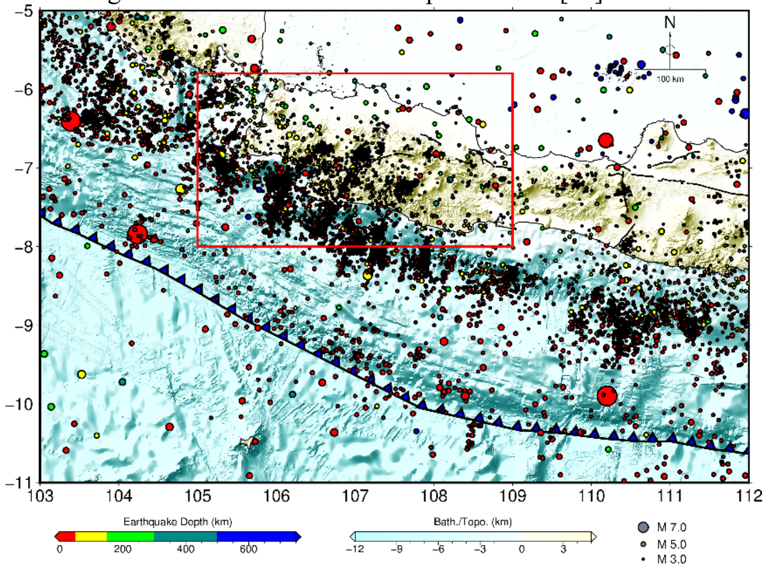

Fig. 1 Seismicity Map of West Java

2. RESEARCH METHOD

This study applies the Deterministic Seismic Hazard Analysis (DSHA) approach using the Maximum of Maxima criterion to determine the worst-case ground-shaking estimate. The research procedure systematically follows the stages presented in Figure 2, starting from data collection to the visualization of the final results. The primary data used consist of an earthquake catalog obtained from the Meteorology, Climatology, and Geophysics Agency (BMKG) for the observation period 2018–2024. This study utilized the updated seismic parameters and earthquake catalogs from BMKG to ensure accurate modeling of both subduction and crustal fault sources, following the latest seismotectonic research in the Indonesian region [12].

The boundaries of the seismic source region are defined within the coordinates 103°–112° E and 5°–11° S, encompassing subduction-related sources and onshore faults that tectonically influence West Java Province [1]. The seismic hazard calculation stage is conducted by dividing the target area into regular spatial grids with a resolution of 0.2 x 0.2 degree. The interpolation was performed using a continuous curvature algorithm in PyGMT. This study utilizes a historical-event DSHA approach directly over the 2018–2024 catalog without sequence declustering, focusing purely on identifying the extreme values. For each grid point, the Peak Ground Acceleration (PGA) value is estimated using an attenuation model or Ground Motion Prediction Equation (GMPE). In this study, the Milne Attenuation Model (Equation 1) is employed, which empirically calculates Peak Ground Acceleration (PGA) expressed in units of gravity (g) based on the earthquake moment magnitude (M) and the hypocentral distance (R) in kilometers [13].

$$PGA = 0.04e^{M}R^{-1.4} \tag{1}$$

In accordance with the workflow shown in Figure 2, the calculation process is performed for all earthquake events in the catalog at each observation point. The highest PGA value at each grid point is then selected as the representative deterministic scenario (Maximum of Maxima). While the inland hazard is predominantly evaluated based on the extreme values from the recent historical seismic records [8], [14], a deterministic worst-case scenario (Maximum Credible Earthquake) for the Sunda Megathrust (M 8.7) was explicitly incorporated into the model. This combination ensures that the resulting hazard map reflects both the direct threat of active crustal faults and the maximum potential energy release from the subduction zone. Finally, the spatial distribution of PGA values is digitally interpolated and visualized using PyGMT software to produce a precise seismic hazard contour map [15].

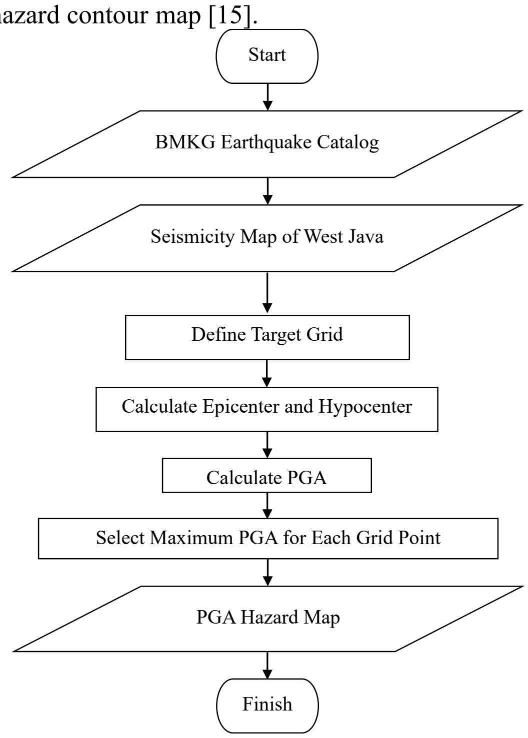

Fig. 2 Flowchart

3. RESULTS AND DISCUSSION

The interpolated PGA map for the West Java region shows heterogeneous seismic hazard characteristics influenced by two main earthquake sources, as presented in Figure 3. The spatial distribution of ground acceleration exhibits significant variation across the study area. The absolute maximum PGA value reaches 0.46 g, triggered by a local shallow earthquake with a magnitude of M 5.8 that occurred on 11 October 2020, with an epicenter located at approximately 108° E and 6.8° S. The concentration of high PGA values in the onshore area reflects the characteristics of shallow crustal earthquakes, which can produce strong ground shaking at local scales despite their relatively moderate magnitudes. From an engineering risk perspective, an absolute maximum PGA of 0.46 g is critical as it can exceed the design basis earthquake standards for typical residential structures, reflecting the massive structural failures seen during recent moderate-magnitude events like the 2022 Cianjur earthquake [3]. The calculated PGA values in these areas often pose a higher immediate threat to urban centers compared to distant megathrust events, as reflected in the recent seismic hazard assessments for Java Island [16].

Meanwhile, the high-hazard zone extending along the southern coast of West Java is controlled by a deterministic worst-case scenario of a Megathrust earthquake with a Maximum Credible Earthquake (MCE) magnitude of M 8.7, modeled at a potential source coordinate of 104.2° E and 7.8° S. The accumulation of PGA contours in this southern region confirms the significant hazard potential associated with the Sunda subduction zone [17]. These results emphasize that seismic risk in West Java is governed by two distinct sources: local shallow crustal earthquakes on land and subduction earthquakes originating from the Megathrust zone.

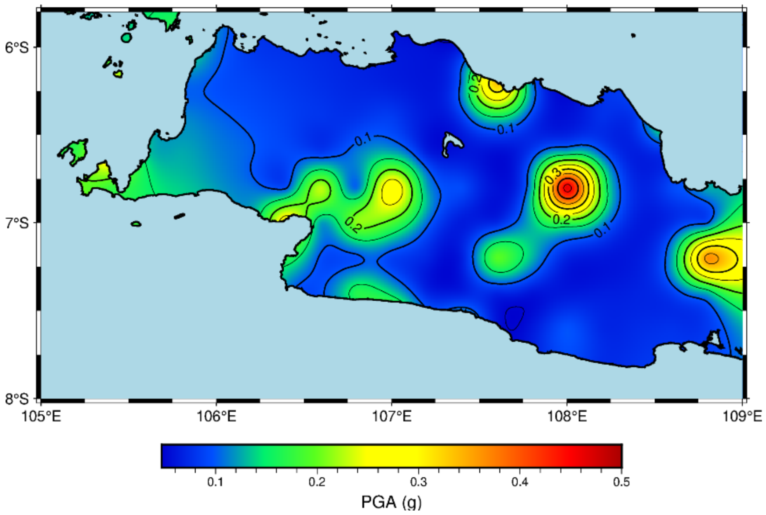

Fig. 3 PGA Hazard Map

The results of the DSHA analysis indicate a bimodal seismic hazard characteristic in the West Java region. The effect of distance is clearly illustrated in Figure 4, where despite the Megathrust earthquake releasing very large amounts of energy (M 8.7), its ground-shaking impact weakens toward inland areas due to the relatively large distance between the earthquake source and population centers in the northern part of the region. This attenuation phenomenon is consistent with the inverse square law in attenuation models, in which seismic energy decreases with increasing wave propagation distance [18].

In contrast, the smaller-magnitude shallow local earthquake (M 5.8) dominates by producing an absolute maximum ground acceleration of 0.46 g in inland areas, primarily due to its proximity to the surface or very shallow hypocentral depth. This finding indicates that shallow crustal faults pose a more direct and potentially more hazardous ground-shaking threat to inland urban areas compared to distant subduction sources [7]. The implications of the results shown in Figure 4 suggest that building and infrastructure planning in West Java should not only consider the potential impact of Megathrust earthquakes, but must also pay close attention to active onshore faults, which often have shorter recurrence intervals and highly destructive local effects [2].

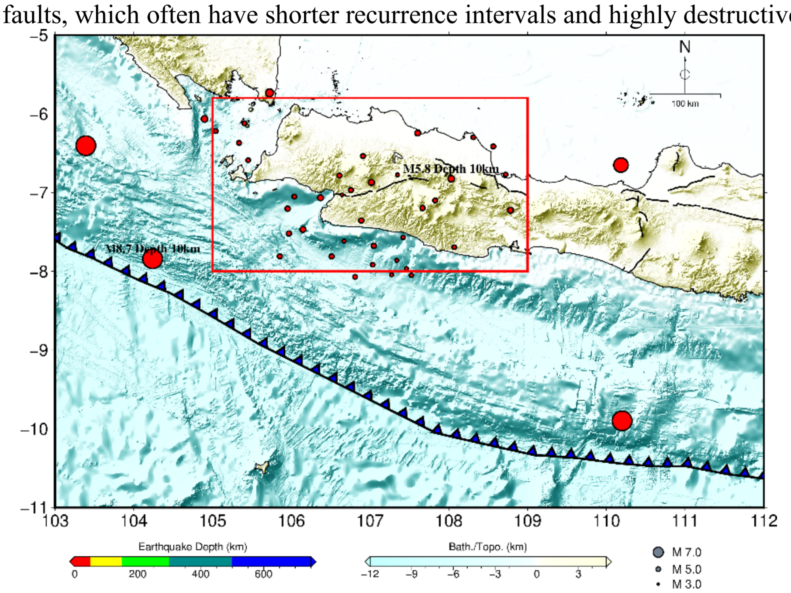

Fig. 4 Map of Maximum Credible Earthquake (MCE)

4. CONCLUSION

This study successfully maps the potential ground-shaking hazard in West Java using the Deterministic Seismic Hazard Analysis (DSHA) approach based on the latest earthquake catalog for the 2018–2024 period. The analysis results indicate that the West Java region exhibits bimodal seismic hazard characteristics, influenced by the Sunda Megathrust subduction zone in the southern part of the region and active onshore fault systems inland. Although the Megathrust source has the potential to generate much larger magnitudes, reaching up to M 8.7, the resulting ground acceleration tends to attenuate as it propagates toward inland areas due to the large hypocentral distances involved.

The main findings show that the absolute maximum Peak Ground Acceleration (PGA) of 0.46 g is instead triggered by a moderate-magnitude shallow crustal earthquake (M 5.8). This result emphasizes that the proximity of the seismic source to the ground surface plays a more dominant role in producing destructive ground shaking than a large earthquake magnitude originating from a distant source. Consequently, the hazard map produced in this study provides an important warning that inland and urban areas in West Java are subject to high risk from local ground shaking generated by active fault systems distributed across the region.

The resulting PGA hazard map is expected to serve as a technical reference for infrastructure planning and the updating of earthquake-resistant building standards in West Java Province. The integration of recent seismicity data with the Milne attenuation model provides a more realistic worst-case scenario for targeted disaster mitigation efforts. Risk-based spatial planning should therefore prioritize structural reinforcement in areas with high PGA values to minimize potential losses in the future. The results of this DSHA mapping provide a technical basis for updating local building codes and align with the national efforts to develop the latest Indonesian Seismic Hazard Maps for better disaster mitigation [19].

REFERENCE

[1] PuSGeN, Buku Peta Sumber dan Bahaya Gempa Indonesia Tahun 2024. Jakarta: Kementerian Pekerjaan Umum, 2024.

[2] Z. Zulfakriza et al., “Seismic source analysis of the destructive earthquake Cianjur (Indonesia) from relocated aftershock Seismic source analysis of the destructive earthquake aftershock,” Sci. Rep., vol. 14, no. 1, p. 12142, 2024.

[3] P. Supendi et al., “Analisis Gempabumi Cianjur (Jawa Barat) Mw 5.6 Tanggal 21 November 2022,” Badan Meteorologi, Klimatologi, dan Geofis., pp. 1–4, 2022.

[4] P. Supendi and R. Purbayan, “Analysis of Local Active Faults in Western Java from Hypocenter Relocation Using BMKG Data,” vol. 21, no. 01, pp. 2016–2018, 2023.

[5] N. Sari, M. S. Rosida, and T. Anggonob, “Double Difference Hypocenter Relocation and Velocity Model Determination in Western Java 2010 - 2024 for Fault Identificat,” Positron, vol. 15, no. 01, pp. 81–93, 2025, doi: 10.26418/positron.v15i1.91097.

[6] R. Tauhidur and R. L. Chhangte, “Estimation of Peak Ground Acceleration (PGA) and Spectral Acceleration (Sa) Vertical Component for Interface Subduction Zone Earthquakes of Northeast India (NEI) and Adjacent Regions,” Res. Sq., 2021.

[7] J. Nugraha, G. Pasau, B. Sunardi, and S. Widiyantoro, “Analisis Hazard Gempa dan Isoseismal untuk Wilayah Jawa–Bali–NTB,” J. Meteorol. dan Geofis., vol. 15, no. 1, pp. 1–11, 2014.

[8] G. Aglia, M. Wijaya, and P. P. Rahardjo, “The Study of Seismic Hazard in Near-Fault Areas Using Probabilistic and Deterministic Approach,” J. Civ. Eng. Forum, vol. 9, no. 2, pp. 117–126, 2023, doi: 10.22146/jcef.5469.

[9] W. E. Prasetyo, L. Y. Irawan, R. Hartono, and E. Budi, “Seismic hazard analysis using Deterministic Seismic Hazard Analysis (DSHA) Method : A case study in Southern Malang District , East Java,” J. Pendidik. Geogr., vol. 28, no. 2, pp. 209–227, 2023, doi: 10.17977/um017v28i22023p209-227.

[10] P. Supendi, A. D. Nugraha, N. T. Puspito, S. Widiyantoro, and D. Daryono, “Identification of active faults in West Java , Indonesia , based on earthquake hypocenter determination , relocation , and focal mechanism analysis,” Geosci. Lett., vol. 31, pp. 4–10, 2018, doi: 10.1186/s40562-018-0130-y.

[11] R. Silvianis and L. Dwiridal, “Estimation of Earthquake Intensity and Peak Ground Acceleration in West Java Using the MC Guire and the Lin & Lee Method,” KAPPA J., vol. 8, no. 3, pp. 331–337, 2024.

[12] P. Supendi, A. Muhari, and N. Rawlinson, “Potential megathrust earthquakes and tsunamis off the southern coast of West Java , Indonesia,” Res. Sq., pp. 1–9, 2020.

[13] J. Douglas, Ground Motion Prediction Equations. 2022.

[14] S. L. Kramer, Geotechnical Earthquake Engineering. Upper Saddle River, New Jersey: Prentice Hall, 1996.

[15] P. Wessel et al., “The Generic Mapping Tools Version 6,” Geochemistry, Geophys. Geosystems, vol. 20, no. 11, pp. 5556–5565, 2019, doi: 10.1029/2019GC008515.

[16] M. Irsyam, M. Asrurifak, Hendriyawan, B. Budiono, W. Triyoso, and A. Firmanti, “Development of spectral hazard maps for a proposed revision of the Indonesian Seismic Building Code,” Geomech. Geoengin., vol. 5, no. 1, pp. 35–47, 2010, doi: 10.1080/17486020903452725.

[17] PuSGeN, Pusat Studi Gempa Nasional (Indonesia)Pusat Penelitian dan Pengembangan Perumahan dan Permukiman (Indonesia). 2017.

[18] J. Douglas, “Ground-motion prediction equations 1964–2010,” Berkeley: Pacific Earthquake Engineering Research Center, 2011.

[19] M. Irsyam et al., “Development of the 2017 national seismic hazard maps of Indonesia,” Earthq. Spectra, vol. 36, no. 1, pp. 112–136, 2020, doi: 10.1177/8755293020951206.

Journal of Computation Physics and Earth Science
ISSN: 2776-2521 (online)
Volume 5, Number 2, February 2026, Page 232 - 243
https://journal.physan.org/index.php/jocpes/index

Solar Radiation Computation from Satellite Weather Data in Batam Using Linear Regression, Random Forest, and Decision Tree

Prayoga Pandapotan Simanjuntak[1], Marzuki Sinambela[2]
[1,2]Undergraduate Program Applied Instrumentation Meteorology Climatology and Geophysics (STMKG)

Article Info

Article history:

Received December 31, 2025
Revised February 28, 2026
Accepted February 28, 2026

Keywords:

Solar Radiation
Weather Forecast
Regression Model
Machine Learning
Linear Regression
Random Forest
Decision Tree
Satellite Data
Renewable Energy
Batam City

A B S T R A C T

This study addresses the necessity of evaluating solar radiation as a renewable energy source in tropical regions, specifically focusing on the challenges of estimation in Batam. The objective is to model daily solar radiation levels using satellite-derived weather data to overcome the lack of surface observation stations. Daily meteorological variables, including air temperature, relative humidity, rainfall, surface pressure, and wind speed, were sourced from the NASA POWER platform for the period January 1, 2020, to July 2, 2025. To ensure robust model generalization and prevent data leakage, the dataset was partitioned chronologically, utilizing data from 2020–2024 for training and the year 2025 for independent testing. Three computational models Linear Regression (LR), Random Forest (RF), and Decision Tree (DT) were applied to the processed data. The evaluation results indicate that the Random Forest model achieved the highest relative performance among the tested algorithms, recording a Mean Squared Error (MSE) of 19.61, a Mean Absolute Error (MAE) of 3.42, and a coefficient of determination R^2 of 0.20. In comparison, the Linear Regression model produced an R^2 of 0.19, while the Decision Tree showed significantly lower predictive accuracy. Despite being the most viable model, an R^2 of 0.20 reveals that the current predictors explain only 20% of the variance in solar radiation, highlighting the inherent complexity of tropical atmospheric dynamics. These findings suggest that while machine learning offers a promising framework for energy planning in Batam, further research incorporating additional explanatory features, such as cloud cover or aerosol indices, is required to improve model reliability.

Corresponden Author:

Prayoga Pandapotan Simanjuntak
Undergraduate Program Appllied Instrumentation Meteorology Climatology and Geophysics (SMKG)
Tangerang, Indonesian
Email: prayogapandapotan@gmail.com

1. INTRODUCTION

Solar radiation serves as the primary source of energy for the Earth and plays an essential role in many environmental and climatic processes [1]. Even slight variations in the amount of solar energy reaching the Earth's surface can lead to significant climatic impacts. Therefore, obtaining accurate estimates of solar radiation is crucial for designing, planning, and evaluating systems used to harness solar energy resources [2]. However, in many regions, particularly in developing countries, ground-based solar radiation measurement stations are still limited in number and spatial coverage [3]. This limitation has encouraged the development of alternative estimation approaches, including physical empirical models and data-driven methods that utilize other meteorological parameters to estimate solar radiation [3].

Indonesia receives relatively high solar radiation, with an average potential of approximately 4.8 kWh/m²/day, making it a promising region for the development of renewable solar energy [4]. Despite this potential, the utilization of solar energy in Indonesia remains relatively low. In areas with limited observational infrastructure, researchers often rely on secondary datasets such as NASA POWER. This satellite-based dataset provides long-term, consistent meteorological and radiation data and has become an important data source for estimating solar energy potential in locations lacking direct radiation observations [3].

Various computational approaches have been developed to predict solar radiation. In recent years, machine learning techniques have gained increasing attention due to their capability to capture complex and non-linear relationships among meteorological variables [5]. Numerous algorithms have been applied in solar radiation studies, including Random Forest, Neural Networks, Support Vector Regression, Decision Trees, Bagging methods, as well as deep learning architectures such as CNN, RNN, and LSTM, often combined with boosting techniques [5]. For instance, Fan et al. reported that machine learning models can achieve better predictive accuracy than traditional empirical approaches for daily solar radiation estimation [2]. Similarly, studies conducted in Türkiye utilized NASA POWER data to train and compare several deep learning and boosting models such as LSTM, GRU, XGBoost, and Random Forest for solar radiation prediction. However, many of these studies focus on specific geographic locations and do not fully consider the performance of prediction models in complex tropical maritime environments [6].

Although machine learning models such as Linear Regression, Decision Tree, and Random Forest have been widely applied in solar radiation studies, their performance in tropical coastal regions such as Batam remains relatively underexplored. Batam is characterized by high humidity, frequent cloud formation, and strong seasonal variability, which may significantly influence solar radiation patterns. Understanding the capability of machine learning models in such environments is important for supporting renewable energy planning in regions with limited observational data.

Therefore, this study aims to evaluate the performance of several classical machine learning models Linear Regression, Decision Tree, and Random Forest in approximating satellite derived solar radiation in Batam using meteorological variables obtained from the NASA POWER dataset. Batam, located in the tropical region of Indonesia, is estimated to have high solar radiation potential, yet direct radiation measurements in this area remain limited. In this study, NASA POWER meteorological data are processed using Python to develop predictive models, and the performance of each method is evaluated using standard regression metrics. The results of this research are expected to provide insights into the applicability and limitations of machine learning approaches for solar radiation prediction in tropical coastal environments, while also contributing useful information for solar energy development and climate mitigation planning in the region.

2. RESEARCH METHOD

This research was conducted through six main steps that were structured to make predictions. The first step involved collecting and cleaning data consisting of air temperature, relative humidity, rainfall, surface pressure, wind speed, and time data. The data was examined to ensure that there were no missing values, duplicates, or outliers that could affect the model results. During the data pre-processing phase, we transitioned from a random split to a chronological data splitting strategy to respect the temporal and seasonal characteristics of the meteorological variables [8]. Specifically, data from January 2020 through December 2024 was used for model training, while the period from January 2025 to July 2025 was reserved for testing. This approach prevents data leakage and ensures the model is evaluated on its ability to generalize to future conditions. In the subsequent data exploration phase, visualizations such as scatter plots and correlation matrices were employed to analyze the relationship patterns between features and the target variable. The analysis confirmed that temperature has a positive relationship with solar radiation, while humidity and rainfall exhibit negative correlations [8].

The next step is machine learning modelling, applying three algorithms: Linear Regression as the base model, Decision Tree to capture non-linear patterns, and Random Forest to improve accuracy using ensemble techniques. Model evaluation was performed using the MAE, MSE, and R^2 metrics. To strengthen the analysis, visualization of the prediction results was performed, including a comparison graph between the predicted and observed values. This served to assess how well the model could reflect the actual data. The last step was the interpretation and analysis of the results, which compared the performance of each model scientifically [2].

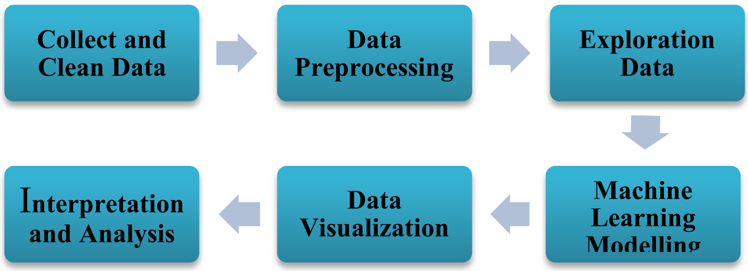

Fig 1. Research Flow

Data Source

The data used in this study was obtained from NASA's POWER (Prediction of Worldwide Energy Resource) platform, which is a global database for reprocessing meteorological and solar radiation information [7]. The NASA POWER dataset provides daily data with international coverage, including variables related to solar radiation and important weather elements. For the case study in Batam City (Riau Islands Province, Indonesia), information was downloaded for coordinates 1.1288° N, 104.0403° E. BT (Batam is at 1.13°N, 104.04°E) for the period from January 1, 2020, to July 2, 2025. The primary variables included are daily solar radiation irradiance at the surface in units of MJ/m²/day, as well as other weather variables such as air temperature, relative humidity, precipitation, surface pressure, and wind speed [7]. One advantage of NASA POWER data is that it provides data for specific locations like Batam. However, it is important to note that model-based reanalysis data (such as MERRA-2 and CERES) may have gaps or inaccuracies, especially in tropical regions with limited field observations [7]. Therefore, before modelling, data cleaning and transformation are necessary to ensure the consistency and completeness of the dataset.

Data processing was performed using Jupyter Notebook with Python programming. Some of the main steps in data processing include:

- Data Download and Division: The large NASA POWER dataset was downloaded based on annual periods (2020–2025) to facilitate file management. Each CSV file stores daily data from that year.
- Initial Reading and Inspection: CSV files were opened and inspected using the panda’s library in Python. The column structure was checked, including the header rows and extreme values (-999 indicates missing data as noted in the metadata).
- Date Conversion: The original data displayed the time in the “YEAR” and “DOY” (day-of-year) columns. We use a Python function to combine YEAR and DOY into a standard date format (YYYY-MM-DD). Then, the time information is expanded by adding separate columns for Month and Day so that seasonal or daily analysis can be performed in more detail.
- Missing Data Handling: Missing or invalid values in the NASA POWER dataset are represented by the placeholder value −999. In this study, these values were first identified and converted into missing entries (NaN). Subsequently, all records containing missing values were removed from the dataset to maintain data consistency and avoid potential bias in the machine learning models. After the cleaning process, the dataset was re-examined to ensure that no missing values remained before proceeding to the modelling stage.
- Data Reorganization: After the data is cleaned and formatted, it is reorganized based on time ranges (e.g., monthly) according to the model's requirements. This process enables more efficient visualization and modelling.

These data preparation steps within the Python ecosystem in Jupyter Notebook provide significant flexibility. The final processed data is then used in the development of predictive models such as linear regression, Random Forest, and Decision Tree. Thus, the data processing and transformation workflow ensures high-quality input for the model, in line with recommendations in the literature on the use of satellite data for renewable energy analysis [7].

Feature Selection

Feature selection is an especially crucial step in developing models for predicting solar radiation, as it can improve the accuracy and effectiveness of the model. By selecting relevant features and removing fewer valuable ones, the complexity of the model can be reduced, thereby reducing the risk of overfitting and speeding up processing time. Good feature selection also ensures that the model only learns from attributes that truly contribute to solar radiation, resulting in improved prediction accuracy. Conversely, irrelevant, or noisy features can degrade model performance. Therefore, the feature selection process is crucial for selecting input variables before model creation [8].

This step aims to convert temporal data into numerical features that can be used by the model. For example, information about the month can capture the seasonal impact of sunlight throughout the year. All the features mentioned earlier are then entered into the model without any being removed, as initial analysis shows that each feature contributes useful information for predicting solar radiation. No features were completely removed from the dataset, as no features were statistically proven to be irrelevant after correlation checks and feature importance assessments [8].

Table 1. Main features considered for the proposed models.

Feature	Significance	Impact
Date (YEAR/DOY)	The combination of year and day-to-n (Day of Year) serves as a time marker that captures seasonal and annual radiation trends.	The addition of time features allows the model to recognize periodic patterns (dry season, rainy season) and long-term trends such as climate change, improving the accuracy of temporal predictions.
Solar Radiation ($MJ/m^2/day$)	Main target/output. Indicates the amount of daily irradiance received by the surface in units of $MJ/m^2/day$.	This is the variable predicted by the model. Its value is strongly influenced by atmospheric factors such as clouds, water vapor, and particles.
Air Temperature (°C)	Describes the average daily air temperature at a height of 2 meters. Affects atmospheric dynamics and surface warming.	Temperature is an important indicator in convection processes and cloud formation, which influence radiation reduction or reflection. This helps the model relate thermal energy fluctuations with daily radiation.
Relative Humidity (%)	Air humidity at 2 meters above the surface. Reflects the water vapor content that affects light transmission and scattering.	High humidity leads to more cloud formation and radiation scattering effects, especially in tropical regions. This feature helps the model predict radiation decreases on cloudy or rainy days.
Rainfall (mm/day)	Corrected precipitation amount in mm/day. Precipitation is strongly correlated with cloud formation and reduced radiation reaching the surface.	Rainfall acts as an indirect predictor of cloud density. This feature allows the model to capture extreme events such as heavy rainfall that significantly reduce radiation values.
Surface Pressure (kPa)	Atmospheric pressure at the surface in kPa. Influences air density and its ability to absorb and reflect radiation.	Pressure fluctuations indicate weather changes (e.g., storms or local convergence). This helps the model detect unstable atmospheric conditions affecting radiation intensity.
Wind Speed (m/s)	Wind speed measured at a height of 2 meters. Wind plays a role in distributing clouds, water vapor, and aerosols in the atmosphere.	Strong winds can disperse clouds or transport moisture to other areas, influencing sky clarity. This feature helps detect sudden weather variations that affect solar radiation.

Research Model

Linear Regression (LR)

Linear regression is a statistical method for analysing and modelling the relationship between one dependent variable and one or more independent variables. The basic purpose of this analysis is to predict the value of the dependent variable using the values of the independent variables. This is achieved by identifying the linear equation that best fits the observed data, reducing the difference between the predicted values and the actual values [8]. This study uses multiple linear regression with the multiple regression equation:

$$Y = b_0 + b_1X_1 + b_2X_2 + \cdots + b_pX_p \tag{1}$$

Explanation:
Y = dependent variable
b_0 = constant
$b_1 = b_2 = \cdots = b_P$ = regression coefficient
$X_1 = X_2 = \cdots = X_P$ = independent variable

Where the prediction variable is solar radiation as the dependent variable, and the predictor or independent variables are air temperature, relative humidity, rainfall, surface pressure, and wind speed.

Decision Tree Regressor

The Decision Tree Regressor builds the model by partitioning the data into subsets that minimize the variance of the target variable. The splitting criterion used is the reduction in Mean Squared Error (MSE), defined as:

$$MSE = \frac{1}{N}\sum_{i=1}^{N}(y_i - \bar{y})^2 \tag{2}$$

where N is the number of samples in the node, y_i is the actual value, and $\bar{y}$ is the mean of the target variable within that node.

Random Forest Regressor

The random forest model is the most popular technique for regression and classification in decision tree learning. This model is very efficient, and, at the same time, its regression accuracy is better than other regression methods. This random model builds many interconnected decision trees in the training phase. After developing several decision trees, the output of the model is obtained by averaging the output values of all individual trees [11].

$$Q = \frac{1}{n}\sum_{i=1}^{n}(y_i - y) \tag{3}$$

Where:

$$y = \frac{1}{n}\sum_{i=1}^{n}(y_i) \tag{4}$$

Explanation:
n = number of data points
y_i = response value
y = predicted value at the node (average response value)

Hyperparameter Configuration

A machine learning algorithm's ability to identify patterns in the data is influenced by hyperparameters, which are crucial parameters that are set prior to training. Appropriate hyperparameter selection enhances predictive models' capacity for generalization and helps balance the bias-variance trade-off [12].

The Scikit-learn Python library was used to implement the machine learning models in this study. The models were run using the default hyperparameter configuration supplied by the Scikit-learn implementation in order to provide a consistent and equitable comparison among the assessed algorithms. This method is frequently used in baseline machine learning research to assess various algorithms' intrinsic prediction power without requiring a lot of hyperparameter adjustment.

As a foundational statistical model, the Linear Regression model was used. In the meantime, potential non-linear correlations between solar radiation and meteorological variables including temperature, humidity, rainfall, pressure, and wind speed were captured using tree-based algorithms like Decision Tree and Random Forest. While the Decision Tree model offers a clear framework for comprehending the connection between predictor variables and solar radiation, the Random Forest model functions as an ensemble learning technique that integrates several decision trees to increase prediction stability through averaging.

Table 2. Hyperparameter configuration of the machine learning models

Models	Hyperparameter	Value	Description
Linear Regression	parameters	default (Scikit-learn)	Baseline linear regression model
Decision Tree	parameters	default (Scikit-learn)	Tree-based regression model
Random Forest	parameters	default (Scikit-learn)	Ensemble regression model

Model Evaluation Criteria

First, compare solar radiation data with air temperature, relative humidity, rainfall, surface pressure, and wind speed data. Plot graphs to help understand and visualize exactly how the available data sets are related. To maximize model performance, minimize the predefined loss function and achieve better results with fewer errors by tuning hyperparameters [12].

Mean square error (MSE) is the simplest function that can be calculated in machine learning. MSE takes the difference between the model's prediction and the actual data or ground truth, squares it, and applies the average across the entire dataset [13][14]. MSE will never be negative with the formula (2)
Explanation:
N = number of data points
y_i = actual data value
y = predicted data value

The mean absolute error (MAE) is a model prediction performance indicator, which is achieved by observing how close the predicted variable is to the observed variable [13]:

$$MAE = \frac{1}{N}\sum_{i=1}^{N}|y_i - y| \tag{5}$$

Explanation:
N = number of data points
y_i = actual data value
y = predicted data value

R^2 is a value that shows how much the independent variable (exogenous) affects the dependent variable (endogenous) [12]. With the formula:

$$R^2 = 1 - \frac{\sum(y_i - \hat{y}_i)^2}{\sum(y_i - y)^2} \tag{6}$$

Explanation:
y_i = actual observed value
$\hat{y}_i$ = predicted value
$\bar{y}$ = mean of observed values

R^2 represents the proportion of variance in the dependent variable that can be explained by the independent variables.

3. RESULT AND DISCUSSION

Data Analysis

Table 3 presents a summary of descriptive statistics for the meteorological variables used in modelling daily solar radiation predictions. The parameters shown include maximum, minimum, average, and standard deviation values, which describe the distribution and diversity of data within the observation range [13].

Table 3. Model Evaluation Summary

Parameters	Max	Min	Mean	Sdt
Solar radiation (MJ/m²/day)	24.96	1.15	17.39	4.85
Air Temperature (°C)	30.18	25.61	28.13	0.88
Relative Humidity (%)	92.43	70.64	81.95	3.61
Rainfall (mm/day)	255.88	0.00	12.01	17.61
Surface Pressure (kPa)	101.30	100.50	100.84	0.13
Wind Speed (m/s).	6.77	0.66	3.02	1.04

The target variable, Solar Radiation, shows a maximum value of 24.96 MJ/m²/day and a minimum value of 1.15 MJ/m²/day, with an average of 17.39 MJ/m²/day and a standard deviation of 4.85. The significant standard deviation indicates a notable daily variation in the intensity of solar radiation received by the Earth's surface. This reflects that the dataset encompasses a range of weather conditions, from very sunny days to days with heavy cloud cover or overcast skies. Air temperature exhibits a more consistent distribution, with an average value of 28.13°C and a standard deviation of only 0.88. The temperature ranges from 25.61°C to 30.18°C indicates that the observation location is in a tropical climate with small daily temperature variations.

This temperature consistency may influence the stability of solar radiation, as temperature is related to atmospheric conditions such as cloud density and sky clarity.

Relative humidity is also within a narrow range, with an average of 81.95% and a standard deviation of 3.61. This indicates that humidity tends to be high and stable, as is typically the case in tropical regions with high air humidity throughout the year. On the other hand, the Rainfall variable shows a very uneven distribution, with a minimum value of 0 mm/day and a maximum of 255.88 mm/day, and a standard deviation of 17.61. This indicates extreme conditions in the dataset, ranging from dry days to heavy rainfall. This is important to note because high rainfall is negatively correlated with solar radiation intensity due to increased cloud cover.

Air surface pressure shows extraordinarily slight variation, with an average of 100.84 kPa and a standard deviation of only 0.13. This indicates that atmospheric pressure changes in the study area are stable, reflecting geographical conditions without extreme topographical or climatic fluctuations. Meanwhile, wind speed has an average of 3.02 m/s with a standard deviation of 1.04. The range of values from 0.66 to 6.77 m/s indicates moderate variation in this parameter. Although not a direct factor influencing radiation values, wind speed can affect cloud distribution and thus influence the amount of radiation reaching the surface. Overall, this descriptive statistical information provides important insights into the characteristics of the data used in modelling. Variability among variables should be considered during the preprocessing stage and in selecting a model capable of addressing high data variability, especially for variables with large fluctuations such as rainfall and solar radiation itself.

Feature-Target Relationship Analysis

To gain insight into how each input variable affects solar radiation values, scatter plots were created to show the relationship between each feature and the target. The results of these graphs provide an initial understanding of the type of interaction (linear, non-linear, or irregular) between the input variables and the predicted results.

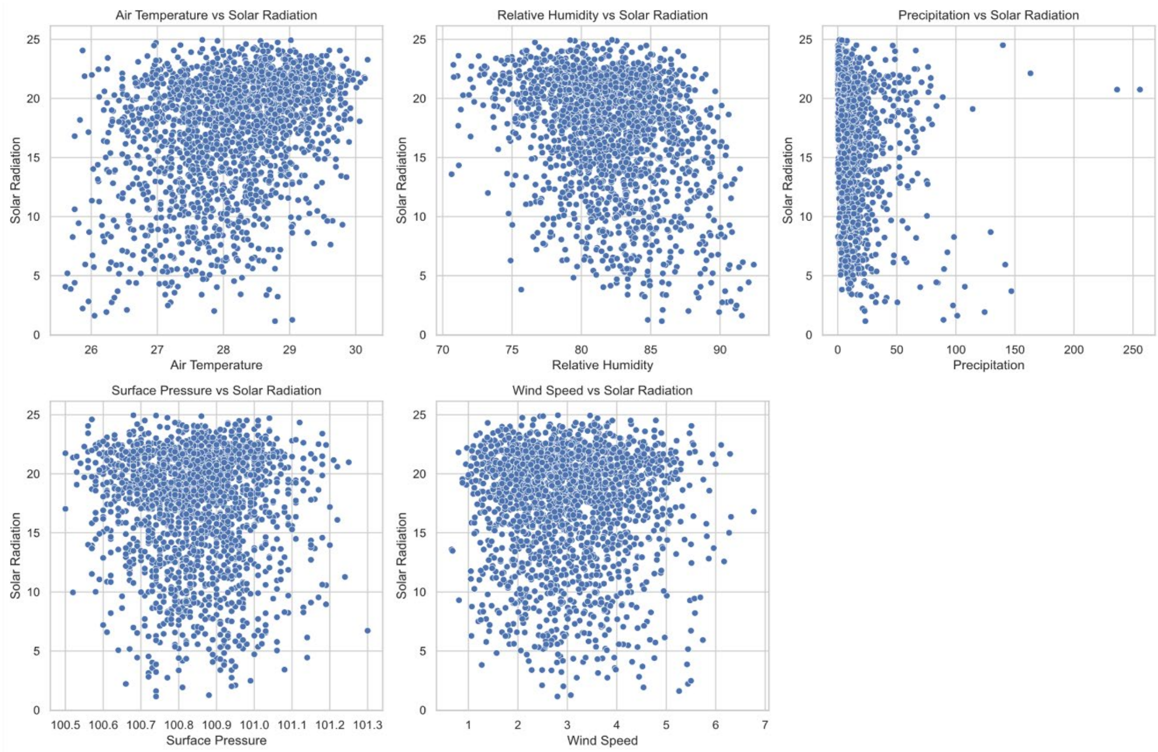

Fig 2. Feature-Target Relationships

Air temperature shows a positive semi-linear relationship with solar radiation, which is consistent with meteorological theory, whereby sunny days tend to have higher temperatures and higher solar radiation. Although this relationship is consistent with a linear model, a non-linear approach may still provide improvements, especially in extreme conditions. Relative humidity shows a non-linear inverse relationship with solar radiation. High humidity, often associated with clouds or fog, is associated with a decrease in solar radiation reaching the surface. This non-linearity suggests that models such as Decision Tree or Random Forest are more effective in describing this dynamic.

Rainfall exhibits a unique threshold effect: solar radiation remains high under dry conditions but decreases sharply even with minimal rainfall. This discontinuous nonlinear pattern underscores the need for flexible modelling methods capable of addressing sudden changes in response behaviour. In this case, wind speed and surface pressure do not show clear or consistent patterns with solar radiation. While there are some noticeable trends, such as a decrease in radiation under exceptionally low or high wind conditions, these variables have limited predictive capability when considered individually, although their importance in multivariate interactions requires further investigation using model-based importance metrics.

Correlation Analysis

To evaluate the linear relationship between variables, a correlation matrix is constructed and displayed via a heat map. This matrix quantitatively shows the extent to which one variable is linearly related to another, measured using Pearson's correlation coefficient, which varies from -1 to 1. Positive values indicate a direct relationship, while negative values indicate an inverse relationship. The explanation below highlights the main patterns related to solar radiation modelling [15].

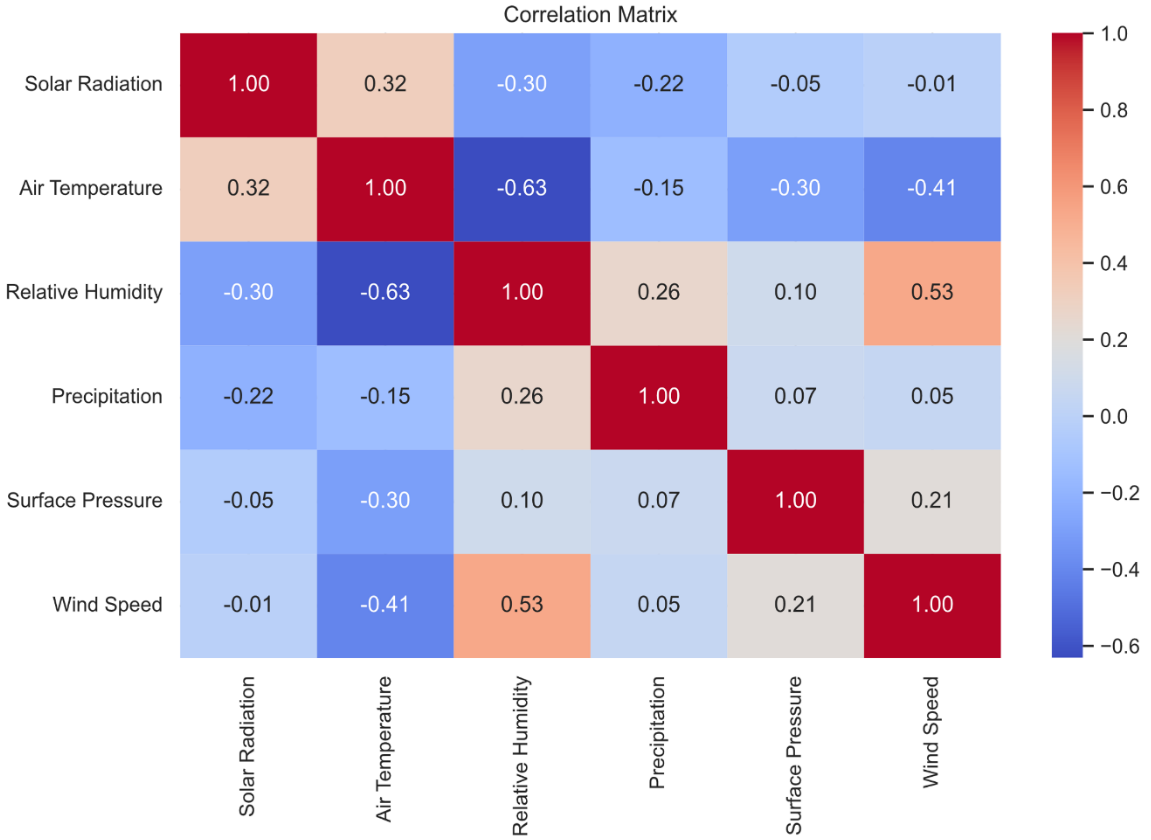

Fig 3. Correlation Matrix

Of all the features available, air temperature shows the highest positive correlation with solar radiation. This is in line with the principle of physics which states that sunny conditions when sunlight reaches its peak often occur simultaneously with higher temperatures. This confirms the role of temperature as the main predictor in solar radiation estimation models. Meanwhile, relative humidity was found to be negatively correlated with solar radiation. This association is intuitive: increased humidity is typically associated with the presence of clouds or rain, both of which contribute to a reduction in the amount of solar energy received. Therefore, relative humidity not only acts as a direct modifier of solar radiation but also as an indicator of atmospheric clarity.

Precipitation also shows a moderate negative correlation with solar radiation. Although the strength of this correlation is lower than that of humidity, there is still an indication that rainy conditions are associated with lower solar radiation. This makes precipitation a valuable element, especially in models designed to manage non-linear changes and sudden shifts. Surface pressure and wind speed have a weak or negligible correlation with solar radiation. However, their role should not be entirely ignored; in the context of specific local meteorological systems or when interacting with other variables, they can contribute marginally to improving prediction accuracy.

Research Results

This study aims to estimate solar radiation on the surface of Batam City using regression-based machine learning methods. The dataset includes daily meteorological variables such as year, date, air temperature, relative humidity, atmospheric pressure, rainfall, and wind speed, with solar radiation as the target variable. The data underwent a preprocessing and cleaning stage to ensure the quality and consistency of the input variables before model training.

Considering the temporal nature of meteorological data, the dataset was divided using a chronological split rather than random sampling. Data from earlier years were used for model training, while the most recent portion of the dataset was reserved for testing. This approach prevents data leakage and better reflects real-world forecasting scenarios, where models are trained using historical data and evaluated on future observations [1].

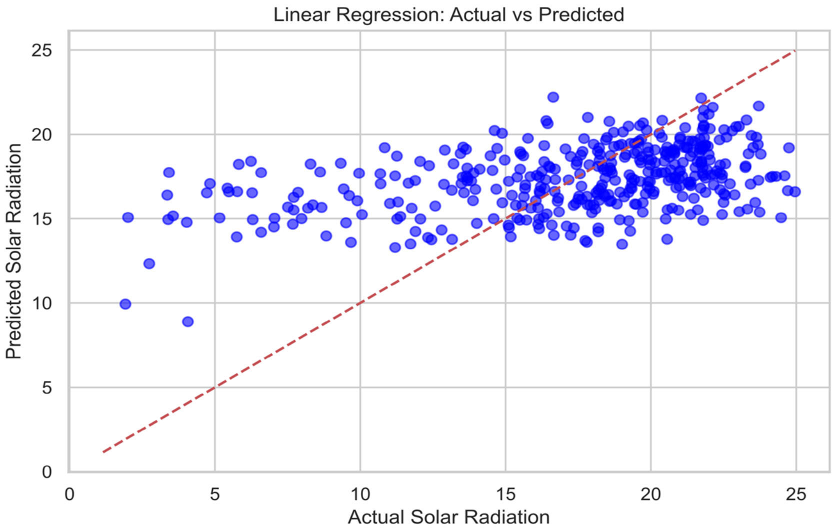

Fig 4. Actual Solar Radiation vs Predicted Solar Radiation Model Linear Regression

The relationship between the actual values and the predicted values in Fig. 4 has an MSE value of 19.78, a MAE value of 3.47, and an R^2 value of 0.19. The points in Fig. 4 appear to be more scattered than the diagonal line. This indicates that Linear Regression tends to underfit, as it is unable to capture the complexity of the non-linear relationship between the input and output variables.

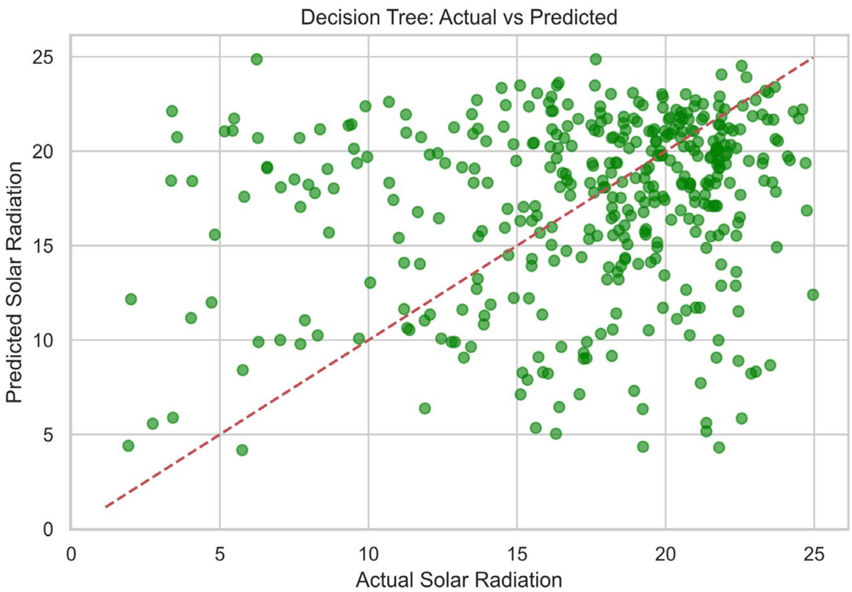

Fig 5. Actual Solar Radiation vs Predicted Solar Radiation Model Decision Tree Regressor

The relationship between the actual and predicted values in Fig. 5 yields an MSE of 37.42, an MAE of 4.58, and an R^2 value of −0.53. A negative R^2 indicates that the Decision Tree model performs worse than a simple baseline prediction based on the mean of the target variable. This suggests that the model failed to capture meaningful predictive patterns within the dataset.

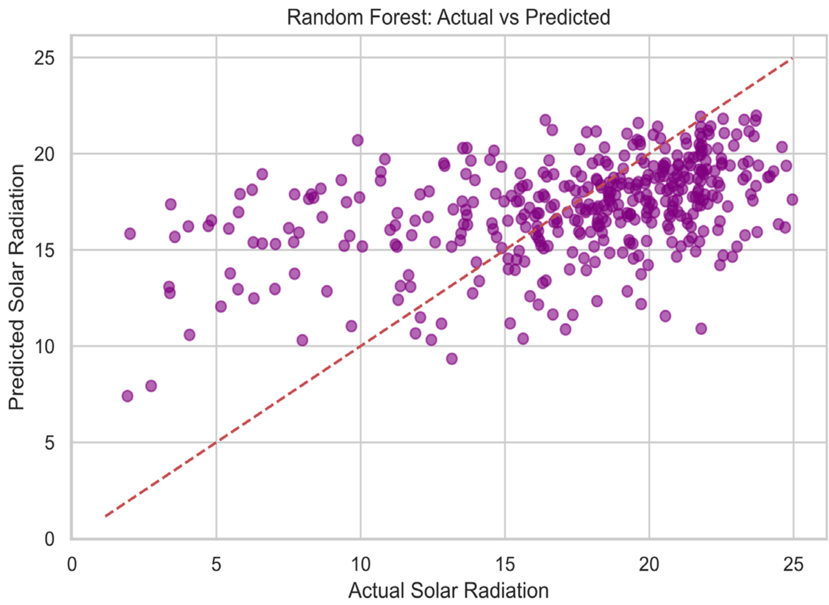

Fig 6. Actual Solar Radiation vs Predicted Solar Radiation Model Random Forest Regressor

The relationship between the actual value and the predicted value in Fig. 6 has an MSE value of 19.61, a MAE value of 3.42, and an R^2 value of 0.20. The points are distributed most densely along the diagonal line, indicating an elevated level of accuracy among the three and good generalization without excessive overfitting.

Discussion

The three machine learning models were trained and evaluated to predict solar radiation based on predetermined variables. The evaluation was conducted using three metrics:

Table 4. Model Evaluation Summary

Model	MSE	MAE	R^2
Linear Regression	19.79	3.47	0.19
Decision Tree	37.42	4.58	-0.53
Random Forest	19.61	3.42	0.20

Table 4 supports the selection of Random Forest achieved the best relative performance among the evaluated models in this study. This model effectively and efficiently balances the bias-variance trade-off. Therefore, it is suitable for predicting solar radiation in the real world even though the data is unstable and the relationship is non-linear.

It is important to note that both the predictor variables and the target solar radiation values were obtained from the NASA POWER dataset. Therefore, this study does not represent a validation against independent ground-based measurements such as pyranometer observations. Instead, the models should be interpreted as learning the internal relationships within the NASA POWER dataset. Thus, the results represent an emulation or approximation of NASA POWER solar radiation estimates rather than an independent validation of solar radiation prediction in Batam.

Implications and Recommendations

This study provides a path for practitioners in energy and environmental management in tropical regions. In practical terms, the Random Forest model obtained is a vital tool for the Batam City government and renewable energy agencies [16]. With an accuracy of ±3.42 MJ/m² in predicting daily solar radiation, the model can enable more precise planning of solar power plant (SPP) infrastructure, thereby maximizing local solar potential [4]. These findings can drive policies for solar power plants in Batam City. However, caution is still needed, as reliance on satellite data risks leaving biases in tropical regions, where dynamic cloud cover may not be fully recorded. Therefore, collaboration with the Indonesian Meteorological, Climatological, and Geophysical Agency (BMKG) is necessary to validate ground-truth data, which is key to mitigating these limitations.

4. CONCLUSION

This research approach indicates that the synergy between open satellite data and artificial intelligence can offer a viable pathway to overcoming energy data scarcity in remote areas. Among the evaluated models, the Random Forest model produced the best performance for predicting solar radiation in Batam City due to its ability to capture non-linear interactions between air temperature, relative humidity, rainfall, surface pressure, and wind speed.

However, while the model recorded an MSE of 19.61 and an MAE of 3.42, the resulting R^2 value of 0.20 must be interpreted with caution. This result indicates that the current meteorological predictors explain only about 20% of the variance in solar radiation, suggesting that predicting solar irradiance in Batam's coastal tropical climate remains challenging with the current set of variables.

The performance of the model highlights both the potential and the limitations of data-driven approaches in the Indonesian context [3]. On one hand, satellite reanalysis data can partially address the scarcity of ground-based radiation observations. On the other hand, the relatively low explanatory power suggests that additional meteorological or atmospheric variables are required to improve predictive capability.

These findings provide an important baseline for future solar energy modelling studies in tropical regions that experience complex atmospheric dynamics. Future research should integrate additional physically relevant predictors such as cloud cover indicators, aerosol proxies, or atmospheric transparency indices to enhance model reliability. In addition, validation using independent ground-based observations would further strengthen the scientific robustness of solar radiation prediction studies in Indonesia.

Overall, this research contributes to understanding the complexity of solar radiation modelling in tropical coastal environments and highlights the importance of interdisciplinary collaboration among meteorological institutions, energy practitioners, and data scientists to support the development of renewable energy systems in Indonesia.

REFERENCE

[1] L. Huang, J. Kang, M. Wan, L. Fang, C. Zhang, and Z. Zeng, "Prediction of Solar Radiation Using Various Machine Learning Algorithms and Its Implications for Extreme Climate Events," Front Earth Sci (Lausanne), vol. 9, April 2021, doi: 10.3389/feart.2021.596860.

[2] J. Fan et al., "Empirical Models and Machine Learning for Predicting Daily Global Solar Radiation from Sunshine Duration: A Review and Case Study in China," Renewable and Sustainable Energy Reviews, vol. 100, pp. 186–212, Feb. 2019, doi: 10.1016/j.rser.2018.10.018.

[3] M. Jamei et al., "Data-Based Model for Predicting Solar Radiation in Semi-Arid Regions," Computers, Materials and Continua, vol. 74, no. 1, pp. 1625–1640, 2023, doi: 10.32604/cmc.2023.031406.

[4] R. Ismayanti and W. Maulana Baihaqi, "Predicting the Potential of an Area to Become a Solar Power Plant Using Machine Learning," JIITE.

[5] V. Demir, "Evaluation of Solar Radiation Prediction Models Using AI: Performance Comparison in the High-Potential Region of Konya, Türkiye," Atmosphere (Basel), vol. 16, no. 4, Apr. 2025, doi: 10.3390/atmos16040398.

[6] Q. Li, M. Bessafi, and P. Li, "Mapping Surface Solar Radiation Predictions with a Linear Regression Model: A Case Study on Reunion Island," Atmosphere (Basel), vol. 14, no. 9, September 2023, doi: 10.3390/atmos14091331.

[7] L. P. Darman, Januhariadi, M. P. Yudha, and Aslan, "Assessment of NASA POWER Reanalysis Products as an Alternative Data Source for Weather Monitoring in West Sumbawa, Indonesia," in E3S Web of Conferences, EDP Sciences, Feb. 2024. doi: 10.1051/e3sconf/202448506006.

[8] I. K. Tanoli et al., "Machine learning for high-performance solar radiation prediction," Energy Reports, vol. 12, pp. 4794–4804, Dec. 2024, doi: 10.1016/j.egyr.2024.10.033.

[9] P. Setiawati et al., "SOLAR ENERGY GENERATION PREDICTION: A Machine Learning Approach for Network Stability and Efficiency," Jurnal Pilar Nusa Mandiri, vol. 21, no. 1, pp. 34–43, Mar. 2025, doi: 10.33480/pilar.v21i1.6126.

[10] U. V. Teja, M. Sai Kiran, V. Karthikeya, M. E. Murali, and T. Kumanan, "Prediction of Solar Radiation Using Machine Learning and Python."

[11] R. Srivastava, A. N. Tiwari, and V. K. Giri, "Prediction of Solar Radiation Using MARS, CART, M5, and Random Forest Models: A Case Study for India," Heliyon, vol. 5, no. 10, October 2019, doi: 10.1016/j.heliyon.2019.e02692.

[12] D. Ardiansyah, "COMPARISON OF SUNRADIATION PREDICTION MODELS BASED ON MACHINE LEARNING AT THE FATMAWATI SOEKARNO BENGKULU METEOROLOGICAL STATION," Megasains, vol. 14, no. 1, Sep. 2023, doi: 10.46824/megasains.v14i1.129.

[13] C. G. Villegas-Mier, J. Rodriguez-Resendiz, J. M. Álvarez-Alvarado, H. Jiménez-Hernández, and Á. Odry,

"Optimized Random Forest for Solar Radiation Prediction Using Sunlight Hours," Micromachines (Basel), vol. 13, no. 9, September 2022, doi: 10.3390/mi13091406.

[14] M. Attya, O. Abo-Seida, H. Mohamed, and A. Mohammed, "A Hybrid Deep Learning Framework for Solar Radiation Prediction Based on Satellite Images and Regional Data," Neural Comput Appl, July 2025, doi: 10.1007/s00521-025-11197-3.

[15] A. N. Oktaviani et al., "Analysis of Solar Radiation Prediction Using Machine Learning Algorithms and Bayesian Optimization Implementation in the Province of DKI Jakarta," Journal of Information Management & Information Systems (MISI), vol. 8, no. 1, 2025, doi: 10.36595/misi.v5i2.

[16] A. Mujtaba, "Towards Sustainable Energy Policies: Machine Learning Applications in Projecting Bio Solar Consumption in Indonesia," 2024, doi: 10.18196/jsp/v15i1.360.